Development of Wood -Thermoset Composites for use in Additive Manufacturing

A Dissertation

Presented in Partial Fulfillment of the Requirements for the

Degree of Doctor of Philosophy

with a

Major in Environmental Science

in the

College of Graduate Studies

University of Idaho

by

Berlinda O. Orji

Approved by:

Major Professor: Armando G. McDonald, Ph.D. (Distinguished Professor)

Committee Members: D. Eric Aston, Ph.D., Michael Maughan, Ph.D., P.E., Lili Cai, Ph.D.

Department Administrator: Jaap Vos, Ph.D.

May 2023

Abstract

This dissertation presents four different projects that aim at developing wood-thermoset composite systems that can be used for additive manufacturing (AM) purposes. AM is a promising technology that can aid in the utilization of sawmill residues with the direct fabrication of complex structures. With this goal in mind, the use of two traditional thermoset resins (phenol resorcinol formaldehyde (PRF) and melamine-modified urea formaldehyde (UF)) and a geo-based adhesive (sodium silicate (SS)) in composite fabrication were explored. Natural fibers of wood (40 and 200 mesh) and denim fibers were considered in high loadings from 50 to 90 wt.%. Material based extrusion technique of AM was used for this study. Curing studies and kinetics of the various resins and blends were explored using modulated differential scanning calorimetry (DSC) and activation energy was determined between 51 kJ/mol and 271 kJ/mol for PRF and wood blends, 100 kJ/mol and 367 kJ/mol for UF and wood blends; and 85 kJ/mol and 125 kJ/mol for SS and wood blends, respectively. The use of CO_2 as an alternative curing mechanism for SS and wood blends was explored at different reaction times, pressure and curing temperatures to aid in the reduction of thermal energy input in the production of composites and promote carbon sequestration. CO_2 uptake increased with exposure time and pressure. Wood 200 mesh fiber-SS composites showed better mechanical and thermal stability properties in comparison to wood 40 mesh-SS composites. The use of three modifiers (eggshells, corn starch and sulfonated castor oil (SCO)) were also studied to improve the processability and properties of the composite's blends. Fabricated composites all showed good shear thinning behavior which is an important factor in AM. Thermal stability analysis of composites which was determined using thermogravimetric analysis (TGA) was improved with the addition of wood fibers. Conclusively, Composites made with 50% wood fibers were successfully extruded with the PRF and SS resins but was not for the UF resin composites.

Acknowledgment

As my Ph. D journey gradually comes to an end, I would also like to express my immense gratitude to my academic advisor, Dr. Armando G. McDonald (Distinguished Professor) for been patient with me, encouraging and above all giving the best fatherly advice whenever needed. Working with him has vastly expanded my knowledge and skills in general research and science.

To my committee members, Drs. D. Eric Aston, Michael Maughan and Lili Cai, thank you so much for your encouraging words, guidance, and motivation all through these years. You all have really been my calm in the chaos.

I wish to express my gratitude to the financial support from the Idaho State Board of Higher Education, Idaho Global Entrepreneurial Mission (IGEM) and the University of Idaho P3 grants that funded me through this phase.

I sincerely thank my colleagues for their moral support and been my family in school away from home. It has really been a treasure having you all by my side all through this. THANK YOU!

Dedication

This thesis is dedicated to God Almighty, my late father, Engr. Peter Orji, my mother, Ezinne Mrs. Joy A. Orji, my husband, Ugonna E. Onwuchuluba, and my brothers (Jude C. Orji and Patrick C. Orji). I wouldn't have made it through on this ride without the support of my family: my late dad's words of encouragement, my mother's prayers, my brothers, and my husband's daily positive attitude towards life. You all mean so much to me and have kept me motivated. To my friends and the families of Jones-Mensah, Bangudu, Popoola, Oduro-Afriyie, Ugwu, Gideon, Kissi, and Onwuchuluba, thank you so much for your constant advice, support, and prayers.

Table of Contents

Abstract ii

Dedication iv

List of Tables xv

List of Abbreviations and Symbols xvii

Statement of Contribution xix

Chapter 1: Background and Research Objectives 1

1.1 Background 1

1.1.1 Thermoset resins 3

1.1.2 Thermoset Resin Curing Methods and Mechanisms 7

1.1.2.1 Thermal Curing 7

1.1.2.2 Photocuring 8

1.1.2.3 Radiation Curing 8

1.1.2.4 Microwave Curing 8

1.1.2.5 Chemical Curing 9

1.1.2.6 Carbonation Curing 9

1.1.2.7 Factors affecting Carbonation Curing 10

1.1.3 Thermoset modifiers 11

1.1.3.1 Egg shells (ES) 12

1.1.3.2 Sulfonated Castor oil 13

1.1.3.3 Corn Starch 14

1.1.4 Natural Fibers as Reinforcement in Thermosets 15

1.1.5 Effect of Fiber Loading and Particle Size in AM of Thermoset Composites 16

1.2 Additive Manufacturing Processes for Thermoset Composites 17

1.2.1 Material Based Extrusion 18

1.2.1 Thermoset Composite Performance Characterization Techniques 19

1.2.1.1 Mechanical Properties 19

1.2.1.2 Thermal Properties 20

1.2.1.3 Dynamic Scanning Calorimetry (DSC) 20

1.2.1.4 Thermogravimetric Analysis (TGA) 21

1.2.1.5 Rheology 21

1.3 Research Objectives 23

Chapter 2: Wood fiber - sodium silicate mixtures for additive manufacturing of composite materials, Orji, B. O., Thie, C., Baker, K., Maughan, M. R., & McDonald, A. G. (2022) 26

2.1 Abstract 26

2.2. Introduction 26

2.3. Materials and Methods 28

2.3.1 Materials 28

2.3.2 Composite Preparation 28

2.3.3 Sample Characterization 29

2.3.4 Thermal Analysis 29

2.3.5 Rheology 30

2.3.6 Extrusion System 31

2.3.7 Curing Extruded rods 31

2.3.8 Flexural, Water Soak, and Fire tests 31

2.4. Results and Discussion 32

2.4.1 Fiber Characterization 32

2.4.2 Blending of Wood-SS and Rheology of Wet mixtures 32

2.4.4. Extrusion of wood-SS blend 39

2.4.5. Flexural, Thermal degradation, Water Soak and Fire properties 42

2.4.6. Water absorption properties 45

2.4.7. Fire Test.....45

2.5. Conclusion 46

2.6. Acknowledgements.....46

Chapter 3: Flow, curing and mechanical properties of thermoset resins–wood-fiber blends for potential additive-manufacturing applications. Orji, B. O., & McDonald, A. G. (2023).....47

3.1 Abstract.....47

3.2 Introduction.....47

3.3 Materials and Methods.....49

3.3.1 Wood Fiber characterization 50

3.3.2 Electrospray Ionization Mass Spectrometry (ESI-MS) of the resins 50

3.3.4 Composite Preparation 50

3.3.5 Thermal analysis 51

3.3.6 Dynamic rheology 52

3.3.7 Extrusion 52

3.3.8 Fourier Transform Infrared Spectroscopy (FTIR) 52

3.3.9 Flexural testing.....53

3.3.10 Water Soak 53

3.3.11 Statistical Analysis 53

3.4. Results and Discussion 53

3.4.1 Wood Fiber Characterization 53

3.4.2 Resin Molar Mass Determination 53

3.4.3 Rheology and curing of resin and wood-resin blends.....54

3.4.4 Mechanical properties of cured composites.....68

3.4.5 Thermal and dimensional stability of cured blends 75

3.5 Conclusions 79
3.6 Acknowledgements 80
Chapter 4: Carbonation Curing and Kinetics of Wood-Sodium Silicate Composites 81
4.1. Abstract 81
4.2. Introduction 81
4.3. Materials and Methods 83
4.3.1. Materials 83
4.3.2. Wood Fiber Characterization and Sample preparation 83
4.3.3. Dynamic Rheology 84
4.3.4. Differential Scanning Calorimetry (DSC) 85
4.3.5. Carbonation curing and CO_2 uptake 86
4.3.6. X-ray Micro Computed Tomography (Micro-CT) Scanning 87
4.3.7. Flexural Properties 88
4.3.8. Thermogravimetric Analysis (TGA) 89
4.3.9. Statistical analysis 89
4.4. Results and Discussion 90
4.4.1. Fiber Characterization 90
4.4.2. Rheology 91
4.4.3. MDSC 92
4.4.2. CO_2 Uptake calculations 97
4.4.3: Microstructure, Density and Carbonation penetration depth 98
4.4.4. Bending Test Results 104
4.4.5. Thermal stability of the wood-SS composites by TGA 106
4.4.6. Statistical Analysis 111
4.5. Conclusions 113

4.6. Acknowledgment 113

Chapter 5: Modifying a Thermoset-Natural Fiber Composite Matrix for Application in Additive Manufacturing 115

5.1. Abstract 115

5.2. Introduction 115

5.3. Materials and Methods 118

5.3.1. Materials 118

5.3.2. Characterization of Wood Fiber and Modifiers 119

5.3.3. Composite Fabrication 119

5.3.4. Rheology 120

5.3.5. Differential Scanning Calorimetry (DSC) 121

5.3.6. Thermal Gravimetric Analysis (TGA) 121

5.3.7. Extrusion 121

5.3.8. Flexural properties 121

5.4. Results and Discussion 122

5.4.1. Characterization of modifiers 122

5.4.2. Rheology of resins and composite mixtures 123

5.4.4. Thermal Analysis 129

5.4.6. Extrusion 136

5.4.7. Flexural Properties 137

5.5. Conclusion 140

5.6. Acknowledgment 141

Chapter 6: Conclusion, Limitations and Future Recommendations 142

6.1 Conclusion 142

6.2 Limitations and Future Recommendations 142

Comprehensive References.....144

Appendix A.....196

List of Figures

Figure 1.1: Diagram showing the stages of thermoset curing (a) low molecular weight monomers, (b) formation of branching and linear growth, (c) gelation and increased network formation but incomplete crosslinking, (d) fully cured thermoset [26] 3
Figure 1.2: Structure of resorcinol [37] 5
Figure 1.3: Carbonation curing procedure on a laboratory scale [91]. 10
Figure 1.4: Chemical modification reactions for castor oil [125].....13
Figure 1.5: Structure of SCO [133].....14
Figure 1.6: Different kinds of reinforcement types: a) continuous long fibers, b) short fibers and c) particles in a matrix [158].....17
Figure 1.7: Different types of material extrusion extruders [171].....19
Figure 1.8: Capillary rheology setup [187].....22
Figure 1.9: Different dynamic rheology geometries [188] 23
Figure 2.1: (a) Optical micrograph (40x) of screened 40 mesh wood fiber and (b) size distribution curve from sieve analysis done on the screened 40 mesh wood fiber 32
Figure 2.2: (a) Elastic (G') and viscous (G") moduli versus frequency plots of SS and wood-SS blends and (b) flow curves (η* vs. frequency) for SS and wood-SS blends.....33
Figure 2.3: (a) Photograph of extrudates from the small and large capillary rheometer and (b) viscosity versus shear rate (flow curves) plots of wood-SS (50:50) blend by dynamic and capillary rheometry at 22^{o}C.....35
Figure 2.4: (a) Nonreversible heat MDSC heat flow thermograms of SS and wood-SS blends and (b) MDSC heat flow thermograms of wood fiber.....37
Figure 2.5: (a) Complex viscosity (η*) plots against temperature and (b) Tan δ plots against temperature for SS and wood-SS blends. 38
Figure 2.6: Isothermal TGA thermograms for wood-SS 50:50 blend at 60 and 105 °C. 39
Figure 2.7: Photographs of (a) smooth extruded wood-SS (50:50) rods and (b) extruded wood-SS showing sharkskin.....40
Figure 2.8: FTIR spectra of wood fiber, SS solution, wood-SS (50:50) wet mix, and wood-SS (50:50) cured at different times and temperatures.....42
Figure 2.9: TGA and DTG thermograms of wood-SS samples cured at different temperatures. 44

Figure 3.1: ESI-MS of (a) PRF resin (negative ion) and (b) UF resin (positive ion) 54
Figure 3.2: Rheological plots of (a) η* versus frequency for PRF resin and wood-resin PRF blends at 30°C, (b) η* versus frequency for UF resin and wood-UF blends at 30°C, (c) η* versus temperature for PRF resin and wood-PRF blends, (d) η* versus temperature for UF resin and wood-UF blends, (e) tan δ versus temperature for PRF resin and wood-PRF blends, and (f) tan δ versus temperature for UF resin and wood-UF blends.....59
Figure 3.3: Photographs of (a) successful wood-PRF (50:50) extrusion, (b) unsuccessful extrusion of wood-UF (50:50) mixture showing resin squeeze out at the end of the die, and (c) unsuccessful extrusion of wood-UF (50:50) mixture showing compaction and accumulation of wood fiber at the end of the screw. 60
Figure 3.4: Frequency sweep dynamic η* for comparable blends extrusion.....60
Figure 3.5: MDSC thermograms showing non-reversible heat flow curves for (a) neat PRF and wood-PRF blends and (b) neat UF and wood-UF blends at four different heating rates.....63
Figure 3.6: Plot of $-\ln(\beta/T_p^2)$ versus $1/T_p^2$ for a) wood-PRF blends and b) wood-UF blends; Conversion (α) plots versus temperature for (c) wood-PRF blends and (d) wood-UF blends at 10 °C/min; and activation energy (E_a) versus conversion (α) for (e) wood-PRF blends and (f) wood-UF blends 66
Figure 3.7: (a) TMA thermograms of cured PRF and UF resins, (b) DMA thermograms of tan δ of cured PRF and UF resins, (c) DMA thermograms of E′ of wood-PRF composites and (d) DMA thermograms of E′ of wood-UF composites, (e) DMA thermograms of tan δ of wood-PRF composites and (f) DMA thermograms of tan δ of wood-UF composites 72
Figure 3.8: FTIR spectra of (a) liquid PRF and cured wood PRF blends and (b) liquid UF and cured wood UF blends.....75
Figure 3.9: Thermogravimetric analysis thermograms of (a) wood-PRF composites and (b) wood-UF composites.....77
Figure 4.1: Perforated aluminum plates for SS-CO_2 rheology experiments (left and center) and 3D-printed chamber (right).....85
Figure 4.2: Schematic of the carbonation curing setup.....86

Figure 4.3 : Time sweep for SS wood blends in the presence of air and CO_2 showing G' and G" for (a) SS cured in air and CO_2 and (b) 40 mesh and 200 mesh air and CO_2 and (c) complex viscosity (η*) curves and (d) Tan δ curves. 92

Figure 4.4: MDSC thermograms showing non-reversible heat flow curves for (a) neat SS and 40 mesh wood-SS blends and (b) neat SS and 200 mesh wood-SS blends at 10 °C/min; Plots of $-\ln(\beta/T_p^2)$ versus $1/T_p^2$ for (c) SS and 40 mesh wood-SS blends and (b) neat SS and 200 mesh wood-SS blends; Activation energy (E_a) versus conversion (α) for (e) neat SS and 40 mesh wood-SS blends and (f) neat SS and wood-SS blends..... 94

Figure 4.5 :Plots of CO_2 uptake with respect to time at different pressure values..... 98

Figure 4.6: Photographs of cross sections of wood-SS cured composites showing the penetration depth of CO_2 treatment time at (a) 7 kPa and (b) 138 kPa 99

Figure 4.7: (a) Micro-CT cross-section slices showing penetration depth (yellow arrows) of reacted CO_2 with wood-SS cured samples plus controls and (b) density maps of reacted CO_2 with wood-SS cured samples plus controls, (c) plot of penetration depth for wood SS samples at different pressures and time 103

Figure 4.8: Thermograms from TGA analysis of cured wood-SS composites (a) % weight loss and (b) DTG curves at 7 kPa CO_2 pressure; and (c) % weight loss and (d) DTG curves at 138 kPa CO_2 pressure for 40 mesh wood-SS samples and, (e) % weight loss and (f) DTG curves at 7 kPa CO_2 pressure; and (g) % weight loss and (h) DTG curves at 138 kPa CO_2 pressure for 200 mesh wood-SS samples 108

Figure 4.9: 3D response surfaces for FM and FS with respect to pressure and time..... 113

Figure 5.1: (a) Loosened warp and weft and denim fibers, (b) optical microscopy image of individually separated warp and weft fibers, (c) SEM micrograph of BMES at 200x and laser scattering particle size distribution of BMES showing (d) volume % distribution and (e) number % distribution. 123

Figure 5.2: Frequency sweep curves of BMES, GCS, SCO modified and unmodified wood-PRF blends..... 126

Figure 5.3 : Comparison of dynamic and capillary rheology results of wood-PRF 50:50 blend. 129

Figure 5:4: Non-reversible heat flow curves for (a) neat PRF, Wood-PRF control, 5 and 10% denim fiber wood PRF blends and (b) PRF-BMES modified resin and (c) Wood-PRF-

BMES blends and (d) PRF-GCS modified blends and (e) Wood-PRF-GCS blends and (f) PRF-SCO modified blends and (g) Wood-SCO-PRF blends 131
Figure 5.5: Thermograms showing (a) TGA and (b) DTG for neat PRF, wood-PRF (control), 5% and 10% denim blend; (c) TGA and (d) DTG for PRF-BMES and Wood-BMES-PRF blends; (e) TGA and (f) DTG for PRF-GCS and wood-PRF-GCS blends; (g) TGA and (h) DTG of PRF-SCO blends and Wood-PRF-SCO blends 134
Figure 5.6: Photographs of successful extrusion runs of wood-PRF blends with the addition of modifiers showing (a) 10% SCO and (b) 10% BMES and (c) 10% GCS composites 137
Figure 5.7: Flexural properties showing (a) modulus and (b) flexural strength for compression molded modified and unmodified wood-PRF composites 138
Figure 5.8: Flexural (a) modulus and (b) strength of extruded modified and unmodified PRF-wood composites 140
Figure A2.1: Herb Grinder 196
Figure A2.2: Hamilton Beach Food Processor 196
Figure A2.3: Custom-built large capillary rheometer schematic: (1) Plunger, (2) Top Plate, (3) Frame Leg, (4) Barrel, (5) Capillary Die, (6) Base Plate. 196
Figure A2.4: Schematic diagram of the developed screw extruder (1) NORD Motor, (2) Shaft Adapter, (3) Bearing Block, (4) Hopper, (5) Barrel, (6) Die, (7) Base, (8) VFD. 197
Figure A3.1: Wood-resin extruder setup 197
Figure A3.2: G′ and G″ plots versus temperature for (a) neat PRF resin and (b) neat UF resin 197
Figure A3.3: Full scale MDSC thermograms showing non-reversible heat flow curves for (a) neat PRF and wood-PRF blends and (b) neat UF and wood-UF blends at four different heating rates 198

List of Tables

Table 1.1: Length and width of some natural fibers [154] 16
Table 2.1: Dynamic viscosity values at 1 Hz and flow behavior index (n) and consistency coefficient (K).....34
Table 2.2: Viscosity values for small and large capillary rheology dies 36
Table 2.3: MDSC peak values for wood and SS samples.....37
Table 2.4: Wet and cured density calculations for extruded wood-SS 50:50 and 60:40 blends. 40
Table 2.5: Bending strength values for wood-SS (50:50 and 60:40) extruded samples cured at different temperatures.....43
Table 2.6: Thermogram peak values for the cured wood-SS composites.....45
Table 3.1: Complex viscosity (η*) of the PRF and UF resins and wood-resin blends at 1 Hz, 30 °C, and power law fitted model parameters K and n as well as goodness of fit (R^2)..56
Table 3.2: Kinetic parameters for neat resin and wood-resin blends calculated using Kissinger's and Cranes model from DSC data.....66
Table 3.3: Mechanical properties of cured wood resin composites.....69
Table 3.4: Thermogravimetric data for wood-PRF and wood-UF composites 77
Table 3.5: Water absorption (WA) and thickness swell (TS) values for the wood-PRF and wood-UF composites after a 24 h water soak test.....79
Table 4.1: Summary of parameters considered for sample preparation. 86
Table 4.2 : Micro-CT tomography scanning parameters..... 88
Table 4.3 : Experimental set up for statistical analysis of wood-SS curing treatments..... 89
Table 4.4: Kinetic parameters for SS, 40 mesh and 200 mesh composite blends calculated using KAS model from the MDSC data..... 96
Table 4.5: CO_2 (%) uptake calculations for the various SS and wood-SS samples at different CO_2 treatment pressures and treatment time 97
Table 4.6: Calculated density of air cured (control) carbonated (CO_2 cured) wood-SS composites. 103
Table 4.7: Mechanical properties of 40 mesh and 200 mesh Wood SS cured composites... 105

Table 4.8: TGA thermogram curve values for thermally cured and carbonated wood SS blends 108
Table 4.9: DTG thermogram curve values for thermally cured and carbonated wood SS blends 110
Table 4.10: Statistical analysis of CO_2 curing process parameters results with respect to FM (GPa) 111
Table 4.11: Statistical analysis of CO_2 curing process parameters with respect to the composites FS response. 112
Table 5.1: Dynamic viscosity values at 1 Hz and flow behavior index (n) and consistency coefficient (K) of neat PRF and wood-PRF, modified PRF with BMES, GCS, SCO, Denim, and modified wood PRF composites 127
Table 5.2: MDSC exothermic peak data for PRF-Wood/denim blends at 10 °C/min 132
Table 5.3: MDSC exothermic peak data for BMES, GCS, and SCO modified PRF and wood-PRF blends at 10 °C/min 132
Table 5.4: TGA thermogram data (T_{onset}, min and max DTG peak, and residual weight at 800 °C) for unmodified and modified PRF and WPRF blends 135

List of Abbreviations and Symbols

Abbreviations

3D	3-dimensional
µCT	Micro Computed Tomography
AM	Additive Manufacturing
ATR	Attenuated total reflection
ß	Heating rate
BMES	Ball-milled Eggshells
CO_2	Carbon dioxide
DMA	Dynamic Mechanical Analysis
DSC	Differential scanning calorimetry
DTG	Derivative thermogravimetry
E_a	Activation energy
ESI-MS	Electrospray ionisation mass spectrometry
FDM	Fused Deposition Modelling
FFF	Fused Filament Fabrication
FM	Flexural Modulus
FS	Flexural Strength
FWO	Flynn–Wall–Ozawa
FTIR	Fourier Transform Infrared
GCS	Gelatinized Corn Starch
KAS	Kissinger–Akahira–Sunose
PRF	Phenol Resorcinol Formaldehyde
SCO	Sulfonated Castor oil
SEM	Scanning Electron Microscopy
SS	Sodium Silicate
UF	Urea Formaldehyde
TGA	Thermogravimetric Analysis

TMA	Thermo-Mechanical Analysis
WA	Water absorption

Symbols

ΔH	Enthalpy
A	Pre-exponential Factor
G’ or E'	Storage modulus
G” or E"	Loss modulus
δ	delta
η*	Complex Viscosity
K	Consistency coefficient
n	Shear thinning component
α	Conversion
T_p	Exothermic Peak Temperature
γ	Shear rate

Statement of Contribution

The following authors made substantive contributions to the publications in Chapter 2 and Chapter 3.

Chapter 2: Wood fiber - sodium silicate mixtures for additive manufacturing of composite materials, Orji, B. O., Thie, C., Baker, K., Maughan, M. R., & McDonald, A. G. (2022)

Orji, B. O.: methodology, validation, formal analysis, investigation, data curation, writing original draft preparation, and visualization.
Thie, C.: methodology, validation, formal analysis, investigation, data curation, and writing original draft preparation.
Baker, K.: conceptualization, project administration and funding acquisition.
Maughan, M. R.: methodology, validation, supervision, project administration and funding acquisition.
McDonald, A. G.: conceptualization, methodology, validation, formal analysis, writing – review and editing, visualization, project administration and funding acquisition.
All authors have read and agreed to the published version of the manuscript.

Chapter 3: Flow, curing and mechanical properties of thermoset resins–wood-fiber blends for potential additive-manufacturing applications. Orji, B. O., & McDonald, A. G. (2023)

Orji, B. O.: conceptualization, methodology, validation, formal analysis, investigation, data curation, writing—original draft preparation, and visualization.
McDonald, A. G.: conceptualization, methodology, validation, formal analysis, writing—review and editing, supervision, project administration and funding acquisition.
All authors have read and agreed to the published version of the manuscript.

Chapter 1: Background and Research Objectives

1.1 Background

Lumber processing over the years has generated large amount of wood residues of which part is used for particle board production and most, for energy [1]. The secondary processing of these 2-dimensional materials or particleboard for the fabrication of new products have also contributed to the accumulation of waste due to the complex machining, sheathing, milling etc. to transform them into final products [2]. These traditional methods of fabricating consume production time, with high energy consumption and low design flexibility. Additionally, industries and consumers have been looking for more sustainable ways to reduce waste whilst having resources that pose less risks to the environment, health, and safety [3]. Most of these wood residues generated from traditional manufacturing processes also end up in landfills with just a little amount recycled into useful products [4]. According to the United States Environmental Processing Agency (EPA), in 2018, landfills received 12.2 million tons of wood and only 17.1% was recycled [5]. A tactical solution and technology which has helped in this reduction and recycling of waste with a more sustainable production is additive manufacturing (AM) [6] [7]. Additive manufacturing (AM) involves the direct fabrication of complex structures using layer to layer distribution of the raw materials to attain the desired end products. This process was introduced in the 1980s, and has aided the reduction of waste, creating cost effective and reliable fabrication of materials [8], [9]. To attain this process, 3-dimensional (3D) printers with a computer aided design (CAD) are utilized which optimizes logistics, improves customization and design accuracy, promotes sustainability and generates high quality products [10].

Different kinds of polymeric materials have been additively manufactured with most falling under the broad matrix categories of thermoplastics and thermosets. Although AM of thermoplastic polymers and composites have been focused on largely in the past years, thermosetting polymeric materials offer superior properties with low viscosities and low temperature handling suitable for AM [11]. Thermoplastics are materials that melt upon heating and solidify on cooling. They can also be reshaped due to the weak bonds and Van der Waal interactions they possess [12]. Thermoplastic polymers in AM undergo certain issues of temperature gradient between layers which results in warping, and weak interfaces.

Thermosets form crosslinks that are chemically joined and, in most cases, cannot be reversed [13]. Thermosetting polymers do not require thermal energy to fabricate which allows them to be processed at room temperature or slightly increased temperature to yield a crosslinked structure with superior properties. Some issues associated with thermoset polymer AM includes long time post curing, complex geometry handling, lower toughness amongst others [14] [15].

Composites are a system comprising of two or more materials put together and are responsible for generating a new material with properties superior to the individual materials used for fabrication of the system. Two distinct phases of a matrix and the reinforcing phase make up a composite system [16]. The matrix phase is mostly a continuous phase and is responsible for keeping or gluing the composite in place whilst protecting the reinforcing phase from issues of chemical exposure, environmental conditions, degradation etc. [17]. Typical categories of these matrix phases are polymeric matrices of thermoplastics and thermosets. In most cases, the reinforced phase is immersed in the matrix. Examples of the reinforcing phases includes, particles and fibers [17]. These reinforcing phases provide additional strength to the matrix, improve stiffness, and impact resistance of the matrix. The final performance of a composite system mostly depends on the volume or mass percentages of the matrix to reinforcements, the types of individual materials used, and how the composite construction is done [18].

Composites can either be fibrous, particulate, or nanoscale based depending on the size of the reinforcements. Fibrous composites could have fibers that vary in length or remain continuous in the system [19]. A random orientation can be used to distribute shorter fibers in a matrix while longer fibers can be oriented differently depending on the required post product application [20]. Lignocellulosic materials including wood can be used as reinforcement or as a filler which promotes the use of natural based materials and decreases the use of petroleum based polymers and materials [21]. This also promotes biodegradability, recyclability and improved properties of the end product [1]. Other common reinforcements used are glass fiber, carbon fiber, and organic fibers amongst others [22]. Important factors to consider in the fabrication of these filled composites are interfacial adhesion between the matrix and the filler, since this will be responsible for better properties. Composites are used

in different applications biomedically, underwater, sporting equipment, construction, transportation applications amongst others [20] [22].

1.1.1 Thermoset resins

Thermoset resins are a class of polymer matrix system that chemically form crosslinks between chains. The formation of these crosslinks is called curing where reactive monomers are converted to a stable three dimensional polymer matrix [23]. These crosslinks can be initiated either thermally, or with the addition of activators or catalysts. The reaction begins with two monomeric components having low molecular weights and covalently bonding to increase their molecular weight (Figure 1.1a). Reaction continues to form a linear growth and branching of prepolymers are formed (Figure 1.1b) and this continues to form a gelled network (Figure 1.1c). Upon complete crosslinking (also known as vitrification) (Figure 1.1d), the reactions and polymers mostly cannot be reformed, reused, or regenerated. They also become insoluble due to the strong covalent bonds present and well bonded three-dimensional structure after complete curing. Due to their thermal resistance, they are well suitable for temperature resistant applications [24] [25].

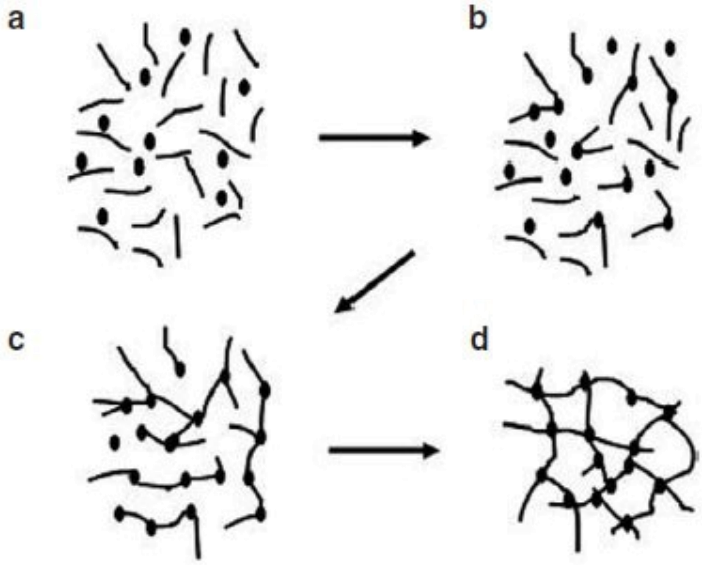

Figure 1.1: Diagram showing the stages of thermoset curing (a) low molecular weight monomers, (b) formation of branching and linear growth, (c) gelation and increased network formation but incomplete crosslinking, (d) fully cured thermoset [26]

There are different classes of thermoset resins which fall broadly under the synthetic (formaldehyde based and epoxies), biobased, or geopolymer based thermosets. Historically, Bakelite, was the first synthetic thermosetting polymer, fabricated from phenol and formaldehyde in 1909 [27]. Alkyds, which are vegetable oil modified polyesters, and urea formaldehyde (UF) amino resins were developed and patented in 1929 and 1923, respectively [28]. Melamine formaldehyde thermosetting polymers were fabricated and patented in 1940 [29]. Dow Corning introduced Silicon based polymers and epoxy resins with its patent in 1942 [30]. The patent of epoxy was granted to Swiss chemists, Schlack and Castan and the American chemist Greenlee in the 1930s even though the polymer had been developed years before that [31].

Most thermosets are synthetic based with common examples of epoxy and formaldehyde-based thermosets. Epoxies are low molecular weight prepolymers that have more than one epoxide group, and are usually synthesized by the reaction between diglyceryl ether of bisphenol A (DGEBA) and epichlorohydrin [32]. Epoxies are commonly used for high performance coatings, for bonding adhesives, laminations and in different fields where they act as fiber reinforcing materials. Epoxies are probably the most used thermosets in AM due to their excellent thermal, chemical resistance, and biocompatibility. A wide array of fillers in form of nano-clay [33], carbon fiber [34], ceramic powder [35] etc., have also been explored to hold its shape and improve mechanical, rheological and electrical properties.

Formaldehyde based class of resins constitute about 50% of the adhesives used today due to their ease of manufacturing, understandable technology/chemistry and easy optimization of their formulations [36]. They are mainly liquids with either linear or branched oligomeric and polymeric molecules. Their curing reactions could either be acidic, or alkaline. A few examples of these thermosets are phenolic resins, urea and melamine-based resins, amino plastic resins and resorcinol resins. Resorcinol in the presence of formaldehyde have been used since World War II and have shown to be durable with great structural and low temperature curing properties in the bonding of wood, wooden beams and arcs [37]. Resorcinol structurally has two hydroxyl groups on the benzene ring located at the 1 and 3 positions (Figure 1.2). The reactive groups are located on the 2, 4 and 6 positions of the ring with 4 and 6 either at the ortho or para position to the hydroxyl groups, making the reactive positions doubly activated [38].

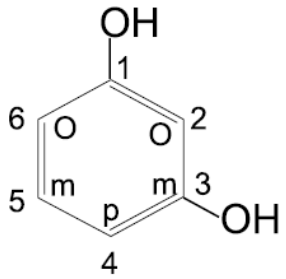

Figure 1.2: Structure of resorcinol [37]

To synthesize phenol resorcinol formaldehyde (PRF) resins, resorcinol is mixed with phenol formaldehyde (PF) resin to accelerate the curing of PF resin with several co-condensation reaction pathways [39]. It is assumed that the resorcinol will react with the hydroxy methyl groups on the PF resin to form methylene linkages. PRF resins are commonly used in structural applications, glulam beams and boat constructions due to their water resistivity. In the presence of resorcinol in PRF resins contribute to its rapid cure to harden in ambient and cold conditions [40].

UF resins are synthesized from the reaction of urea and formaldehyde which react to form intermediates like methylol urea and dimethylol urea. The synthesis can vary with the addition of different chemical additives like melamine which can alter the properties of the UF resin and reduce the emissions of formaldehyde. Generally, the synthesis occurs in two stages with the first stage involving the hydroxymethylolation of urea by the addition of formaldehyde to form mono-, di-, and tri-methylol ureas under basic conditions. The second stage involves the condensation of the methylol ureas to low condensation polymers which is dependent on an acidic pH to yield methylene bridges and methylene ester linkages [41] [42]. UF resins are a major binder used for wood composites, particleboards, plywood etc. Although they have issues of low water resistance, and formaldehyde emissions, they are less expensive with a high curing rate and good adhesion [43]. The use of UF and PRF thermosets in AM is still a new area of research with few studies exploring their use. Extrusion based 3D printing of UF resin with up to 25 wt.% wood fibers was explored yielding composites with non-structural application properties [44]. AM of wood waste floor and glass fibers in the presence of UF was explored with tensile strength increasing by 73% for the additively manufactured composites [45].

Issues of formaldehyde emissions from formaldehyde-based thermosets have resulted in the generation of eco-friendly bio-based adhesives with reduced environmental hazards. Biobased thermosets are polymeric materials synthesized from renewable raw materials or, resources that promote sustainability and have the potential for reducing its CO_2 footprint [46]. These renewable sources are mostly from plant sources in form of vegetable oils [47]. The functional groups in the oils are easily utilized with the carbon-carbon bonds polymerized either by free radical or cationic polymerization reactions to produce thermosets by triglycerides crosslinking [48] [49]. Epoxidized soybean oil is a commercially available plant oil synthesized resin used as a lubricant, plasticizer, lubricant, pigment dispersing agent amongst other uses. Other examples of natural based oil used for thermosets are cardanol for DGEBA/anhydride systems, rosin for rosin based epoxies, lignin for epoxy resins amongst others [50]. These thermosets, due to their raw material and low cost, are a good substitute for synthetic based thermosets to reduce the ecological effect of hazardous emissions from the latter thermosets [51].

Geopolymers are amorphous inorganic macromolecules formed by condensation reactions of aluminosilicates materials [52] [53]. They are fabricated by combining an aluminosilicate source material with an alkaline activator, such as sodium silicate (SS), to form a geopolymer gel. This gel hardens to form glass like material with properties similar to concrete [54]. A few examples of geo-polymeric materials are rice husk ash, metakaolin, blast furnace slag amongst others. Geopolymer materials are used in different applications for building materials, 3D printing, as catalysts, coatings, decorating materials amongst others [55] [56] [57] [58]. The use of geopolymers of the poly sialate-disiloxo type, which hardens like thermosetting resins for adhesives have been studied and considered in the past years. Their high flame retardant properties and mechanical strength makes them useful for sustainable and structural applications [59] [52]. They are more eco-friendly in comparison to formaldehyde-based thermosets. They have the potential of promoting CO_2 capture while reducing greenhouse gas emissions.

SS or water glass, a geo-based polymer, is a widely used raw material industrially which is mostly produced from the fusion of sodium carbonate and high quality quartz sand at high temperatures between 1300 °C and 1600 °C [60]. Several studies have implemented the use of SS in AM with 3D printed objects having improved strength and exhibiting

properties similar to ceramics [61]. Henke and Treml (2012), explored the use of sodium silicate as binder for wood chips in 3D printing of large scale solids [62]. SS has also been explored as a binding agent for the 3D printing of diamond powders [63]. The use of SS in the 3D bioprinting of scaffold to eliminate biological bone tissue defects has also been investigated [64].

Although there are different types of hybrid thermosets available in the current market which are not discussed here, this dissertation will focus on PRF, UF, a geo-based resin (SS) and their use in natural fiber composites and AM.

1.1.2 Thermoset Resin Curing Methods and Mechanisms

The outstanding mechanical properties of thermosets which make them reliable in different applications can be attributed to the proper curing and crosslinking reactions that occur within the matrix. A few types of curing methods are discussed and summarized below.

1.1.2.1 Thermal Curing

Thermal curing is the most implemented curing method which uses external heat from ovens but, this is time dependent and mostly results in an overuse of energy [65]. This reaction involves the exposure of the thermoset sample to high temperatures to facilitate the crosslinking reaction in the matrix. The temperature and time of crosslinking is dependent on the type of polymer and expected properties of the final material. Cooling of the cured polymer is essential to ensure the stability of the crosslinked networks. Thermal curing can be classified either under convection, conduction, inductive heating, ultrasonic heating amongst others with each having their pros and cons [66]. Disadvantages of thermal curing includes high energy usage, thermal expansion coefficient issues with different metals used, temperature differences arising from heat transfer and resins shrinkage during cure [67]. A few resin systems that are commonly thermally cured are phenol, melamine, and urea formaldehyde-based thermosets. These resin systems typically undergo different condensation reactions to achieve the required high molecular weight crosslinked structure [68] [69].

1.1.2.2 Photocuring

This curing process requires the use of a photo initiator to initiate photo polymerization or photocuring. Resins or thermosets that are cured using this could either be classified under free radical or ionic depending on the reaction scheme [70]. Typically, a photosensitive material or monomer is exposed to ultraviolet (UV) light to start polymerization or crosslinking. An optical absorber is used to monitor the penetration depth of the light and the polymerization process [70]. Photocurable resins are used for a wide range of applications from dental, automotive, to thin films applications in different industries. Epoxies, acrylates and vinyl esters are examples of photocurable polymeric resins commonly used [71]. High crosslinking and photopolymerization yield increased stiffness and improved mechanical properties. The process of photocuring also offers faster curing times, low energy requirements and unique material properties [15].

1.1.2.3 Radiation Curing

This involves the use of X-rays, ultra-violet (UV) light, and electron beams for the curing of thermosets. The crosslinking of the thermoset polymers is associated with their exposure to these rays. The penetration depth of the individual rays varies with X-rays having more penetration than UV light and electron beams (EB) even though curing time with X-rays is longer. It has been suggested that X-rays work better with thick samples and electron beams for thinner samples [72]. UV and EB curable resin types include polyesters, acrylics, urethane bismaleimides, urethane acrylates, epoxies amongst others [65] [73]. Serious radiation hazards are also connected to the utilization of these curing methods. Epoxies are an example of thermosets that can be cured using this method. Radiation curing of thermosets offers advantages of high modulus, good adhesion to surfaces and low viscosity but with brittleness and penetration issues into thick layers [74].

1.1.2.4 Microwave Curing

The use of microwaves serves as an alternative to thermal curing of thermoset composites but is not popularly considered due to less availability of appropriate equipment [75]. The dielectric properties of the resin to be cured is essential to allow the selective heating of the adhesive. Its advantages over thermal curing include the easy turn on and off

reactions, uniform cure and easier penetration into thicker polymers with increased rate of reactions [76]. Microwave curing uses a wave range of 1 to 90 GHz and thermal conductivity properties of the material should be understood to enable he proper adjustments as dielectric properties change with temperature [77]. Several studies have employed the use of microwave curing on epoxies, tung oil based thermosets, and polydimethylsiloxane elastomers with reported improved properties in comparison to other curing methods [78], [79] [80].

1.1.2.5 Chemical Curing

Chemical curing involves the addition of a chemical catalyst to the thermoset which triggers the crosslinking reaction. Reactions can occur at room temperature or slightly elevated temperatures with the addition of initiators or catalysts to the matrix [81]. Phenolic resins, epoxies, can be easily catalyzed through this process. Resorcinol resins will be catalyzed with the addition of formaldehyde to initiate crosslinking [82] [83]. Epoxy resins require an amino based hardener or can be catalyzed by thiol or alcoholic compounds [84]. Aromatic polyester-based resins are catalyzed with the addition of a free radical initiator such as organic peroxides or aliphatic ketones which initiate fast polymerization . The presence of accelerators further shortens the gelation time of the polyester resins and quickens the polymerization process.[85], [86].

1.1.2.6 Carbonation Curing

Carbonation curing is the exposure of reactive components to a CO_2 rich environment with less energy consumption over a period of time [87]. This process in previous years have been popularly used in foundry cast molds for increased strength [88] [89]. Carbonation curing can also be used with other curing methods like heat (thermal) or water curing (for cement composites) to achieve the required crosslinking and properties of the composite [90]. These other curing methods are called post curing conditioning methods to allow for the proper reaction of reactants that did not fully react with the CO_2 gas. The CO_2 acts as a reactant when absorbed in the medium which causes the binding of the networks in the matrix with improved properties depending on the duration of sample exposure to CO_2. [91]. This process of curing is mostly used for cementitious, geopolymer materials and binders. The fixation of CO_2 into the calcium and magnesium carbonate composition of fresh

concrete creates stable minerals thermodynamically which improves the properties of the system [92]. Alkali activated materials (AAM) like fly ash, blast furnace slag which show similar properties to cement in the presence of alkali materials like sodium hydroxide (NaOH) or SS, can be CO_2 cured and have been investigated to have better mechanical strength in the presence of the gas [93] [94]. This is an efficient curing process that can help mitigate the greenhouse gas emissions that are causing environmental and health hazards. Typically, the process of carbonation on laboratory scale involves a three-phase processing approach (Figure 1.3) which can vary depending on the mixtures used. Most of these lab-scale studies are carried out in closed chambers or reactors to promote the proper diffusion of the gas and obtain a higher carbonation rate [95].

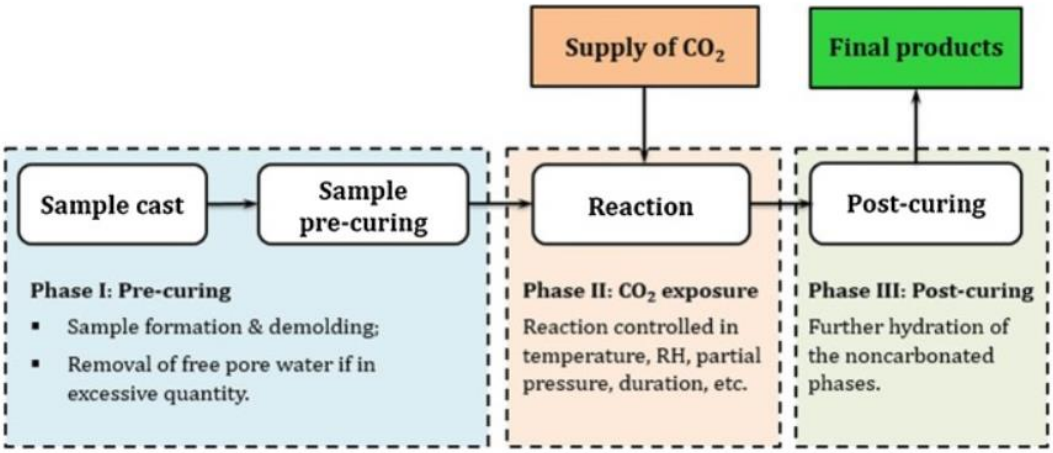

Figure 1.3: Carbonation curing procedure on a laboratory scale [91].

Improved mechanical, flame retardant and thermal degradation properties have also been recorded in studies that incorporated carbonation, validating the use of the process and creating more research focus on its use [96] [97] [98].

1.1.2.7 Factors affecting Carbonation Curing

A few major factors that affect the carbonation curing of materials range from time of carbonation, moisture, relative humidity, temperature pressure to concentration of CO_2.

Moisture plays an important role in carbonation curing of fresh concrete and AAM, but its quantity will have to be monitored to give room for the proper absorption of the CO_2 gas. An excess of moisture or water in the pores will block the diffusion of CO_2 limiting the

degree of carbonation in the matrix [99] [100]. The diffusion of CO_2 through the pores of the system or cement or AAM composites and carbonation degree is influenced by high pressure and concentration. Zhan et al (2016) observed that with the increase of CO_2 pressure from 0.01 MPa to 0.05 MPa, carbonation degree increased by 4.4% [101]. Increased compressive strength was also observed in a study of CO_2 cured dry cement pressed pastes from 1 to 20% [102]. At low CO_2 concentrations, a longer sample exposure time will be required to attain a higher degree of carbonation [103].

Temperature with carbonation reactions is very important since at high temperatures, CO_2 solubility in water decreases, but reaction kinetics increases [104]. A study on the effect of temperature on CO_2 curing of carbonated cement pastes showed the increase in carbonation depth and strength with an increase in temperature from 5 to 20°C [105]. Curing time with respect to concentration and pressure influences the strength of cured samples. Yan and Wang (2021) obtained an increased carbonation curing and compressive strength with longer CO_2 exposure time in their study of biochar-blended mortar using accelerated carbonation [106]. Some studies have also stipulated that an extended period of carbonation curing can cause a reduction in the properties of the cured samples due to the expansion of the composites that can lead to voids and cracks [107] [108]. Other factors that can directly or indirectly affect carbonation curing include the composites pH, the kind of additives and reactants used, and the porosity of the composite [109].

1.1.3 Thermoset modifiers

The major issues accompanied with thermoset polymers during AM are the extended time required for curing at high temperatures and flowability of the resin matrix. Since most materials are required to hold their shape during AM for successive layer stacking this can cause curing issue during the AM process. Issues of resin cost, hazardous emissions, composite production cost, influence the total fabrication of end products, hence the need for solutions. To aid the resolving of these issues, the use of additives or modifiers and reinforcements have been studied to give the required rheological behavior, reduce emissions during high temperature curing, and optimize production cost by reducing resin requirement for the AM process [110] [111]. Polymer additives or modifiers are broadly categorized under stabilizing and functional modifiers. Stabilizing modifiers aids in reducing the

degradation of polymers at high temperatures giving them an improved thermal stability. Functional modifiers are responsible for improving the mechanical, flame retardant, flow properties etc. of the polymer. These modifiers could either be in liquid, or solid state depending on the application [112]. Plasticizers, which are a type of functional modifier, improves the processability of the material and reduces the brittleness of polymers and improve flexibility. Examples of plasticizers include phthalates, adipates, benzoates, and citric esters. Lubricants, another form of functional modifier, helps to improve the flow properties of polymers. Examples are fatty acid salts, esters and waxes [113]. The use of fillers as modifiers also helps to increase the polymer bulk and improve properties [114]. There are so many examples of modifiers used in previous studies but for this dissertation, the use of eggshells (ES), sulfonated castor oil (SCO) and corn starch will be evaluated and discussed.

1.1.3.1 Egg shells (ES)

Chicken ES is a popular domestic and industrial biowaste material generated in significant quantity that is mostly discarded or used as fertilizer, for absorbing of heavy metals amongst other applications [115]. The unused proportions of this biowaste end up disposed in landfills and can pose environmental hazards and soil pollution if not properly handled [116]. It is an organic material with about 94 to 96% calcium carbonate ($CaCO_3$). Due to its nano porous structure and good mechanical properties, it has been considered as a modifier for most epoxies and polymeric materials [117] [118]. Carbonized and uncarbonized forms of ES have been used in the fabrication of glass fiber filled thermoset composites with improved mechanical properties [119]. A calcinated form of poultry ES powder has also been combined as a filler with pineapple fiber and epoxy which improved thermal, mechanical properties, hydrophobicity and wear properties of composites [120]. For AM, different compositions of ES powder has been studied and used to enhance the thermal stability, flow, thermal, decomposition, tensile strength of polylactic acid (PLA), epoxy, poly(ε-caprolactone), and polyester matrices [121] [122] [123] [124]. These studies confirm the importance of ES in AM and composites.

1.1.3.2 Sulfonated Castor oil

Castor oil, which is an organic oil extracted from a large shrub which notably grows in the wild, is a triacylglycerol that contains different fatty acids and glycerol. The fatty acids comprises of up to 90% ricinoleic acid which makes it very useful for different applications in the chemical industry [125]. It possesses different chemical and physical properties, and it has been ascertained that heating it up to higher temperatures expands the possibilities of its application. Due to it not been an edible oil, it is not in the competitive market with edible oils which makes it suitable for industrial based purposes. It is also used as a lubricant for equipment in extreme conditions due to its high viscosity even at high temperatures. In recent years, it is been used as a functional fluid, for paints, polymers, foams etc. [126]. Castor oil can be chemically modified into other polymers via different reactions as seen in Figure 1.4 depending on the functional group [127].

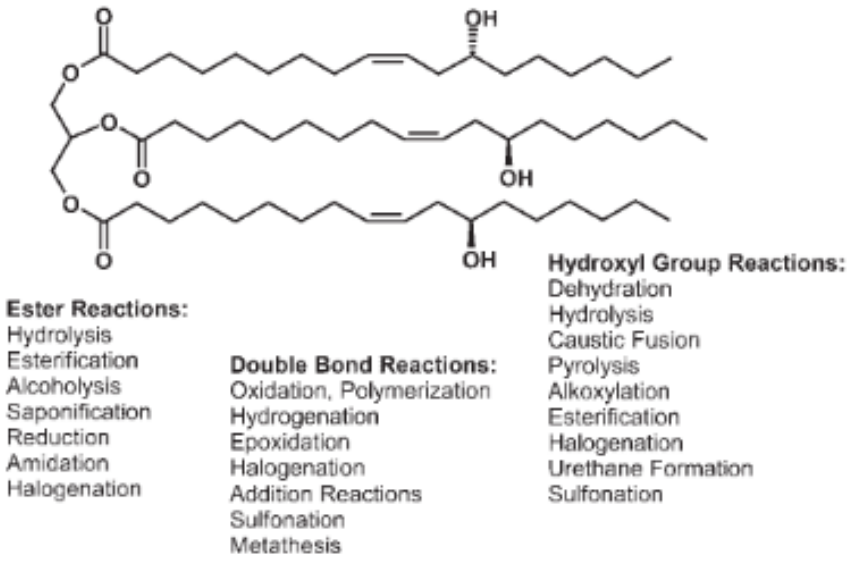

Figure 1.4: Chemical modification reactions for castor oil [125]

One of these chemical modification reactions is its sulfonation where sulfuric acid is directly added to produce sulfonated castor oil (SCO) (Figure 1.5). It is a fast and direct reaction that yields an oil that is soluble in water and can be used for its emulsification and dispersant properties [128]. A major reaction in the sulfonation results in the esterification of the hydroxyl groups of the ricinoleic acid making it have better hydrolytic stability [129]. SCO has also been used to improve the lubricity of downhole fluids in drilling [130]. SCO

has played an important role in a traditional leather fat liquoring agent [131]. Modified castor oil was used in a study to improve the melt processing, mechanical, thermal and rheological properties of PLA [132].

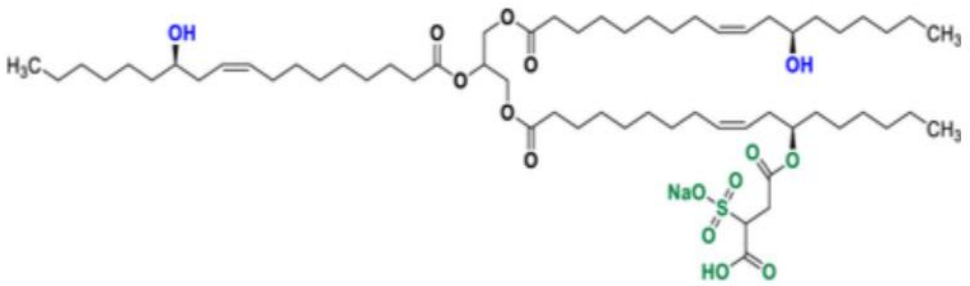

Figure 1.5: Structure of SCO [133]

Domínguez-Robles et al (2019) used castor oil for the proper dispersion and coating of PLA and tetracycline pellets in the bio-3D printing of lignin-based antioxidant PLA composites [134]. Since SCO is an emulsifier, and helps with dispersion, this study aims to use SCO for proper dispersion of PRF on natural fibers while promoting dispersibility and rheological properties of the blended mixture.

1.1.3.3 Corn Starch

Starch contains two major polymers of amylose which is linear and amylopectin which is a highly branched polymer. They both have the same repeating unit of D-glucose, but the connecting linkages are different. Starch is a major abundant polysaccharide in plants with the amylose structure connected by the α(1,4) bond and amylopectin by the α(1,4) bond with 5 to 6% of α(1,6) at the branched points. Its glycosidic and hydroxyl groups are responsible for its reactivity [135]. In natural starch, polysaccharide chains are packed in granules with sizes from 1 to 100 μm. It is a polymer used in several industries for the fabrication of food, chemicals, textiles amongst other complex polymers which makes it a challenge due to its competitive market demand [136]..The different properties of starch such as size, amylose to amylopectin ratio, obtained from varying sources are affected by environmental conditions, agricultural practices, amongst other factors. These different properties will affect its interaction with other polymers [137] [138]. The hydrophilicity of starch also makes its useful in commercial applications [139]. The solubility and reactivity of

corn starch in cold environments is low and calls for necessary modifications like gelatinization which activates the hydroxyl groups, pore size increase and interfacial adhesion with different matrices [140]. Gelatinization also disrupts the crystalline structure when heat and water are applied, which makes the granules swell. Gelatinization enables the granular opening and increase in surface area of the starch molecules for better reactivity in a mix [141]. The structural changes that occur during gelatinization of starch significantly affects the rheological properties [142].

Corn starch has been used in low amounts to toughen thermosets and improve their mechanical properties [143]. The shear thinning and thixotropic properties of corn starch also makes it a good rheological enhancer and good material as an additive for 3D printing [144].

1.1.4 Natural Fibers as Reinforcement in Thermosets

The use of fibers as reinforcement for thermoset composites have been widely explored due to their availability, recyclability, biodegradability, and low cost [145]. Natural fiber materials can be used as fillers to improve processing, reduce the brittle nature of thermosets, optimize density, enhance thermal, flame retardancy, mechanical and electrical characteristics of the thermoset composites [119]. Utilization of fiber reinforced thermoset composites can be seen in especially structural, automotive, aerospace applications as a result of their outstanding thermal stability, mechanical properties and chemical resistance over time [146]. Natural fibers of kenaf, jute, carbon, cotton, and wood have been used to reinforce thermosetting polymers of epoxy, urethane, phenolic, polyester amongst others with reported improved mechanical strength [145], [147], [148], [149].

In AM of thermosets, reinforcements aid in the proper stacking of layers and improved structural strength. He et al. (2021) developed a printing method using a polyamine thermoset and nano clay at volume of up to 36% to enhance the shear thinning effect and ink shear rate for 3D printing [150]. They obtained a successful process that enabled the freestanding 3D printing for efficient deposition of reinforcement fibers in 3D space. Zhong et al. (2001), used chopped glass fibers in the fused deposition modelling printing process with acrylonitrile butadiene styrene (ABS). Increase in interlayer bond strength with increased fiber content was observed [151], however most studies have had challenges in

incorporating high amount of fibers reinforcements in AM due to issues of high motor power and pressure needed to print the material [11].

1.1.5 Effect of Fiber Loading and Particle Size in AM of Thermoset Composites

Reinforcements used in AM of thermoset composites which are broadly categorized under continuous (long), particulate (powder, nano etc.) or short (Figure 1.6), allows for different load variations to be used in the matrix to attain the desired properties [152] [153]. Aspect ratio, which is the length to width ratio of fibers plays an important role in improving the properties of composite materials. Studies have shown that with increasing aspect ratio, composite strength increases until it reaches a maximum level [154]. Natural fibers (Table 1.1) have shown to have better aspect ratios in comparison to synthetic fibers. These natural fiber aspect ratios with the cellulosic content of the fibers play a major role in influencing composite properties. A high aspect ratio which is above its critical value will allow a maximum stress transfer in the composite before failure occurs [155].

Table 1.1: Length and width of some natural fibers [154]

Fiber	Average length (mm)	Width (mm)
Cotton	10–60	0.02
Flax	5–60	0.012–0.027
Hemp	5–55	0.025–0.050
Juta	1.5–5	0.02
Straw	1–3.4	0.023
Kenaf	2.6–4	0.018–0.024

Nawafleh and Celik (2020) used milled short fiber carbon fiber loading volume of up to 46% to fabricate 3D printed epoxy composites with improved mechanical properties [11]. Continuous fibers have been studied to have greater loading capacity but milled fibers allow for higher reinforcement fractions [156]. Li et al. (2019) had glass fiber powders of up to 80% for phenol formaldehyde and epoxy AM using a selective laser sintering AM method [157]. They reported that with an increase in glass fibers, mechanical properties increased.

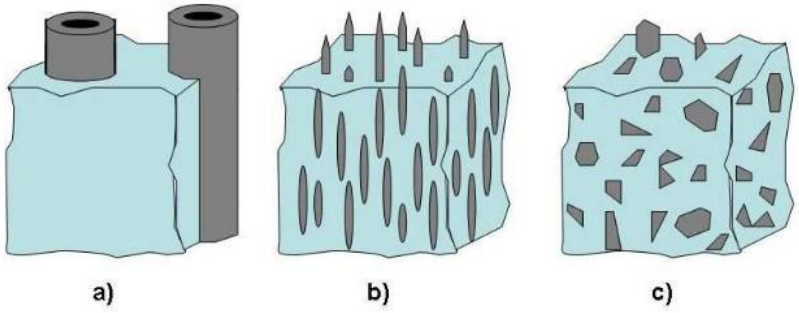

Figure 1.6: Different kinds of reinforcement types: a) continuous long fibers, b) short fibers and c) particles in a matrix [158].

Particle-matrix interface adhesion and particle size play major roles in affecting mechanical properties of a composite. Particle size of reinforced fibers which could be macro, micro, or nano based influence the dispersion and overall properties of thermoset composites [159]. Strength depends on the stress transfer between reinforcements/fillers and the matrix. For larger reinforcement particles or fibers, strength can be passed on to the particles but with poorly crosslinked particles, reduction in strength occurs [160]. A few studies have reported that nanoparticles give high rigidity and yield strength while small particle sizes gives higher fracture toughness [161] [162] [163]. Particle size is also dependent on fiber loading to attain the required strength. But in AM, challenges associated with these still make the use of high fiber loading challenging. This dissertation covers the modification of a PRF thermoset with high fiber loadings for use in AM via material-based extrusion.

1.2 Additive Manufacturing Processes for Thermoset Composites

Recent studies using different AM fabrication methods for thermoset composites will be explored in this section. AM fabrication methods are broadly divided into jetting, binder jetting, vat photopolymerization, powder bed fusion, material extrusion, energy deposition and sheet lamination processes [164] [165]. These different methods can be used depending on the different types of base material (solid, liquid, powder based) used for the production process [166].

Material jetting, which is like a two-dimensional inkjet printer, involves the jetting of the liquid material in droplets with the support materials or reinforcements onto the platform.

The deposited droplets partially soften the initially dropped layer and the final single piece is cured using ultraviolet light before removal from the platform [167]. Limitations of decreased mechanical properties of its products over time, and high material cost makes it not a viable option for most applications. Binder jetting is like the jetting process but requires the deposition of a liquid bonding agent between each layer to form the whole part. It has advantages of high printing speeds whilst making room for complex designs [168]. Vat polymerization involves the fabrication of solid products out of a vat of liquid photocurable resins whilst using a laser to cure the photosensitive liquid [15]. Powder bed fusion uses laser to fuse together powder particles to 3D printed objects. The process helps to reduce waste, enable customizable parts, and enables multilateral designs. A few disadvantages include slow print time, weak structural properties, and possible thermal distortion [169]. Energy deposition is more of a complex process that uses an electron beam to melt the material before depositing it layer by layer. Sheet lamination involves the stacking and layering of thin sheets of material through bonding ultrasonic welding or brazing to get a product which is finished off by laser cutting or computer numerical control (CNC) machining. Material based extrusion which is the process of focus in this study will be discussed below in detail [15].

1.2.1 Material Based Extrusion

The basic principle of this process requires the ejection of the loaded material through a die at constant pressure in a continuous flow to form layer on layers until the final geometry or product is formed. It is also the most used form of AM and can be called fused filament fabrication (FFF) or fused deposition modelling (FDM). Different types of extruders (Figure 1.7) which could be plunger-based, screw based, or filament based, can be used for this process. The process is simple, affordable and popularly used by industries, consumers and researchers for the fabrication of products [170] [9].

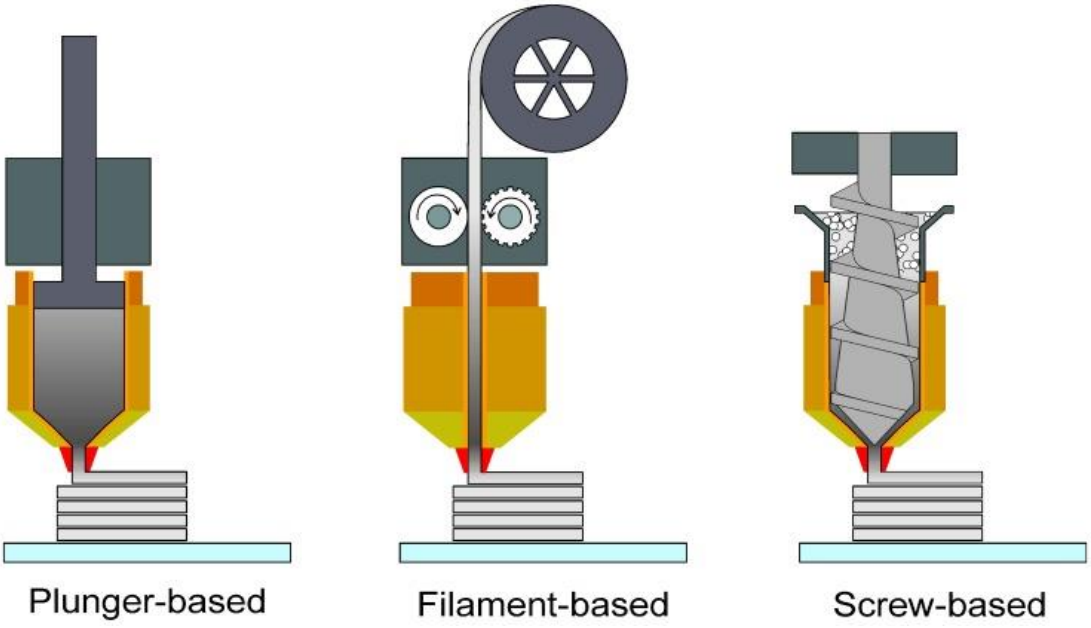

Figure 1.7: Different types of material extrusion extruders [171]

For a viscous thermoset liquid, the process of Liquid deposition modelling (LDM) is mostly used to eject the liquid resin through a printer head moving in the x-y direction. Rosenthal et al (2017), used this technique to print a wood methylcellulose mixture with suggestions of better printer modifications [172]. 3D structures from glass and carbon fiber reinforced polymer composites have been fabricated with good thermal, rheological and mechanical properties [173]. LDM can also be used for continuous fiber composites, but it requires nozzle impregnation of the thermoset. The continuous fibers are pulled through a thermoset bath and later fed into the printing head [15].

1.2.1 Thermoset Composite Performance Characterization Techniques

To ensure that the properties of thermoset composites are standardized and within the required limits for its specific application, characterization of the matrix, reinforcement, and fabricated composites must be performed. These characterization methods could either be mechanical, rheological, physical, chemical, or thermal related. A few essential characterization methods for thermoset composites in AM are summarized below.

1.2.1.1 Mechanical Properties

Applications of AM thermoset composites require that mechanical properties be good enough and tough to withstand impact resistance, with little to no failures over a long time.

An increase in tensile properties ensures the increased stiffness of the composite which increases the modulus. Flexural properties measure the maximum bending strength that composites can have when subjected to load conditions. This helps in understanding the bending performance for structural applications [174]. Impact resistance measures resistance against load without failure. Generally, mechanical properties are dependent on fiber/matrix bonding, particle size, and loading of the filler [175].

1.2.1.2 Thermal Properties

Thermal properties include curing temperatures, thermal degradation, curing kinetics, thermal stability, and decomposition of the polymers under different thermal conditions. Different factors that can affect the thermal properties of thermoset composite materials include type of fiber/filler, modifiers, fiber treatments, orientation, loading, and manufacturing process [176]. Thermal stability and characteristics are also essential to optimize processing conditions for a polymer. A few important thermal characterization methods are summarized.

1.2.1.3 Dynamic Scanning Calorimetry (DSC)

DSC measures the thermal events that occur in a polymer as a function of temperature and time from curing to melting (T_m), degree of cure, decomposition, glass transition (T_g), to kinetic parameters [177] . The relative degree of cure is defined as the total amount of generated heat from start of experiment to a particular time. The T_g is the thermal property when an amorphous polymer, such as a cured thermoset resin, transitions from a stiff to flexible/rubbery state by the movement of the molecules in the polymer. The superior thermal properties of thermosetting polymers make them desirable, and with the addition of fillers, reinforcements, and additives, curing kinetic reactions become complex and require adequate understanding [178].

Two major modes used to understand materials under DSC are isothermal and non-isothermal modes. These two modes can be performed at different heating rates which can aid in understanding the curing kinetics of a system. A wide range of kinetic models have been considered in the curing kinetics study of thermoset composites to create a relationship between temperature, time, extent of cure to the chemical reactions that go on in the system. Generally, two main kinetic model categories are explored, the phenomenological (model-

free or iso-conversional) and mechanistic models (model fitting). An n^{th} order rate equation is used to express the phenomenological model with less kinetic parameters required while the mechanistic which is more complex requires more parameters for better analysis [179]. Iso-conversional methods fall under two major categories of the differential (Friedman (FR) method) and integral methods (Flynn–Wall–Ozawa (FWO) or Kissinger–Akahira–Sunose (KAS)) [180]. Each of these methods have their limitations, but proper understanding of the complexity of the system to be analyzed is essential to select the appropriate method.

1.2.1.4 Thermogravimetric Analysis (TGA)

TGA ascertains the weight loss or thermal degradation (pyrolysis) of a sample with respect to time and temperature. It is a quantitative analytical technique that is also used to measure kinetic events in a thermoset material. Sample placed on a precision balance in a furnace and analyzer, is heated or cooled either under isothermal or non-isothermal conditions and sample mass changes with respect to temperature used [181]. This experiment is mostly done in a controlled atmosphere of gases (nitrogen, air, CO_2, helium, etc.). Results are dependent on the type of sample, heating rate and flow rate of the gases. Differentiating the TGA curves gives the differential thermogravimetric (DTG) curves which gives quantitative and qualitative information about the sample [182]. Qualitative analysis allows for the identification of different materials and differentiating chemical curing reactions while quantitative analysis shows peak height and maximum weight loss at corresponding temperatures [180].

1.2.1.5 Rheology

With thermosets, curing involves complex chemical reactions with gelation and vitrification been the most important phenomena in the process. In order to understand the flow behaviors, and deformation changes, rheology is an important process used. As curing begins, formed linear chains expand and branch with the increase in molecular weight and further crosslinking [183]. Gelation, which is the transformation of a viscous liquid to an elastic gel depends on the reactants present and the set parameters of temperature, frequency, time, strain, stress etc. A major important property required for AM of thermosets is a good shear thinning behavior. This is a process that occurs for non-Newtonian fluids which allows the reduction in viscosity under shear stain and increased frequency [184]. This phenomenon

will allow for proper dispensing of the material during AM. Dynamic rheological properties of complex viscosity (η*), storage modulus (G′), loss modulus (G″), and tan delta (G″/G′) need to be measured to ensure that polymers and composites are suitable enough for material extrusion AM. There are two major types of rheological experiments widely used: capillary and dynamic rheology. These are summarized below.

1.2.1.5.1 Capillary Rheology

Capillary rheology is an important type of rheological experiment for understanding material-based AM. The process is used to obtain shear viscosity data at high shear rates (γ). It mimics the material extrusion process where material filled in a barrel is extruded using a plunger (Figure 1.8) through different sets of dies at different high γ [185]. Corrections for pressure drop, shear rates, wall slip, are applied to the data using the Bagley, Weissenberg-Rabinowitsch and Mooney analysis corrections, respectively [186].

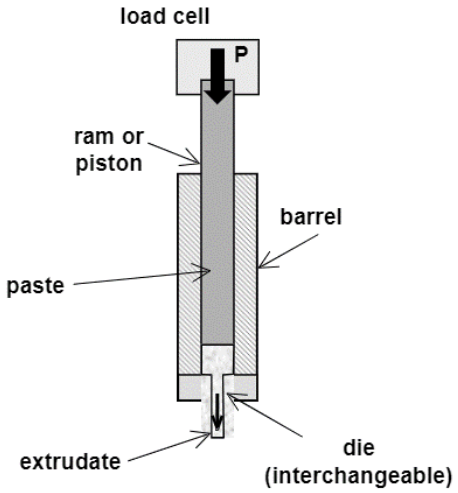

Figure 1.8: Capillary rheology setup [187]

1.2.1.5.2 Dynamic Rheology

Dynamic rheology focuses on obtaining shear viscosity, G', G' and tan δ at lower γ. Curing curves for thermosets with respect to time, temperature and frequency can also be evaluated using this method. Different geometries ranging from cone plates, parallel plates, to concentric cylinders (Figure 1.9), are available for this process [188].

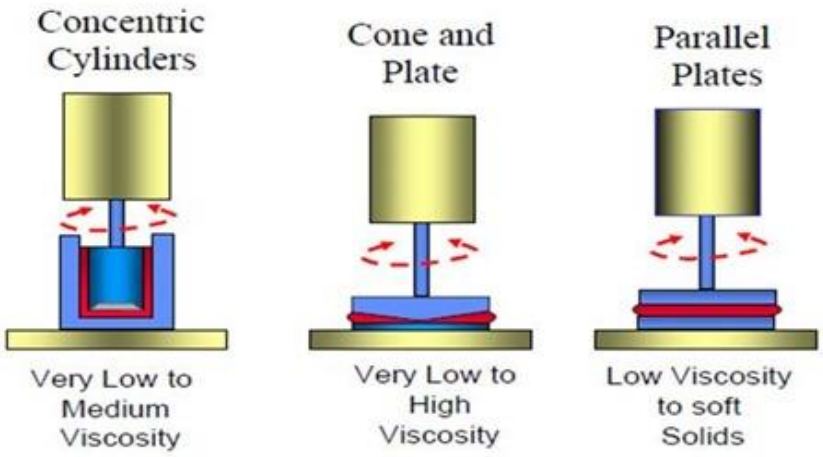

Figure 1.9: Different dynamic rheology geometries [188]

For highly filled polymers like in this study, parallel plates are used. With parallel plates, an oscillatory motion is applied to the sample between the plates under applied shear [189].

1.3 Research Objectives

From the reviewed literature above, there are not a lot of studies that have focused on the AM of thermosets with high natural fiber volume. Studies that have considered the use of geo-based polymers like SS have also not centered on understanding the curing reactions and kinetics involved with SS and its composites. The alternative use of CO_2 for the curing of SS is scarcely seen in the literature and these are the critical gaps that are covered in this dissertation. The aim of this dissertation is to develop and optimize thermoset composite systems with natural fibers in high loadings, that can be used for AM and possess good rheological, cure behavior, post thermal and mechanical properties. The major objectives of this study involved the optimization of fiber reinforced thermoset composites using wood/denim fillers, a geo-based sodium silicate (SS) resin and synthetic PRF and UF binders in composite fabrication as potentials for AM. The specific objectives that would be used to achieve the stated aim include, the evaluation of the thermal curing characteristics, rheological behavior of the thermosets in the presence of different modifiers or additives and investigating the influence of carbonation curing pressure and temperature on the post properties of cured composites. The extrudability of the fabricated composites via material-based extrusion (ME) would also be examined to completely validate the studies. ME of fiber

reinforced composites with high fiber volume (~40% wt.) which has been a challenge was investigated in this dissertation and the comprehensive summary of the research objectives is stated below.

For a more detailed summary of the studies in this dissertation, Chapter 1 gives a general summary and literature review on the use of thermosets composites in AM, characterization methods and types of natural fibers that have been studied over the years.

Chapter 2 explored the use of SS with 50 to 60 wt.% of 40 mesh wood fibers to fabricate a composite. DSC analysis was used to understand the curing behavior of SS and the uncured composites. Dynamic and capillary rheology were used to observe shear thinning and viscosity changes of the wet blends. The composites were pressed and extruded, cured at different temperatures to understand the effect of curing temperatures on the mechanical properties. To determine the effect of the curing temperature on the cured blends, TGA was used. Flammability properties were obtained from a simple Bunsen burner fire test and water absorption properties of the cured blends were ascertained.

Chapter 3 investigated the study of two commercially available thermosets PRF and UF in the presence of 50 to 90 wt.% of wood fibers. This study was performed to observe the curing kinetics and extrudability of the blends for AM. DSC was used for the curing kinetic analysis of the individual freeze-dried blends to determine activation energy and conversion. Dynamic rheology curves of the resins and wet wood composites were used to understand the curing behavior of the resin in the presence of wood. Bending properties, TGA analysis on pressed, cured samples were conducted. Dynamic mechanical analysis (DMA) and thermomechanical analysis (TMA) were used for post-cured mechanical viscoelastic properties and softening temperatures respectively of the cured composites. The extrudability of the wet composite mix with 50 wt.% wood fibers for both resins were explored for use in AM manufacturing.

Chapter 4 which is a proof of concept, explored an alternative curing method for SS and composites using carbon dioxide (CO_2) with the aim of reducing the amount of energy put into curing and sequestering carbon. Two wood particle sizes of 40 and 200 mesh were studied in the presence of CO_2 with wood. Fleshly blended fiber and SS resin (50/50) samples were exposed to CO_2 at two different pressures, post cured at two different temperatures and analyzed for mechanical and thermal degradation properties. Dynamic

rheology curing at room temperature of the fleshly blended wood-SS (50/50) mixture in the presence of CO_2 was analyzed.

Chapter 5 investigated the use of ball-milled eggshells (BMES), sulfonated castor oil (SCO), gelatinized corn starch (GCS) and waste cotton denim as modifiers and fillers for PRF - wood (50/50) composites. Blended mixtures of varying compositions of wood, resin, and additives were pressed, cured, and characterized. Mechanical properties were determined using the three-point bending method, TGA was used for thermal degradation analysis. The goal was to minimize the quantity of PRF in composite fabrication, reduce formaldehyde emissions, which in the end will optimize production cost whilst making them suitable for the environment and extrudable in AM.

Statistical analysis on analyzed results was used for most of the studies to determine the effect of wood composition on the mechanical properties of the cured composites. ANOVA tests were used to determine the significant effect of the fillers in the composite mechanical properties. Response surface methodology (RSM) was used to determine the effect of factors at different CO_2 pressures and curing temperatures on the response values of post cured mechanical properties of the composites.

Chapter 2: Wood fiber - sodium silicate mixtures for additive manufacturing of composite materials, Orji, B. O., Thie, C., Baker, K., Maughan, M. R., & McDonald, A. G. (2022)

"Wood fiber-sodium silicate mixtures for additive manufacturing of composite materials", Orji, B. O., Thie, C., Baker, K., Maughan, M. R., & McDonald, A. G. ***European Journal of Wood and Wood Products*****, vol 81, no 1, 2022, p. 45-58, https://doi.org/10.1007/s00107-022-01861-z.**

2.1 Abstract

A composite mixture of wood fiber and sodium silicate (SS) binder has been explored as a viable material for use in additive manufacture of wood based composite materials. Mixtures of 50-60% wood fiber and 50-40% sodium silicate were explored. The curing behavior of these formulations were examined by differential scanning calorimetry (DSC) and dynamic rheometry. An exothermic curing peak of 83 °C was observed for SS and increased to 153 °C and 163 °C with the addition of wood fiber. Rheology viscosity curves showed higher viscosity values for 50/50 blends and lower values for SS. A custom extrusion system was fabricated and 50/50 wet blends were extruded, cured at different temperatures, and characterized for flame retardancy, mechanical, thermal, and water absorption properties. Surface chemistry changes before and after curing were determined by Fourier transform infrared (FTIR) spectroscopy. Mechanical properties, determined by three-point bend testing, improved with the addition of the wood fiber but varied with different curing temperatures and thermal stability of the composites increased with curing temperature. This extruded wood-SS composite shows promise for use in additive manufacturing.

2.2. Introduction

Sawmill residues (sawdust and planar shavings) is a useful resource that can be utilized as a sustainable feedstock and in the U.S.A, 83.4 million tons of primary timber wood residues were generated in 2010 and 85% was used in wood composites [190]. Waste wood is also commonly used in composite wood panels (particleboard) and composite decking (wood plastic composites) [191]. The production of composite panels requires

binders which are mostly synthetic resins (urea-formaldehyde and phenol-formaldehyde) that require curing in a heated press and can release formaldehyde emissions which pose environmental and health risks [192] [193]. However, the use of wood residues has not been explored in additive manufacturing applications.

The global additive manufacturing and materials market was $12.8 billion in 2018 and is expected to grow annually by 25% by 2023 [194]. This expansion has been driven by rapid advancements in materials used, new additive manufacturing technologies, and shifting from prototyping to parts fabrication. This process typically involves a layer-by-layer deposition process which is repeated until the part is created. The most common and known form of additive manufacturing is fused filament fabrication (FFF) or fused deposition modeling (FDM) [21]. A new method of 3-D printing called fused particle fabrication (FPF) or fused granular fabrication (FGF) uses thermoplastic powders/pellets that feed into an extruder that produces a filament *in-situ* for printing [195]. This process can also form composite materials by combining reinforcing particles/fibers and plastic waste to form components but via a melt process [196]. An alternative method of additive manufacturing involves the use of a liquid resin-based 3D printing that uses UV-light curing (stereolithography and digital light processing) and this has been applied for high-resolution printing applications, however the resins used are expensive [197]. Ming et al. had produced epoxy-continuous fiber composites but also required high temperature curing [198]. For construction applications, cement-based systems have been used for but require long curing times of 28 days and has high embodied energy [199]. There is a gap in additive manufacturing technology to produce low temperature cured, formaldehyde free, inorganic based thermoset resin-wood composite materials.

Sodium silicate (SS), also known as water glass, is an example of an inorganic binder used due to its eco-friendly nature, affordability, ease to handle and prepare, high strength, weather resistant, and flame retardant properties [200]. It is commonly used in thermal insulation, as a binder for sand-cast molding in foundries, and to modify natural fiber surfaces [201] [202] [203] [204]. SS has been impregnated into solid wood lumber and wood surface treatments to protect wood from biodegradation, improve its physical, mechanical and flammability properties [205] [206] [207]. Composites made with natural fibers like

sugarcane bagasse, hemp fiber, coconut, raffia palm, and sisal using SS as binder have been produced and resulted in materials with improved mechanical properties [208] [209] [210].

Studies have shown that the curing of SS can be attained using different methods including the use of alkali activators like sodium hydroxide or potassium hydroxide, use of weak acids, catalysts, the removal of water through heating, the use of carbon dioxide (CO_2), and the use of liquid ester hardeners [204] [211]. SS acts as a binder through its formation of silicate, silicic acid, and precipitated gel bonds when cured. The gel further stiffens into a solid "glass" due to the water molecules which are drawn and adsorbed to the surface of the gel and the crosslinking and polymerization of the solid material into complex chains and networks [212] [213] . Although the use of SS is common in various applications, a limited number of studies on the rheology, thermal, and curing studies of SS in the presence of wood fiber have been documented [214] [215].

The aim of this study was to explore the use of SS with wood fiber from sawmill residues to produce an extruded wood composite material. The study explored the mixing, formulation, and effect of wood particle size and composition on composite properties. Curing behavior was determined by differential scanning calorimetry (DSC) and dynamic rheology. The rheology of a wood-SS paste was determined by a combination of dynamic and capillary rheology. The wood-SS paste was extruded into rod for studying the influence of curing temperature on flexural properties of the composite. The thermal stability of the composites was determined by thermogravimetric analysis (TGA) and a flame test.

2.3. Materials and Methods

2.3.1 Materials

Sawmill residues were obtained from Plummer Forests Products, Post Falls, ID., USA. Wood residues (100 g batches) were screened using a 40 mesh standard US screen, collected, and pooled together. Commercial SS solution (37 wt.%, ThermoFisher Scientific, Waltham, MA, USA), pH 12.5, 1.39 g/cm^3 at 20 °C, was used as received.

2.3.2 Composite Preparation

Wood fiber moisture content was determined using a HB43-S Halogen Moisture Analyzer (Mettler Toledo, Columbus, OH, USA) for 2.6 g to 3.5 g of samples in triplicate.

Screened 40 mesh (0.425 mm) wood fiber and SS were mixed in ratio of 50:50 and 60:40 ratio on a weight basis, respectively. Small batches (2 g total weight) were mixed (30 s) using an herb grinder (Appendix Figure A2.1) for dynamic rheology tests and larger batches (200 g total weight) were mixed (1-2 mins) using food processor (Hamilton Beach model 70730 (450W, 10 cup capacity)), (Appendix Figure A2.2) for capillary rheometry and extrusion studies.

2.3.3 Sample Characterization

Wood fiber morphology (length and width) was determined on 400 particles by optical microscopy (Olympus BX51 microscope with a DP70 digital camera at 40x, San Diego, CA, USA). Images were analyzed using Fiji ImageJ software (version 2.1.0/1.53c, Java 1.8.0_172 (64bit)). Sieve analysis was performed on 100 g of the screened 40 mesh wood fibers for 10 min using a standard shaker to pass through 40, 60, 80, 100 and 200 US standard mesh screens. The total weight of samples between sieves was determined and the cumulative percent weight was determined to ascertain size distribution.

Wet and cured extruded wood-SS blends were analyzed (in triplicate) by FTIR spectroscopy using a Nicolet-iS10 spectrometer (64 scans, Thermo-Scientific, Madison, WI, USA) with an attenuated total reflectance (ATR) accessory (Smart Orbit, Diamond). The spectra were baseline and ATR corrected and averaged using the Omnic v9.8.3 software.

2.3.4 Thermal Analysis

Each blended wood-SS formulation was freeze-dried prior to DSC analysis. To improve sensitivity of traditional DSC, modulated DSC (MDSC) experiments were performed on blends (5 mg – 10 mg) using a Q200 DSC (TA instruments, New Caste, DE, USA) under nitrogen (20 mL/min) and refrigerated cooling. Samples were equilibrated at 40 °C, modulated at ± 3.183 °C for 60 s, kept isothermal for 2 mins and ramped from 40 °C to 200 °C, at a heating rate of 10 °C/min. Data was analyzed using the TA Universal analysis software.

Thermal degradation and curing behavior of wet and cured wood-SS blends under different curing regimes were determined using a Perkin-Elmer TGA-7 instrument (Shelton, CT, USA) under nitrogen (30 mL/min). Isothermal runs were performed on wet sample

blends wood-SS (50:50, 30 mg) from 40 °C to the desired curing temperatures of 60 or 105 °C at 200°C /min and held isothermally for 24 hrs. Temperature ramp scans were done on wet and cured sample blends (4 - 6 mg) from 40 °C to 900 °C at 20 °C/min. Data were analyzed using the Pyris v13.3.1 software.

2.3.5 Rheology

Curing and flow behavior of wet wood-SS molded discs (2.00 mm (h) x 25 mm (Ø) were determined from dynamic rheology measurements (complex viscosity (η*), storage modulus (G'), and Tan δ) performed on a Discovery Hybrid Rheometer (DHR2, TA instruments, New Caste, DE, USA) between two serrated parallel plates. For SS curing experiments, flat parallel plates (25 mm Ø) were used. Temperature ramp experiments were from 30 to 200 °C at 2 °C/min with 0.1% strain and frequency of 1 Hz. Frequency sweep experiments were performed isothermally at 22 °C using a Peltier plate with a 0.1% strain from 0.01 Hz to 100 Hz to obtain lower shear rate flow property values with controlled sample temperature. Results were analyzed using the TRIOS software v5.1.1.

Capillary rheology experiments were performed using two capillary rheometers to determine the flow curves of the wet wood-SS blends at higher shear rates. Experiments were performed at room temperature (22 °C) using an Instron 5500R-1137 universal testing machine at crosshead speeds 2, 6, 10, 20, 60, and 100 mm/min. The small capillary rheometer (Instron model 3213) was originally used with a barrel diameter of 9.55 mm, two dies of different lengths (14 mm and 55 mm) and diameter of 4.0 mm equipped with a 44 kN load cell. To produce larger diameter rods a larger custom-built capillary rheometer was used with a barrel diameter of 44.45 mm, a die length of 19.05 mm, and die diameter of 8.89 mm. It was equipped with a 133 kN load cell (Appendix Figure A2.3). Data were acquired and analyzed using the Bluehill v3 Instron software according to the ASTM D3835-02 standard. Rheological data were also fitted to the Ostwald's power law model of Equation 2.1.

$$\sigma = K\gamma^{n} \qquad \text{(Equation 2.1)}$$

Where σ is the shear stress , γ is the shear rate, K is the consistency index and n is the flow behavior index which is dimensionless [216] [217].

2.3.6 Extrusion System

An extruder was custom-built to extrude wood-SS mixtures (Appendix Figure A2.4). The screw (5 mm pitch) and barrel, with a 35 mm Ø barrel and 420 mm length, were provided by RobotDigg (Shanghai, China). A mild steel 13.5 mm Ø die was secured to the end of the extruder barrel. The screw was coupled to a geared motor (745.7 W, 0-40 RPM, NORD, USA) with a variable frequency drive (Altivar 12). Blend of wood-SS (200 g) were manually fed into the extruder and run for 3 mins, with slow screw speeds 0-20 rpm and high screw speeds 21-40 rpm to produce extruded rods.

2.3.7 Curing Extruded rods

The wet extruded rods were cured separately using five different temperature regimes which includes 11 d at 22 °C, 2 d at either 45 °C, 50 °C or 60 °C, and at two different temperatures (1 d at 60 °C and then 1 d at 105 °C). The wood-SS (60:40) sample rods were only cured for 2 d at 50 °C. Density was determined on wet and cured samples using the mass per unit volume method.

2.3.8 Flexural, Water Soak, and Fire tests

Flexural three-point bending tests were performed on cured extruded rod specimens (13.5 mm Ø x 240 mm, 5 replicates), using a Mecmesin MultiTest-dV 2.5 test machine (Virginia, USA), using a support span of 216 mm and crosshead speed of 5 mm/min. Data were acquired and analyzed using the Vector Pro v6.11 software. Data were statistically tested using single factor ANOVA using Excel (Microsoft Office 2017) with a 95% confidence interval.

Dimensional stability of the various cured extruded wood-SS rods (10 mm x 13.5 mm Ø) was determined after soaking in water for 24 h at 22 °C. Percent weight gain and thickness swell were determined based on original and soaked dimensions.

A simple Bunsen burner fire test was performed on wood-SS (50:50) cured composites, in triplicate, for smoldering and flame retardancy. Samples were exposed to the tip of the Bunsen burner flame (1000-1100 °C) and monitored for 5 min via a thermocouple and video camera. Images taken from the video were analyzed every minute for sample changes and final weight loss recorded.

2.4. Results and Discussion

2.4.1 Fiber Characterization

The screened wood fiber had a moisture content of 5.2%. Wood fiber dimensions (width and length) were determined by optical microscopy (Figure 2.1a) in conjunction with image analysis. Sieve analysis plot for 40-mesh screened wood fibers is shown in Figure 2.1b. The fiber length ranged from 18 µm to 1929 µm with a mean of 206 ± 242 µm. The fiber width ranged from 12 µm to 1716 µm with a mean of 192 ± 227 µm. The average aspect ratio of the fibers was 1.3. Longer fibers passed through the mesh screens vertically hence the length was larger than the screen holes. Sieve analysis of the fibers (Figure 2.2b) shows the 40-20 mesh (250-420 µm) fraction was 37 w/w% while the size range 60-200 mesh (73-250 µm) contained 46 w/w%. 17 w/w% of fibers was > 40 mesh (>420 µm). Sieve analysis supports the presence of long fibers as observed by image analysis.

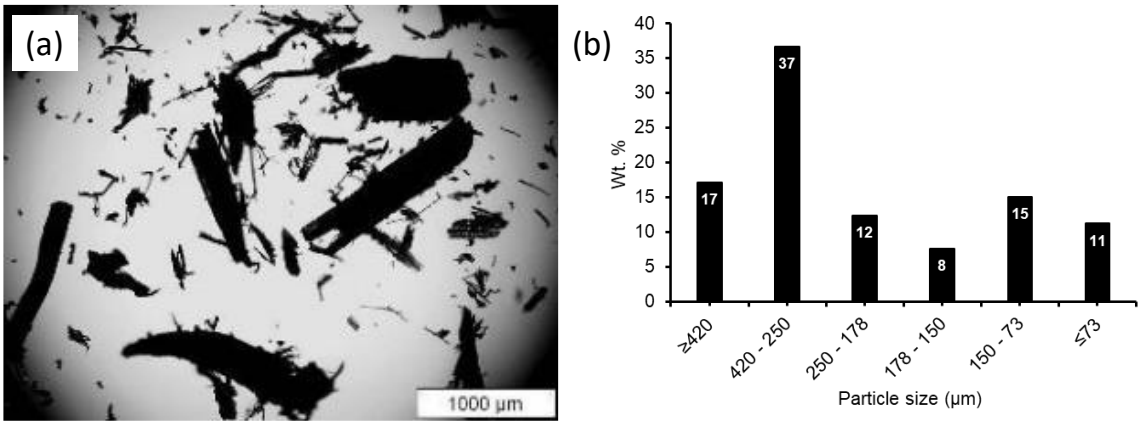

Figure 2.1: (a) Optical micrograph (40x) of screened 40 mesh wood fiber and (b) size distribution curve from sieve analysis done on the screened 40 mesh wood fiber

2.4.2 Blending of Wood-SS and Rheology of Wet mixtures

Wood-SS wet samples were freshly mixed and homogenized for each experiment to minimize drying and curing reactions from occurring prior to analysis. To understand the flow properties and steady shear rheological behavior, dynamic rheology frequency sweep and capillary rheology experiments were performed on wood-SS and SS samples.

Frequency sweep experiments at 22°C were done to determine the influence of shear rate (Hz) on the elastic (G′) and loss (G″) moduli of SS and wood-SS wet blends as seen in

Figure 2.2a. G′ and G″ both increased with an increase in shear rate and generally G′ > G″ showing more elastic behavior. The lower G″ was associated with the molecular friction and loss of energy in the viscous material [218]. A rapid increase in G′ was observed for SS due to the viscoelastic nature of the material [219]. Cross over points, where G′ = G″, is assigned to the gel point which did not occur for the wood-SS blends. However, for SS a cross-over frequency of 0.04 Hz was observed. Reducing the binder content from 50% to 40% in the wood-SS blend resulted in a 65% decrease in G′ at 1 Hz.

Flow curves (complex viscosity (η*) vs. shear rate) for wet wood-SS blends are shown in Figure 2.2b and η* values at 1 Hz are documented in Table 2.1. Shear thinning behavior of SS and wood-SS blends was observed for all samples [220]. In contrast, Yang et al. had shown a shear thickening behavior for SS solutions from 17 to 34% concentrations [221]. The η* of SS at 1Hz was 13 kPa.s and increased by 286 % upon addition of 50% wood fibers. Adding more wood fiber to 60% reduced the η*. This finding was in contrast to previous studies which have shown an increase in viscosity with wood content in wood plastic composites systems [222] [223] [224] [225] [226].

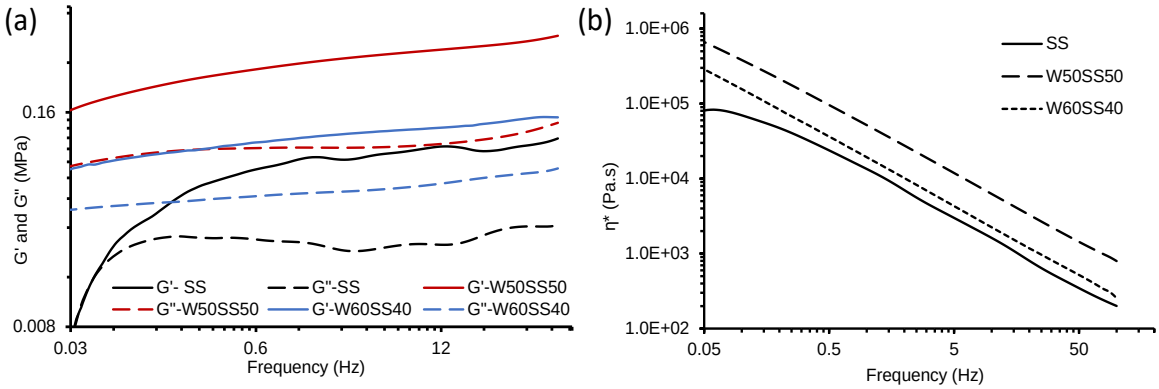

Figure 2.2: (a) Elastic (G') and viscous (G") moduli versus frequency plots of SS and wood-SS blends and (b) flow curves (η* vs. frequency) for SS and wood-SS blends.

The flow curves for SS and wood-SS blends generally followed a power law fit model. The power law parameters fitted well with coefficient R^2 values (Table 2.1) of 0.82 and higher for SS and wood blends. The tendency for the viscosity to change with shear rate can be explained with the flow behavior index (*n*) [217]. The samples have *n* values between 0.83 to 0.91 indicative of a pseudoplastic material [227]. The *n* value increased with the

addition of wood fiber to SS and increased fiber content from 50% to 60%. In contrast to this, Feng et al. recorded a reduction in *n* values with increased fiber content due to stronger shear thinning behavior in the study of sisal fiber and poly-butylene-succinate composites [228]. Manning et al. stated that there was a decrease in *n* values with increased addition of a polyether amine and a nano-clay filler causing a decrease in the shear thinning behavior [229]. The magnitude of K increased with the addition of wood fiber to the SS and reduced with increased wood composition from 50% to 60% [217] [230].

Table 2.1: Dynamic viscosity values at 1 Hz and flow behavior index (n) and consistency coefficient (K)

Sample	η* at 1Hz (kPa.s)	K (kPa.s)	*n*	R^2 values
SS	13	11	0.83	0.8191
wood-SS (50:50)	52	47	0.87	0.9604
wood-SS (60:40)	19	18	0.91	0.9575

Capillary rheology (in the small system) was used to study the extrudability of the wood-SS (50:50) blends at high shear rates (γ) comparable to extrusion using two die lengths at room temperature (20-23 °C). Images of the extrudates for the small and large capillary rheometer are shown in Figure 3a. Bagley and Rabinowitch corrections were performed on the rheological results according to ASTM D3835 to obtain true viscosity (η_{true}) and γ values (Figure 3b and Table 2). The γ obtained was between 2 and 100 s^{-1}. The η_{true} decreased with γ and values obtained were from 49.4 to 1.2 kPa.s (Table 2.2). Shear thinning and pseudoplastic behavior was also observed with an increase in shear rate as seen with most polymer melts [217]. The flow curve followed a power-law fit model and the model parameters (*n* and K) are given in Table 2.2. The power law component, *n* for the wood-SS (50:50) decreased to 0.76 and consistency coefficient value, K, increased to 92 kPa.s in comparison to the dynamic rheology results showing a higher shear thinning behavior at higher shear rates [226].

A large capillary rheometer was constructed to produce large diameter rods for evaluation. The large capillary rheometer had a single die length and η was calculated with an intercept pressure value considered as zero. Values for γ were from 1.4 s^{-1} to 69 s^{-1} and

with a concomitant shear η from 225 to 12.4 kPa.s (Table 2.2). The η values from the small capillary rheometer were lower than those obtained with the larger system. Values from the larger capillary rheometer were not corrected for true shear stress according to Bagley since only one die length was used (ASTM D3835) hence the higher range of η_{true} values. Bagley corrections are essential to account for pressure losses sustained by the sample in motion from the barrel to the capillary die, die entrance and effects with different die lengths [226]. The flow curves also followed a power-law fitted model (Table 2.2 and Figure 2.3b). A 25% increase was observed for the power law index *n* in the large capillary rheometer and K values increased over 200%. The rheological measurements on the wood-SS (50:50) blend from the dynamic, and two capillary rheometers are shown together in Fig. 3b. In comparison to the dynamic rheology, the capillary rheology true viscosity values are slightly higher due to the influence of the pressure driven methodology and increased shear rate which causes the increase in viscosity values [226]. All flow curve plots (dynamic and capillary) had similar slopes, but a definite offset (K) was observed.

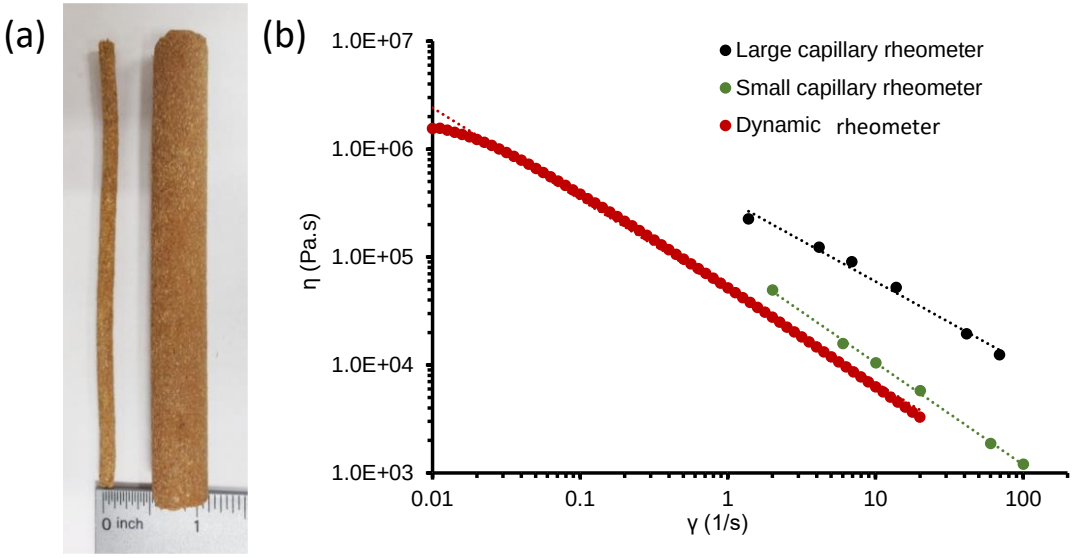

Figure 2.3: (a) Photograph of extrudates from the small and large capillary rheometer and (b) viscosity versus shear rate (flow curves) plots of wood-SS (50:50) blend by dynamic and capillary rheometry at 22^{o}C.

Table 2.2: Viscosity values for small and large capillary rheology dies

Shear rate (1/s)	η_{true} (kPa.s)	*n* values	K values (kPa.s)	R^2
Small capillary rheology				
2.0	49.4	0.76	92	0.998
6.0	15.7			
10.0	10.5			
20.1	5.8			
60.2	1.9			
100.3	1.2			
Large capillary rheology				
1.4	225.0	0.95	339	0.979
4.1	123.1			
6.9	90.1			
13.8	52.2			
41.4	19.4			
68.9	12.4			

2.4.3 Curing of wood-SS blends (DSC, Isothermal TGA and temp ramp rheology)

The curing of SS and wood-SS blends was monitored by DSC. To improve the resolution of the analysis of these wet materials modulated DSC (MDSC) was used to obtain the reversible and non-reversible heat flow and heat capacity data. Curing reactions were observed by the presence of exothermic peaks in the DSC thermograms of SS and wood-SS blends (Figure 2.4a). The peak temperature and enthalpy of SS and wood-SS blends are given in Table 2.3. To verify these exotherms, MDSC curves of the wood particles were obtained (Figure 2.4b), and exothermic peaks were not seen except between 45 °C to 60 °C. The area under each curve was measured for the enthalpic heat of reaction. Kelley et al. (1987) in a study of spruce wood attributed the DSC peak at 50 °C to enthalpy relaxation which is closely associated to the glass transition temperature (T_g) [231]. The enthalpy of curing and the intensity of exotherms also increased with the addition of wood. It is assumed that with an increase in wood content, the curing of SS occurred at a lower temperature due

to the free movement of SS molecular chains [232]. Curing peak temperatures were seen at 83 °C, 163 °C and 153 °C for SS, Wood-SS blends at 50:50 and 60:40, respectively. Zhou et al. (2009) observed two endothermic peaks for SS at 88.3 °C and 126.1 °C for the dehydration condensation of the silanol groups in SS and further condensation, respectively [233].

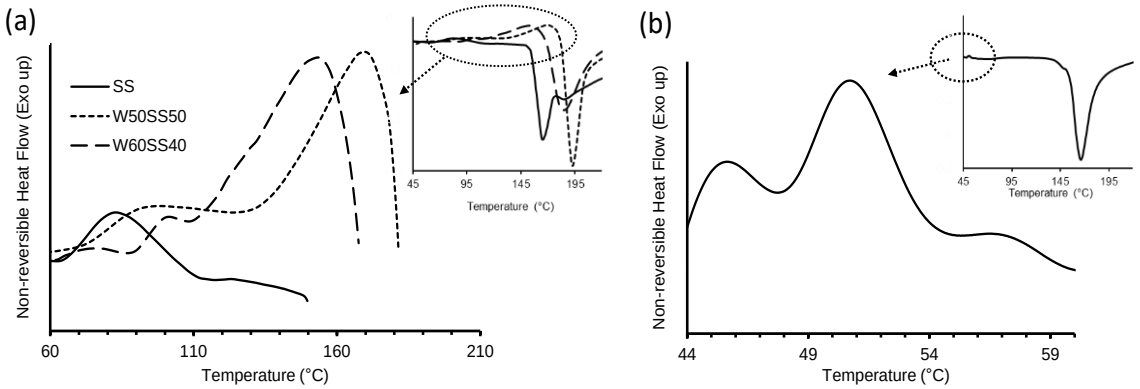

Figure 2.4: (a) Nonreversible heat MDSC heat flow thermograms of SS and wood-SS blends and (b) MDSC heat flow thermograms of wood fiber.

Table 2.3: MDSC peak values for wood and SS samples

Sample	Major Exothermic Peak (°C)	Enthalpy (J/g)
SS	83 (±0.6)	6.4 (±0.5)
Wood-SS (50:50)	163 (±9.2)	23.2 (±8.2)
Wood-SS (60:40)	153 (±2.0)	31.5 (±6.9)

The curing behavior of SS and wood-SS blends was also examined by dynamic rheology (η^* and tanδ) using a temperature ramp (Figure 2.5). This approach was used by Katoueizaha et al, and Pham et al. to investigate the gelation of SS [214], [215]. At low temperature (30-50 °C), the curing reaction is slow and a slight increase in η^* is observed. As the temperature increases from 50 to 105 °C the η^* decreases due to softening of SS. Finally, >105 °C there is a rapid rise in η^* as the SS goes from a liquid to a gel and then to a vitrified glass [234]. During the curing of SS, foaming and spreading of the solution occurred with an increase in temperature leaving a foam-like residue. Subasri and Nafe (2008) recorded that

this foaming reaction occurs between 400 °C and 750 °C for pure SS followed by the crumbling of the structure [235]. The sharp increase in η^* of SS shows the start of gelation under the low strain used. With the addition of wood fibers to SS, the mixture has a higher η^* [236] [237]. For the wood-SS blends the temperature at maximum η^* were 110 °C for 50:50 mix and 103 °C for 60:40 mix were assigned to gelation. The max η^* for the wood-SS 50:50 blend was higher than the 60:40 blend and could be attributable to a decrease in SS content.

Tan δ (G″/G′) plots against temperature (Figure 2.5b) was used to establish gelation of the SS. Tan δ for the formulations is dependent on fiber volume fraction, temperature and type of fibers [237]. As temperature increased tan δ increased to a maximum (104 °C for SS, 108 °C for 50:50 blends and 96 °C for 60:40 blend) which corresponded to more molecular mobility (liquid behavior). Tan δ then decreased to a minimum with temperature (120 °C for 60:40 blend and 135 °C for 50:50 blend) and this was assigned to the gelation point. Tan δ was highly influenced by wood content (fiber fraction) which can restrict polymer chain movement [232] [238].

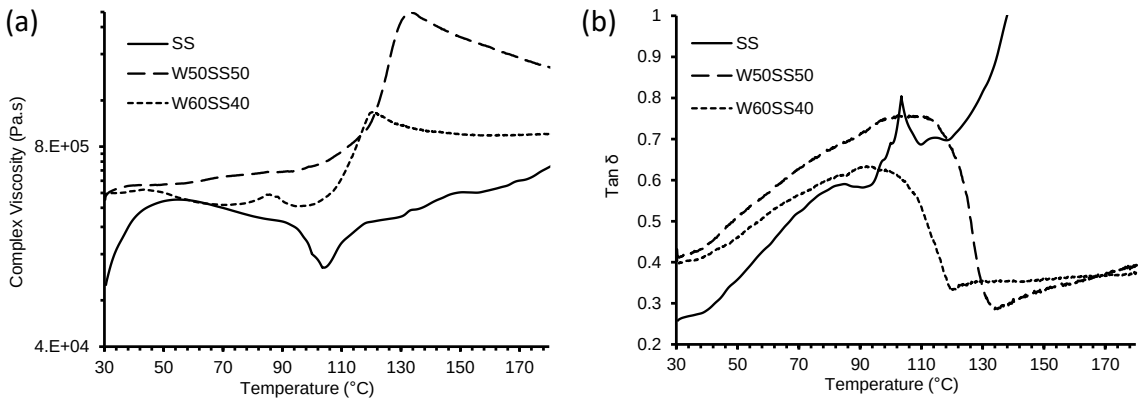

Figure 2.5: (a) Complex viscosity (η*) plots against temperature and (b) Tan δ plots against temperature for SS and wood-SS blends.

The curing behavior of wood-SS 50:50 blend was also studied by isothermal TGA by examining temporal loss in weight of water (Figure 2.6). The thermograms' curves show a weight loss of 37% at 10 min while being cured at 105 °C. While at 60 °C curing took 24 min to achieve a 37% weight loss. The final weight loss after 24 h of isothermal curing at 60 °C and 105 °C was about 40-41%.

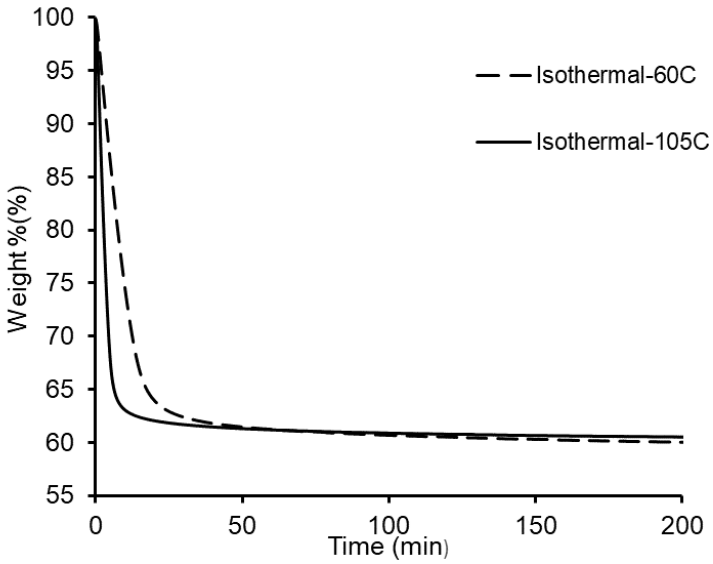

Figure 2.6: Isothermal TGA thermograms for wood-SS 50:50 blend at 60 and 105 °C.

2.4.4. Extrusion of wood-SS blend

The wood was blended into SS in a 50:50 or 60:40 ratio using high shear mixer and a slight warming of the mix was observed which was attributed to an exothermic reaction of SS reacting with ambient CO_2, which was about 400 ppm [213] [239]. The mixture was fed into the extruder and the screw speed was shown to greatly influence the surface smoothness (< 20 rpm) or roughness (Figure 2.7). At higher screw speed 21-40 rpm, shark skin (surface fracture) was observed in the extruded rod due to elastic surface instability [240]. Several arguments have also attributed this occurrence to some stick-slip phenomena which occurs at the die-exit [241].

The extruded rods were initially cured at 105 °C and surface cracks were formed and possibly due to differential stresses caused by a moisture gradient. Therefore, different curing regimes (22, 45, 50, 60 and 105 °C at different times) were explored to mitigate crack formation. Crack formation can be attributed to the rapid shrinkage of the composite surface, at higher temperature, whilst loosing water due to thermal stresses [242].

Figure 2.7: Photographs of (a) smooth extruded wood-SS (50:50) rods and (b) extruded wood-SS showing sharkskin.

The density of the wet extruded rods ranged between 0.96 to 1.42 g/cm^3 (Table 2.4). The density of the rods decreased after curing to between 0.79 and 0.92 g/cm^3. This decrease in density resulted from water removal [243] [244].

Table 2.4: Wet and cured density calculations for extruded wood-SS 50:50 and 60:40 blends.

Sample	Curing time (d = days) and temperature	Wet Density (g/cm^3)	Cured Density (g/cm^3)
Wood-SS (50:50)	11 d at 22°C	1.42 (±0.02)	0.92 (±0.02)
	2 d at 45°C	1.34 (±0.02)	0.86 (±0.02)
	2 d at 50°C	1.33 (±0.02)	0.83 (±0.02)
	2 d at 60°C	1.33 (±0.04)	0.79 (±0.03)

Table 2.4 cont'd

	1 d at 60°C + 1 d at 105°C	0.96 (±0.03)	0.84 (±0.02)
Wood-SS (60:40)	2 d at 50°C	1.30 (±0.05)	0.89 (±0.05)

Note: Standard deviation in parentheses.

The chemical features of wood fiber and SS blends were determined by FTIR spectroscopy (Figure 2.8). The main absorption bands for SS were seen between 500 and 1200 cm^{-1} and assigned to vibrations of the silicate group [245] [246] [247]. The distinct band at 1001 cm^{-1}, which has two shoulders was attributed to the Si-O-Si stretching vibrations. This band is known to shift to higher frequency with an increase in the degree of polymerization of silicate ions in SS [245]. The two shoulders at 888 cm^{-1} and 1100 cm^{-1} were assigned to Si-OH bonds [246] [247]. The bands at 3364 cm^{-1} and 1639 cm^{-1} were due to the presence of water and O-H stretching modes. The low intensity bands between 2100 cm^{-1} and 2400 cm^{-1} were assigned to hydrogen bridging in the silicate lattice [248], [249] [250].

The wood fiber spectrum (Figure 2.8) showed an intense O-H stretching band at 3329 cm^{-1}. A C-H stretching band at 2880 cm^{-1} was also observed and assigned to wood polymers and extractives [251]. The band at ~1100 cm^{-1} was assigned to C-O stretching of cellulosic polysaccharides. Bands at 1507 cm^{-1} and 1600 cm^{-1} were assigned to lignin aromatic units [252]. The band at 1730 cm^{-1} was assigned to an ester carbonyl (C=O) groups in hemicellulose [253], [254].

FTIR spectroscopy was employed to examine the chemistry of the cured wood-SS material performed at different curing regimes (Figure 2.8). The wet wood-SS mixture showed a large O-H stretching band at 3334 cm^{-1} and 1639 cm^{-1} due to the presence of water [248]. In addition, the mix had bands associated with wood and SS, as described above. Upon curing of the wood-SS mix the O-H stretching band (centered at 3300 cm^{-1}) decreased in intensity and was temperature dependent. This decrease was attributed to the removal of hydroxyl groups, dehydration and crosslinking reactions that occurred [255].

During curing the C-H stretching (methylene) bands at 2800 cm^{-1} and 3000 cm^{-1} became visible. The Si-O-Si, C-O stretching and Si-O symmetric stretching bands centered at 1000 cm^{-1} also increased in intensity [251], [256], [257]. Si-O-C vibrations were also seen at 1260-1270 cm^{-1} for all cured samples [258]. The lignin aromatic units in wood were also

detected at 1508 and 1600 cm^{-1}. The skeletal C-C band centered at 1420 cm^{-1} was shown to increase in intensity with curing temperature. In addition, the carbonyl band around 1700 cm^{-1} associated with hemicellulose was also observed [252] [259]. These results show that FTIR spectroscopy clearly showed chemical functional group differences between wood-SS blends cured at different temperatures.

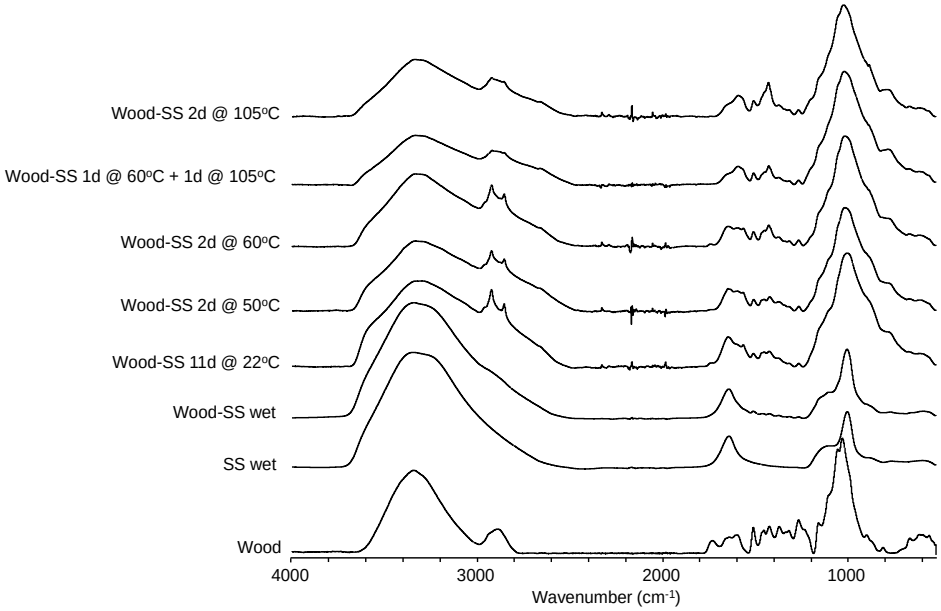

Figure 2.8: FTIR spectra of wood fiber, SS solution, wood-SS (50:50) wet mix, and wood-SS (50:50) cured at different times and temperatures.

2.4.5. Flexural, Thermal degradation, Water Soak and Fire properties

The flexural strength and modulus of the extruded wood-SS (50:50 and 60:40) cured rods were determined and the results are given in Table 2.5. The flexural strength of the 50:50 blend rods cured between 22 and 60 °C was about 24 MPa and not significant. The strength significantly decreased to 11 MPa for wood-SS cured using the 2-step regime (60 °C plus 105 °C). Lower values of flexural strength in pine, SS and clay composites were observed when cured at 75 °C [260]. The decrease in strength may be attributable to (i) non-homogenous cross-linked structures [261] and/or (ii) the formation of voids in the matrix due to water formed bubbles as evident of its low wet density [262]. Changing the wood-SS blend ratio from 50:50 to 60:40 (cured at 50 °C) did not significantly change the flexural strength of the composite.

The flexural modulus of the 50:50 blend rods cured between 22 and 60 °C was about 4.5 GPa and was not significant (Table 2.5). The modulus decreased significantly by half when the wood-SS mix was cured at higher temperature. By increasing the wood content from 50 to 60% (cured at 50 °C) there was no significant change in flexural modulus.

Table 2.5: Bending strength values for wood-SS (50:50 and 60:40) extruded samples cured at different temperatures.

Cured wood-SS sample	Flexural Stress (MPa)	Modulus of Elasticity (GPa)
50:50 blend		
11d at 22°C	23.5 (±1.5)[a]	4.3 (±0.2)[b]
2d at 45°C	23.9 (±2.0)[a]	4.6 (±0.2)[b]
2d at 50°C	24.7 (±2.2)[a]	4.6 (±0.4)[b]
2d at 60°C	23.2 (±3.7)[a]	4.4 (±0.6)[b]
1d at 60°C + 1d at 105°C	11.1 (±1.1)[b]	2.3 (±0.2)[a]
60:40 blend		
2d at 50°C	25.0 (±2.0)[a]	4.3 (±0.6)[b]

Note: Standard deviation in parentheses. Samples with different superscript letters (a, b, c) are statistically different ($p < 0.05$) using a single factor ANOVA test.

The thermal stability of the cured wood-SS materials and the effect of increased wood composition in the blends was studied by TGA. Thermograms and TGA values are seen in Figure 2.9 and Table 2.6, respectively. The wood-SS (50:50) sample cured for 11 d at 22 °C had the lowest residual weight of 57% (Figure 2.9). As the curing temperature increased the higher the residual weight remained (65% at 60 °C + 105 °C). The weight loss of the cured wood-SS occurred in 2 stages, as observed by two negative DTG peaks, between 40 - 140 °C and 140 - 440 °C. Water loss occurred between 40 - 140 °C [212] [263] [264]. The intensity of the water loss DTG peaks are seen to reduce with increased curing temperature. Li et al (2013) reported a similar range of degradation temperature for SS from 75 to 221 °C associated with water loss [265]. The second degradation stage is associated with the breakdown of silanol groups and wood components [230] [266].

With an increased in wood content to 60%, a lower residual weight was recorded at 55% in comparison to 61% for wood-SS (50:50) samples which were cured at 50 °C. This is due to the presence of unbonded wood particles and low thermal stability of the lignocellulosic components in wood fiber. Natural fillers like wood in increased amounts are known the reduce the thermal stability of composites hence the observed residual weight reduction [267].

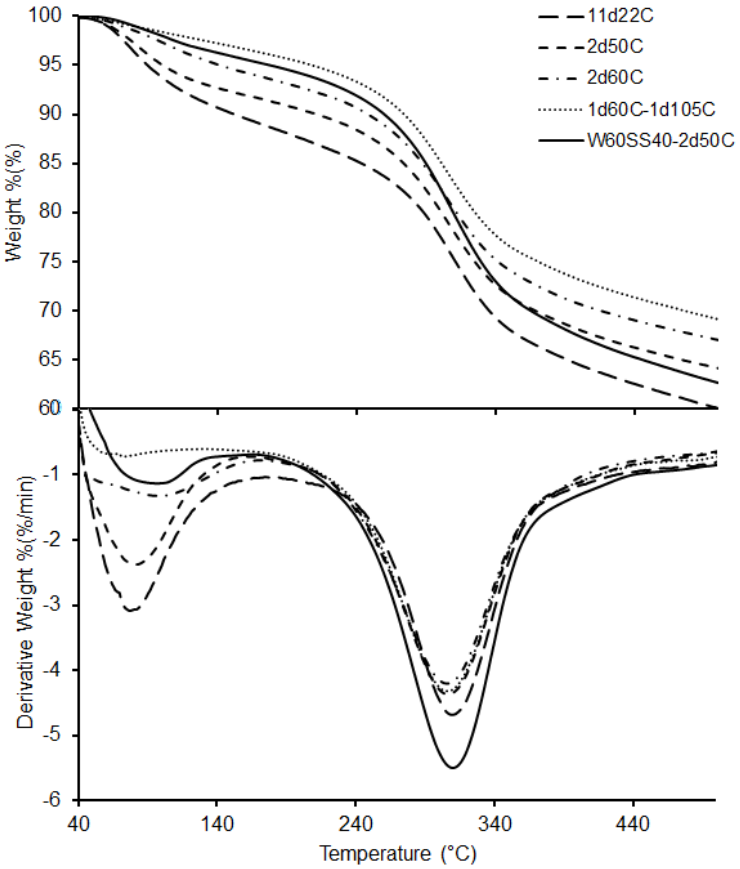

Figure 2.9: TGA and DTG thermograms of wood-SS samples cured at different temperatures.

Table 2.6: Thermogram peak values for the cured wood-SS composites.

Curing time and temperature	First Peak (°C)	Second Peak (°C)	Residual (%)
50:50 blend			
11 d at 22°C	79 (±4.5)	310 (±2.3)	57 (±1.1)
2 d at 45°C	76 (±2.1)	305 (±1.1)	57 (±1.4)
2 d at 50°C	77 (±3.7)	307 (±1.2)	61 (±0.5)
2 d at 60°C	103 (±6.2)	305 (±2.4)	63 (±0.5)
1 d at 60°C + 1 d at 105°C	-	307 (±1.9)	65 (±0.7)
60:40 blend			
2 d at 50°C	77 (±5.3)	309 (±2.6)	55 (±3.0)

Note: Standard deviation in parentheses.

2.4.6. Water absorption properties

The wood-SS composites were evaluated for their water resistance by performing a 24 h water soak test. All the wood-SS composites cured between 22 and 60 °C disintegrated after 24 h water soaking. The wood-SS sample cured at the higher temperature (1 d at 60 °C + 1 d at 105 °C) remained intact after water soaking (80% weight gain and 21% thickness swell). It appears that curing at low temperature removed the water from the wood-SS mix but did not cross-link the SS and that the higher curing temperature resulted in SS crosslinking [268] .

2.4.7. Fire Test

The wood-SS (50:50) composite cured at the higher temperature was evaluated for its fire resistance using a Bunsen burner test over 5 min (Figure 2.10). At 1 min the composite bent slightly. After 5 min the sample exhibited no smoldering once the flame was removed and an average weight loss of 20% was recorded. Visual inspection of the flame tested sample (Figure 2.10d) showed some small sub-mm diameter perforations (holes) on the surface and confirms that the wood-SS composite was qualitatively fire resistant.

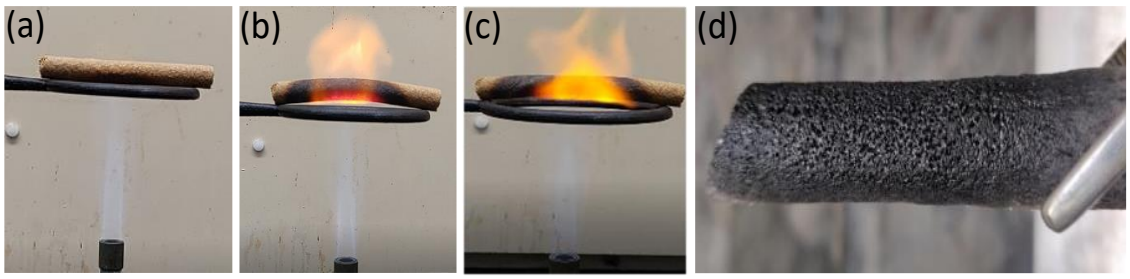

Figure 2.10: Photographs of the wood-SS (50:50) composite during a Bunsen burner flame test at (a) 0 min, (b) 2 min, (c) 4 min, and (d) after 5 min (test completed).

2.5. Conclusion

Composites made from wood-SS were successfully blended, extruded into 2-dimensional rods, and cured. The wood-SS blends were shown to have good rheological properties suitable for extrusion. Wood-SS (50:50) samples exhibited good thermal stability, burning properties and flexural properties. The flexural properties decreased with higher curing temperatures. The water soak performance of the low temperature cured composites was not satisfactory; however, at higher temperature curing the composites performed well. The wood-SS composite material shows potential for use in additive manufacturing for interior applications. Furthermore, SS is an inexpensive non-toxic binder in fire retardant/resistant natural fiber composites. To move this technology forward further work is required to (i) fully understand the curing mechanism of SS in wood blends, (ii) improve the curing process to have good water performance as well as flexural properties, and (iii) explore the use of acidic catalysts to accelerate curing.

2.6. Acknowledgements

The authors would like to acknowledge (i) the Idaho State Board of Education-Higher Education Research Council-IGEM award # IGEM 20-002 for their financial support, (ii) USDA-CSREES grant 2007-34158-17640 for support in the purchase of the DSC, and the University of Idaho College of Natural Resources for support in the purchase of the FTIR spectrometer.

Chapter 3: Flow, curing and mechanical properties of thermoset resins–wood-fiber blends for potential additive-manufacturing applications. Orji, B. O., & McDonald, A. G. (2023)

"Flow, curing and mechanical properties of thermoset resins–wood-fiber blends for potential additive-manufacturing applications", Orji, B. O., & McDonald, A. G. (2023), ***Wood Material Science & Engineering*****, https://doi.org/10.1080/17480272.2022.2155873.**

3.1 Abstract

This study examined the use of softwood mill residues (50-90%) with two thermosetting resins (i) urea-formaldehyde (UF) and (ii) phenol-resorcinol-formaldehyde (PRF) resin for potential use in additive manufacturing (AM) of wood composite materials. The curing behavior of these blends was evaluated using differential scanning calorimetry and dynamic rheology. Curing kinetics was determined using the Kissinger and Cranes method. The presence of wood fibers reduced the curing peak temperatures for both resin blends at the same heating rates but curing peak temperatures increased with heating rates. Activation energy (E_a) increased with the addition of wood for the wood-PRF blends but reduced for the wood-UF blends in comparison to the neat resins. E_a values were between 51 kJ/mol and 271 kJ/mol for PRF and wood-PRF samples and 100 kJ/mol and 367 kJ/mol for UF and wood-UF samples. Frequency sweep flow curves of the green wood-resin blends showed shear thinning behaviors with viscosity values between 10^3 to 10^8 Pa.s at 30 °C. Mechanical properties of the wood-resin composites generally showed a reduction in flexural modulus with an increase in wood content. Wet wood (50%)-PRF blend was successfully extruded and shows promise for use in AM, however the wood-UF blend was not successful.

3.2 Introduction

The production of wood based composites using wood residues and thermosets has been an efficient way over the years to reduce the environmental issues of full log utilization [269]. These wood residues are commonly converted into flat non-structural wood composite panels such as particle board and medium density fiber board [270] [271]. These products are mostly produced in volume using a large forming line and hot-press. These composite panels

can be routed, trimmed, drilled to produce the final product (e.g. furniture) which generates waste [272] [273]. Commonly used adhesives in wood composites are formaldehyde based such as phenol formaldehyde (PF), phenol-resorcinol-formaldehyde (PRF), urea-formaldehyde (UF), and melamine-urea-formaldehyde (MUF) resins [274]. These resin systems are used based on their cost, mechanical, rheological, thermal, and curing properties in wood-based products [275]. The main process for producing densified wood-based composites involve hot pressing to obtain the required density profile, curing, heat, and mass transfer reactions [270]. Resorcinol in PRF resins make them cold setting resins in applications such as glulam beam, where high strength, weather resistant bonds and waterproof properties are required [276] [277]. Melamine modified UF resins, though expensive, have imparted good bonding and water resistance properties [278]. However, there are some issues with formaldehyde-based resins including free formaldehyde emissions over time. The use of melamine in UF resins, even in small amounts, has also been recorded to reduce formaldehyde emissions [279].

In recent years, additive manufacturing (AM) has been used to directly formulate products of unique shapes and sizes whilst reducing post machining waste. This technique can serve as an alternative for waste wood products production but requires more research to understand the necessary properties that will facilitate AM processes [280] [281] [282]. AM in the presence of wood fiber fillers (<10%) have been studied over the years, primarily using thermoplastic and UV-cured thermosetting binders [62] [283] [45] [44]. Bio-epoxy based inks with sawdust and lignin (≤35% w/v) has been successfully 3D printed using a developed technique of delayed extrusion of cold masterbatch (DECMA) to enable proper layer to layer deposition [10]. The use of wood fiber will reduce wood waste and promote sustainability in AM [284] [285] [286]. Good interfacial adhesion is required between the wood fiber and the resin matrix to impart good mechanical performance. Thermoset resins generally have improved performance (thermal resistance, deformation resistance, and good mechanical properties) over thermoplastic resins due to their cross-linked structure [45]. Recent work by Orji et al. has shown that wood-sodium silicate formulations could be extruded and potentially used in AM [287].

Understanding the curing behavior and rheological properties of these blends, such as wood content and resin type, is very crucial to enable the proper optimization of AM process

designs and improving the properties of the product [288] [289]. The importance of rheology in AM in a study involving the mechanisms that cause collapse for tall thin printed walls using nano clay and fumed silica epoxy feedstocks [290]. Curing kinetics of resins which has been studied over the years contributes to understanding the bond changes and crosslinking reactions, but little information has been recorded on the rheology and curing kinetics of different wood content thermoset blends. The influence of liquified wood on the curing kinetics of melamine urea formaldehyde has also been analyzed using DSC to account for curing reactions in developing industrial processes [291]. The effect of filler load on the curing behavior of oil palm shell thermoset composites with a maximum filler loading of 33 wt.% and curing reactions were monitored to aid the understanding of filler loading on curing rate [267]. Extruded wood thermoset composite was studied using a novolac phenolic resin with 50 to 62 wt.% of wood fibers, but this was only achievable because of the thermoplastic modifier [292]. They also stated that with higher wood content, extrusion was barely possible because of issues of restricting flow properties and friction. The goal of this study involves understanding the rheology, curing behavior of composites formulated from two formaldehyde resins, PRF (cold setting resin) and UF (hot setting resin) in the presence of high wood fiber content (50 to 90 wt.%) to establish which wood loading would be best for extrusion and AM. Dynamic rheology and differential scanning calorimetry (DSC) were used to study the curing properties and understand their flow properties for possible AM applications. Thermal and mechanical properties of the cured composites were also ascertained from thermogravimetric analysis (TGA), dynamic mechanical analysis (DMA) and flexural tests.

3.3 Materials and Methods

Softwood mill residues were obtained from Plummer Forests Products (Post Falls, ID, USA) and screened to pass through a standard 40 mesh screen. Commercial resins were a cold setting PRF (Cascophen (TM) 4001-8 / Cascoset (TM) 5830 E (2.5:1) by Hexion, pH = 10.2) for glulam beam applications and hot setting melamine modified UF Resin (60% solids, Leaf C2 636A26, Georgia Pacific, pH = 8.5) for particleboard.

3.3.1 Wood Fiber characterization

Moisture content of the wood fiber was determined using 2.6 g to 3.5 g of samples in a HB43-S Halogen Moisture Analyzer (Mettler Toledo, Columbus, OH, USA). Wood pH was determined on an aqueous extract of the wood fiber (5 g) in water (40 g) that was refluxed for 10 min, cooled, and measured using an Accumet AP61 (Hampton, NH, USA) pH meter. Length and width dimensions of the 250 screened wood particles was determined using optical microscopy (Olympus BX51 microscope with a DP70 digital camera at 40x, San Diego, CA, USA). Fiji ImageJ software (version 2.1.0/1.53c, Java 1.8.0_172 (64bit)) was used to analyze the micrographs to determine aspect ratio [287].

3.3.2 Electrospray Ionization Mass Spectrometry (ESI-MS) of the resins

The average molar mass distribution of the resins was determined by ESI-MS on a Finnigan LCQ-Deca instrument (ThermoQuest) between m/z 100 and 2000. PRF was analyzed in the negative ion mode while the UF resin was analyzed in the positive ion mode. Resin (1 mg) was dissolved in methanol (1 mL) and introduced at 10 µL/min. Ionic and spray voltages were respectively 4.5 kV and 50V a 275 °C. The weight average molar mass of the resins was calculated using the formula $M_W = \Sigma N_i M_i^2 / \Sigma N_i M_i$ with N_i been the intensity of ions and M_i the mass after charge account.

3.3.4 Composite Preparation

Screened wood fibers (50 to 90%) were blended with either a UF or PRF resin on dry weight basis. For small samples (2 g batch), an herb grinder was used for mixing (2 min) and preparing dynamic rheology specimens (2.00 mm (h) x 25 mm Ø) by cold pressing in a 25 mm Ø pellet die with 0.45-tonne load. For larger batches of wood-resin blends (50-100 g) a coffee grinder (Pinlo, 200 W) was used for mixing (2 min) and the mixture transferred to a 75 mm Ø pellet die set and pressed into discs at 160 °C for 10-15 min at 1.2-ton load (PHI hydraulic press, City of Industry, CA, USA). After pressing, the disc samples were kept flat by placing a 500 g weight and conditioned at room temperature for 24-48 h at ambient conditions. Density of cured samples were determined by measuring its dimensions and weight. Cured neat resins and wood fibers density was determined in nitrogen using an Ultra-Pycnometer 1000 (Quantachrome, USA) at room temperature.

3.3.5 Thermal analysis

Wood-resin blends and resins were freeze-dried prior to DSC analysis. Modulated DSC (MDSC) on freeze dried samples (5 mg) was performed in hermetically sealed Tzero Aluminum pans on a Q200 DSC (TA instruments, New Caste, DE, USA) under nitrogen (50 mL/min) and refrigerated cooling from 40 °C (2 min) and ramped to 250 °C at either 5, 10, 15 or 20 °C/min. Samples were equilibrated at 40 °C for 2 min, modulated at amplitudes of +/- 0.8, 1.6, 2.4 and 3.2 °C for respective heating rates every 60 s, and ramped to 250 °C. Data was analyzed using the TA Universal analysis software. The kinetic parameters were determined using the Kissinger-Akahira-Sunose ((KAS) iso-conversional) and Crane methods [293] [294]. The enthalpy of curing was calculated from the total area under the exotherm curve and used with the Kissinger equation (3.1). The Crane equation (3.2) was used to determine the reaction order (*n*) values.

$$-\ln\left(\frac{\beta}{T_p^2}\right) = \frac{E_a}{RT_p} - \ln\left(\frac{AR}{E_a}\right) \qquad \text{(Equation 3.1)}$$

$$\frac{dln(\beta)}{dln(\frac{1}{T_p})} = \frac{-E_a}{nR} \qquad \text{(Equation 3.2)}$$

Where, β is the heating rate (K/min), E_a is the activation energy in J/mol, T_p is the exothermic peak temperature, R is the gas constant (8.314 J/mol/K), and *A* is the pre-exponential factor (1/s). To determine E_a, a plot of $-\ln(\beta/T_p^2)$ versus $1/T_p^2$ for and the slope is used. To determine the pre-exponential factor *A*, the intercept of the plot was used. For the reaction order (*n*) values, the linear slope obtained from the plot of ln (β) vs $1/T_p$ in the Crane's equation was used. To determine the E_a at every degree of conversion, the KAS equation below was used.

$$-\ln\left(\frac{\beta}{T^2}\right) = \frac{E_a}{RT} - \ln\left(\frac{AR}{E_a g(\alpha)}\right) \qquad \text{(Equation 3.3)}$$

where, T is the temperature at a given degree of conversion (K).

Thermal stability of wet and cured samples (5 mg) was determined using a Perkin-Elmer TGA-7 instrument (Shelton, CT, USA) under nitrogen (30 mL/min). Non-isothermal scans were performed from 40 to 900 °C at 20 °C/min and data analyzed using the Pyris v13.3.1 software.

The softening temperature of the cured resins (~1 mm thick pieces were determined using a PerkinElmer TMA-7 instrument under nitrogen (30 mL/min) with refrigerated

cooling, from -25 to 350 °C at a rate of 5 °C/min. Data was analyzed using the Pyris v13.3 software.

Viscoelastic properties of the cured composites (3 mm x 4 mm x 15 mm) were performed in duplicate using a Perkin Elmer DMA-7 instrument in 3-point bend mode (15 mm span, 1 Hz and 0.1% strain) on rectangular sample from -30°C to 350°C at 5 °C/min. For cured PRF and UF resins (4 mm x 4 mm x 1 mm) compression mode (1 Hz and 0.1% strain) was used from 30 °C to 350 °C at 5 °C/min. Data was analyzed using the Pyris v13.3 software.

3.3.6 Dynamic rheology

Flow, curing characteristics and rheology properties (complex viscosity (η*), storage modulus (G'), Tan δ) were performed on wet discs (2 mm x 25 mm Ø) and neat resins using a Discovery Hybrid Rheometer (DHR2, TA instruments, New Caste, DE, USA) between two serrated parallel plates (for wood resin blends) and disposable aluminum plates (for neat resins). Measurements were determined using (i) temperature ramp from 30 to 200 °C at 2 °C/min with 0.1% strain and frequency of 1 Hz and (ii) isothermal (30 °C) with 0.1% strain and a frequency sweep from 0.01 to 100 Hz.

3.3.7 Extrusion

To determine the extrudability of wood-resin blends (50 g batch, 50:50 and 60:40) for use in AM, wet sample blends were extruded using a RobotDigg (Shanghai, China) extruder (200 W motor and 17 rpm) with a 20 mm Ø barrel, 200 mm length, 8.5 mm pitch and a 9 mm Ø die for a run time of 10 min (Appendix Figure A3.1).

3.3.8 Fourier Transform Infrared Spectroscopy (FTIR)

Fourier transform infrared (FTIR) spectroscopy was performed on a Nicolet-iS10 spectrometer (Thermo-Scientific, Madison, WI, USA) with an attenuated total reflectance (ATR) accessory (Smart Orbit, Diamond). The spectra were ATR and baseline corrected using the Omnic v9.8.3 software.

3.3.9 Flexural testing

Flexural properties of cured samples cut into 5 rectangular specimens (63.5 mm x 13.5 mm x 3 mm) were determined according to ASTM D790 using an Instron 5500R-1132 universal testing machine (5 kN load cell, 48 mm span, and cross head speed of 1.1 mm/min). Data was collected and analyzed using Bluehill v3.3 Instron software.

3.3.10 Water Soak

Thickness swell (TS) and water absorption (WA) of cured specimens (15 mm x 15 mm x 3 mm) were determined after a 24 h water soak test. Percent weight gain and thickness swell were calculated from original and final dimensions and weight.

3.3.11 Statistical Analysis

Flexural properties and water soak test results were evaluated using a one-way ANOVA test for individual test results with a 95% confidence interval in QI Macros 2018 (Microsoft Excel).

3.4. Results and Discussion

3.4.1 Wood Fiber Characterization

The wood fiber had a moisture content of 5.6%. The fibers have been previously characterized and shown to have an average length 208 µm with an aspect ratio of 1.2 [287]. Fiber aspect ratio is an important parameter in promoting good mechanical properties in wood composites [295] [296]. The pH of the wood was 4.85. The acidity of the fiber will aid in catalyzing UF resins while retarding curing in PRF resins [297] [298].

3.4.2 Resin Molar Mass Determination

The weight average molar mass (M_w) of the PRF was 885 g/mol (Figure 3.1a) and UF was 921 g/mol (Figure 3.1b) were calculated from the ESI-MS data. The negative ion ESI-MS of PRF showed major peaks with tentative assignments at m/z 109 (resorcinol (R), $[R\text{-}H]^-$), m/z 321 (resorcinol$_2$-methylol$_3$, $[R_2M_3\text{-}H]^-$), m/z 443 ($[R_3M_4\text{-}H]^-$), m/z 639 ($[R_5M_2\text{-}H_2O\text{-}H]^-$), m/z 761 ($[R_6M_2\text{-}H_2O\text{-}H]^-$), and m/z 549 (phenol$_5$methylol$_2$-$H_2O$-H]$^-$) based on Pizzi et al., (2004). The positive ion ESI-MS of UF (Figure 3.1b) gave major peaks with

tentative assignments at m/z 185 (urea$_2$-methylol, $[U_2M+Na]^+$), m/z 215 ($[U_2M_2+Na]^+$), m/z 245 ($[U_2M_3+Na]^+$), m/z 257 ($[U_3M+Na]^+$), m/z 287 ($[U_3M_2+Na]^+$), m/z 317 ($[U_3M_3+Na]^+$), and m/z 391 ($[U_4M_3+Na]^+$) based on H. Wang et al., (2018). The resins both have oligomers with methylene bridges [301] [302].

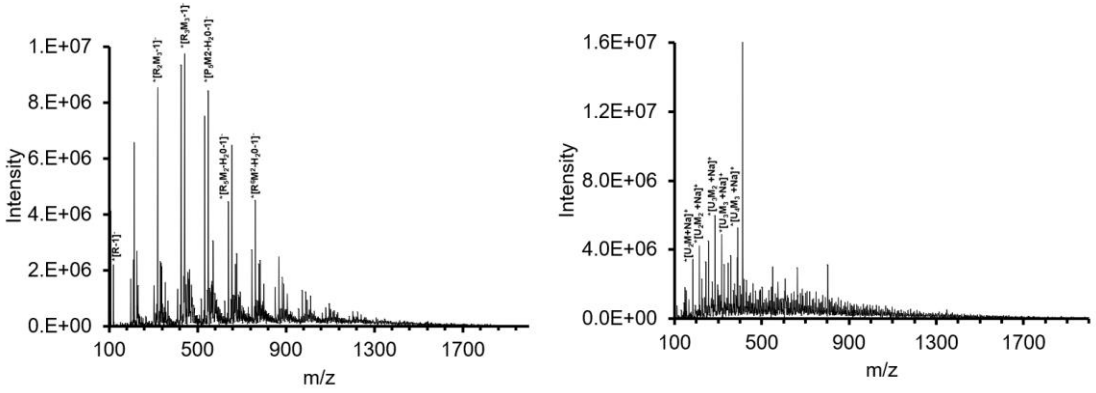

Figure 3.1: ESI-MS of (a) PRF resin (negative ion) and (b) UF resin (positive ion)

3.4.3 Rheology and curing of resin and wood-resin blends

The curing of neat resins and wood-resin blends (Figure 3.2)(Appendix Figure A3.2) were examined by dynamic rheometry as a function of temperature and frequency. The elastic (G′) and viscous (G″) moduli, tan δ and complex viscosity (η*) rheological properties were measured.

The flow (curve) characteristics of the resin and wood-resin blends were determined using a rheological frequency sweep experiment to determine the influence of shear rate on η* at 30°C (Table 3.1 and Figure 3.2a and 3.2b). The temperature used was considered an expected extrusion operating temperature for AM. For PRF resin, linear shear thinning behavior was seen >0.1 Hz, but deviated at low frequencies (0.03 to 0.08 Hz). Shear thinning influences the ability for the wood-resin blends to be extruded through a nozzle and its ability to relax adequately after shear has been applied [303]. In addition, the applied shear forces will break up any agglomerates. The addition of wood to PRF increased the η* by about 2 orders of magnitude (10^2 times) at 1 Hz (Table 3.1). Shear thinning behavior was observed for the wood-PRF blends. The η* of 350 kPa.s for wood-PRF at 50% wood content dropped by nearly half by increasing wood content to 90%. This phenomenon of η* reduction could be attributable due to the presence of excess wood starving the interaction between resin

droplets hence creating a network that has less internal friction and lower fluid consistency. The UF resin showed a similar behavior to PRF and was independent of shear rate or frequency [304]. The η* values increased by 3 orders of magnitude (10^3 times at 1 Hz) with the addition of wood fiber to UF resin. The η* of 155 kPa.s for wood-UF at 50% wood content nearly doubled by increasing wood content to 90%, which was an opposite trend to wood-PRF. Also shear thinning behavior was observed for all the wood-UF blends and although low η* is required for extrusion, too low η* values could cause dripping from the printing nozzle [303]. To interpret the flow curves further analysis was required.

The flow curves (η* versus frequency plots) were analyzed by two different models. Both the PRF and UF resins plots deviated from a straight line below about 0.05 Hz. These resins exhibited zero shear viscosity at low frequencies and were analyzed between 0.02 and 100 Hz using the Carreau-Yasuda model [305] which accounts for relaxation and transition times from Newtonian to non-Newtonian behavior as seen in equation below

$$\eta^* = \eta_\infty + (\eta_0 - \eta_\infty)(1 + \lambda^2\gamma^2)^{\frac{m-1}{2}} \qquad \text{(Equation 3.4)}$$

where, η* is the neat resin complex viscosity, η_∞ is viscosity at infinite shear rate, η_0 the zero-shear viscosity, λ is the time constant, *m* is the power and γ is the shear rate. For PRF resin the model parameters were η_∞ = 262 Pa.s, η_0= 11,000 Pa.s, λ = 8.3s, and *m* = 0.244. For UF resin the model parameters were η_∞ = 9.85 Pa.s, η_0= 726 Pa.s, λ = 13.9 s, and m = 0.200. Both UF and PRF resins had a model goodness of fit (R^2) > 0.98. Fluids with *m* values approaching 0 have low shear thinning behavior while *m* values approaching unity have high shear thinning behavior [306].

The addition of wood fibers to the resins increased their η* (Figure 3.2a and 3.2b). The rheological data (η*) were quantitatively analyzed by fitting to a modified Power–law model by exchanging the steady shear terms with dynamic viscosity terms in Equation 3.5.

$$|\eta^*(\omega)| = \mathrm{K}(\omega)^{n-1} \qquad \text{(Equation 3.5)}$$

Where, *n* is the non-Newtonian or flow behavior, and index K is the consistency coefficient. The results (η* at 1 Hz, K, *n* and R^2) for the power law models for the wood-resin blends are given in Table 3.1. Power law models for PRF and UF resins gave poor goodness of fit

values (R^2 ~ 0.53-0.55) as compared to the Carreau-Yasuda model (R^2 >0.98). The wood-resin formulations gave better η* versus frequency plots resulting in R^2 values >0.9 for the power-law models. For successful extrusion of the wood-resin blends, a good shear thinning component *n* is required. Studies have shown that liquids with low *n* have greater shear thinning behavior and may back flow during AM [307] [303]. Wood-PRF blends have higher *n* values than wood-UF blends at the same wood content. The K values for the wood-PRF blends were comparable and the η* (at 1 Hz) decreased with wood content. From a previous study, the η* increased with wood fiber content and the molecular mobility and bond strength reduced which in turn increased the force exerted to extrude the material [308].

Table 3.1: Complex viscosity (η*) of the PRF and UF resins and wood-resin blends at 1 Hz, 30 °C, and power law fitted model parameters K and n as well as goodness of fit (R^2).

Resin	η* at 1Hz (kPa.s)	K (kPa.s)	*n*	R^2 values
PRF blends				
100% PRF	2.5 (2.4)[a]	2.1	0.456	0.530 (0.983) [a]
50% PRF	350	327	0.880	0.902
40% PRF	321	303	0.882	0.950
30% PRF	256	244	0.920	0.971
20% PRF	177	174	0.931	0.991
10% PRF	159	150	0.923	0.997
UF blends				
100% UF	0.1 (0.09) [a]	0.09	0.538	0.554 (0.988) [a]
50% UF	155	149	0.804	0.967
40% UF	278	240	0.813	0.943
30% UF	244	227	0.867	0.959
20% UF	273	252	0.889	0.966
10% UF	243	224	0.890	0.967

[a] Values in parentheses are from the Carreau-Yasuda model

To determine the extrudability of the wood-resin blends, a 50:50 wood-resin ratio was selected. The wood-PRF blended sample was successfully extruded into a rod (Figure 3.3a) with little die swell observed and this shows that this formulation shows promise for AM. In contrast, the wood-UF blend, was not successfully extruded. For the 50:50 wood-UF mix the UF resin was shown to squeeze out from the end of the die (Figure 3.3b) and the wood fiber being compacted and accumulated at the end of the screw (Figure 3.3c) and thus blocked the die. The wood-UF (60:40) mix was also tried to increase its viscosity comparable to PRF-wood (50:50) (Figure 3.4) but extrusion was not successful. Contributing factors to its poor performance could be due to the UF resin low viscosity relative to PRF (Table 3.1). This shows that the rheology of the wood-resin mix (e.g., resin type, wood-resin ratio) is important for obtaining an extrudable formulation. To validate this, the dynamic rheology η* curves for 50% PRF, UF and an already studied geo-based resin (sodium silicate) [287] were compared (Figure 3.4). The η*for 50% UF was decreased by 56% and 80% in comparison to 50% PRF and 50% sodium silicate, respectively, showing the effect of rheology η* on the extrusion.

This study compared cold and hot-setting resins for their suitability in AM of wood composites. The PRF and UF resin η* vs. temperature (curing) curves are shown respectively in Figures 3.2c and 3.2d. The moduli curves (G′ and G″) of the resins exhibited similar temperature characteristics to η* (Appendix Figure A3.2). The G′ curves show the elastic (solid-state) behavior and the G″ curves show the viscous (liquid state) behavior of the resins.

For the PRF resin, a cold setting resin, an initial increase in η* was observed from 30 °C to 37 °C followed by softening and a decrease of η* from 37 °C to 42 °C. The rapid increase in η* showed gelation and onset of curing/crosslinking of the resin from 42 to 53 °C which is consistent with a cold setting resin. A plateaued region for η* was observed from 53 °C to 200 °C for PRF showing a constant stiffness and vitrification of the resin. The crossover points of G′ and G″ was seen at 38 °C showing this resin gel point (Appendix Figure A3.2). A slight decrease in modulus and η* was observed for the PRF resin from 100 °C to 112 °C due to the removal of water. With the addition of 50% wood to PRF resulted in an increase in η* of >100% at 30 °C due to the reinforcing nature of the fiber on the matrix. Onset curing temperature also increased with the addition of wood to PRF and a higher η* was observed with 50% wood and this reduced with wood content.

The tan δ peak height was used to help understand the cure of the neat resins and wood-resin blends (Figure 3.2e and 3.2f). For neat PRF, a maximum tan δ peak (0.12) was observed at 63 °C which shows its transition from a gel to a vitrified state. For the wood-PRF blends, tan δ values shifted slightly to higher temperatures, to 65 °C - 72 °C, due to the presence of wood fibers. The tan δ peak values initially reduced with wood content from 30 °C to 50 °C. The tan δ peak values generally increased with an increase in wood content (50, 60, 70, 80 and 90%) for wood-PRF blends were 0.34, 0.39, 0.41, 0.48 and 0.26, respectively. High mobility of polymer chains has been stated to increase tan δ values due to the strong resin water-polymer interactions. Good extrudability is also promoted by high tan δ values as seen with values from 50% to 80% PRF content [309] [310].

For UF resin (Figure 3.2d), the η* decreased from 37 °C to 86 °C, then gelation occurred from 86 °C to 157 °C due to cross-linking consistent with a hot setting resin. Continued cross-linking resulted in vitrification of the UF resin from 157 °C to 200 °C. A similar curing trend was observed with MUF with gelation starting at 92 °C and a stable plateau observed above 159 °C [311]. Two crossover points for the G′ and G″ were observed for the neat UF resin at 51°C and 124°C, respectively (Figure A3.2). The later crossover point was associated with gelation. The addition of wood fibers to UF resin dramatically increased η* by 2 orders of magnitude (10^2 times) at 30 °C (Figure 3.2d, Table 3.1). The η* increased from 50 to 70% wood content. At the 80% and 90% wood contents a slight reduction in η*was observed due to the low resin content and possible slippage between wood fibers with little or no resin coverage [312] [313].

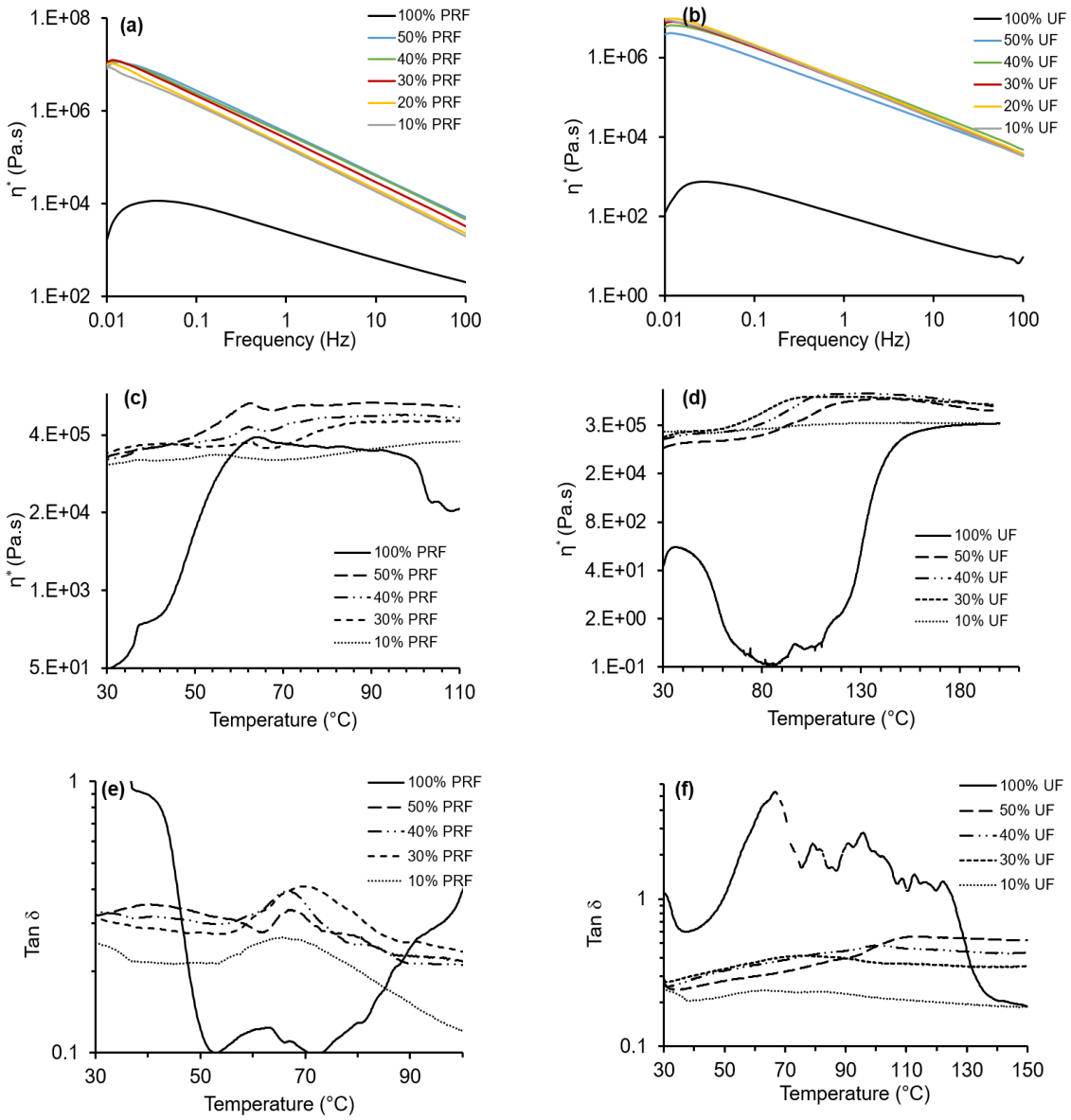

Figure 3.2: Rheological plots of (a) η* versus frequency for PRF resin and wood-resin PRF blends at 30°C, (b) η* versus frequency for UF resin and wood-UF blends at 30°C, (c) η* versus temperature for PRF resin and wood-PRF blends, (d) η* versus temperature for UF resin and wood-UF blends, (e) tan δ versus temperature for PRF resin and wood-PRF blends, and (f) tan δ versus temperature for UF resin and wood-UF blends

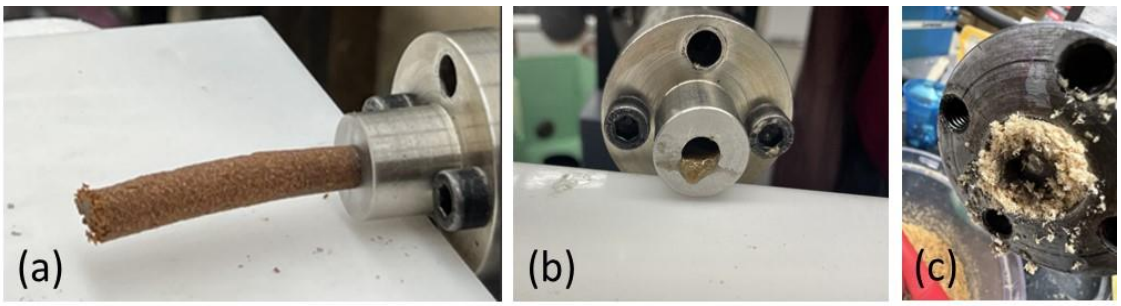

Figure 3.3: Photographs of (a) successful wood-PRF (50:50) extrusion, (b) unsuccessful extrusion of wood-UF (50:50) mixture showing resin squeeze out at the end of the die, and (c) unsuccessful extrusion of wood-UF (50:50) mixture showing compaction and accumulation of wood fiber at the end of the screw.

For neat UF resin, tan δ reached a maximum around 67ºC when the resin started to cross link and gel. Also, tan δ values were variable between 70 and 125ºC. This is typical of material which continually flows as temperature increases and with high mobility of UF chains [309]. The addition of wood to the UF resin reduced the tan δ value relative to UF resin. Tan δ values decreased from 0.55 to 0.38 with wood content from 50 to 90% (Figure 3.2f). T_g values were observed between 50 and 130 °C and were higher than the wood-PRF blends. Materials having low tan δ values (~ 0) show more elastic behavior while tan δ values close to unity have more viscous behavior [314]. Low tan δ values result in materials with lower damping, modulus, energy absorption and energy dispersal properties as seen for the 90% wood-UF resin [315].

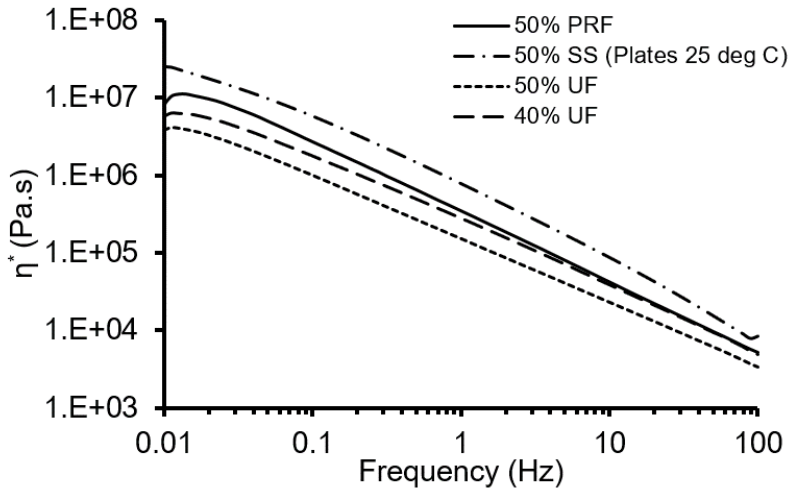

Figure 3.4: Frequency sweep dynamic η* for comparable blends extrusion

To understand the curing behavior of the resin and wood-resin blends, DSC was used, and non-reversible heat flow curves obtained (Figure 3.5). DSC thermograms showing an extended temperature range is shown in Figure S3. Kissinger and conversion plots were produced (Figure 3.6) and reaction kinetics determined by calculating their activation energy (E_a) and reaction enthalpies (ΔH) from the plots (Eq. 3.1 and 3.2) and data given in Table 3.2. Moisture content of 18% and 33% were recorded after freeze drying the PRF and UF resins respectively. A single exothermic peak was observed for the curing of both PRF and UF resins and the exothermic peak temperature increased with heating rate, and conversely the enthalpy reduced with heating rate. The PRF exothermic peak temperature increased from 93 °C to 123 °C changing the heating rate from 5 to 20 °C/min which was in the range to those reported in a previous study for two PRF resins (93 and 99 °C at 10 °C/min) [276].

For the UF resin, the exothermic peaks were close, 141-142 °C, for all four heating rates. ΔH which correspond to the amount of released during a curing reaction was higher for UF than that of PRF resin at comparable heating rates. Curing peak temperatures from 95 to 102 °C were recorded in a previous study for three different freeze-dried UF resins containing melamine at 10 °C/min [316]. These values were slightly lower than the observed values in this study.

The addition of wood to the resin generally reduced the exothermic curing peak temperature for both resins (Figure 3.4). This led to the reduction in ΔH (Table 3.2) with an increase in wood content due to the restricted mobility of the resin in the wood fiber network [317]. The reduction in the exothermic peak also reduced the resin curing rate [318]. For example, for wood-PRF (50:50) the ΔH was 19 J/g and reduced to 2 J/g at 90:10 wood-PRF and a similar trend was observed for wood-UF blends. The curing of the resins in the composite might be influenced by the presence of wood fibers which decreases mobility of the resin molecules and reduces reactive groups [317] [178]. Acidic wood (low pH) is also known to catalyze the cure of UF resins [317]. Furthermore, the reduction in ΔH could be attributed to the reduced resin content relative to wood content [319]. Onsets and end set curing temperatures (T_{onset} and T_{endset}) for each sample increased with increasing heating rate due to the large temperature gradient within the sample which caused differences in bulk and surface temperature resulting in a thermal lag effect. This increasing reaction rate caused a reduced degree of conversion since the samples did not have time to react [291] [320].

The DSC peak curing temperatures (at 5 °C/min) were higher than those obtained by rheology (at 2 °C/min) tan δ peaks for all samples and this is a kinetic effect of the different heating rates. There might also be an effect of freeze drying the resin prior to DSC analysis as compared to rheological tests that were performed on liquid samples and this phenomenon has also been observed in a previous study [321]

The E_a can be used as a reference to monitor the curing behavior of resins. E_a was calculated from the plots of $-\ln(\beta/T_p^2)$ versus $1/T_p^2$ (Figure 3.5a and 3.5b). The calculated E_a for the PRF and UF resins were 51 kJ/mol and 367 kJ/mol respectively (Table 3.2). Curing for phenolic resins have been studied to occur under basic conditions which results in a lower E_a [322]. In the presence of resorcinol, more alkaline pH is obtained which accelerates crosslinking and reduces the E_a [277]. For UF, an increase in E_a has been possibly accredited to the lower pH of the resins [322]. UF resin curing is known to be promoted in acidic conditions and at elevated temperatures [317] [318]. A high E_a of 287 kJ/mol for liquid UF resin has also been previously reported [323]. The value of E_a for the UF used in this study was high probably due to the freeze drying of the sample which increased the restricted mobility of the resin molecules in the blend since water plays a major role in the curing process [316] [321]. The plots of $-\ln(\beta/T_p^2)$ versus $1/T_p^2$ had R^2 coefficients of 0.882 for PRF and 0.306 for UF and pre-exponential factor (*A*) of 3.6×10^6 for PRF and 4.3×10^{46} for UF were determined. A high *A* value, according to the collision theory, is due to a large reaction resulting from the total number of successful collisions. This in turn means that a resin with a high *A* value will require a high temperature to cure completely [324] [325]. There were very similar linear relationship slope values obtained from the Kissinger and Crane plots showing an accurate relationship between theoretical and experimental data [326]. The calculated *n* values were 0.900 and 0.982 for PRF and UF, respectively.

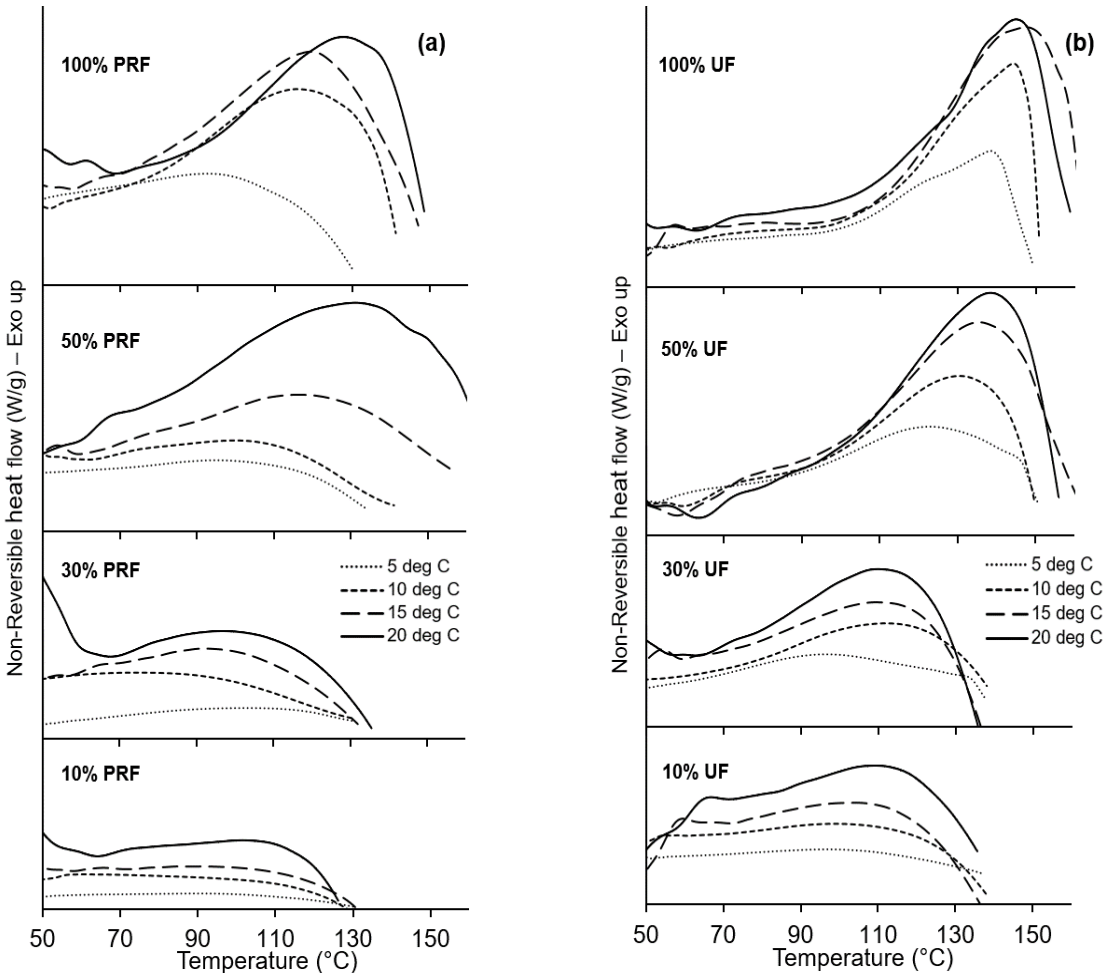

Figure 3.5: MDSC thermograms showing non-reversible heat flow curves for (a) neat PRF and wood-PRF blends and (b) neat UF and wood-UF blends at four different heating rates.

The curing reaction of both the PRF and UF resins in the presence of wood fibers were examined by DSC and data generated was used to determine the E_a [322]. The calculated E_a (using Eq. 3.1 and 3.2) and corresponding R^2 (>0.82 for wood-PRF and >0.96 for wood-UF) values are given in Table 2. For the wood-PRF blends the E_a values were from 73 kJ/mol (50% wood) to 218 kJ/mol (90% wood). E_a values generally increased with wood content. [322] recorded E_a values for phenolic resin between 65 to 89 kJ/mol which increased with softwood content from 20 to 50%. Due to the acidic pH of the wood extract (4.85) and basic conditions of PRF (10.2), a lower pH is likely to occur which gives a high E_a. With reduced pH values of a PF resin, an increase in E_a in comparison to a more basic PF resin was observed in a study of the curing kinetics of PF resin in the presence of wood [322]. The pre-exponential factor *A* was seen to increase with the addition of wood for wood-PRF

blends. This increase in *A* may be due to the number of active sites in wood and collisions for the system with respect to the collision theory [325].

The E_a for the wood-UF blends ranged from 108 kJ/mol (50% wood) to 115 kJ/mol (90% wood). The values of E_a for the wood-UF blends were low in comparison to the neat UF. This is probably due to the restricted mobility of the resin molecules in the presence of wood [316]. Studies have also observed the reduction in E_a for melamine-UF resin in the presence of high surface area aluminum silicate nano clays [327]. This was attributed to low diffusion of the urea which caused the nanoparticles to reduce the curing behavior of the melamine crosslinks. The presence of acidic wood will catalyze the UF curing reaction and decrease the E_a [328] [329]. A decrease in *A* was observed for wood-UF blends with wood content. The high values of *n* (0.920-0.978) for both wood-resin blends suggests a more complex reaction is occurring in these systems [291]. Analysis methods with multiple heating rates, like Kissinger, have proven to be a reliable method (good R^2 values) to monitor cure [330].

The conversion (α) plots were generated using the TA universal analysis software which gives the running integral of the DSC exothermic peak and shows the polymer conversion and composition with increase in temperature [287]. Reaction α plots were prepared for both wood-resin blends from MDSC data at 10 °C/min (Figure 3.6c and 3.6d). It was noted that at higher wood content for the blends, a lower temperature is required to attain the same degree of α. The α degree for wood-PRF blends were at a lower temperature (due to being a cold setting resin) than the corresponding wood-UF blends [277]. In addition, for a wood-resin blend the higher the wood content the lower the conversion temperature. In other words, an increase in wood content, less time and temperature are needed for curing [291].

The plots of E_a versus α are shown in Figure 3.6e and 3.6f. The curing of PRF resin is mostly considered complicated since the addition and condensation reactions occur simultaneously. With the addition of wood, the reactions get more complicated with the reaction occurring with the wood in the matrix [331]. With this complexity, understanding the relationship between the E_a and α is necessary. E_a values were generally constant for neat PRF, 50%, 30% and 20% PRF in wood blends. For the neat PRF, E_a started at 45 kJ/mol and slowly reduced. With the addition of 60% wood, the dependence of E_a on α was changed with high E_a observed at the beginning of the reaction. The E_a was higher for 90 % wood

content because in the presence of high levels of acidic wood, the crosslinking and chemical molecular movements will be hindered causing an increase in E_a [327].

For the wood-UF blends, E_a gradually increased with α for neat UF and 50, 40, 30, and 10% UF in wood blends, except for 20% UF blends. The wood-UF (50:50) blend showed a large increase in E_a from ~100 kJ/mol at α = 0.1 to ~330 kJ/mol at α = 0.9 probably due to the presence of wood. Resin mass also decreased with increasing wood fiber content leading to faster curing in comparison to composites with 50 % wood content [291]. In the presence of a high molecular weight resin, mobility of the molecules reduces proceeding with a diffusion controlled reaction which increases E_a as a result of diffusion hindrance [316].

These results clearly show that the curing behavior of the wood-resin formulations will be critical to ensure complete cure after processing, such as post extrusion.

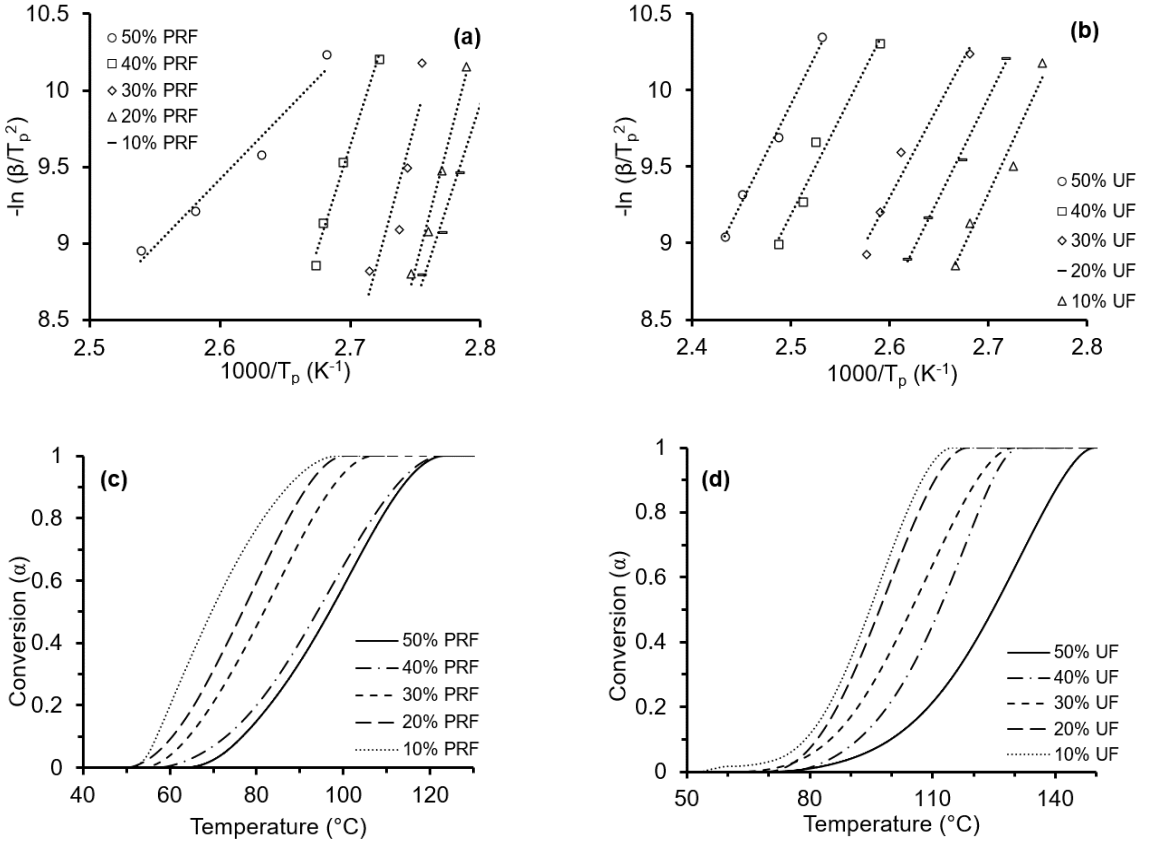

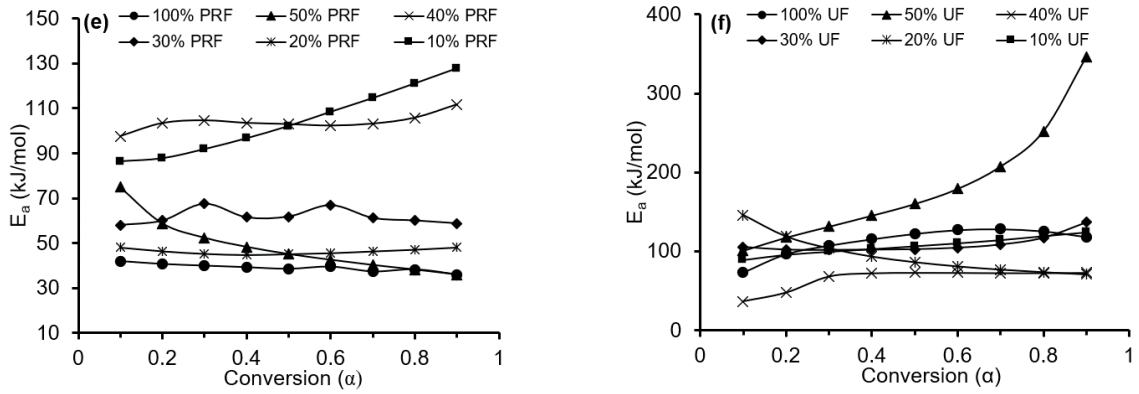

Figure 3.6: Plot of $-\ln(\beta/T_p^2)$ versus $1/T_p^2$ for a) wood-PRF blends and b) wood-UF blends; Conversion (α) plots versus temperature for (c) wood-PRF blends and (d) wood-UF blends at 10 °C/min; and activation energy (E_a) versus conversion (α) for (e) wood-PRF blends and (f) wood-UF blends

Table 3.2: Kinetic parameters for neat resin and wood-resin blends calculated using Kissinger's and Cranes model from DSC data

Resin	β (°C /min)	T_p (°C)	ΔH (J/g)	E_a (kJ/mol)	*A* (1/s)	*n*	R^2
	PRF blends						
PRF	5	96 (±3.2)	27 (±13)	51	3.6×10^6	0.8895	0.8895
	10	117 (±1.9)	43 (±8.0)				
	15	119 (±1.5)	35 (±18)				
	20	123 (±6.4)	27 (±2.9)				
50% PRF	5	100 (±7.0)	17 (±5.6)	73	6.0×10^9	0.9198	0.9669
	10	107 (±2.9)	19 (±5.1)				
	15	114 (±7.9)	28 (±11)				
	20	121 (±1.5)	50 (±10)				
40% PRF	5	94 (±6.7)	23 (±6.5)	223	6.2×10^{31}	0.9732	0.9867
	10	98 (±6.5)	11 (±2.3)				
	15	100 (±7.7)	32 (±9.4)				
	20	101 (±8.0)	15 (±9.9)				

Table 3.2 cont'd

30% PRF	5	90 (±8.1)	12 (±4.4)	260	4.4×10^{37}	0.9772	0.8238
	10	91 (±9.8)	6 (±5.3)				
	15	92 (±11)	10 (±4.8)				
	20	95 (±8.0)	34 (±33)				
20% PRF	5	86 (±17)	7 (±6.4)	271	3.5×10^{39}	0.9783	0.9874
	10	88 (±6.5)	3 (±1.4)				
	15	89 (±0.2)	9 (±1.4)				
	20	91 (±8.6)	4 (±1.0)				
10% PRF	5	83 (±9.3)	2 (±0.7)	218	8.6×10^{31}	0.9734	0.9879
	10	86 (±4.3)	2 (±0.8)				
	15	88 (±8.9)	4 (±0.4)				
	20	90 (±2.7)	3 (±0.2)				
	UF blends						
100% UF	5	141 (±3.0)	75 (±17)	367	4.3×10^{46}	0.9815	0.3056
	10	143 (±0.8)	68 (±20)				
	15	144 (±3.1)	52 (±34)				
	20	142 (±4.5)	65 (±26)				
50% UF	5	122 (±2.3)	81 (±11)	108	7.4×10^{13}	0.9414	0.994
	10	129 (±5.0)	33 (±13)				
	15	135 (±3.2)	59 (±21)				
	20	137 (±6.6)	36 (±8.8)				
40% UF	5	112 (±9.7)	27 (±14)	105	7.5×10^{13}	0.9415	0.9666
	10	123 (±6.7)	24 (±11)				
	15	125 (±3.8)	29 (±5.2)				
	20	129 (±8.6)	23 (±6.0)				
30% UF	5	100 (±1.4)	33 (±7.3)	100	4.4×10^{13}	0.9407	0.9607
	10	110 (±6.6)	23 (±3.7)				
	15	113 (±12)	12 (±1.6)				
	20	115 (±5.2)	15 (±5.5)				

Table 3.2 cont'd

20% UF	5	95 (±12)	14 (±6.0)	108	1.1 x 10^{15}	0.9454	0.9944
	10	99 (±3.1)	7.2 (±1.8)				
	15	106 (±7.1)	19 (±4.3)				
	20	109 (±0.3)	9.0 (±8.1)				
10% UF	5	90 (±8.6)	10 (±2.6)	115	2.1 x 10^{16}	0.9494	0.9590
	10	94 (±5.1)	2 (±0.4)				
	15	101 (±7.9)	8 (±4.2)				
	20	102 (±2.9)	5 (±2.0)				

Note: Standard deviation in parentheses.

3.4.4 Mechanical properties of cured composites

The various wood-resin formulations were blended, and compression molded into composites to see the effect of resin type and wood content on mechanical properties. The bending properties and densities of these composites are given in Table 3.3. The density of the wood fibers was 1430 kg/m^3. Average density of the cured PRF and UF resins (at 105°C) were 1241 kg/m^3 and 1486 kg/m^3, respectively. The calculated average densities for the wood-PRF composites were between 769 to 1067 kg/m^3 and for wood-UF composites between 865 and 1059 kg/m^3. For wood-PRF composites, as resin content increased, the density of the cured composites increased as seen by [332]. The wood-UF composites the density increased from 878 to 1059 kg/m^3 with an increase in UF resin content of 10 to 30% and then decreased to 865 kg/m^3 at 50% UF resin content.

For the wood-PRF composites the flexural modulus (FM) was shown to decrease with wood fiber content (Table 3.3). For example, the wood-PRF (50% wood) composite had an FM of 3.5 GPa and decreased to 1.5 GPa at 90% wood. In addition, the flexural strength (FS) for these composites also decreased with wood content from 53.7 (50% wood) to 9.8 MPa (90% wood). Studies have found that with the increased replacement of PF resins with lignocellulosic components, strength properties reduced [333] [334].The flexural properties of these composites were related to its density. Studies on particleboard have shown that their mechanical properties were positively related to its density [332] [335]. With an increase in

density, PRF resin content, improved mechanical interlocking between wood fiber and resin occurs and thus better mechanical properties [336].

The wood-UF (50:50) composite had the lowest performance (FM of 1 GPa and FS of 6.8 MPa) of all the UF composites. This was attributed to the resin squeeze out during pressing, also observed during extrusion, and clearly shows that there was an excess of resin relative to fiber content thus the brittle nature of the UF resin dominated its behavior [337] [338]. With an increase of wood content from 50% to 60% the FM and FS increased by over 100% showing the effect of saturated wood-resin wettability in the matrix. FM values for 10% UF composites were similar to values observed by Maraghi et al., (2018) for particleboard with a similar density (750 kg/m^3).

FM and FS values for wood-PRF composites were higher than the wood-UF composites [336]. This is due to PRF resins being stronger and used for structural wood composite applications than UF resins which are used for non-structural applications. In contrast, particleboard made with UF resin has also shown to have higher FM than PF resin [339].

Table 3.3: Mechanical properties of cured wood resin composites

Composite resin content (%)	Density (kg/m^3)	Flexural Modulus (GPa)	Flexural Stress (MPa)
PRF blends			
50% PRF	1067 (±35)^a	3.5 (±0.4)^a	43.7 (±3.2)^a
40% PRF	1047 (±17)^a	2.8 (±0.5)^b	41.3 (±4.6)^a
30% PRF	978 (±31)^a	2.5 (±0.4)^b	27.4 (±6.7)^b
20% PRF	896 (±21)^b	1.9 (±0.2)^c	19.7 (±1.8)^b
10% PRF	769 (±13)^b	1.5 (±0.3)^c	9.8 (±3.0)^c
UF blends			
50% UF	878 (±19)^a	1.0 (±0.1)^a	6.8 (±0.4)^a
40% UF	962 (±14)^a	2.9 (±0.1)^b	18.9 (±1.1)^b
30% UF	1059 (±11)^b	2.6 (±0.6)^b	16.8 (±2.7)^b
20% UF	967 (±28)^a	2.1 (±0.2)^b	18.7 (±3.5)^b
10% UF	865 (±48)^a	1.4 (±0.1)^a	13.0 (±1.7)^c

Note: Standard deviation in parentheses. Each sample property with different superscript letters ($^{a, b, c}$) are statistically different ($p < 0.05$) using the ANOVA test.

The ANOVA results show a statistically significant difference in the density of the blends containing 80 and 90% wood content in PRF blends. This difference was also observed for the FM of wood-PRF blend (50:50) showing a significant effect of wood content in the blend in comparison to other compositions. The FS of wood-PRF at 70 and 80% wood content were not significant. The Densities of wood-UF blends were not significantly different except for the 70% wood content blend, and this also affected the FM values for most blends. The FS for wood-UF blend and 50 and 90% wood contents were significantly different ($p < 0.05$) than the other blends.

TMA was used to determine the softening temperature (T_s) of the cured resin (Figure 3.7a). The T_s for cured PRF and UF were respectively at 222 °C and 209 °C. Generally, T_s is correlated to the glass transition temperature (T_g) [340]. Furthermore, a higher T_g is associated with an improved performance of a thermoset material. The high T_g for PRF also was reflected in its wood composites bending properties than the wood-UF composites [341].

DMA was performed to determine the viscoelastic properties of the cured resin (tan δ) and wood composites (storage modulus (E′) and tan δ) (Figure 3.7). The cured PRF and UF resin had tan δ maxima at 172 °C (0.3) and 123 °C (0.32), respectively (Figure 3.7b) and were assigned to their T_g. These T_g values were considerably lower than the T_s values determined by TMA. Tan δ plays a major role is showing the energy dissipation of a material after deformation load has been applied to it [342]. An increased tan δ value shows a restricted flow of materials, more energy dissipation and reduced storage modulus [312]. In comparison, a lower T_g peak at 160 °C was observed for pure PF resin in the study of the curing and thermal properties of tannin-PF resins [343]. A similar T_g has also been recorded for pure UF resin at 122 °C [344].

E′ values from DMA for the cured composites are seen in Figure 7c and 7d. Generally, E′ reduced with increase in temperature because of chain softening of the resin structures [345]. For the PRF composites, E′ was observed to decrease with an increase in wood content at lower temperatures (up to 40°C). These results were comparable to the bending properties obtained. 50% PRF composites showed a higher E′ due to a higher stiffness and rigidity of the chains and increased energy stored in the material [346]. The E′ onset was observed from 160 °C for 50% PRF and 180 °C for 10% PRF signifying the transition and phase change of the resin chain networks in the matrix [347]. The E’ onset

which can is related to the thermal softening temperature of the composite before T_g peak was observed to increase with increasing wood content showing the start of chain network changes. At high temperature of 250 °C, the high E′ for the 50% PRF composites shows the stronger interaction of the PRF and resin in the matrix [348].

For the UF composites, E′ vs. temperature plots for the 50% wood content were lowest in comparison to higher wood content composites (>60%). An excess UF resin content has been studied to reduce the properties of particleboards making them more brittle [338]. With an increase in wood content, E′ onset shifts to higher temperature showing the effect of wood fillers in aiding stress distribution within the matrix [349].

The wood composites for both resins had a similar increase in tan δ with the addition of wood. Two major transitions were seen for the cured wood-resin blends with an increase in temperature. The first transition was seen between 40 °C and 140 °C which maybe attributable to a β transitions due to the movement and vibrations of side group chains [350]. The second transition between 140 °C and 250 °C known as the α transitions or T_g occurs as a result of the movement of the main structural chains [350] [351]. Movement of polymer chains were reduced with wood content and short resin crosslinks were formed yielding an increased dampening effect [352]. These transitions occur at slightly higher temperatures and lower tan δ values for wood-PRF cured blends showing better strength, stability and crosslinking of the matrix which correlates with the flexural properties [350]. Wood degradation was shown to occur >250 °C for the wood-resin composites showing the probable breakdown of wood polymeric constituents [353].

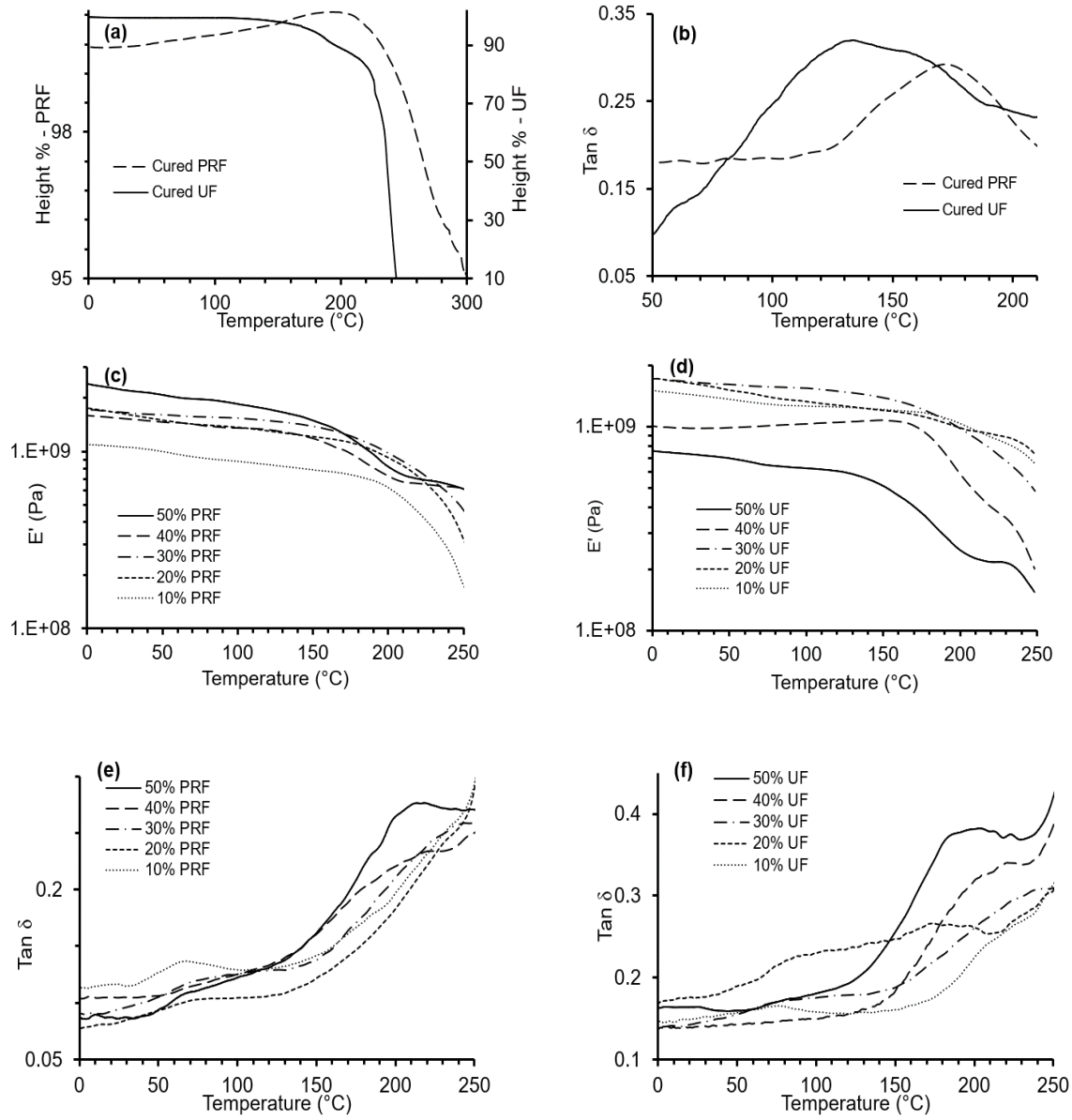

Figure 3.7: (a) TMA thermograms of cured PRF and UF resins, (b) DMA thermograms of tan δ of cured PRF and UF resins, (c) DMA thermograms of E′ of wood-PRF composites and (d) DMA thermograms of E′ of wood-UF composites, (e) DMA thermograms of tan δ of wood-PRF composites and (f) DMA thermograms of tan δ of wood-UF composites

FTIR spectroscopy was employed to observe the chemical changes that occur in the resin and composite before and after curing. The FTIR spectra for the liquid resin samples and cured wood-resin composites are shown in Figure 3.8a and 3.8b, respectively. The primary bands for liquid PRF were at 3327 cm^{-1} showing O-H stretching of hydroxyls, CH_2

and CH_3 at 2945 cm^{-1}, the aromatic vibrations of C=C at 1594 cm^{-1} and 1455 cm^{-1}, asymmetric stretch of C-O-C at 1235 cm^{-1}, ether links -C–O–C groups at 1081 cm^{-1}, C-O deformation of the hydroxymethyl group at 1035 cm^{-1}, and 755 cm^{-1} due to C-H bond vibrations in the benzene rings [354] [355]. For the cured wood-PRF composites characteristic resin bands were observed as well as those from wood. The hydroxyl groups band (~3327 cm^{-1}) reduced slightly and the band intensity of the methylene and methyl groups between 2850 cm^{-1} and 2961 cm^{-1} increased due to removal of water during composite curing and the presence of wood, respectively. Changes were also observed in the aromatic vibrations at 1593 cm^{-1} with the different wood contents and C-O-C stretching band between 1256 cm^{-1} and 1265 cm^{-1}. The C-H bond stretching also reduced with the increase in wood content between 790 cm^{-1} to 820 cm^{-1}, while the cellulose C–O–C band associated with glycosidic bonds between 900 and 1220 cm^{-1} increased with an increase in wood in the cured composite showing the interaction between PRF and wood [356].

For the liquid UF spectrum, a strong band at 3324 cm^{-1} shows the hydrogen bonded NH- stretching and O-H stretching. A symmetric C-H stretching of -CH_2OH, and the -CH_2- of an ether was observed in a low intensity band at 2971 cm^{-1}. The stretching of primary amide (I) and the C=O functional groups were seen in the band at 1622 cm^{-1}. C–N and secondary amine stretching bands were observed between 1498 and 1584 cm^{-1}. Weak C–H absorption bands were seen between 1350 and 1480 cm^{-1}. Deformation (-OH) in the -CH_2OH was observed in the band at 1251 cm^{-1}. Stretching band vibration between 1139 and 1200 cm^{-1} was assigned to the –N–CH_2–N– group and C–O asymmetric stretching band was centered at 1001 cm^{-1} [357] [358]. For the cured wood-UF composites, the O-H stretching band decreased in intensity leaving a visible N-H stretching band. C-H stretching bands of methylene groups were seen between 2850 $cm^{-1}$and 2930 cm^{-1}.

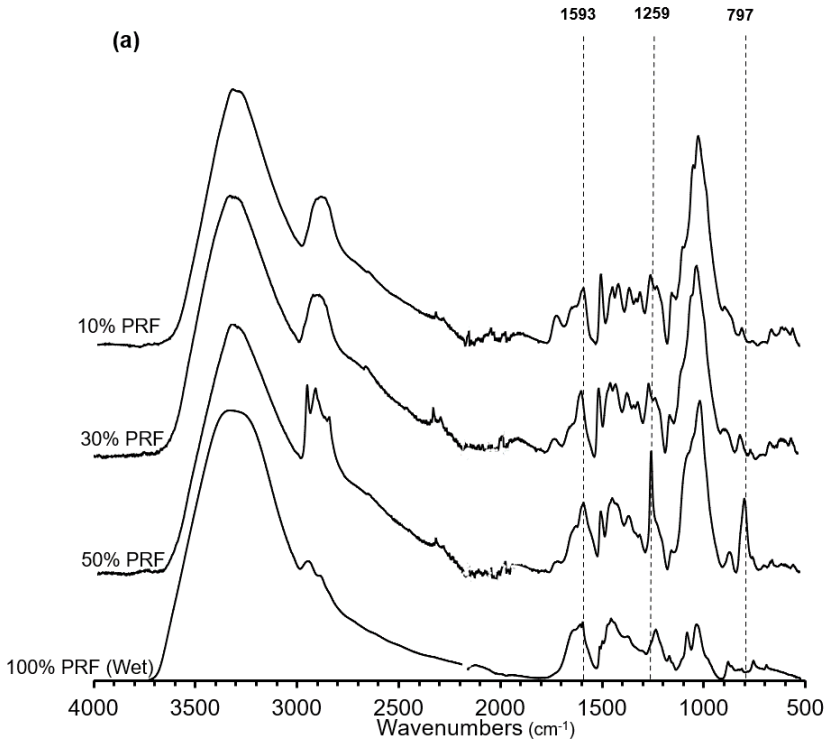
(a)
1593
1259
797
10% PRF
30% PRF
50% PRF
100% PRF (Wet)
4000
3500
3000
2500
2000
1500
1000
500
Wavenumbers (cm-1)

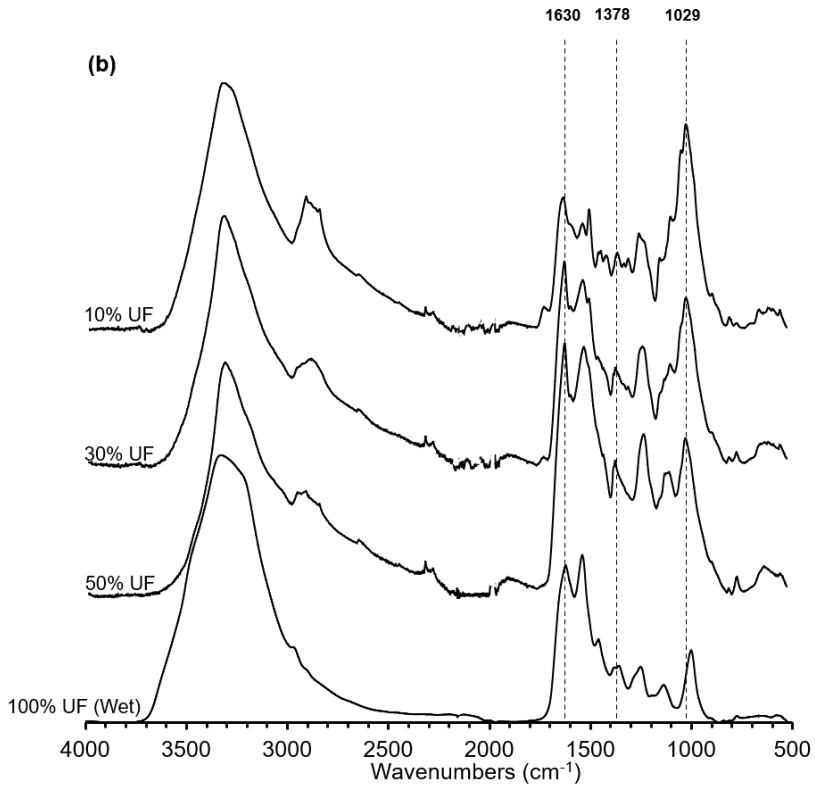

Figure 3.8: FTIR spectra of (a) liquid PRF and cured wood PRF blends and (b) liquid UF and cured wood UF blends

Lignin associated aromatic stretching and aromatic ring vibrations were observed 1600-1650 cm^{-1} and 1509 cm^{-1}, respectively. Carboxylic acid stretching vibrations were observed at 1451 cm^{-1} and C-H vibrations at 1378 cm^{-1}. Additional bands were observed for lignin between 1240 and 1300 cm^{-1} and cellulose between 900 to 1100 cm^{-1} [356] [359]. These cellulosic bands between 900 and 1100 cm^{-1} also show the interaction between the UF resin and wood and were intensified with the addition of more wood fibers.

3.4.5 Thermal and dimensional stability of cured blends

The thermal stability/degradation behavior of the cured wood-resin composites were deteremined by TGA and differential thermogravimeric (DTG) analysis (Figure 3.9 and Table 3.4). The major onset degradation temperature (T_{onset}) for the wood-PRF/UF composites increased with wood content. The T_{onset} ranged between 272-293 ^{o}C for wood-PRF composites and 266-294^{o}C for the wood-UF composites and is suspected to be attributable to wood degradation. Also the residual weight (at 900 $^{\circ}$C) for the wood-PRF

composites reduced from 37 to 24% with an increase in wood content from 50 to 90% (Figure 3.9a). However, no major variations for residual weight (19-22%) were observed for the wood-UF composites with wood content (Figure 3.9b). Composites with low resin content (10%) had the lowest residue content. Studies have shown that an increase in filler load reduces the overall thermal stability of cured composites [360]. Although the amount of residuals reduced with increased wood filler content, onset degradation temperatures for wood composites with high wood content were more thermally stable than those with low wood content [267] .

The DTG thermograms were use to determine the major decomposition transition(s) for the wood-resin composites (Figure 3.9 and Table 3.4). The first DTG peak centered around 60 $^{\circ}$C was attributed to water loss and/or formaldehyde loss [361]. The wood-PRF composites showed a minor DTG peaks centered around 225 $^{\circ}$C and a major DTG peak centered around 336-356°C. The major DTG peak temperatures for wood-PRF composites increased from 336 to 356 $^{\circ}$C with an increase in wood content from 50 to 90%. This major DTG peak was attributed to degradation of both cellulosic and phenolic resin components [336]. Wood-PRF blends showed more thermal stability with higher residue content than the wood-UF blends due to better cross-linking density and stable bonds [362] [336].

The wood-UF composites showed a minor DTG peak around 60 $^{\circ}$C (water loss) and two major DTG peaks around 190-340 $^{\circ}$C and 340-430 $^{\circ}$C (Figure 3.9). The first major DTG peaks decreased with a decrease in resin content and therefore was assigned to resin decomposition [363]. While, the second major DTG peak increased with wood content supporting its association with wood degradation [364].

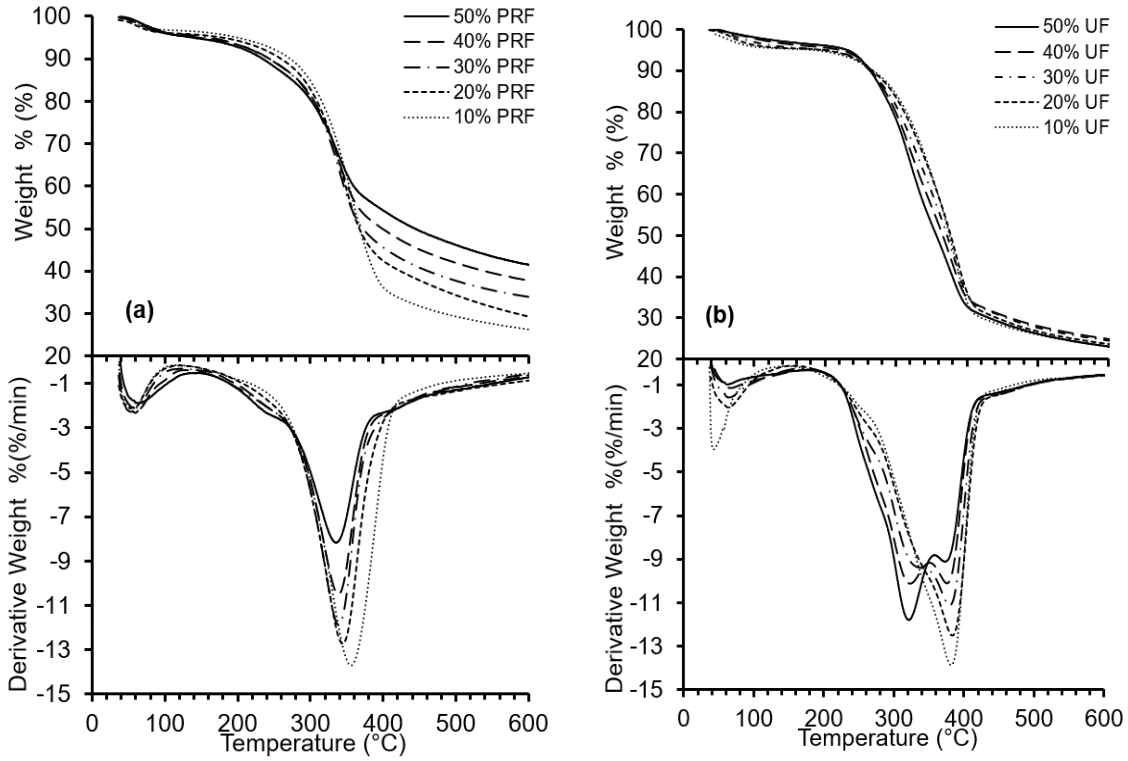

Figure 3.9: Thermogravimetric analysis thermograms of (a) wood-PRF composites and (b) wood-UF composites

Table 3.4: Thermogravimetric data for wood-PRF and wood-UF composites

Composite Resin content	Major onset T_{onset} (°C)	DTG Peak maxima (°C)	Residual at 900°C (%)
PRF blends			
50% PRF	272 (±7.8)	336 (±1.6)	37 (±2.0)
40% PRF	274 (±5.6)	339 (±3.4)	34 (±1.2)
30% PRF	274 (±0.7)	339 (±1.1)	30 (±0.4)
20% PRF	287 (±13.6)	346 (±0.5)	27 (±2.0)
10% PRF	293 (±4.2)	356 (±0.5)	24 (±0.9)
UF blends			
50% UF	266 (±0.1)	321 (±0.9), 375 (±1.2)	20 (±2.4)
40% UF	268 (±4.4)	322 (±2.4), 376 (±0.8)	22 (±0.7)
30% UF	270 (±0.8)	325 (±1.6), 380 (±2.5)	22 (±1.3)

Table 3.4 cont'd

20% UF	277 (±1.7)	330 (±5.9), 383 (±1.0)	21 (±1.0)
10% UF	294 (±1.3)	382 (±1.6)	19 (±0.9)

Note: Standard deviation in parentheses.

Another key composite property is its dimensional stability (water absorption (WA) and thick swell (TS)). The wood composites were exposed to a 24 h water soak test and the results are given in Table 3.4. For the wood-PF composites, the WA was shown to increase from 24 to 88% with wood content from 50 to 90%. These increased WA values was influenced by their density (Table 3.3) and wood content (a porous material) which led to higher porosity of the cured composites [365]. Samples with higher resin and density had a better packed structure with less voids and thus reduced the permeability of water [336]. Also, the TS (11-28%) of the wood-PRF composites generally increased with fiber content. For the wood-UF composites WA ranged from 29% (70% wood) to 62% (90% wood). The TS of the wood-UF composites ranged from 8.7 to 19% and generally increased with fiber content. Wood-PRF with a high percentage of resin showed lower absorption in comparison to wood-UF blends. UF resin has been studied to be more susceptible to moisture especially when exposed to high temperatures and thus used for interior uses [366]. [298] had shown that particleboard made from melamine modified UF with more acidic resins yielded low TS boards. The penetration of thermosets into wood fibers in particleboards stabilizes its structure by creating less voids which reduces the moisture absorbed and prolongs its shelf life over a long period of time [367]. ANOVA analysis showed a significant effect of wood content on the WA of the composites with samples having 90% wood fiber having the lowest p values. TS for the wood-UF composites were mostly not significantly different in comparison to the wood-PRF composites showing a low effect of wood composition on the TS properties.

Table 3.5: Water absorption (WA) and thickness swell (TS) values for the wood-PRF and wood-UF composites after a 24 h water soak test

Resin	WA (%) after 24 hours	Thickness swell (%) after 24 hours
PRF blends		
50% PRF	23.9 (±6.8)[a]	13.5 (±2.0)[a]
40% PRF	25.2 (±3.6)[a]	10.9 (±2.0)[b]
30% PRF	32.0 (±8.3)[b]	14.8 (±0.9)[a]
20% PRF	54.9 (±6.3)[c]	21.4 (±1.1)[c]
10% PRF	87.5 (±8.7)[d]	28.2 (±1.8)[c]
UF blends		
50% UF	49.4 (±7.5)[a]	8.7 (±0.7)[a]
40% UF	36.1 (±1.6)[b]	10.4 (±2.0)[a]
30% UF	28.8 (±2.3)[c]	15.8 (±4.9)[b]
20% UF	30.1 (±3.7)[c]	12.2 (±2.2)[a]
10% UF	62.3 (±7.5)[d]	19.3 (±0.3)[b]

Note: Standard deviation in parentheses. Each sample property with different superscript letters ([a, b, c]) are statistically different ($p < 0.05$) using the ANOVA test.

3.5 Conclusions

Composites were successfully prepared from wood fiber (50 to 90%) and PRF and UF resins. Rheological results for the blended wood-resin mixture showed shear thinning behaviors which are an essential property for material extrusion. The wood-PRF (50:50) blend was successfully extruded, based on its rheological properties, and shows promise for additive manufacturing applications. However, the wood-UF blends were not extrudable due to its low viscosity and water content. The curing characteristics of the resins in the composite were determined and the curing activation energy increased with wood content. Also, the pH of wood influenced resin cure. The PRF resin, being a cold setting resin, cured faster and at lower temperatures than UF resin being a hot setting resin. The thermal stability from the onset degradation temperatures of the composites increased with increasing wood content. The wood-PRF composites exhibited good flexural properties and were influenced

by its resin content. Dimensional stability of the composites improved with resin content. This study clearly shows that finding a suitable resin (e.g., PRF) and wood-resin formulation, that can cure at ambient temperatures, were critical in the creation of an extrudable composite for potential use in additive manufacturing of wood composite structures.

3.6 Acknowledgements

The authors would like to acknowledge (i) the Idaho State Board of Education-Higher Education Research Council-IGEM award # IGEM 20-002 for their financial support, (ii) USDA-CSREES grant 2007-34158-17640 for support in the purchase of the DSC, and the University of Idaho College of Natural Resources for support in the purchase of the FTIR spectrometer.

Chapter 4: Carbonation Curing and Kinetics of Wood-Sodium Silicate Composites

4.1. Abstract

This study investigates the effect of carbonation curing pressure, reaction time, particle size and post curing temperature on the thermal, and mechanical properties of wood-sodium silicate (SS) composites. A mixture of 50 wt.% wood (40 and 200 mesh) and SS was used to fabricate composites that were considered for carbonation curing. Dynamic rheological behavior of the blends was determined in the presence of air and CO_2 with a higher complex viscosity observed for CO_2 samples. The penetration depth of CO_2 was evaluated via X-ray microcomputed tomography (micro-CT) scans and results showed increasing penetration depth with carbonation time and pressure. %CO_2 uptake for samples was observed to increase with increasing CO_2 exposure time and pressure. Curing kinetics of neat SS and composites of different wood compositions (50 – 70 wt.%) were examined using modulated dynamic scanning calorimetry (MDSC). MDSC curing peak temperatures increased with heating rates and E_a ranged from 85 to 125 kJ/mol with the highest values obtained for 200 mesh SS composites. From the flexural bending test results, 200 mesh SS composites exhibited better mechanical properties with flexural modulus (FM) between 0.8 GPa to 11.2 GPa and flexural strength (FS) between 3.5 MPa to 59.2 MPa. Generally, thermal stability of carbonated composites was influenced by particle size and curing temperature. Statistical summary data based on a response surface methodology (RSM) coded data and a polynomial fit showed that pressure, time, and carbonation pressure had significant effects on the mechanical properties of carbonated cured composites.

4.2. Introduction

Greenhouse gas (GHG) emissions are a continuous growing environmental concern especially with carbon dioxide (CO_2) emissions which accounts for more of the GHG [368]. CO_2 in the United States of America (USA) decreased by 11% from 2019 to 2020, due to decrease in transportation emission as a result of the COVID 19 pandemic [369], [370]. But energy consumption alone in the USA in 2021 produced a total of 4.9 billion metric tons of

CO_2 emissions which was 7% more than 2020 levels [371]. With this data, the need for more ways of carbon sequestration in the environment is increasingly needed. Carbon sequestration is an interesting method used by modern technology to capture CO_2 into depleted oil and gas fields, coal seams, natural based materials etc. where they would stay locked up for years [372]. Another alternative is the carbonation curing of cement-based materials, geopolymer based (such as SS) and alkali activated materials (AAM). The fundamentals behind these are that these materials are reactive with CO_2 in their hydrated state forming stable carbonate materials or solidified forms of aluminosilicate glass [373], [92].

Carbonation curing which is the diffusion of CO_2 into the pores of a matrix has been used in different studies with common uses in composites made of natural fibers like wood and cement to stabilize and improve the mechanical properties of the materials [374], [375],[376],[377]. The presence of CO_2 can help increase the density of the pores structure in the composites which also improves the durability of the composites [378]. The use of wood fibers in composites for carbon sequestration and storage will aid the reduction of its carbon footprint while improving the mechanical properties of the composites over time [379]. The potential of carbonation curing of wood geopolymer based composites will ensure their broad range in various construction applications. But understanding how they perform mechanically, thermally will aid in the establishing of proper optimization processing methods, and overcoming their disadvantages of low strength, and vulnerability to fire [380]. The compatibility of wood and SS also reduces the requirement of pretreated wood waste with toxic and non-biodegradable chemicals industrially. This combination of wood and SS presents advantages of high strength, fire resistance and durability as observed in a previous study [287]. In the presence of CO_2, SS reacts to form silica gel with the subsequent removal of water to form a hardened glass material and a byproduct of as seen in chemical equation 4.1 and stoichiometric equation in equation 4.2.

$$Na_2\,SiO_{2(aq.)} + CO_2 \rightarrow SiO_{2(aq.)} + Na_2CO_3 \qquad \text{Equation 4.1 [381]}$$

$$Na_2O\,.\,nSiO_2 + 2nH_2O + CO_2 \rightarrow Na_2CO_3 + nSi(OH)_4 \qquad \text{Equation 4.2 [376]}$$

The major factors that affect the carbonation curing of composites includes, particle size, porosity of the composite, moisture, time, water binder ratio and amount of geo based

material used in the matrix [382]. Particle size of fibers used for composite preparation can affect the penetration (diffusion rate) of CO_2 during sequestration which in turn affects their mechanical properties. Initial densified pores of composites which is influenced by particle size, plays a major role in improving the interaction in the matrix which yields higher strength and properties upon carbonation [383]. It has been studied that pore volume during carbonation decreases as a result of the densification of the structure in a continuous carbonation test [384].

This study focuses on the sequestration of CO_2 in wood SS composites as an alternative curing method. The influence of particle size, surface area, CO_2 exposure time, CO_2 pressure, on the carbonation depth, mechanical properties and thermal properties were explored. There is a limited amount of literature that have researched on the use of wood fibers and SS which makes this study innovative. Rheological behavior of the wood-SS blend in the presence of CO_2 was investigated. Curing behavior and kinetics of SS with wood was also evaluated. The research will aid in reducing the amount of thermal energy required to cure wood-SS composites and create a cost-effective process for composite fabrication. The relationship between SS with high wood composition and CO_2 will be understood to create the use of the mixture in more applications industrially.

4.3. Materials and Methods

4.3.1. Materials

Wood fiber residues were obtained from Plummer Forests Products, Post Falls, ID., USA (Douglas-fir (DF) and American Wood Fibers 80 mesh, USA (Maple). DF wood fibers were screened using a standard 40 mesh US screen (~0.425 mm). The 200 mesh maple fibers were produced by ball-milling maple fibers and passed through a standard 200 mesh US screen [385]. SS solution was used as purchased (37 wt.%, pH 12.5, 1.39 g/cm^3 at 20 °C, ThermoFisher Scientific, Waltham, MA, USA).

4.3.2. Wood Fiber Characterization and Sample preparation

Length and width of the DF 40 mesh and maple 200 mesh wood fibers have been characterized in previous studies via optical microscopy (Olympus BX51 microscope with a

DP70 digital camera, San Diego, CA, USA) and light scattering single particle optical sensing (Particle Sizing Systems, Inc. Model 770 AccuSizer) [385], [287]. Moisture content of the wood fibers was ascertained in duplicates using a HB43-S Halogen Moisture Analyzer (Mettler Toledo, Columbus, OH, USA). Density of the wood fibers were determined using an ultra-pycnometer 1000 (Quantachrome, USA) in nitrogen at room temperature.

The specific surface area analysis of the wood fibers was determined using the Brunauer–Emmett–Teller (BET) analyzer on 0.5 g of samples in duplicates using Micromeritics FlowSorb 2300 instrument according to ASTM D6556-10. pH of the wood fibers was determined using an Accumet AP61 (Hampton, NH, USA) pH meter on an aqueous extract of the wood fiber (5 g) in water (40 g) refluxed for 10 min, cooled, filtered, and measured.

Screened 40 and 200 mesh wood fiber samples were mixed individually with SS in a ratio of 50:50 on dry weight basis. Small batches for dynamic rheology were mixed using an herb grinder (1-2 g) and cold pressed under 0.5-ton load in a 25 mm Ø pellet die. Large batches for carbonation curing (40 g), were mixed in a coffee grinder (Pinlo, 200 W). For each disc used for carbonation curing, 17 g of wet mix was cold pressed in 76.2 Ø mm pellet die mold with an applied load of 1.5-ton (PHI hydraulic press, City of Industry, CA, USA).

4.3.3. Dynamic Rheology

The flow behavior (storage (G'), loss (G") modulus, complex viscosity (η*), Tan δ) of SS and wood-SS blends in either the absence or presence of CO_2, dynamic rheology characteristics of SS and wet pressed discs were determined. SS and wet discs (2 mm x 25 mm Ø) were either exposed to ambient air or CO_2 (10 psi (69 kPa), ~25 mL/min) in a Discovery Hybrid Rheometer (DHR2, TA instruments, New Caste, DE, USA). Serrated parallel plates were used for the wood SS blends to avoid slip and fabricated disposable aluminum plates with perforated holes (Figure 4.1 left and center) were used for SS to allow for uniform penetration and distribution of CO_2 gas. A 3-D printed chamber made of acrylonitrile butadiene styrene (ABS) was constructed to enclose the parallel plates and used to have a blanket of CO_2 gas around the plates (Figure 4.1 right). Time sweep measurements were collected for 6 h at 23 °C, 0.1% strain and frequency of 1 Hz.

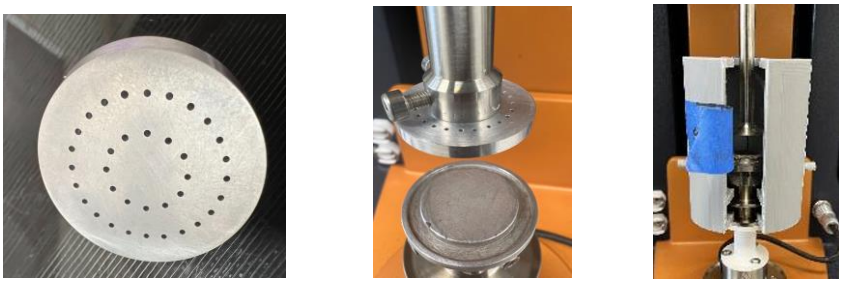

Figure 4.1: Perforated aluminum plates for SS-CO_2 rheology experiments (left and center) and 3D-printed chamber (right)

4.3.4. Differential Scanning Calorimetry (DSC)

Curing kinetics of SS and wood blends were determined using a modulated DSC (MDSC) on 5 mg of freeze-dried samples in a Q200 DSC (TA instruments, New Caste, DE, USA) under nitrogen (50 mL/min) and refrigerated cooling. Samples were equilibrated at 40 °C (2 min), modulated at amplitudes of +/- 0.8, 1.6, 2.4 and 3.2 °C for respective heating rates of 5, 10, 15, 20 °C/min every 60 s and ramped to 250 °C. MDSC runs were performed in hermetically sealed T_{zero} aluminum pans and data was analyzed using the TA Universal Analysis software. Kinetics of the blends was determined using the Kissinger-Akahira-Sunose ((KAS) iso-conversional) method [293]. Enthalpy of curing which was determined as the total area under the exothermic peak was calculated and used to calculate the activation energy (E_a) with equation 4.3. From the slope of the plot of $-\ln(\beta/T_p^2)$ versus $1/T_p^2$, E_a was calculated. To determine the pre-exponential factor *A*, the intercept of the plot was used. E_a at every degree of conversion was determined using equation 4.4.

$$-\ln\left(\frac{\beta}{T_p^2}\right) = \frac{E_a}{RT_p} - \ln\left(\frac{AR}{E_a}\right) \qquad \text{(Equation 4.3)}$$

$$-\ln\left(\frac{\beta}{T^2}\right) = \frac{E_a}{RT} - \ln\left(\frac{AR}{E_a g(\alpha)}\right) \qquad \text{(Equation 4.4)}$$

β is the heating rate (K/min), E_a is the activation energy in J/mol, T_p is the exothermic peak temperature, R is the gas constant (8.314 J/mol/K), *A* is the pre-exponential factor (1/s) and T is the temperature at a given degree of conversion (K).

4.3.5. Carbonation curing and CO_2 uptake

To determine the effect of carbonation pressure and CO_2 exposure time on the properties of SS and wood-SS composites, four cold pressed wet wood-SS discs per experiment were placed in a Parr Instruments 1 L pressure vessel (102 mm x 152 mm Ø) (Figure 4.2) and separated with 40 mesh wire stainless steel discs to allow for the penetration of CO_2. Two particle sizes of wood were examined 40 and 200 mesh. Wood-SS discs were exposed to CO_2 at two different treatment pressures of 7 kPa (1 psi) and 138 kPa (20 psi) and at different reaction times of 0.5, 1, 2, and 24 h for each experiment. The pressure vessel was placed in a water bath at 60 °C to facilitate CO_2 absorption [93]. Silica gel (self-indicating) was added to the pressure vessel to trap excess water. After exposure to CO_2, the wood-SS samples were post cured at either 60 °C or 105 °C for 48 h in an oven prior to characterization giving a total of 36 experiments (Table 4.1). Each experiment had 4 replicate specimens to account for reproducibility and accuracy of results. Control wood-SS samples were only cured thermally (60°C or 105 °C) for 48 h. Dimensions and weight of cured samples were used to calculate their density.

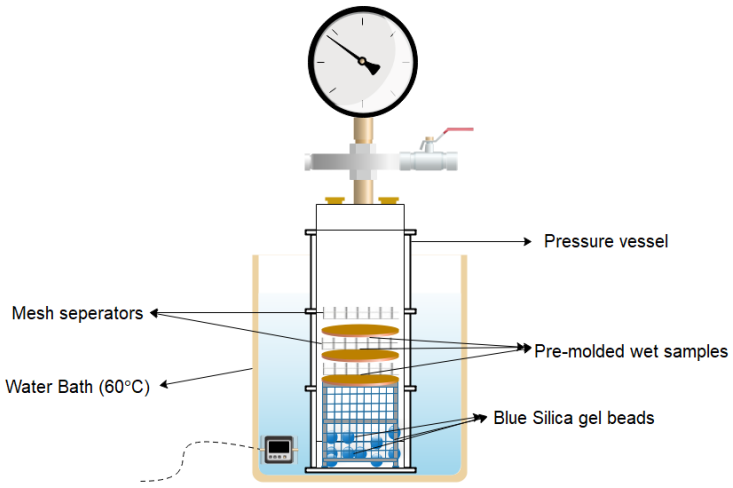

Figure 4.2: Schematic of the carbonation curing setup

Table 4.1: Summary of parameters considered for sample preparation.

Wood fiber size (mesh)	40 and 200
Carbonation Pressure (kPa)	7 and 138
Carbonation time (h)	0.5, 1, 2 and 24

Table 4.1 cont'd

Post curing temperature (°C)	60 and 105

The amount of CO_2 absorbed by each experiment sample at different times in the pressure vessel during carbon sequestration, was calculated by the mass change in the carbonation cured wood-SS composites using the equation below [386]:

$$CO_2 \text{ uptake } (\%) = \frac{(m_{final} - m_{initial} + m_{evaporated})}{(m_{reactive\ SS\ in\ the\ sample})}\ x\ 100\% \qquad \text{(Equation 4.5)}$$

With m_{final} , $m_{initial}$ are the weight of the SS and wood-SS composite after and before carbonation, respectively. $m_{evaporated}$ is the mass of water that was lost during curing which was obtained from the weight of the silica gel after carbonation and using an absorbent paper towel (for condensed moisture on the walls of the pressure vessel). $m_{reactive\ SS\ in\ the\ sample}$ is the weight of the SS reacted solids content in the composite.

From previous studies, the total water lost during carbonation curing has not been accurately accounted for, and a similar occurrence was experienced in this study [386]. The use of a different method to achieve the mass of evaporated water in the system was explored which involved the mass balance of the total amount of water in the system for each batch before and after carbonation curing. Calculations were performed based on the assumption that the rest of the water was lost or chemically bonded at the end of carbonation curing for each sample. The initial amount of water in the composite and weight of the sample before thermal curing were important parameters used for this mass balance calculation. It was important to have the same number of specimens per experiment and with approximate weight for each experiment of curing to enable uniform distribution and rate of CO_2 absorption.

4.3.6. X-ray Micro Computed Tomography (Micro-CT) Scanning

To observe the microstructure, density variations, and CO_2 penetration depth through the samples after carbonation curing, a Skycscan 1275 (Bruker, PA, USA) X-ray Micro-CT (μCT) scanner with an aluminum (1 mm) filter was used. Cured composite samples (8 mm (h) x 13 mm Ø) for each SS-wood particle size composite, exposed to different CO_2 pressures and at different times, mounted on a rotation stage, and a scout scan was

performed. A source voltage of 60 kV, current of 82 μA and camera pixel of 15 μm were used. Micro-CT image slices were obtained with samples rotations of 0.16° and the N-Recon reconstruction program was used to reconstruct the 2-D slices obtained. The CT Vox graphics software (Bruker, PA, USA) was used to build 3-D images of the scanned specimens and create density profile images for the samples. Parameters used are given in Table 4.2.

Table 4.2 : Micro-CT tomography scanning parameters

Object to source	52.9 mm
Camera to source	286 mm
Image pixel size	15 μm
Source Voltage	60 kV
Source current	82 μA
Beam hardening correction	20%
Rotation step	0.1°
Scanning position	11.39 mm
Exposure	115 ms
Ring artifact correction	10
Camera resolution	High resolution

Measurement of penetration depth of samples was analyzed using CTVOX images and Image J software version (2.1.0/1.53c, Java 1.8.0_172 (64bit)).

4.3.7. Flexural Properties

Effect of carbonation time and pressure on the mechanical properties of the carbonated cured composites samples (63.5 mm x 13.5 mm x 2.5 mm) was determined using a three-point bend fixture on an Instron 5500R-1132 universal testing machine (5 kN load cell, 40 mm span, and cross head speed of 1.5 mm/min) according to ASTM D790. Data was collected and analyzed using Bluehill v3.3 Instron software.

4.3.8. Thermogravimetric Analysis (TGA)

To determine the effect of wood particle size, CO_2 curing pressure and curing temperature on the thermal stability of the post cured composites, TGA was performed on cured samples (6 mg) in a Perkin-Elmer TGA-7 instrument (Shelton, CT, USA) under nitrogen (30 mL/min) from 40 to 900 °C at 20 °C/min. Data was analyzed using the Pyris v13.3.1 software.

4.3.9. Statistical analysis

Statistical analysis was performed in the R studio environment and the effect of the independent variables, carbonation pressure (x1), curing temperature (x2), CO_2 time (x3) and particle size (x4) on the response variables of FM and FS as seen in Table 4.3 [387]. Response surface methodology (RSM) package was only used to code the raw data in levels with a minimum of -1 and a maximum of +1. The data analysis was set up by fitting a polynomial model with all linear interactions, and quadratic terms. The best model was retained based on the Akaike's Information Criteria (AIC). To validate the selected model, Shapiro-Wilk's test was used to check for normality. Ramsey tests was used to check for linearity in regression parameters, using the R package "lmtest" [388]. The experiment was composed of 36 mixtures (Table 4.3) used for the analysis. Statistical tests were concluded using a confidence level of 95%.

Table 4.3 : Experimental set up for statistical analysis of wood-SS curing treatments

Mixture ID	Pressure (x1) (kPa)	Curing (x2) Temp (°C)	Time (x3) (hours)	Particle mesh size (x4)	Modulus (GPa)	Flexural Strength (MPa)
1	138	60	0.5	40	0.864	4.193
2	138	105	0.5	40	0.905	4.458
3	138	60	1	40	0.640	2.603
4	138	105	1	40	0.584	1.966
5	138	60	2	40	0.284	1.140
6	138	105	2	40	0.161	0.898
7	138	60	24	40	0.146	0.686
8	138	105	24	40	0.087	0.520
9	0	60	0	40	2.357	11.274
10	0	105	0	40	2.098	8.505

Table 4.3 cont'd

11	**7**	**60**	**0.5**	**40**	**1.854**	**9.620**
12	7	105	0.5	40	2.315	9.570
13	7	60	1	40	1.729	10.510
14	7	105	1	40	2.730	10.680
15	7	60	2	40	2.110	10.662
16	7	105	2	40	2.183	10.003
17	7	60	24	40	1.014	5.992
18	7	105	24	40	1.747	7.307
19	138	60	0.5	200	11.223	59.278
20	138	105	0.5	200	9.054	39.593
21	138	60	1	200	3.574	29.968
22	138	105	1	200	4.619	27.505
23	138	60	2	200	2.400	13.280
24	138	105	2	200	3.677	20.224
25	138	60	24	200	0.767	3.510
26	138	105	24	200	0.955	4.800
27	0	60	0	200	6.742	40.863
28	0	105	0	200	4.714	15.810
29	7	60	0.5	200	8.950	45.048
30	7	105	0.5	200	7.920	36.923
31	7	60	1	200	7.346	45.288
32	7	105	1	200	7.808	27.016
33	7	60	2	200	8.830	45.490
34	7	105	2	200	8.150	38.668
35	7	60	24	200	1.529	3.453
36	7	105	24	200	1.367	4.794

4.4. Results and Discussion

4.4.1. Fiber Characterization

Mean fiber length results obtained from previous studies were 206 μm and 33 μm for the DF 40 mesh and maple 200 mesh wood fibers with aspect ratio of 1.3 and 1.9 respectively [287], [385]. The 40 and 200 mesh wood fiber had a moisture content of 5.5% and 5.8%, density of 1636 kg/m^3 and 1501 kg/m^3, and BET specific surface area of 0.25 m^2/g and 2.35 m^2/g, respectively. Similar values of 0.261 m^2/g for Douglas-fir sapwood in the mesopores in wood cells at dry and wet state have been reported [389]. Specific surface area

tends to increase with decreasing particle size hence the high surface area value for the 200-mesh maple fiber. With a high surface area, high adsorption and reactions with other materials is expected to occur at an increased rate [390]. The pH of the DF fiber was 4.85 and that of maple fiber was 4.66.

4.4.2. Rheology

Rheological characteristics (G', G", complex viscosity (η*) and Tan δ) of SS and wood-SS blends in the presence of CO_2 and air with respect to time at 23 °C are shown in Figure 4.3. The temperature of 23 °C was selected to understand the reactivity of the sample blends at room/ambient temperature and for understanding of flow behavior with the various blends. With oscillatory shear in motion, SS showed a rapid increase in G', G" and η*(Figure 4.3a and 4.3c) when exposed to air and CO_2. The G' and G" plots increased due to the increase in stiffness of the matrix and molecular weight [391]. There was no crossover point which is usually associated with gelation for G' and G" of SS in air and CO_2. G' was higher than G" throughout the time sweep scans. Around 5000 s (83 min), G', G" and η* generally stopped increasing in air and similarly when exposed to CO_2 (Figure 4.3a and 4.3c). The ambient concentration of CO_2 in air (412 ppm) is sufficient to cure the SS [392]. The η* for the CO_2 cured SS was higher by 20% than the air cure SS at 330 min and this is most likely attributable to a higher degree of crosslinking. The rapid increase in η* is a result of intermolecular crosslinking, by exposure to CO_2, within the SS matrix to form a further stable network [393].

With the addition of 50% wood fiber to SS, a similar increase in G', G" and η* occurred and plateaued again around 83 min in both air and CO_2 atmospheres. The η* of the CO_2 cured wood-SS mixtures (40 and 200 mesh) were two-times higher (2×10^6 Pa.s) than the air cured samples at 330 min. The 200-mesh wood-SS had a slightly lower viscosity than the 40-mesh wood-SS mixtures. This low viscosity could be due to the small particle size of the 200-mesh fiber. It has been mentioned by Chen et al. (2021) that a small particle size distribution of fillers can restrict the movement of molecules in a system hence reducing the G' and G" [394].

Tan δ was used to examine the transition of the SS from a liquid to a gel during curing (Figure 4.3d). Tan δ decreased rapidly for SS with reaction time (<80 min) due to the

sample crosslinking and having lower viscous properties. Based on the plots in Figure 4.3d, gelation occurred <83 min for the air and CO_2 cured samples. The CO_2 cured sample had twice the tan δ (0.1) at > 160 min than that of the air-cured SS. The addition of wood fibers to SS resulted in an initial decrease in tan δ and then started to increase or plateaued around 30 min. Tan δ values were highest for 40 and 200 mesh wood-SS materials exposed to CO_2 by 44% and 48% after 360 min, as compared to air cured samples. These results clearly show that vitrification occurs in SS in both air and CO_2 atmospheres.

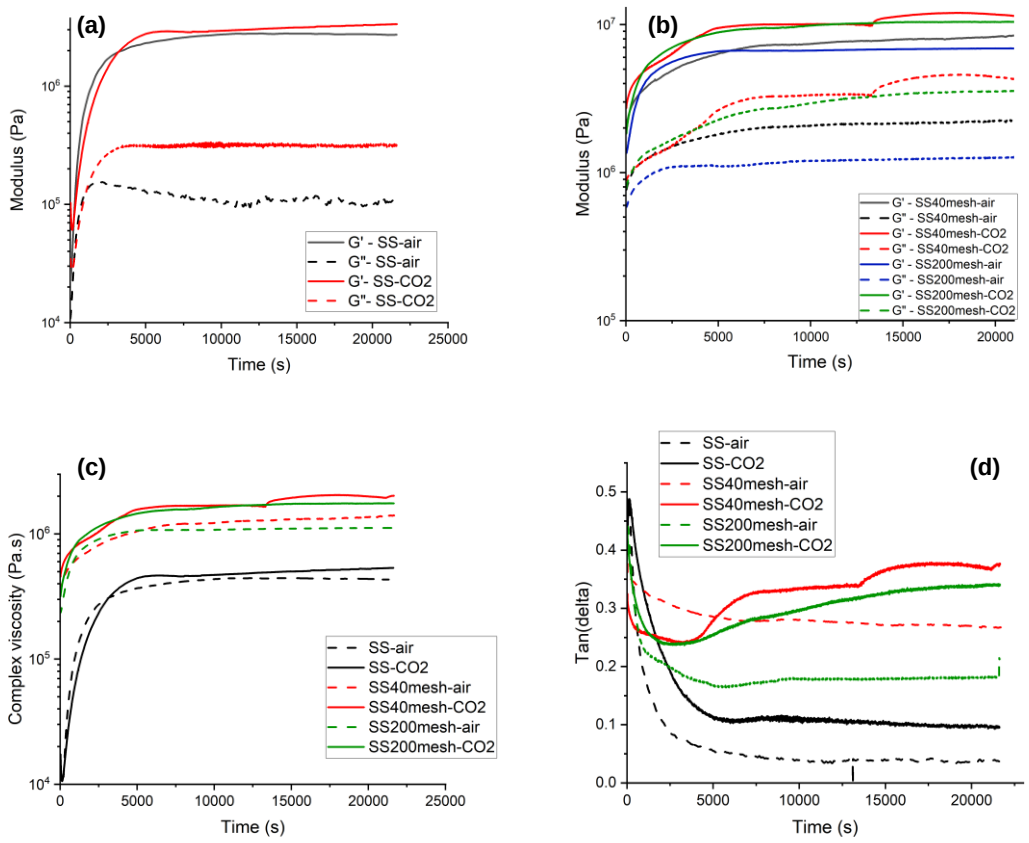

Figure 4.3 : Time sweep for SS wood blends in the presence of air and CO_2 showing G' and G" for (a) SS cured in air and CO_2 and (b) 40 mesh and 200 mesh air and CO_2 and (c) complex viscosity (η*) curves and (d) Tan δ curves.

4.4.3. MDSC

To understand the curing kinetics of SS in the presence of different wood compositions, MDSC was used with non-reversible exothermic heat flow curves at different

heating rates (Figure 4.4). Figures 4.4a and 4.4b show MDSC thermograms at 10°C/min of SS-wood (40 mesh) and SS-wood (200 mesh) blends, respectively. The curing kinetic values are given in Table 4.4. Kissinger plots of $-\ln(\beta/T_p^2)$ versus $1/T_p^2$ for the calculation of E_a and conversion plots with respect to temperature are shown in Figures 4.4c, 4.4d. 4.4e and 4.4f. An exothermic peak was observed for SS curing at 85 ^oC and increased with heating rate to 99 °C. While the enthalpy was reduced with increased heating rates. This behavior occurs because with an increase in heating rate, the curing properties of the system lags behind causing the reaction to occur later at higher temperature [395]. Since SS is in solution form and this complicates the MDSC thermogram with the water vaporization peak overlapping with the SS reaction peak. Thus, the SS and wood-SS samples were freeze dried prior to MDSC analysis to eliminate the water peak.

With the addition of 40 and 200 mesh wood fibers to SS, two exothermic curing peaks were observed, and the curing peak temperature increased (Figure 4.4a and b). As the wood content increased from 50 wt.% to 70 wt.%, the height of the curing peak reduced. This is likely attributable to the fact that SS cures under acidic conditions and the addition of wood which is acidic will help catalyze the reaction and shift to lower temperatures [396]. With an increase in wood content from 50 wt.% to 70 wt.% the exothermic peak area was reduced. Furthermore, this coincides with a lower SS content. This trend was also observed by Liu et al (2015) using modified and unmodified SS stating the effect of reduced curing of SS with the addition of fillers or additives [397]. The curing peak temperatures for 200 mesh maple wood-SS composites were significantly higher than those for the 40 mesh DF wood-SS. Chemical variation between DF softwood and maple hardwood might also be a factor that affects the curing of SS in the mix [398]. The pH of the DF and maple fiber were similar hence the larger surface area of the 200 mesh fiber likely contributes to an increase in curing peak temperatures. An increase in surface area and number of particles of a filler also affects the curing conditions of a thermoset matrix causing an increase in heat transfer and curing peak temperatures [399].

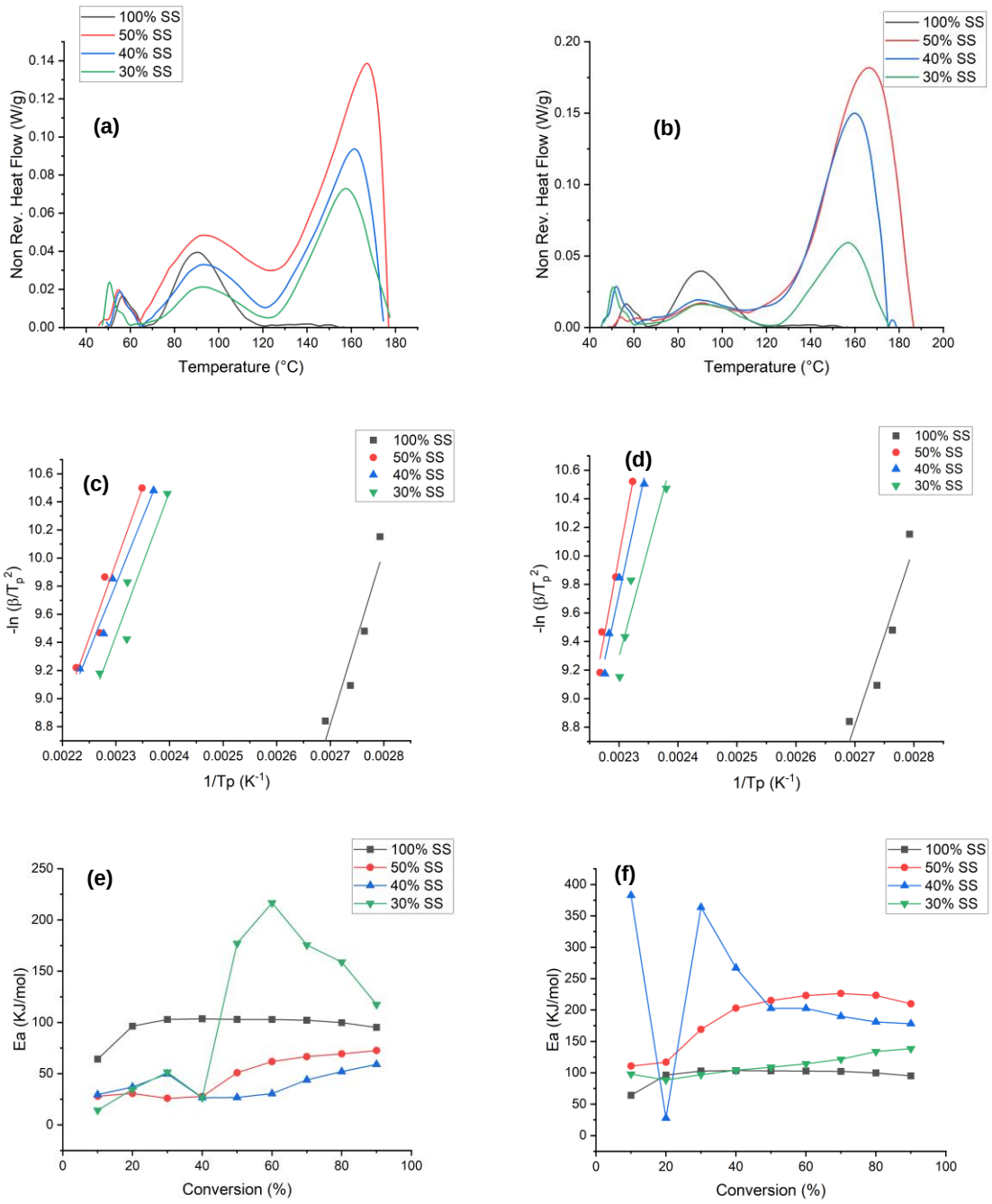

Figure 4.4: MDSC thermograms showing non-reversible heat flow curves for (a) neat SS and 40 mesh wood-SS blends and (b) neat SS and 200 mesh wood-SS blends at 10 °C/min; Plots of $-\ln(\beta/T_p^2)$ versus $1/T_p^2$ for (c) SS and 40 mesh wood-SS blends and (b) neat SS and 200 mesh wood-SS blends; Activation energy (E_a) versus conversion (α) for (e) neat SS and 40 mesh wood-SS blends and (f) neat SS and wood-SS blends.

E_a which was obtained from the analysis of the Kissinger plots and for SS was a 104 kJ/mol and this serves as a reference point for monitoring curing. An *A* of 7.7 x 10^{14} was observed with an R^2 coefficient of 0.839. E_a of the 40-mesh wood-SS composites ranged from 85 to 89 kJ/mol and 128 to 185 kJ/mol for 200 mesh wood-SS composites. Particle size of fillers in composites also play a role in the amount of energy that is required for molecules to interact. With smaller particle size (e.g. 200 mesh) comes an increased surface area thus increased interactions with SS which increases the E_a [400]. The plots of $\ln(\beta/T_p^2)$ versus $1/T_p^2$ showed R^2 coefficients between 0.868 to 0.964 showing reliable data for both 40 and 200 mesh composites and *A* values between 1.4 x10^9 to 1.6 x 10^{22} (1/s). A higher *A* value means a larger reaction occurring, and this was observed for the 50 wt.% 200 mesh wood-SS composites. This suggests that there were a higher number of active sites in the system as a result of the high surface area of the fiber [325].

The plots of E_a versus conversion (α) are shown in Figure 4.4e and 4.4f for 40 mesh and 200 mesh wood-SS blends, respectively. Curing kinetics of thermosets tends to be complex in the presence of wood due to the chemical components present but the plots of E_a at different conversion (α) degrees can give a clearer understanding of the energy changes within the system as temperature increases. For neat SS, E_a starts at 64 kJ/mol and increases to 95 kJ/mol at 90% α. With the addition of 50 wt.% 40 mesh wood fiber, E_a showed a major increase from 28 kJ/mol (40% α) to 73 kJ/mol (90% α). A similar increase in E_a was observed with 60 wt.% wood around 40% α. With the 70 wt.% 40 mesh fibers, there was an increase in E_a at 50% α (177 kJ/mol) from a 40% α value of 27 kJ/mol. The use of 200 mesh maple fibers generally showed an increase in E_a starting at 111 kJ/mol which increased to >200 kJ/mol. The 60 wt.% wood-SS for the 200-mesh fiber showed a different trend at other wood contents. This phenomenon cannot be explained to why there was a spiked increase to the 40 wt.% SS E_a at low α.

Table 4.4: Kinetic parameters for SS, 40 mesh and 200 mesh composite blends calculated using KAS model from the MDSC data

SS content (%)	β (°C /min)	T_p (°C)	ΔH (J/g)	E_a (kJ/mol)	*A* (1/s)	R^2
40 mesh						
100	5	85 (±1.5)	6.7 (±1.3)	104	7.7×10^{14}	0.839
	10	89 (±1.4)	4.6 (±0.5)			
	15	92 (±3.3)	3.8 (±1.9)			
	20	99 (±3.1)	3.9 (±0.9)			
50	5	153 (±0.2)	15.6 (±5.7)	89	2.4×10^{10}	0.930
	10	167 (±2.6)	18.1 (±3.8)			
	15	168 (±6.9)	34.7 (±4.6)			
	20	176 (±5.9)	38.0 (±0.3)			
40	5	149 (±6.7)	18.7 (±4.5)	79	1.4×10^{9}	0.951
	10	163 (±3.1)	17.3 (±0.1)			
	15	166 (±3.7)	24.9 (±4.0)			
	20	175 (±3.5)	26.9 (±5.9)			
30	5	146 (±2.3)	15.0 (±3.9)	85	1.4×10^{10}	0.868
	10	158 (±1.0)	34.2 (±3.5)			
	15	160 (±1.9)	34.2 (±3.5)			
	20	170 (±4.3)	24.7 (±4.1)			
200 mesh						
50	5	157 (±3.5)	55.0 (±29.1)	185	1.6×10^{22}	0.964
	10	163 (±5.4)	64.9 (±17.2)			
	15	167 (±0.7)	42.8 (±6.1)			
	20	166 (±2.4)	43.0 (±5.8)			
40	5	154 (±2.6)	33.1 (±8.1)	158	1.1×10^{19}	0.963
	10	162 (±0.6)	58.8 (±3.9)			
	15	164 (±0.6)	49.2 (±0.2)			
	20	165 (±1.8)	43.6 (±5.0)			
30	5	149 (±1.8)	17.8 (±9.6)	128	3.6×10^{15}	0.881
	10	160 (±0.2)	34.0 (±8.6)			
	15	162 (±6.1)	28.9 (±10.7)			
	20	164 (±4.9)	27.4 (±8.5)			

Note: Standard deviation in parentheses.

4.4.2. CO_2 Uptake calculations

Since CO_2 reacts with SS, it is important to determine the extent of CO_2 uptake during the curing of SS and wood-SS composites. To determine a mass balance of water lost to the environment for the process, several assumptions were made for each experiment to account for carbonation absorption and post carbonation treatment (equation 4.5). The amount of CO_2 absorbed was determined and the results are given in Table 4.5 and a linear relationship was observed (Figure 4.5). To account for water lost to the environment, asides the one collected by the silica gel, mass balance on the solid and moisture content before and after carbonation curing would provide a value. During the CO_2 curing process, it was generally observed that samples exposed to 138 kPa CO_2 pressure absorbed more in comparison to treatments at 7 kPa. Higher CO_2 uptake was also recorded with an increase in reaction time, except for SS samples exposed at 138 kPa. An increase in reaction time from 2 to 24 h showed a 100% increase in CO_2 uptake.

Table 4.5: CO_2 (%) uptake calculations for the various SS and wood-SS samples at different CO_2 treatment pressures and treatment time

Treatment Time (h)	CO_2 uptake (%)					
	SS		40 mesh		200 mesh	
	7 kPa	138 kPa	7 kPa	138 kPa	7 kPa	138 kPa
0.5	2.9	5.4	7.4	8.7	7.1	6.4
1	3.3	6.1	7.8	9.7	8.8	8.1
2	4.8	9.2	12.5	15.6	13.5	30.8
24	46.6	40.6	59.7	83.6	64.9	86.5

200 mesh samples also absorbed more CO_2 at 2 (13.5% and 30.8%) and 24 (30.8%) h than the 40 mesh samples. This increase could be attributable to the increased contact area and larger surface area of the 200 mesh fibers as compared to the 40 mesh fibers [90] [401]. Zhan et al (2014) also observed more carbonation with materials that had 5-10 mm sized particle in comparison to 14-20 mm sized particle on recycled concrete aggregates [402]. From the plots in Figure 4.5, all samples showed a linear relationship with an increasing CO_2

uptake with time. R^2 values were more >0.9 stating the linear changes in absorption with time. CO_2 uptake begins slow within the first 1h but gradually increases as time progresses. This process was slower for SS at 24 h but faster for the composites (>50% increase in all cases), due to the porosity and voids present in the solids which allows for easier diffusivity of the gas [403].

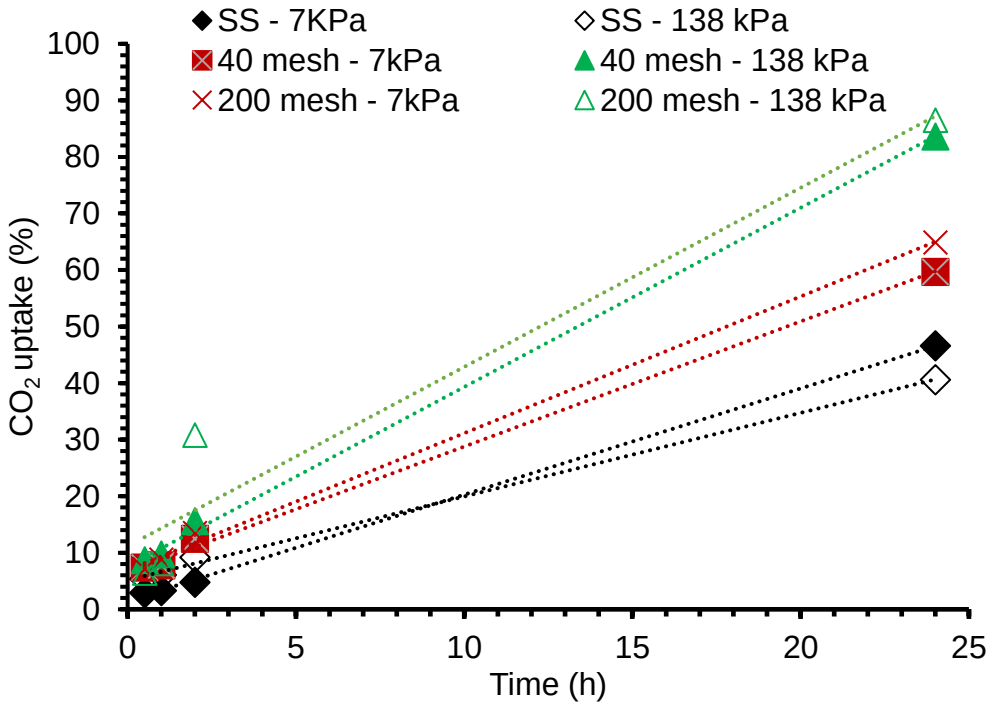

Figure 4.5 :Plots of CO_2 uptake with respect to time at different pressure values

4.4.3: Microstructure, Density and Carbonation penetration depth

Cross section photographs of CO_2 cured wood-SS samples are seen in Figure 4.6a and 4.6b for 40 mesh and 200 mesh samples respectively at different pressures. The sample exposed to CO_2 for 24 h had a thickness swell of more than 20% for both 40 mesh and 200 mesh with an increased CO_2 reaction time. The penetration depth of CO_2 (which is the whitish boundary towards the corners) was also observed to increase with curing time and

pressure. The depth was more visible for 200 mesh maple samples due to their darker morphology.

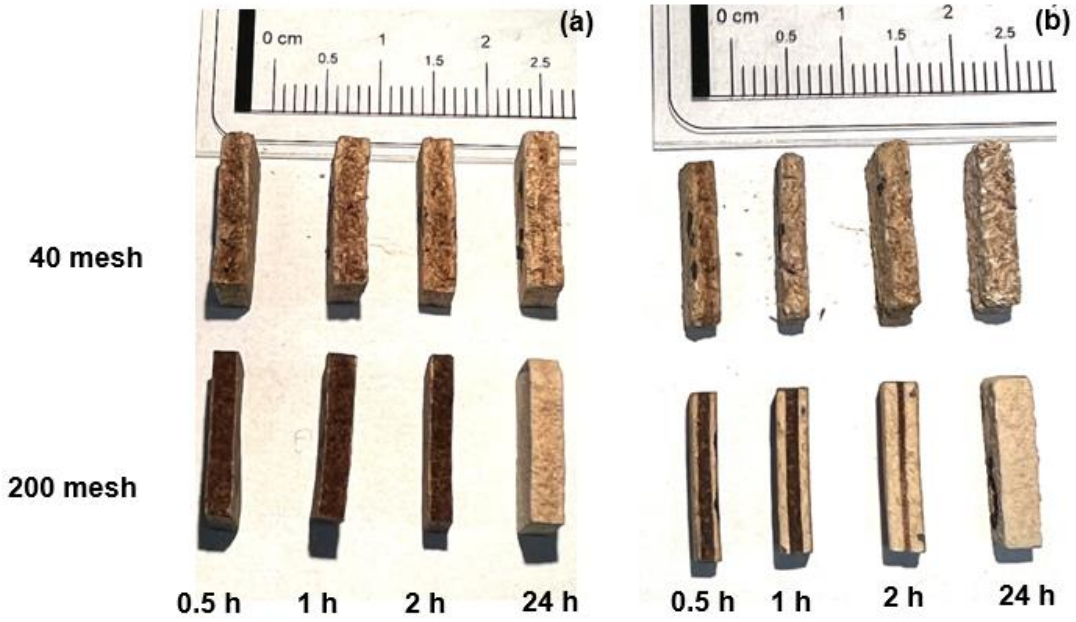

Figure 4.6: Photographs of cross sections of wood-SS cured composites showing the penetration depth of CO_2 treatment time at (a) 7 kPa and (b) 138 kPa

X-ray micro-CT images were obtained for the CO_2 reacted and post-cured wood SS composites to examine the inner structure of the composites using different fiber sizes, treatment time and pressure (Figure 4.7a). Density maps of the various wood-SS composites samples are shown in Figure 4.7b. Plots of penetration depth are seen in Figure 4.7c. From the CTVOX analyzed images (Figure 4.7a), the penetration of CO_2 creates a reaction layer with reaction to SS towards the outer part of the sample. This layer increases inwards with reaction time. No reaction layer was visible for the air/thermally cured wood-SS controls. The microstructure of the wood-SS samples were observed to have distinct features of boundary layers and filled voids created by the CO_2 reaction. For all wood-SS composites reacted with CO_2 for 24 h CO_2, there were fractures observed internally (Figure 4.7a). These fractures/defects could attributed to temperature and CO_2 pressure during curing creating differential stresses [404]. This carbonation zone has also been observed by Chavez Panduro et al. (2019) and found to be mostly amorphous silica [405].

During carbonation of the wood-SS composites, changes in density were observed on the surface as shown in Figure 4.7b. The density was calculated density for each sample and given in Table 4.6. Density of all the composites exposed to CO_2 increased in comparison to the air/thermally cured control samples. However, the density reduced with increasing CO_2 pressure and reaction time. These phenomena can be clearly observed by the density maps in Figure 4.7b. The reaction layer increased for samples exposed from 30 min to 2 h and shown to have medium density creating a carbonation front as the reaction layer progresses inwards in comparison to the core [406]. Due to the large particle size of the 40 mesh samples, there appears to be good diffusion of CO_2 into the core. The 200-mesh wood-SS composites were of a higher density than the 40-mesh wood-SS composites. Particle sizes with a high surface area like 200-mesh, are highly packed within their composites increasing their density and upon absorption of CO_2, density increases since the CO_2 fills the voids and spaces [407]. Density increase was also caused by mass gain in the presence of chemically and non-chemically bonded CO_2 forming sodium bicarbonate species in the matrix [408].

The changes in CO_2 penetration depth boundary layer with increase in reaction time and pressure is seen Figure 4.7c. As time progressed, CO_2 penetrating depth generally increased for the 40-mesh and 200-mesh samples. At 7 kPa, the 40-mesh samples had lesser penetration depths (0.09 mm to 0.69 mm) than the 200-mesh samples (0.16 mm to 1.31 mm). This is because at lower pressure, more time is used to fill the voids in the 40 mesh composites before a boundary layer starts to form. At 138 kPa, the microstructure of the 200-mesh composites, reduced the penetration depth with time (0.23 mm to 0.45 mm) of the CO_2 in comparison to the 40-mesh composites (0.40 mm – 0.63 mm) [409]. Samples exposed with CO_2 for 24 h , had no boundary layers to be measured as seen in Figure 4.7a and 4.7b, hence the absence of plots.

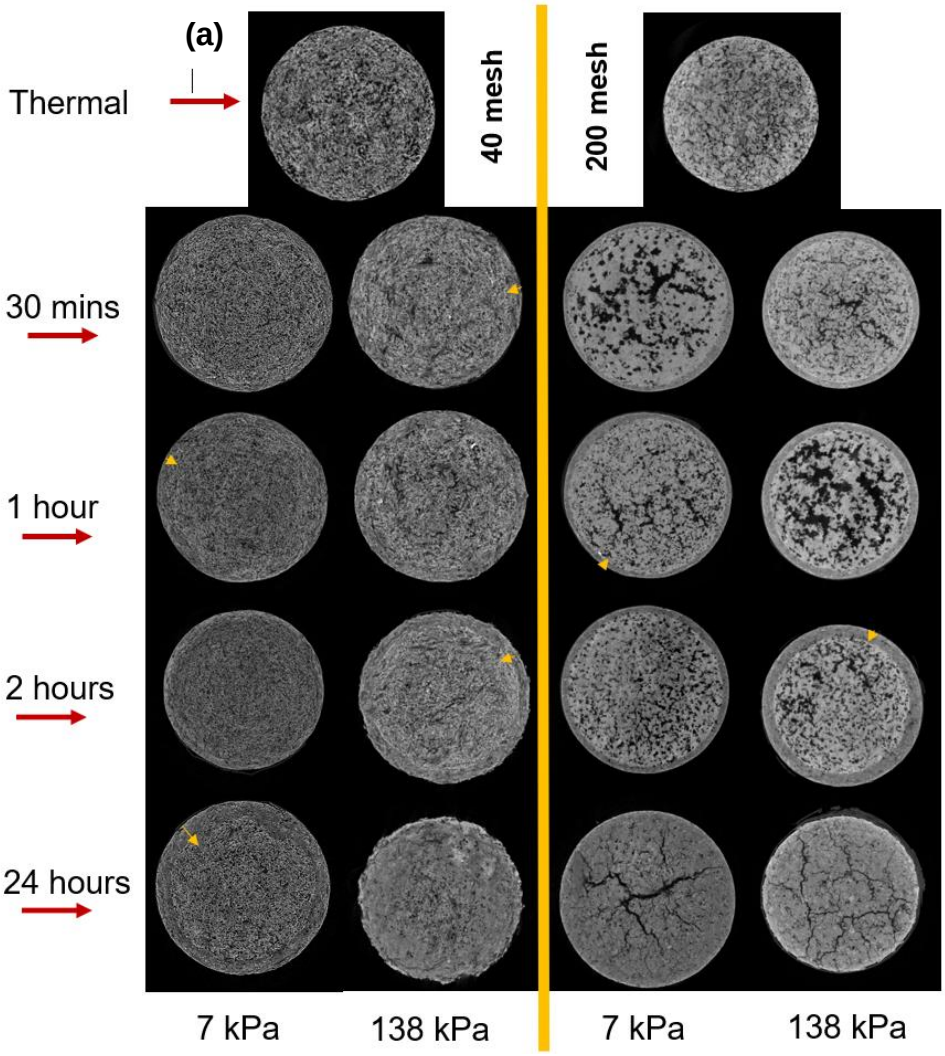
(a)
Thermal
40 mesh
200 mesh
30 mins
1 hour
2 hours
24 hours
7 kPa
138 kPa
7 kPa
138 kPa

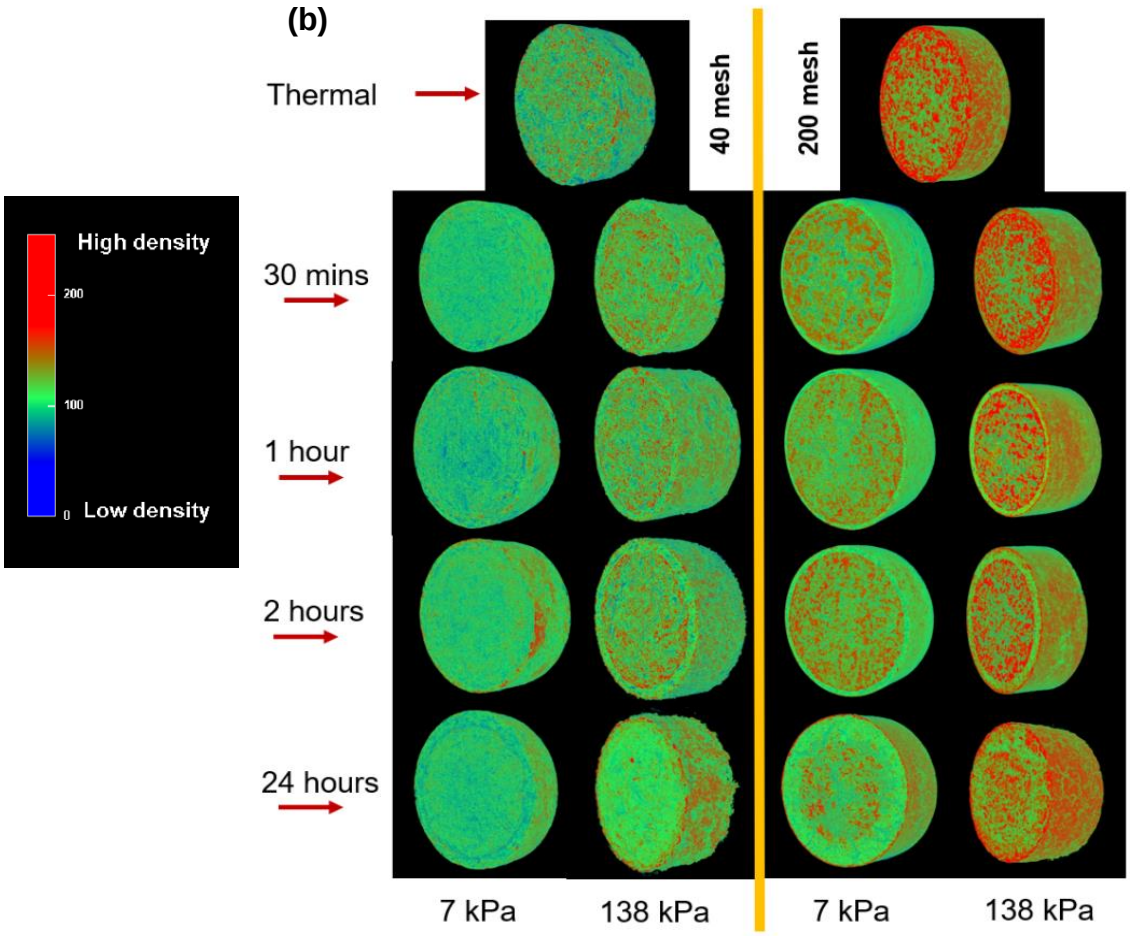
(b)
Thermal
40 mesh
200 mesh
High density
200
100
0
Low density
30 mins
1 hour
2 hours
24 hours
7 kPa
138 kPa
7 kPa
138 kPa

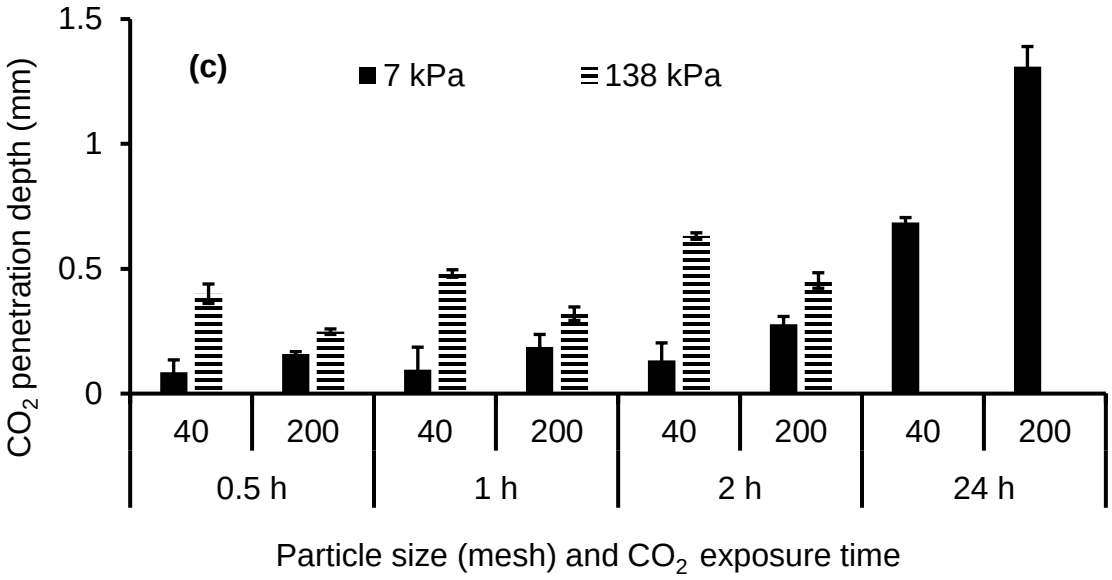

Figure 4.7: (a) Micro-CT cross-section slices showing penetration depth (yellow arrows) of reacted CO_2 with wood-SS cured samples plus controls and (b) density maps of reacted CO_2 with wood-SS cured samples plus controls, (c) plot of penetration depth for wood SS samples at different pressures and time

Table 4.6: Calculated density of air cured (control) carbonated (CO_2 cured) wood-SS composites.

CO_2 Treatment time (h)	**CO_2 Pressure (kPa)**	**Density (kg/m^3)**	
40 mesh blends			
Curing Temperature ➞		60 °C	105 °C
0 (control)	-	755 (±13)	727(±1)
0.5	7	1055 (47)	954 (±54)
	138	800 (±11)	763 (±5)
1	7	791 (±3)	764 (±1)
	138	806 (±23)	751 (±24)
2	7	793 (±69)	748 (±23)
	138	850 (±11)	764 (±11)

Table 4.6 cont'd

24	7	754 (±55)	734 (±8)
	138	597 (±34)	576 (±34)
200 mesh blends			
0 (control)	-	967 (±79)	908 (±102)
0.5	7	1183 (±48)	1151 (±124)
	138	1302 (±47)	1243 (±59)
1	7	1018 (±36)	920 (±50)
	138	891 (±18)	850 (±56)
2	7	1109 (±91)	1006 (±105)
	138	1108 (±5)	1039 (±63)
24	7	896 (±23)	865 (±42)
	138	873 (±13)	708 (±13)

Note: Standard deviation in parentheses.

4.4.4. Bending Test Results

The composites were tested for their flexural properties to evaluate their use in either structural or non-structural applications. The FM and FS results of the wood-SS composites reacted with CO_2 at different times, pressure, particle size, CO_2 pressures, and post-cure temperatures are given in Table 4.7. In general, 200 mesh wood-SS composites exhibited better flexural properties with the highest FM at 11.2 GPa and FS at 59.2 MPa with a 30 min CO_2 reaction time, and post-curing temperature of 60 °C. These values were significantly higher than the FM of 7.1 GPa obtained by Cabral et al (2018) for carbonated cured cement bonded balsa particleboard [374]. The lowest FM wood-SS composite was from 40-mesh samples cured at 138 kPa CO_2, and post cured at 60 °C. The lowest FS was recorded for 40 mesh samples cured at 138 kPa CO_2 and post cured at 105 °C. With respect to exposure time, FM, and FS both reduced with increased CO_2 reaction time. For the larger particle size 40 mesh wood-SS composites, CO_2 reaction time adversely affected the flexural properties and could be attributable to lower, mechanical interlocking due to a lower surface area. The wood-SS composites made with the 200 mesh fiber showed a more densified structure with improved fiber-SS interactions [410]. The low and high CO_2 treatment pressures had a

significant effect on the FM and FS properties [411]. For the 40 mesh blends post-cured at 60 °C and 7 kPa, FM values ranged from 1 GPa to 2.1 GPa, whilst at 138 kPa CO_2 under the same conditions, FM was from 0.2 GPa to 0.9 GPa, showing a decrease. The same influence of CO_2 pressure was seen for 200 mesh samples at 7 kPa CO_2 and post cured at 105 °C with FM values between 1.4 GPa to 8.2 GPa and 138 kPa CO_2 between 1.0 GPa to 9.1 GPa.

Studies have shown that an increase in carbonation pressure can reduce toughness of composites and reduce the bonding between the fiber and matrix [412]. A study by Wang et al (2017) in the CO_2 curing of wood and cement also confirmed that samples with increased thickness swelling did not possess good mechanical properties because of the presence of water soluble extractives in wood that can hinder early strength development in carbonation curing [413]. For this study, a water bath temperature of 60 °C was used to accelerate CO_2 diffusivity and promote curing, whilst removing excess water from the composite during carbonation. But the curing temperature did not seem to have any significant effect on the bending properties. This was validated by Zhan et al (2016) on the carbonation of concrete blocks. They found that increasing carbonation temperature from 20 °C to 80 °C had limited effect on the degree of carbonation on concrete blocks however, with an increased temperature between 80 °C and 100 °C, a significant degree of carbonation was observed with an increase in strength [101].

Table 4.7: Mechanical properties of 40 mesh and 200 mesh Wood SS cured composites

CO_2 Treatment time (h)	**CO_2 Pressure (kPa)**	**Flexural Modulus (GPa)**		**Flexural Strength (MPa)**	
40 mesh blends					
Curing Temperature ➡		**60**	**105**	**60**	**105**
No CO_2	-	2.4 (±0.1)	2.1 (±0.0)	11.3 (±0.6)	8.5 (±0.4)
0.5	7	1.9 (±0.2)	2.3 (±0.1)	9.6 (±0.8)	9.6 (±0.2)
	138	0.9 (±0.1)	0.9 (±0.1)	4.2 (±0.5)	4.5 (±0.2)
1	7	1.7 (±0.1)	2.7 (±0.1)	10.5 (±0.6)	10.7 (±0.5)
	138	0.6 (±0.1)	0.6 (±0.0)	2.6 (±0.2)	2.0 (±0.1)
2	7	2.1 (±0.1)	2.2 (±0.5)	10.7 (±0.4)	10.0 (±0.5)

Table 4.7 cont'd

	138	0.3 (±0.0)	0.2 (±0.0)	1.1 (±0.1)	0.9 (±0.1)
24	7	1.0 (±0.0)	1.8 (±0.0)	6.0 (±0.4)	7.3 (±0.4)
	138	0.2 (±0.0)	0.9 (±0.0)	1.9 (±0.3)	0.5 (±0.0)
200 mesh blends					
No CO_2	-	6.7 (±0.7)	4.7 (±0.5)	40.9 (±3.2)	15.9 (±1.8)
0.5	7	8.9 (±0.3)	7.9 (±0.3)	45.0 (±6.5)	36.9 (±1.9)
	138	11.2 (±3.6)	9.1 (±0.2)	59.2 (±3.1)	39.6 (±2.4)
1	7	7.3 (±0.0)	7.8 (±0.2)	45.3 (±1.9)	27.0 (±1.2)
	138	3.6 (±0.1)	4.6 (±0.2)	30.0 (±0.5)	27.5 (±1.1)
2	7	8.9 (±0.3)	8.2(±0.2)	45.5 (±5.0)	38.7 (±2.5)
	138	2.4 (±0.1)	3.7 (±0.1)	13.3 (±1.0)	20.2 (±0.5)
24	7	1.5 (±0.3)	1.4 (±0.0)	3.5 (±0.3)	4.8 (±0.8)
	138	0.8 (±0.0)	1.0 (±0.0)	3.5 (±0.0)	4.8 (±0.1)

Note: Standard error in parentheses.

4.4.5. Thermal stability of the wood-SS composites by TGA

The thermal stability of the composites was evaluated by TGA. The TGA-DTG thermograms for thermally cured wood-SS controls and carbonated wood-SS samples cured at different pressures are shown in Figure 4.8. The thermal degradation onset (T_{onset}), and residual (ash) values are given in Table 4.8. From Table 4.8, all thermally cured control composites exhibited higher T_{onset} in comparison to carbonated composite samples. With increasing CO_2 pressure, T_{onset} was generally higher for wood-SS CO_2 treated at 138 kPa, showing the effect of carbonation pressure. 40 mesh composite samples post cured at 60 °C and 7 kPa CO_2 pressure had T_{onset} from 247 °C to 261 °C while those cured with 138 kPa CO_2 pressure had T_{onset} between 260 °C to 318 °C. The same observation was seen for the 200 mesh composites post cured at 60 °C and 7 kPa CO_2 pressure with T_{onset} values ranging from 251 °C to 264 °C and the samples cured with 138 kPa CO_2 pressure had values from 276 °C to 290 °C. With respect to carbonation time, there was also a slight increase in T_{onset}. The 40-mesh composite samples post cured at 105 °C showed a T_{onset} at 265°C at 30 mins

CO_2 treatment which increased to 310 °C with a 24 h CO_2 treatment. Under the same conditions, 200-mesh samples had a 0.7% increase in T_{onset} values. For the 40 mesh composites with a 24 h CO_2 treatment showed better thermal stability (T_{onset}) by 9.4% post cured at 60 °C and a 7.4% increase when post cured at 105 °C. The residual "ash" content at 900 °C, for wood-SS composites post-cured at 60 °C had the lowest ash residue content. Residual ash values were 57-62% for 40 mesh wood-SS composites post-cured at 60 °C and for composites post-cured at 105 °C were 58-64%. Residual ash values for the 200-mesh wood-SS composites post-cured at 60 °C were 56-63% and 58-66% for post-cured composites at 105 °C. These values were typically influenced by curing temperature and pressure.

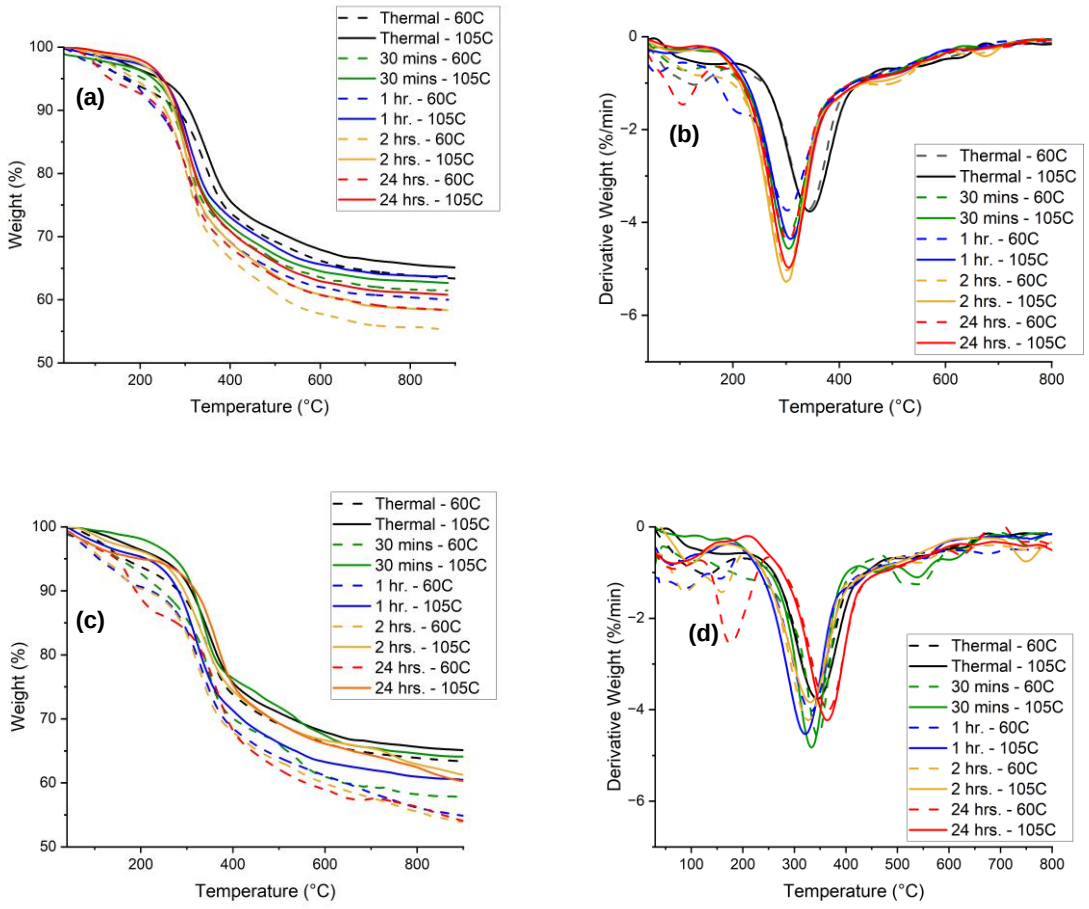

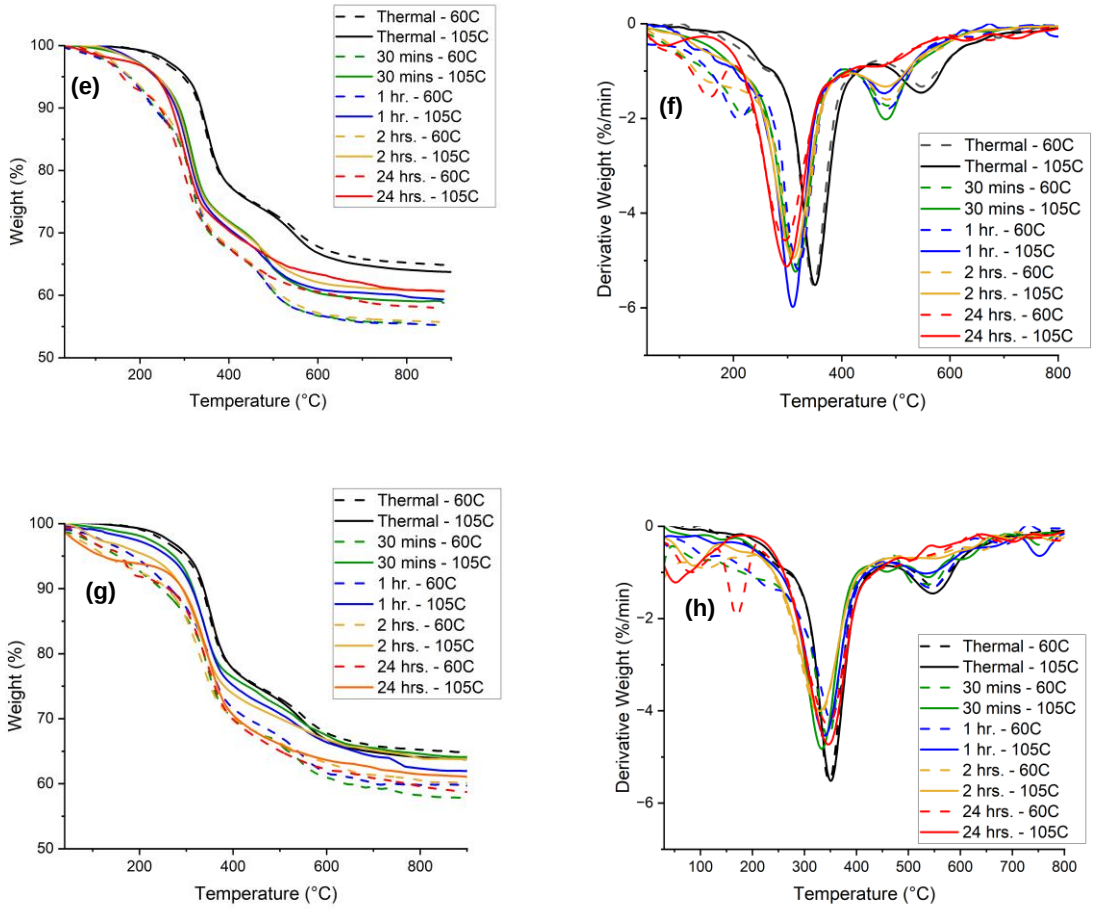

Figure 4.8: Thermograms from TGA analysis of cured wood-SS composites (a) % weight loss and (b) DTG curves at 7 kPa CO_2 pressure; and (c) % weight loss and (d) DTG curves at 138 kPa CO_2 pressure for 40 mesh wood-SS samples and, (e) % weight loss and (f) DTG curves at 7 kPa CO_2 pressure; and (g) % weight loss and (h) DTG curves at 138 kPa CO_2 pressure for 200 mesh wood-SS samples

Table 4.8: TGA thermogram curve values for thermally cured and carbonated wood SS blends

CO_2 Treatment time (h)	**CO_2 Pressure (kPa)**	**T_{onset} (°C)**		**Residual weight at 900 °C (%)**	
40 mesh blends					
Curing Temperature ➡		**60**	**105**	**60**	**105**
No CO_2	-	294 (±0.1)	279 (±5)	62 (±4)	64 (±2)

Table 4.8 cont'd

0.5	7	261 (±4)	247 (±11)	61 (±1)	63 (±1)
	138	260 (±6)	265 (±6)	58 (±1)	58 (±4)
1	7	247 (±11)	250 (±9)	61 (±1)	63 (±2)
	138	271 (±10)	269 (±4)	57 (±1)	60 (±2)
2	7	256 (±2)	252 (±3)	60 (±4)	58 (±2)
	138	283 (±4)	276 (±3)	57 (±2)	61 (±4)
24	7	255 (±5)	253 (±2)	59 (±2)	62 (±2)
	138	318 (±6)	310 (±10)	58 (±2)	62 (±1)
200 mesh blends					
Curing Temperature ➡		**60**	**105**	**60**	**105**
No CO_2	-	290 (±2)	307 (±1)	63 (±0)	66 (±2)
0.5	7	264 (±6)	270 (±3)	56 (±1)	60 (±1)
	138	290 (±16)	285 (±2)	60 (±2)	63 (±2)
1	7	253 (±3)	264 (±7)	56 (±1)	59 (±1)
	138	288 (±6)	291 (±4)	60 (±1)	63 (±1)
2	7	251 (±8)	252 (±8)	56 (±0)	61 (±0)
	138	276 (±6)	272 (±6)	61 (±0)	65 (±1)
24	7	254 (±1)	254 (±1)	58 (±1)	58 (±1)
	138	287 (±2)	287 (±2)	60 (±1)	62 (±1)

Note: Standard deviation in parentheses.

From the DTG thermograms of wood-SS composites the temperature of major DTG peaks are given in Table 4.9. If samples contain sodium bicarbonate (Na_2CO_3) and silicon dioxide (SiO_2) components, degradation peaks could be seen in the DTG peaks and the thermal degradation of other specific components in the matrix can also be identified. Thermal degradation below 150 °C was attributed to loss of water and volatiles [265], [414]. The second peak between 200 °C and 400 °C was due to the degradation of wood and silanol components [230]. The removal of carbonate groups is observed from 500 °C to 900 °C, especially sodium carbonate [415]. These peaks between 500 °C to 900 °C have the lowest

intensity for the 40-mesh wood-SS CO_2 treated at 7 kPa. This could be attributed to the poor packing of the 40 mesh wood fibers and lower interaction with SS and the reacted CO_2.

Table 4.9: DTG thermogram curve values for thermally cured and carbonated wood SS blends

CO_2 Treatment time (h)	**CO_2 Pressure (kPa)**	**Major DTG peak between 250 °C and 600 °C (°C)**		**Major DTG peak between 600 °C and 900 °C (°C)**	
40 mesh blends					
Curing Temperature →		**60**	**105**	**60**	**105**
No CO_2	-	344 (±4)	341 (±4)	577 (±29)	706 (±67)
0.5	7	306 (±5)	306 (±3)	694 (±31)	676 (±5)
	138	316 (±7)	311 (±5)	745 (±16)	742 (±57)
1	7	304 (±1)	305 (±4)	651 (±24)	676 (±32)
	138	325 (±9)	324 (±7)	699 (±43)	692 (±60)
2	7	300 (±2)	302 (±3)	667 (±2)	677 (±2)
	138	331 (±4)	335 (±5)	732 (±24)	770 (±22)
24	7	300 (±3)	305 (±2)	697 (±17)	667 (±12)
	138	364 (±1)	363 (±7)	654 (±30)	674 (±10)
200 mesh blends					
Curing Temperature →		**60**	**105**	**60**	**105**
No CO_2	-	349 (±3), 544 (±3)	346 (±5), 547 (±4)	750 (±18)	-
0.5	7	317 (±2), 486 (±2)	312 (±3), 486 (±3)	668 (±6)	724 (±21)
	138	341 (±4), 539 (±2)	335 (±4), 545 (±2)	739 (±14)	762 (±32)
1	7	316 (±5), 485 (±1)	311 (±2), 485 (±4)	671 (±30)	732 (±77)
	138	345 (±5), 545 (±3)	338 (±4), 559 (±29)	666 (±20)	748 (±34)
2	7	316 (±0), 489 (±0)	308 (±1), 489 (±2)	748 (±0)	683 (±29)
	138	324 (±6), 572 (±69)	324 (±6), 548 (±16)	809 (±16)	754 (±28)

Table 4.9 cont'd

24	7	296 (±1), 485 (±3),	300 (±4), 485 (±7)	687 (±14)	646 (±22)
	138	344 (±1)	345 (±3)	781 (±7)	659 (±62)

Note: Standard deviation in parentheses.

4.4.6. Statistical Analysis

RSM was used to optimize the treatment process variable for final composite product properties, such as FM and FS [416]. The regression tables for the response variables of FM and FS are given in Table 4.10 and 4.11, respectively. The results from the quadratic model fits show that the factors significantly affect FM, explaining 77% of its variability. Specifically, FM does not vary with curing temperature (x2), however it varies significantly with the factors pressure (x1), time (x3), and particle size (x4). The effect of x4 on FM was a linear function of reaction time (h). At time t = 0 h, a unit increase of x4 results in a 1.45 GPa increase in FM on average. However, after an incremental time (h) increase, there was a decrease by 1.26 GPa (e.g., t = 2 h, each unit increase in x4 results in 1.45 – 2 * 1.26 = 1.07 GPa decrease in FM on average). From the Shapiro-Wilk normality test, W = 0.94217 and p-values ≤ 0.05 depicting normality. Ramsey tests showed the linearity of the model used for both FM and FS.

Table 4.10: Statistical analysis of CO_2 curing process parameters results with respect to FM (GPa)

Term	Variables	Estimate	Error	t-value	P-value
	(Intercept)	8.23	4.00	2.06	**0.049**
Pressure (kPa)	x1	-0.86	0.27	-3.24	**0.003**
Curing Temperature (°C)	x2	-0.04	0.25	-0.14	0.888
Time (h)	x3	-1.99	0.35	-5.68	**<0.001**
Particle size mesh	x4	1.45	0.30	4.86	**<0.001**
I(Pressure^2)	I(x1^2)	-11.32	4.76	-2.38	**0.025**

Table 4.10 cont'd

I(Time^2)	I(x3^2)	6.03	3.02	2.00	0.056
Curing temp : Particle size	x2:x4	-0.14	0.25	-0.54	0.591
Time : Particle size	x3:x4	-1.26	0.31	-4.09	**<0.001**

Overall significance: $F_{(8, 27)} = 16.39$; p-value <0.001, $R^2 = 77.86\%$

The FS properties were also fitted to a quadratic model. A 79.5% variability was observed, and FS varied significantly with the factors x1, x3, and x4. The effect of x4 on FS was also a linear function of time (h) and from the Shapiro-Wilk normality test, W = 0.94004 for FS, respectively and p-values ≤ 0.05 showing the normality of the data.

Table 4.11: Statistical analysis of CO_2 curing process parameters with respect to the composites FS response.

Term	Variables	Estimate	Error	t-value	P-value
	(Intercept)	39.87	19.60	2.03	0.052
Pressure (kPa)	x1	-3.33	1.33	-2.51	**0.018**
Curing Temperature (°C)	x2	-2.05	1.25	-1.64	0.113
Time (h)	x3	-10.32	1.74	-5.93	**<0.001**
Particle size mesh	x4	7.20	1.48	4.85	**<0.001**
I(Pressure^2)	I(x1^2)	-52.85	23.31	-2.27	**0.032**
I(Time^2)	I(x3^2)	27.18	15.03	1.80	0.082
Curing temp : Particle size	x2:x4	-1.89	1.25	-1.51	0.142
Time : Particle size	x3:x4	-7.00	1.53	-4.57	**<0.001**

Overall significance: $F_{(8, 27)} = 17.81$; p-value <0.001, $R^2 = 79.5\%$

The 3D response surfaces associated with the significant effect of the statistical results for pressure (x1) and time (x3) are shown in Figure 4.9 at the slices for curing Temp = 293° C, and 164 ° C and particle mesh size = 99.04 mesh and 33.5 mesh size for FM and FS respectively that correspond to the plot.

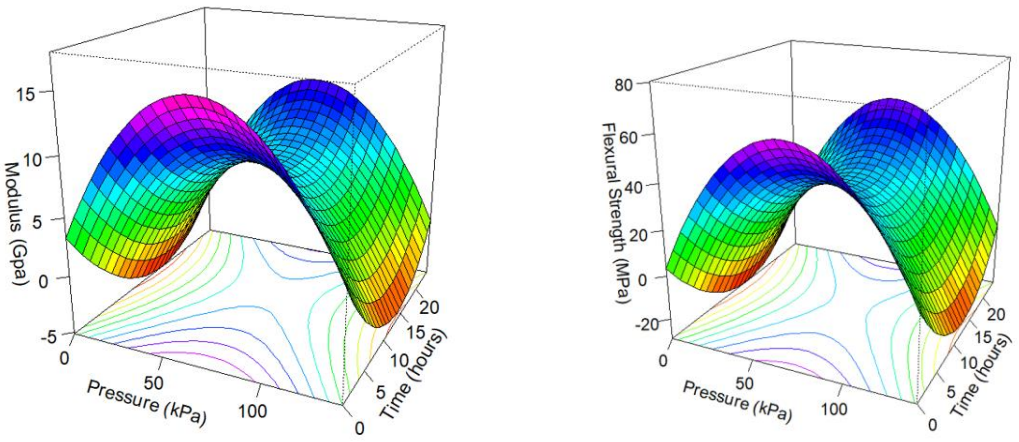

Figure 4.9: 3D response surfaces for FM and FS with respect to pressure and time

4.5. Conclusions

In this study, carbon sequestration of wood SS composites with different wood fiber particle sizes of 40 and 200 mesh, at different CO_2 times and pressure were successfully examined. Conclusively, CO_2 uptake significantly increased with carbonation pressure, particle size differences and time. Rheology time sweep showed the timely reaction of SS in wood composites in the presence of CO_2 with different wood mesh sizes. 200 mesh wood SS showed better mechanical properties in comparison to 40 mesh fiber composites. E_a increased with the addition of the 200 mesh fibers in comparison to the 40 mesh because of its increase surface area. Thermal stability of the carbonated composites showed variable reactions and degradation under increased temperature. This study clearly shows that the wood-SS composites can be cured with CO_2 to sequester carbon and improve the mechanical properties of the composite materials. Further studies are required to implement this technology for real world applications in construction materials.

4.6. Acknowledgment

The authors would like to acknowledge (i) the Idaho State Board of Education-Higher Education Research Council-IGEM award # IGEM 20-002 for their financial support, (ii) USDA-CSREES grant 2007-34158-17640 for support in the purchase of the DSC, (iii) National Science Foundation award # 2119809 for their financial support, (iv) The

University of Idaho P3 grant, (v) the M.J. Murdock Charitable Trust for support in the purchase of the Micro-CT scanner, and (vi) Robert Carne for the 3D printed ABS chamber.

Chapter 5: Modifying a Thermoset-Natural Fiber Composite Matrix for Application in Additive Manufacturing

5.1. Abstract

This study examined the augmentation of phenol resorcinol formaldehyde (PRF) resin using three different types of modifiers (ball-milled eggshells (BMES), gelatinized corn starch (GCS) and sulfonated castor oil (SCO) combined with wood fibers and waste denim fibers to form extrudable composites for additive manufacturing (AM). A 50/50 mix of wood-PRF was used. The modifiers were added at a loading of 1, 2, 5 or 10 wt.% on a PRF basis. Denim fiber was substituted for wood at 5 and 10 wt.%. Neat PRF with modifiers exhibited good shear thinning behavior with reduced complex viscosity (η* at 1 Hz) ranging from 1.5 kPa.s to 2.7 kPa.s for BMES, 1.9 kPa.s to 4.8 kPa.s for GCS and 1.0 kPa.s to 2.1 kPa.s for SCO as observed from the dynamic rheology. The addition of denim fiber to wood reinforcement on the modified PRF increased the flexural strength (FS) from 44 MPa to 53 MPa. Exothermic curing peak temperatures for the modified PRF filled composite moved to higher temperatures in comparison to the unfilled modified PRF systems. Curing peak temperatures ranged from 116 to 137 °C for BMES blends, 113 to 134 °C for GCS blends, 112 to 128 °C for SCO blends and 121 to 129 °C for denim blends. Thermal stability of the modified PRF blends decreased with the addition of wood. Successful extrusion of the wet modified wood-PRF blends was achieved with all modifiers but not with the denim fibers. FS of the extruded blends increased within the range of 4.8% to 28% in comparison to the pressed samples showing the positive influence of extrusion on mechanical properties of the extruded post cured blends and potential for use in AM.

5.2. Introduction

Issues of wood waste from lumber production and two dimensional panels, such as particleboard, during machining, sheathing, and cutting, to convert them to final products have generated environmental concerns [417]. It is estimated that 1 ton of wood waste comprising of sawdust, shavings edgings etc., is generated from every 100 board feet of lumber [418]. These wastes end up in landfills or are being used as energy with just a few

percent getting recycled. In 2021, only 2.1% of the wood waste generated was used for energy in the USA [4]. This calls for more solutions to curb this waste. An innovative technology that can be used to reduce this waste and directly make complex 3-dimesnional (3D) products by additive manufacturing (AM).

AM involves the layer-to-layer deposition and fabrication of complex geometries without the need for machining or tooling [419]. AM allows for cost efficiency improvement whilst reducing energy consumption [420]. This process can be done with different kinds of materials including thermoplastics and thermosets, with thermoplastics commonly used [421]. There are different methods used for AM with the most common been material extrusion which extrudes the mixture out of a nozzle [422]. Material extrusion is considered a simple and affordable process with either a plunger based, filament based, or a screw base extruder system setup.

The use of thermosets in additive manufacturing has been considered cheaper due to the non-requirement of thermal energy for the process [14]. Thermosets are considered to give superior materials due to their influence on the improved mechanical properties and thermal resistance [15]. Different thermosets are currently studied and used with most been epoxy based since they do not generate volatile by products like formaldehyde emissions [8] [9]. Most thermosets like epoxy still require high post curing temperatures after extrusion to hold their required shape and crosslinked structure. Because of this, the need for more reactive thermosets, reinforcements and modifiers is essential [10] [11]. A previous study has investigated the use of a thermoset resin (phenol-resorcinol-formaldehyde (PRF)) together with wood fiber for use in AM, however had some challenges with extrusion of the material [425].

PRF resins which are cold setting resins due to the resorcinol present in them requires low energy for curing and have a high reactivity due to the resorcinol nucleophilicity [39]. Due to the high cost of resorcinol, the presence of phenol and fillers will help reduce the resins cost whilst creating products with post curing improved mechanical properties [426]. Thermosets mostly have viscosity issues during AM and are fragile and brittle after the process thus the need for reinforcements like modifiers, fillers etc. A few of these reinforcements includes natural fibers (wood, cotton etc.), glass fiber, carbon fiber, and nanocellulose components amongst others [427] [428]. Natural fibers have increasingly been

used for reinforcements or fillers due to their contribution to increased mechanical properties of the end products, renewal resource, non-toxicity, low cost, and availability [429]. Although the use of wood has been employed in AM but not vastly studied, its use in thermoset additive manufacturing creates innovative and sustainable materials [285]. Studies on waste denim fibers which contains 100% cotton, have high rigidity and better tear resistance, and have shown to improve the mechanical properties of thermoplastic composites [430], [431]. Denim has also been used in the fabrication of thermoset composites for structural applications [432].

With the AM of thermosets in the presence of natural fibers, low loadings have been considered, and just a few studies have considered high fiber contents [10] [7] [433] [419]. In the presence of high fiber content, issues of flow, high motor loads, porosity and fabrication failure will have to be modified for a more sustainable AM fabrication process[11] [62] [172]. Nozzle blockage in the presence of high fiber content is a major concern in additive manufacturing of thermoset composites and homogenous flow and mixtures is essential. To attain this homogeneity and flow, the binders or thermosets can be modified to attain better wettability, flowable viscosity with improved post curing properties in the matrix [44]. Several studies have considered different modifiers which give the thermosets different properties of rubbery, anti-shrinkage, impact resistance etc. [82], [434]–[437].

Egg shells which contain a high content of mineral salts has shown to play a role as a rheology modifier in small amounts [438]. Their low cost, availability and high content of calcium carbonate (95 - 97%) and organic components (3 – 5%), has proven to give materials and composites good impact strength and mechanical properties [115] [439]. With the presence of its nanopores, it has also be considered a good reinforcement for thermosets since it creates better interfacial adhesion between filler and matrix with the formation of high performance composites [440] [441] [121].

Corn starch is commonly used as viscosity modifier in foods and adhesives. The gelatinization of starch is often employed, enhanced in alkaline conditions, to aid extrusion of materials [442]. With this, starch-based adhesives have been studied to wet the polar surfaces of cellulose, penetrate crevices and pores, and, thus, form strong bonds in composites or materials they are used to fabricate [443] [444].

Castor oil produced from castor beans, is a non-competitor with edible oils having a triglyceride structure which makes it easily modified (high solubility, small hydrodynamic diameter, and low melting point). The presence of its hydroxyl groups influence its reactivity, melting point, viscosity, solubility, polymorphism and heat of fusion [445]. The carboxylic group aids esterification, double bond hydrogenation and the hydroxyl group helps acetylation and alkoxylation [446]. In some studies, it has also been modified into epoxy and used as a curing agent through a substitution reaction [447], [448]. Castor oil based composites haven shown to have good damping properties which is essential for a good additively manufactured product [446] [449]. Sulfated castor oil (SCO) which is one of the first derivatives of castor oil is stable and the only oil which is soluble/dispersible in water and it has been used as a viscosity modifier in polymeric materials [450]. SCO is also used in the textiles industry to improve its wettability and homogeneity of dyes [451] [452]. SCO has been used for lubrication and emulsification in cosmetics and inks due to its excellent solubility [453], [454].

The aims of this study will evaluate the effect of three different types of modifiers (ES, SCO, and GCS) on the extrudability of PRF-wood composites for use in AM. The use of denim fibers as long fiber reinforcement will also be assessed. The influence of these modifiers and fillers on the rheological properties of the green wood-PRF formulations together with the thermal and flexural properties of the cured composites will be evaluated for their suitability and potential use in AM fabrication of thermoset composites.

5.3. Materials and Methods

5.3.1. Materials

Commercial cold setting PRF resin was acquired from Hexion (Cascophen 4001-8 / Cascoset 5830 E, pH = 10.2), and mixed in a ratio of 2.5:1. Waste wood mill residues were obtained from Plummer Forest Products (Post Falls, ID. USA) and screened through a US standard 40 mesh using a standard screen shaker.

Waste denim (cotton) fibers were obtained from old denim jeans and the threads loosened to obtain the weft and warp. The denim threads were cut using a paper guillotine into 3 to 5 mm fiber lengths. Waste chicken eggshells were obtained from a home bakery,

boiled for 10 min to sterilize, dried in an oven at 105 °C and ball milled in a 1-gallon porcelain jar with porcelain balls for 24 h at about 10-15 rpm to obtain the ball-milled eggshells (BMES). Corn starch (Bobs Red mill) was gelatinized by dispersing 50 g of starch in 1 L of water, boiled for 20 min, cooled, and freeze dried (GCS). Sulfated castor oil (SCO) was sourced from Natural Transverse Bay Bath and Body, Michigan, USA.

5.3.2. Characterization of Wood Fiber and Modifiers

Width (100 measurements) of individually separated denim weft and warp fibers were measured via optical microscopy (Olympus BX51 microscope with a DP70 digital camera, San Diego, CA, USA). Specific surface area of BMES (0.4 g) and screened wood fibers (0.4 g) were determined using the Brunauer–Emmett–Teller (BET) analyzer on the Micromeritics FlowSorb 2300 instrument according to ASTM D6556-10. Density of the denim fibers, GCS, BMES and wood fibers were determined at room temperature in nitrogen using an ultra-pycnometer 1000 (Quantachrome, USA).

To determine the particle size distribution of the BMES (0.3 g) was diluted and mixed in 100 mL of deionized water and analysis was determined by light scattering single particle optical sensing (Particle Sizing Systems, Inc. Model 780 AccuSizer). Triplicate analysis was performed, and results were analyzed using the SW 788 software V.1.55. To obtain additional size and morphology measurements of BMES powder was examined by scanning electron microscopy (SEM) on a Zeiss Supra 55 VP-FEG instrument at 20 kV after carbon coating. Morphology measurements were taken for 60 particles using the Image J software version (2.1.0/1.53c, Java 1.8.0_172 (64bit)).

5.3.3. Composite Fabrication

Various wood-PRF composite formulations using the 3 modifiers were fabricated. Each of the modifiers at 1, 2, 5 and 10 wt.% loadings were mixed with the PRF resin. Subsequently, screened wood fibers (50 wt.%) were added to the resin mix. Formulations including denim fiber (5 or 10%) were substituted for wood fiber at a total composition of 50 wt.%. Wet PRF or modified-PRF were mixed by hand using a spatula, and the composite blends (2 g total) were mixed in a small herb grinder for dynamic rheology analysis.

For extrusion, capillary rheology and bending tests, larger batches (25 to 50 g total batch size) of composite blends were mixed using a Pinlo coffee grinder (200 W) for 1 min to prevent exothermic heat buildup and reaction prior to extrusion. For every 50 g batch, 2 ml of water was added to help homogenize the mix. The time taken from mixing samples to starting an experiment for capillary rheology was 4 min. This time was considered during the dynamic rheology characterization which was used to compare the capillary rheology experiment. For bending tests, wet blends were transferred to a 76 mm Ø pellet die set, pressed into discs, and cured at 160 °C for 5 to 10 min at a load of 1.2 tons (PHI hydraulic press, City of Industry, CA, USA). For extrusion trials, wet blends of modified PRF-wood were extruded into rods, flattened in a press to stops (3.2 mm thick), and then cured between heated plates (105 ^{o}C) to obtain samples for flexural testing.

5.3.4. Rheology

The effect of the modifiers on the flow properties (complex viscosity (η*)) of PRF and its wood blends were determined via dynamic rheology on a Discovery Hybrid Rheometer (DHR2, TA instruments, New Caste, DE, USA). Wet sample discs (2 mm x 25 mm Ø) containing modified PRF, and wood fiber were prepared using a 25 mm Ø pellet die. Frequency sweeps were performed at 0.1% strain from 0.05 Hz to 100 Hz at 30 °C on neat PRF, modified PRF, and blends with wood/denim fibers.

Capillary rheology, which plays an important role in the understanding flow behavior of blends at high shear rates, was performed on a wood-PRF blend without modifiers. Investigation of high shear rate properties was determined using wet wood-PRF blends (9 g) in an Instron 5500R-1137 universal testing machine at crosshead speeds 6, 10, 20, 60, and 100 mm/min. The capillary rheometer (Instron model 3213) had a barrel diameter of 9.55 mm, equipped with a 44 kN load cell. Three dies of lengths (24.30 mm, 48.60 mm, and 72.90 mm), entrance angle of 70° and diameter of 4.86 mm were used. Data were obtained using the Bluehill v3.3 Instron software and analyzed according to the ASTM D3835-02 standard with the necessary corrections. Rheological data were also fitted to the power law model of Equation 5.1.

$$\sigma = K\gamma^{n} \qquad \text{(Equation 5.1)}$$

Where σ is the shear stress , γ is the shear rate, K is the consistency index and n is the flow behavior index which is dimensionless [455]. With the consideration of the mixing time (4 minutes), a batch for dynamic rheology testing at 25 °C was performed to compare viscosity trends between the two rheometers.

5.3.5. Differential Scanning Calorimetry (DSC)

Curing behaviors of the PRF with different modifier compositions and wood fiber were performed on freeze dried batches using a Q200 DSC (TA instruments, New Caste, DE, USA) under nitrogen (50 mL/min) and refrigerated cooling. Samples were scanned in modulated DSC mode at 10 °C/min at +/- 2.4 and ramped from 40 °C to 250 °C. Data was analyzed using the TA universal analysis software and baseline was corrected using Origin 2023 software.

5.3.6. Thermal Gravimetric Analysis (TGA)

Thermal stability of the cured modified PRF and wood/denim-modified PRF composites samples (4 to 6 mg) was determined on a Perkin-Elmer TGA-7 instrument (Shelton, CT, USA) under nitrogen (30 mL/min). Samples were scanned non-isothermally from 40 to 900 °C at 20 °C/min and data analyzed using the Pyris v13.3.1 software.

5.3.7. Extrusion

To understand the effect of modifier addition to PRF resin in wood/denim composites in their extrudability, wet blends (50 g batch size) were extruded in a single screw extruder (RobotDigg, Shanghai, China). The extruder (20 mm Ø barrel, 200 mm length, 8.5 mm flight pitch) was equipped with a 200 W motor and operated at 17 rpm and a 9 mm Ø die. Run time per batch was 15 min. To minimize barrel heating due to friction and exothermic resin curing, the barrel was tightly wrapped with a coil of ¼” copper tubing and ice water was pumped (380 L/h) through the coil. After extrusion, rods were pressed, and post cured at 105 °C for flexural bending tests.

5.3.8. Flexural properties

Mechanical properties of the pressed and extruded cured wood-PRF composite samples (63.5 x 13.5 x 3 mm^3) were determined on an Instron 5500R-1132 universal testing

machine (5 kN load cell, 48 mm span, and cross head speed of 1.1 mm/min) according to ASTM D790. Data was collected and analyzed using Bluehill v3.3 Instron software.

5.4. Results and Discussion

5.4.1. Characterization of modifiers

Images of the loosened warp and weft (length = 3 mm to 5 mm) fibers are shown in Figure 5.1a. These loosened fibers were a cluster of individual fibers that were separated to obtain their individual width using optical microscopy (Figure 5.1b). The average width for 100 measurements was 29 μm (±8.8 μm). The calculated aspect ratio was between the range of 103 and 172. The BMES was analyzed for particle size by a combination of SEM (Figure 5.1c) and light scattering particle analysis (Figure 5.1d and 5.1e). Image analysis was performed on the SEM micrographs on 600 particles and showed a mix of particle sizes for BMES ranging between 1 and 74 μm with a median value of 4.4 μm. The micrographs also show the sharp surface and layer structure of the BMES particles which has been stated to be as a result of high calcium content [456], [457]. From the light scattering analysis, the volume (Figure 5.1d) and number average (Figure 5.1d) distributions were obtained. The volume average distribution diameter of the BMES ranged from 2 μm to a 130 μm with a peak mode of 45 μm. The number average distribution ranged from 30 μm to 100 μm with a peak mode of 75 μm.

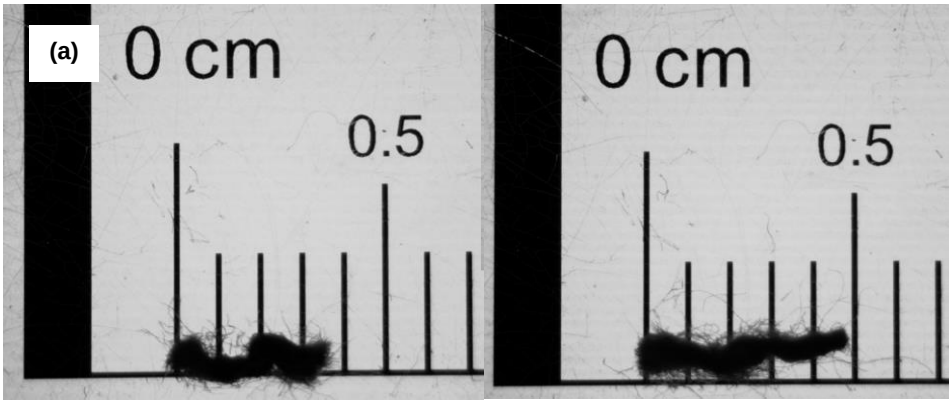

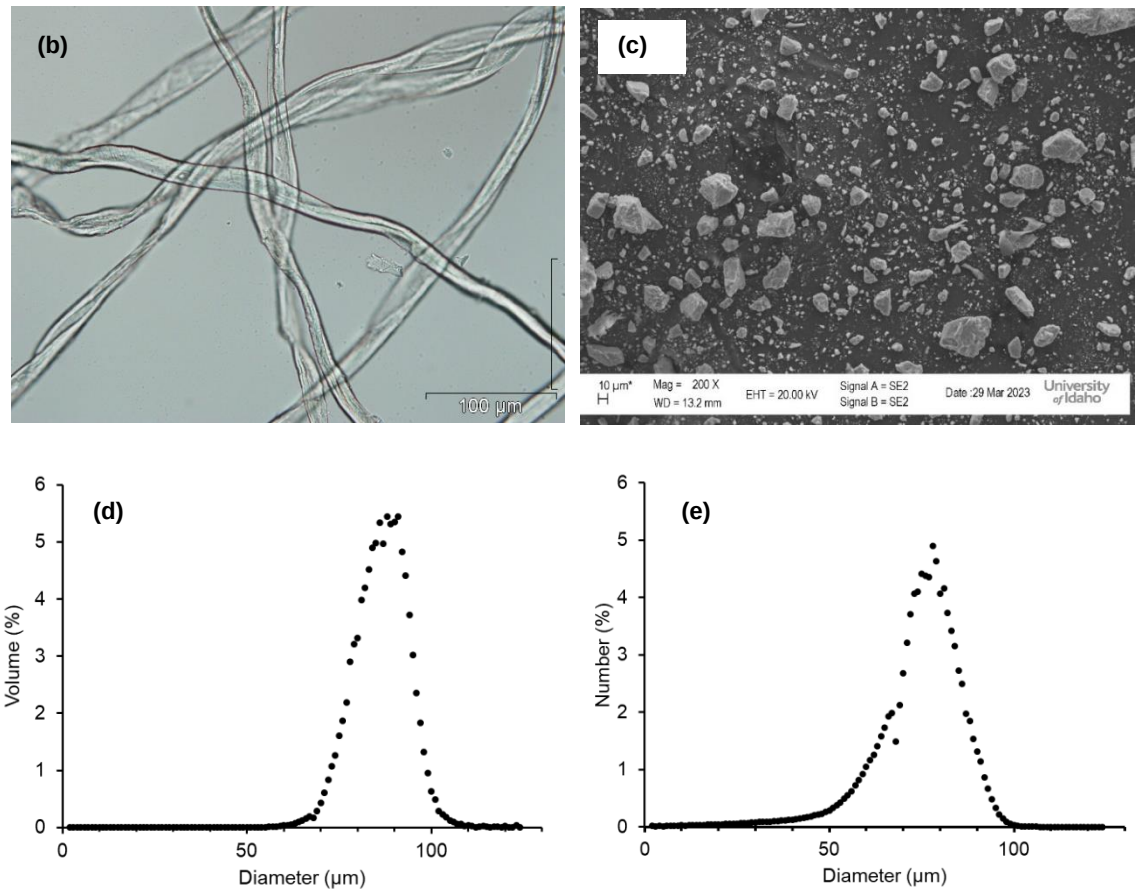

Figure 5.1: (a) Loosened warp and weft and denim fibers, (b) optical microscopy image of individually separated warp and weft fibers, (c) SEM micrograph of BMES at 200x and laser scattering particle size distribution of BMES showing (d) volume % distribution and (e) number % distribution.

The density of the BMES, GCS, denim fibers and wood fibers were 2537 kg/m^3, 1421 kg/m^3, 1571 kg/m^3 and 1535 kg/m^3, respectively. The BMES possessed the highest density because of the calcium carbonate it contains which has a high-density of 2710 kg/m^3. These values of density were within the range of the literature [458]. Specific surface area of BMES and 40 mesh wood fibers were 2.54 m^2/g and 0.235 m^2/g, respectively.

5.4.2. Rheology of resins and composite mixtures

Complex viscosity (η^*) at low shear rates of the PRF, PRF with and without modifiers and wood fiber were determined using dynamic rheology (Figure 5.2). This was used to ascertain the shear thinning behavior of the blends which is an essential characteristic needed

for extrusion and AM. Flow curves (η^* vs shear rate) are shown in Figures 5.2a to 5.2g for neat PRF, PRF and modifiers and modified PRF-wood blends. All PRF-wood blends showed good shear thinning behavior and η^* values varied depending on the modifier used. For neat PRF (Figure 5.2a), a η^* of 2.4 kPa.s was observed at 1 Hz which was reduced to 1.5 – 2.7 kPa.s with addition of BMES. PRF modified samples showed η^* values between 1.9 – 4.8 kPas with GCS and 1.0 – 2.1 kPas with SCO, respectively. These values show the reduction in viscosity with the modifiers which will aid in the extrusion process when wood is added [459]. In the presence of 50% wood, the η^* of the PRF formulations increased by over 100-fold to 350 kPa.s at 1 Hz. Substituting 3-5 mm denim fibers (Figure 5.2a) for wood fibers showed an even higher η^* value (185% and 148% for 5% and 10% denim contents) than the wood-PRF mix.

For the BMES modified PRF (Figure 5.2b), the best shear thinning behavior was observed with 2% BMES with a η^* of 1.5 kPa.s . At 1 Hz, η^* increased with the addition of BMES modifier from 1.5 kPa.s to 2.7 kPas. The reinforcement properties of BMES have been utilized in different studies with reported increase in rheological properties [460], [461]. With the addition of wood fiber (Figure 5.2c), a lower η^* value from 784 to 524 kPa.s was obtained with 10% BMES. This shows that the shear thinning behavior of eggshells would be beneficial for AM. The changes in η^* also show a good relationship between the BMES egg shells and the PRF resin when mixed with wood [462].

The supplementation of GCS (Figure 5.2d) to PRF allows for improved rheological properties [463]. The η^* reduced with GCS and showed shear thinning behavior with an increase in frequency. At frequency of 1 Hz, η^* increased from 1.9 kPa.s to 4.9 kPa.s going from 1% GCS to 10% GCS. With the addition of wood, η^* increased to 788 kPa.s and with 1% GCS reduced to 557 kPa.s. However, with subsequent increases in GCS to 5% and 10%, η^* increased again by 51% and 26%, respectively. This increase in η^* might be because of entanglements/interactions between starch molecular chains and wood [464] . The formulation of wood-PRF with 2% GCS had the lowest η^* and good shear thinning behavior (Figure 5.2e).

Sulfonated castor oil (SCO) which is used mostly as a dispersant and lubricant exhibited the lowest η^* at 1% loading with PRF (Figure 5.2f). The η^* increased from 1.1 kPa to 2.1 kPa with increased SCO content. 100% SCO showed a shear thinning behavior from

0.05 Hz to 5 Hz and then a shear thickening behavior was observed from 5 Hz to 100 Hz (Figure 5.2f). In the presence of wood (Figure 5.2g), SCO lubrication properties were observed with an increase in shear rate and the 10% mix showed the lowest η^* values depicting its lubricity properties [465]. For the wood-PRF blends, the η^* increased from 463 kPa.s at 1% SCO to 595 kPa at 5% SCO and then reduced to 433 kPa.s at 10% SCO showing the thinning effect with increase in shear rate (Figure 5.2g). The addition of SCO will aid in the processability of the composite blends by extrusion for AM. This will also help reduce the driving pressure and motor load of the extruder at high shear [466].

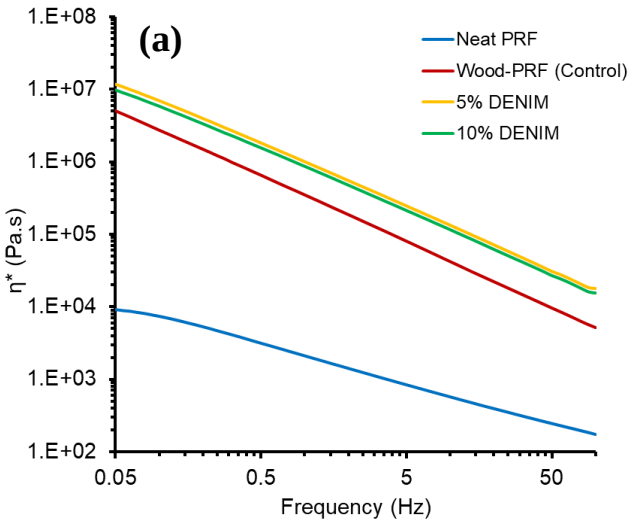

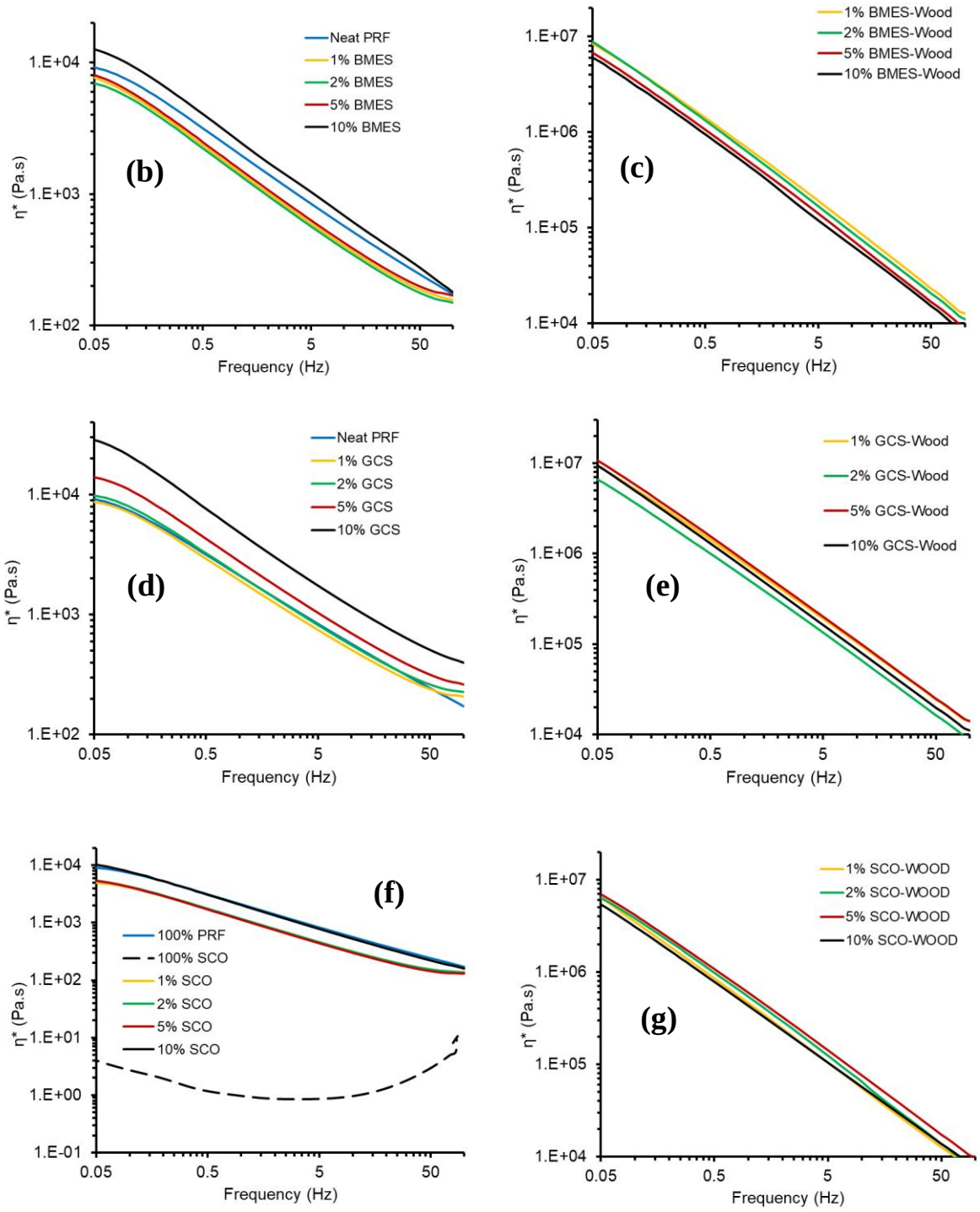

Figure 5.2: Frequency sweep curves of BMES, GCS, SCO modified and unmodified wood-PRF blends.

Dynamic rheological plots were analyzed using the power law fit model and values are given in Table 5.1. PRF and modified PRF showed good fits to the power law with goodness of fit values (R^2) >0.9 for neat PRF and >0.90 PRF with modifiers.

The fitted values for the wood-denim blends, unmodified and modified PRF-wood blends showed good R^2 values >0.99. The power law model has been stated to be more valid at low shear rates and shows the probability of shear thinning using the flow behavior index (*n*). The *n* values for unmodified and modified PRF were >0.5 depicting good shear thinning behavior. All unmodified and modified wood blends showed *n* values >0.8, showing the good shear thinning behavior required for AM. Overall, wood-SCO-PRF blends showed the best *n* components between 0.870 to 0.906 due to the lubricity of the SCO at high shear rates in the presence of wood. The consistency coefficient (K) components were comparable to the η^* at 1 Hz and values varied with different modifiers and wood blends as seen in Table 5.1.

Table 5.1: Dynamic viscosity values at 1 Hz and flow behavior index (n) and consistency coefficient (K) of neat PRF and wood-PRF, modified PRF with BMES, GCS, SCO, Denim, and modified wood PRF composites

Composition (%)	η^* at 1Hz (kPa.s)	K (kPa.s)	*n*	R^2 values
WPRF blends				
100% PRF	2.4	2.1	0.550	0.909
50% PRF-wood	350	343	0.909	0.999
PRF - BMES blends				
1% BMES	1.5	1.6	0.555	0.996
2% BMES	1.5	1.5	0.553	0.994
5% BMES	1.6	1.7	0.553	0.996
10% BMES	2.7	2.6	0.577	0.992
PRF – GCS blends				
1% GCS	1.9	1.9	0.545	0.990
2% GCS	2.1	2.2	0.549	0.991
5% GCS	2.8	2.8	0.572	0.993

Table 5.1 cont'd

10% GCS	4.8	4.9	0.601	0.996
PRF – SCO blends				
1% SCO	1.1	1.2	0.527	0.992
2% SCO	1.2	1.2	0.534	0.995
5% SCO	1.1	1.1	0.541	0.997
10% SCO	2.1	2.0	0.572	0.997
Wood-PRF - BMES blends				
1% BMES	784	738	0.870	0.996
2% BMES	724	694	0.891	0.998
5% BMES	585	556	0.882	0.997
10% BMES	524	493	0.884	0.997
Wood-PRF - GCS blends				
1% GCS	788	764	0.870	0.998
2% GCS	557	535	0.878	0.998
5% GCS	843	822	0.886	0.999
10% GCS	703	685	0.897	0.999
Wood-PRF - DENIM blends				
5% DENIM	1,003	969	0.871	0.998
10% DENIM	868	862	0.863	0.998
Wood-PRF - SCO blends				
1% SCO	463	447	0.906	0.999
2% SCO	539	504	0.906	0.996
5% SCO	595	566	0.879	0.998
10% SCO	433	400	0.870	0.999

To compare dynamic η^* values at low shear rates for the wood-PRF formulation to those at high rates, capillary rheology was used. Bagley and Weissenberg corrections were performed to attain true viscosity values (η_{true}). The comparative plot of a dynamic (4-minute mixing time comparison) and capillary rheology plots are seen in Figure 5.3. The η_{true} values

for the capillary rheology were between 218 kPa to 1.2 MPa for shear rates of 13 to 0.8 s^{-1}. The η_{true} values also reduced with an increase in shear rate. A correlation between low and high shear rate viscosity values from the plot shows the effect of both experiments.

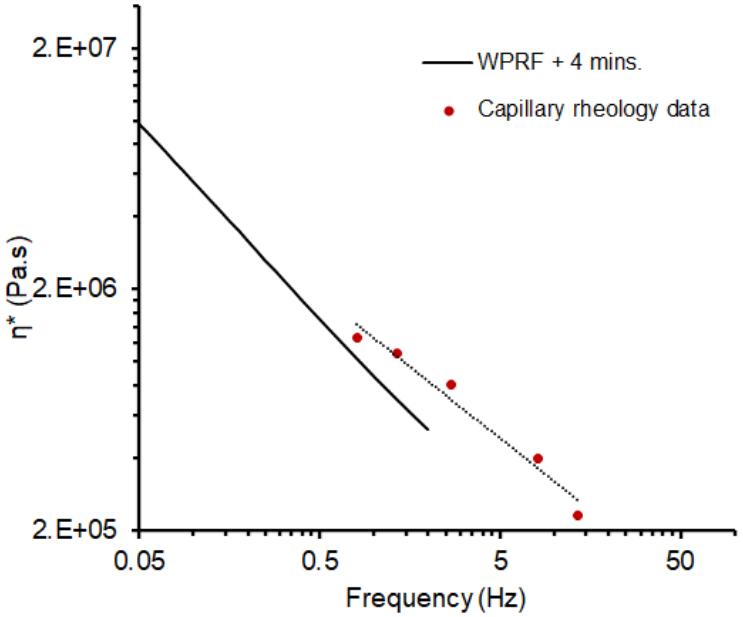

Figure 5.3 *:* Comparison of dynamic and capillary rheology results of wood-PRF 50:50 blend.

5.4.4. Thermal Analysis

The curing behavior of thermoset resins is an important variable in composite materials manufacturing [467]. To determine the curing exothermic peak values of the blends in this study, modulated DSC was used, and non-reversible heat flow curves are shown in Figure 5.4 and results given in Tables 5.2 and 5.3 for all modified and unmodified blends of PRF and wood PRF. All the PRF and modified-PRF resins and PRF-wood formulations cured showing a single exothermic peak. For most of the modified PRF mixtures, exothermic peak temperatures increased with an increase in modifier content. PRF exhibited a curing temperature of 114 °C and was reduced to 106 °C in the presence of 50% wood. With the addition of 5% and 10% denim fibers the peak temperatures were 129 °C and 121 °C, respectively. All modified-PRF samples cured above 100 °C.

BMES addition to PRF moved the exothermic curing peak temperature to higher temperatures (116 °C to 120 °C). This is likely due to the presence of the eggshells with high calcium carbonate ($CaCO_3$), which reduced the reactivity of the resorcinol and formaldehyde hence retarding the curing [468]. $CaCO_3$ has shown to either have a strong neutralization or reaction ability in the elongated gel time of $CaCO_3$ modified UF resins [468]. With the further addition of wood to the BMES-PRF resin the sample cured between 129 °C and 137 °C. This was the highest range of curing temperatures recorded amongst the three modifiers. The ΔH values of the PRF-BMES blends were higher with values between 70 J/g to 120 J/g since more energy was required for curing. The presence of small ball-milled particles required more energy to enable adequate heat transfer among particles for curing of the blend. With wood addition, ΔH reduced and ranged from 40 J/g to 42 J/g which was higher than the PRF-wood blend. For PRF-GCS blends, curing peaks were from 113 °C to 123 °C. These values increased to 128 °C for 1% GCS and 134 °C for 10% GCS in the presence of wood. Modified PRF-SCO blends cured between 112 °C to 120 °C and had the lowest curing peak values of 90 °C to 122 °C in the presence of wood. ΔH were also minimal for modified PRF-SCO blends from 46 J/g to 120 kJ/mol and between 44 J/g to 47 J/g with wood. With the addition of the 5% denim fibers, curing peak temperature increased by 22 % and reduced to 14 % with the 10% denim . The ΔH required for curing was higher for the 10% denim at 70 J/g and at 5% denim the value was low at 41 J/g. Knowing these curing temperatures aids in controlling the cure rate for extrusion to avoid premature curing in the extruder barrel.

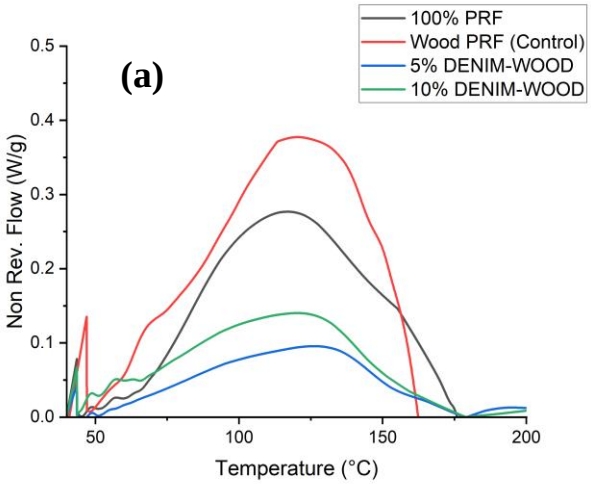

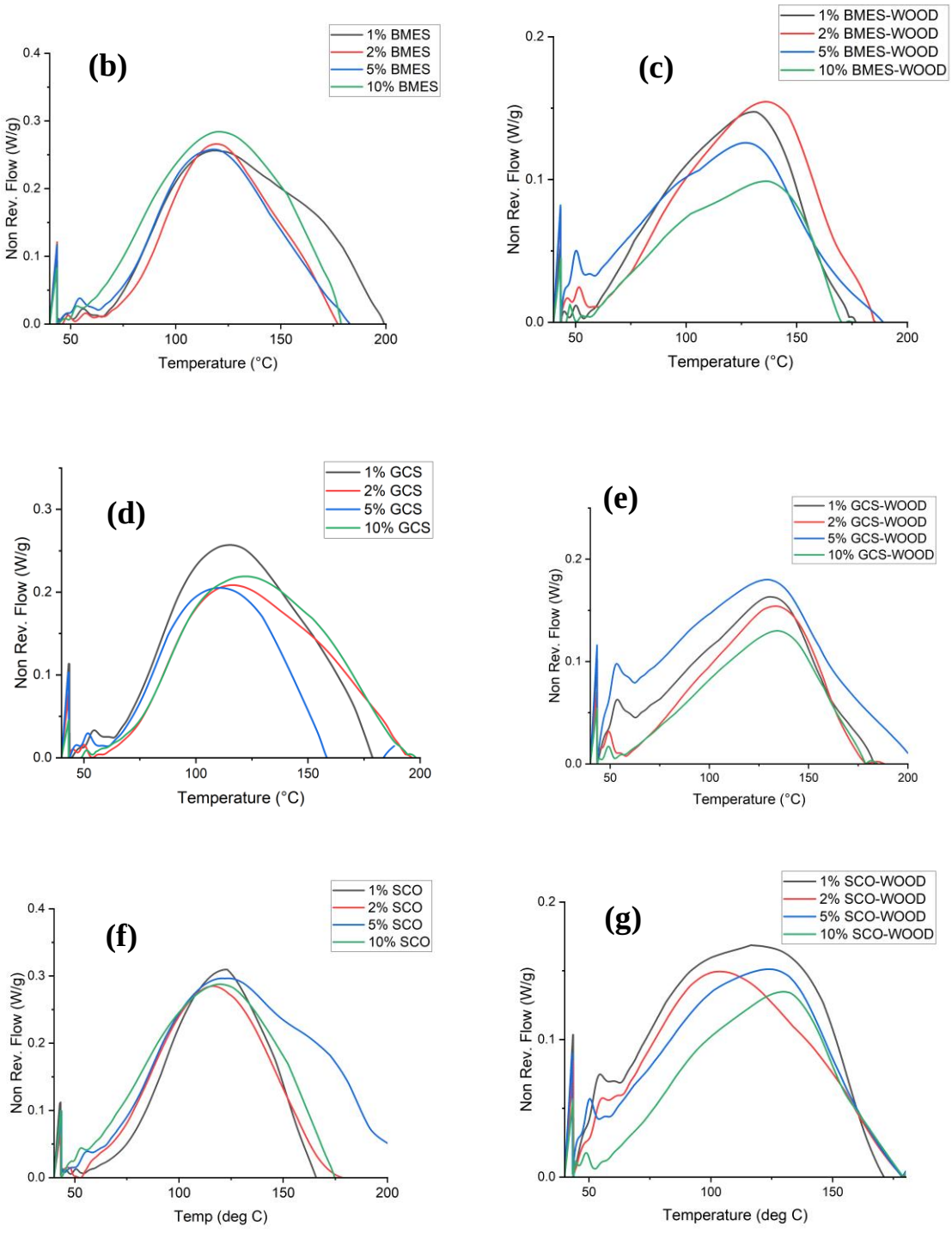

Figure 5:4: Non-reversible heat flow curves for (a) neat PRF, Wood-PRF control, 5 and 10% denim fiber wood PRF blends and (b) PRF-BMES modified resin and (c) Wood-PRF-BMES blends and (d) PRF-GCS modified blends and (e) Wood-PRF-GCS blends and (f) PRF-SCO modified blends and (g) Wood-SCO-PRF blends

Table 5.2: MDSC exothermic peak data for PRF-Wood/denim blends at 10 °C/min

Composition (%)	T_p (°C)	Enthalpy (ΔH (J/g))
Wood-PRF		
100 PRF	114 (±1)	77 (±13)
50 PRF	106 (±3)	19 (±5)
Denim blends		
5 DENIM	129 (±2)	41 (±4)
10 DENIM	121 (±5)	70 (±11)

Note: Standard deviation in parentheses

Table 5.3: MDSC exothermic peak data for BMES, GCS, and SCO modified PRF and wood-PRF blends at 10 °C/min

Main component	Modifier (%)	BMES		GCS		SCO	
		T_p (°C)	ΔH (J/g)	T_p (°C)	ΔH (J/g)	T_p (°C)	ΔH (J/g)
PRF	1	116 (±2)	111 (±21)	113 (±2)	116 (±36)	112 (±7)	46 (±25)
	2	117 (±1)	70 (±16)	117 (±1)	72 (±10)	116 (±1)	100 (±11)
	5	118 (±3)	111 (±16)	118 (±2)	110 (±22)	119 (±3)	94 (±24)
	10	120 (±3)	120 (±42)	123 (±1)	113 (±19)	120 (±3)	120 (±42)
Wood-PRF modifier blends							
Wood-PRF	1	129 (±1)	40 (±2)	128 (±1)	63 (±8)	122 (±3)	46 (±1)
	2	133 (±2)	51 (±3)	130 (±2)	54 (±3)	99 (±10)	44 (±4)
	5	134 (±3)	40 (±6)	127 (±1)	87 (±13)	124 (±2)	44 (±8)
	10	137 (±2)	42 (±15)	134 (±2)	63 (±11)	128 (±5)	47 (±8)

Note: Standard deviation in parentheses

Thermal stability of the cured PRF, modified PRF and mdofied PRF-wood blends were determined using TGA. The TGA and DTG curves of the cured blends are shown in Figure 5.5a to 5.5h. The T_{onset}, DTG max peak and residual weight at 800 °C and values for the TGA/DTG peaks are given in Table 5.5. The T_{onset} of neat PRF was at 300 °C and

decreased to 272 °C with the addition of 50% wood. With the presence of 5% and 10% denim the T_{onset} shifted to 281 and 282 °C, respectively. For PRF-BMES mixes, T_{onset} occurred from 282 °C to 328 °C, but reduced with the addition of wood fibers to 266 – 277 °C. A similar phenomenon was observed for the PRF-GCS blends with a T_{onset} of 252 – 260 °C and decreased in the presence of wood to 237 - 266 °C. The T_{onset} for the modified PRF mostly increased with increasing modifier content and wood content, except for wood-denim composites. Modified PRF samples had the highest residual weights from 44 to 59% in comparison to all modified wood-PRF blends with residual weight between 34 to 59%. This is because the cellulosic components of wood degrade at a lower temperature. The mass loss for modified PRF-wood blends increased with the addition of wood for all composite samples [469].

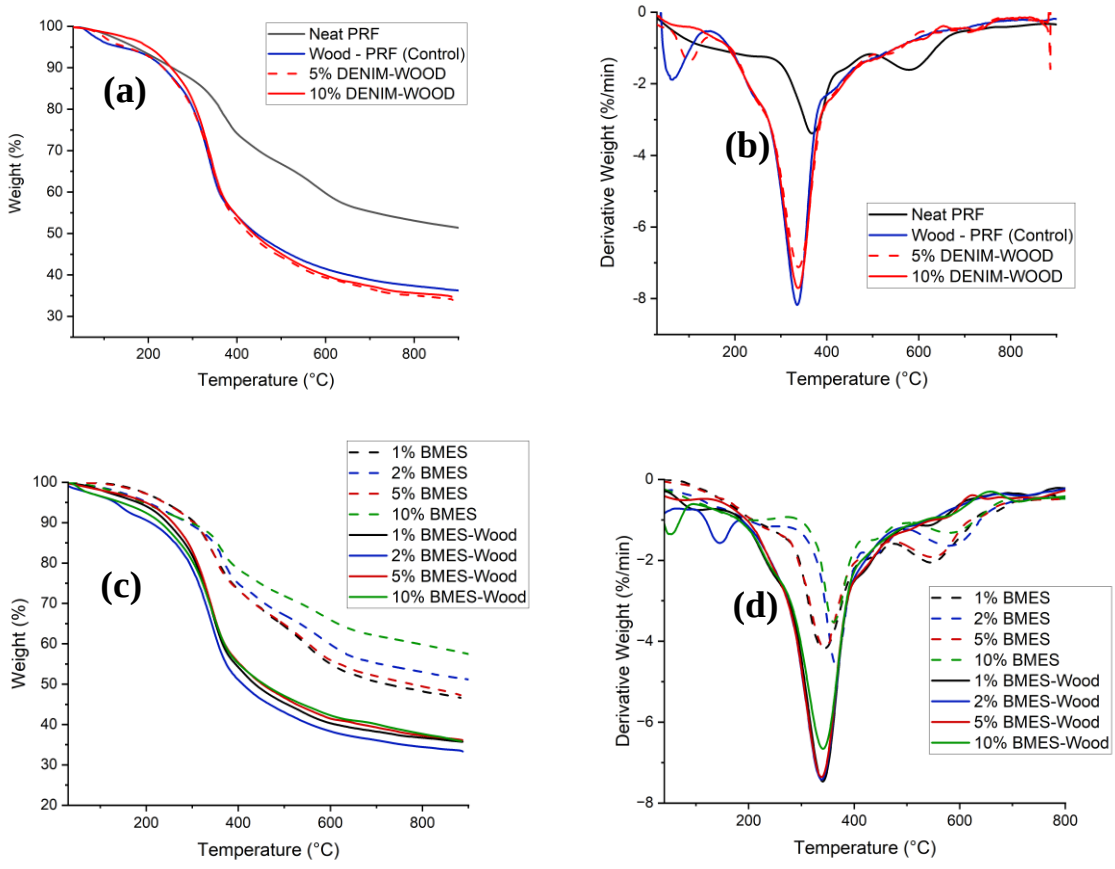

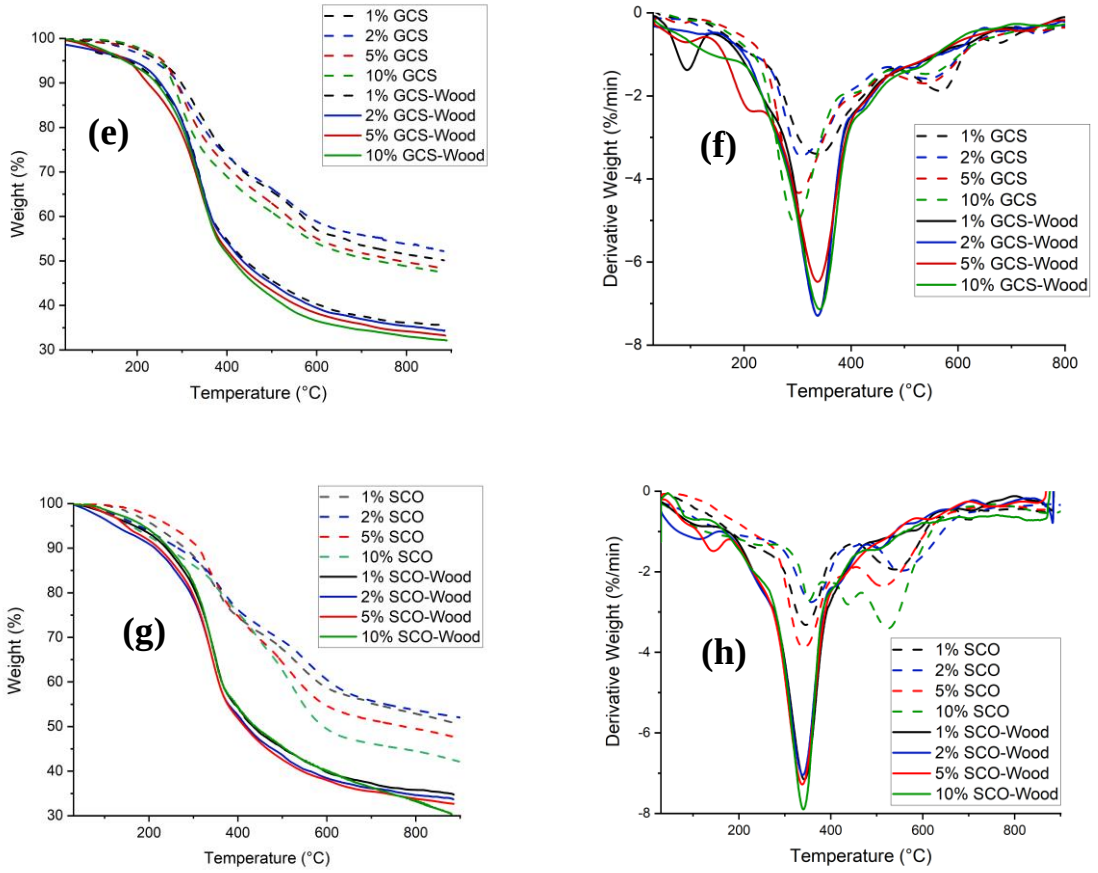

Figure 5.5: Thermograms showing (a) TGA and (b) DTG for neat PRF, wood-PRF (control), 5% and 10% denim blend; (c) TGA and (d) DTG for PRF-BMES and Wood-BMES-PRF blends; (e) TGA and (f) DTG for PRF-GCS and wood-PRF-GCS blends; (g) TGA and (h) DTG of PRF-SCO blends and Wood-PRF-SCO blends

From the DTG curves (Figure 5.5b,d,f,h), thermal degradation took place at different stages depending on the modifier used. In general, degradation occurred in three stages. The first stage was for components that degraded below 150 °C and associated with water and volatile components. For the wood-PRF modified blends with denim fibers which are cellulosic, degraded in the same range as wood between 200 °C and 500 °C [469]. Modified PRF with BMES showed two degradation peaks. The first major peak was because of the degradation of phenolic components while the second peak from 500 to 800 °C was due to calcium carbonate degradation. With the BMEs-PRF wood-blends, wood was seen to degrade (large DTG peak) between 250 °C and 450 °C. GCS modified PRF samples had

major DTG peaks that were shifted to lower temperatures due to starch and decomposition between 250 °C and 400 °C.

Table 5.4: TGA thermogram data (T_{onset}, min and max DTG peak, and residual weight at 800 °C) for unmodified and modified PRF and WPRF blends

Composition (%)	Major onset T_{onset} (°C)	Min and Max DTG Peak (°C)	Residual at 800°C (%)
PRF – BMES blends			
1% BMES	284 (±5)	344 (±4), 554 (±4)	48 (±2)
2% BMES	320 (±6)	362 (±7), 587 (±3)	54 (±1)
5% BMES	282 (±9)	347 (±7), 565 (±14)	49 (±0)
10% BMES	328 (±9)	361 (±7), 588 (±3)	59 (±2)
PRF – GCS blends			
1% GCS	253 (±7)	329 (±13), 562 (±9)	51 (±2)
2% GCS	260 (±5)	309 (±5), 552 (±8)	51 (±2)
5% GCS	255 (±1)	299 (±2.5), 554 (±0.7)	49 (±0.8)
10% GCS	252 (±6)	295 (±0.2), 558 (±1.4)	48 (±1.5)
PRF – SCO blends			
1% SCO	279 (±3)	345 (±0), 544 (±4)	52 (±4)
2% SCO	300 (±4)	357 (±1), 567 (±7)	51 (±2)
5% SCO	296 (±3)	336 (±3.4), 524 (±0.9)	50 (±1)
10% SCO	355 (±7)	354 (±10), 434 (±6.0)	44 (±1)
Wood-PRF BMES blends			
1% BMES	285 (±5)	339 (±2), 560 (±15)	37 (±1)
2% BMES	278 (±5)	338 (±0), 554 (±20)	35 (±1)
5% BMES	276 (±0)	338 (±1), 573 (±11)	38 (±1)
10% BMES	275 (52)	339 (±6), 558 (±37)	37 (±1)
Wood-PRF GCS blends			
1% GCS	260 (±8)	336 (±2), 606 (±2)	36 (±0)

Table 5.4 cont'd

2% GCS	266 (±0)	337 (±1), 579 (±3)	35 (±0)
5% GCS	237 (±1)	338 (±1), 663 (±6)	35 (±0)
10% GCS	262 (±3)	341 (±0), 537 (±8)	34 (±0)
Wood-PRF SCO blends			
1% SCO	279 (±8)	340 (±2), 540 (±69)	37 (±0)
2% SCO	276 (±6)	339 (±1), 556 (±38)	36 (±0)
5% SCO	283 (±2)	337 (±1), 553 (±43)	35 (±1)
10% SCO	291 (±6)	339 (±1), 471 (±38)	34 (±1)
Wood – PRF blends			
100% PRF	300 (±4)	362 (±2), 580 (±2)	51 (±3)
50% PRF	272 (±8)	336 (±2)	37 (±2)
5% DENIM	281 (±2)	338 (±1), 551 (±7)	36 (±1)
10% DENIM	282 (±7)	339 (±2), 537 (±1)	37 (±2)

Note: Standard deviation in parentheses

5.4.6. Extrusion

The extrudability of the various blended modified PRF-wood formulations were examined using a single screw extruder. Figure 5.6 shows extruded 10% BMES-PRF-wood, 10% SCO-PRF-wood and 10% GCS-PRF-wood formulations. All PRF-wood and modified PRF-wood formulations were successfully extruded into a rod and suitable for AM. However, extrusion of denim reinforced wood composites with 5% and 10% was not feasible and it clogged the die as well as screw-barrel. This is most likely due to the fiber length (3-5mm) and high aspect ratio of the denim fibers (100-130) which can be readily entangled thus making it difficult to process. Thermoset composites with long fibers will require a twin-screw extruder to compound and extrude the material for AM purposes.

Figure 5.6: Photographs of successful extrusion runs of wood-PRF blends with the addition of modifiers showing (a) 10% SCO and (b) 10% BMES and (c) 10% GCS composites

5.4.7. Flexural Properties

The flexural properties (FS and FM) of the modified PRF and composites prepared by compression molding were determined to establish possible applications (Figure 5.7). The FS for wood-PRF composites was 44 MPa and the FM was 3.6 GPa. Both the FS and FM of the wood-PRF composites increased with the addition of the modifiers BMES, GCS, SCO, and denim fibers. BMES-PRF-Wood composites had FS values between 56 MPa and 64 MPa, higher than the wood-PRF composites because of the reinforcing modifier. FM for the BMES-PRF-wood composites were between 3.9 GPa to 4.2 GPa. BMES has been shown to improve mechanical properties of composites even at low loadings when used as reinforcements and this has been observed in the literature [470], [458]. The mechanical properties of concrete were shown to improve with incorporation of egg shells [139]. The GCS modifier improved the PRF-wood composites FS and FM between 42 MPa to 58 MPa

and 3.2 GPa to 4.2 GPa, respectively. The modifier SCO also improved FS (41 MPa to 50 MPa) and FM (3.3 GPa to 3.9 GPa) of the wood-PRF composites. GCS-PRF-wood composites exhibited the highest FS (58 MPa) and FM amongst all other modifiers. The gelatinization properties of corn starch help to bind the wood fiber and PRF resin matrix contribute to the increased mechanical properties [471].

Wood-PRF composites incorporating denim fibers improved the FS to 53 MPa and FM of 3.7-3.9 GPa. The presence of long fibers mixed with the short wood fibers creates better mechanical properties because of the fiber entanglement and mechanical interlocking to enhance the composite properties [472], [430].

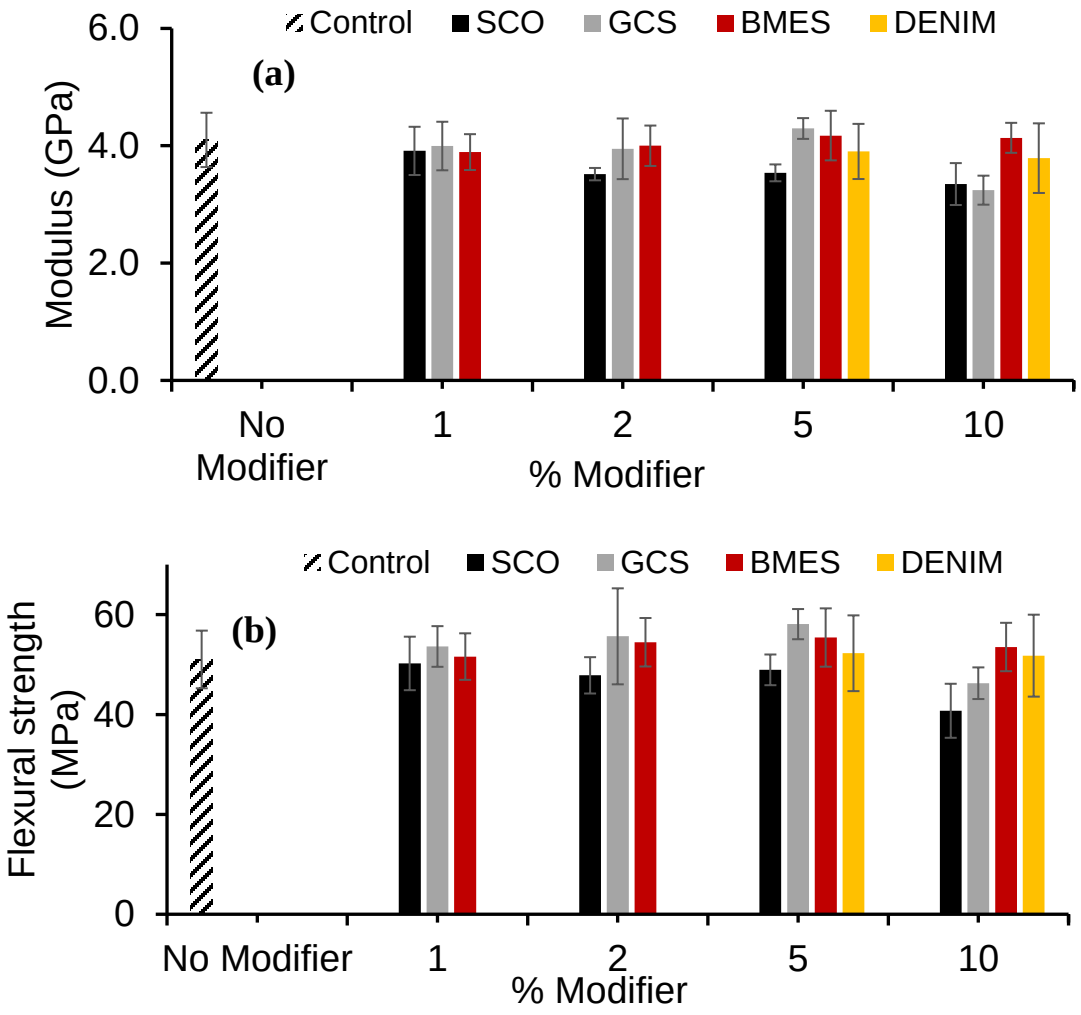

Figure 5.7: Flexural properties showing (a) modulus and (b) flexural strength for compression molded modified and unmodified wood-PRF composites

The extruded PRF-wood composite formulations were tested for their flexural properties (FS and FM) as shown in Figure 5.8. The FS and FM for the extruded wood-PRF composites were generally greater than the compression molded composites. The process of extrusion is likely to enhance the properties by improving the penetration of the resin into the wood fibers thus improved mechanical interlocking and stress transfer between the fiber and resin matrix [473], [474], [475]. For the extruded wood-PRF blends, have a FS of 65 MPa and FM of 5.5 GPa and these were 27% and 34% higher in comparison to the compression molded composites.

For the extruded wood-PRF-BMES samples, the FS were between 55 MPa and 68 MPa (10% BMES) having the highest FS in comparison to the other modified PRF-wood composites. FM values for the BMES modified PRF-wood composites were between 4 GPa (2% BMES) and 6 GPa (10% BMES). Increasing the amount of BMES improved the bonding between the fiber and matrix and thus better stress transfer from matrix to the fibers in the composites [476], [477].

The GCS modified PRF-wood composites had FS values between 58 MPa and 65 MPa and FM between 4.6 GPa and 4.9 GPa. FS (9-26%) and FM (9-44%) values were higher for the extruded composites as compared to the compression molded composites. GCS improved the extrudability (visual observation) of the PRF-wood mixture and easier to flow through the die and this phenomenon has been previously observed [478], [479].

SCO modified PRF-wood composites exhibited the lowest FS properties (45 MPa and 61 MPa) for the extruded blends in comparison to the other modifiers used. This is likely due to the SCO being a good emulsifier and lubricant. FS values were shown to reduce with SCO content. The FM were between 4.5 GPa and 4.8 GPa and these values were higher (15-45%) than the compression molded composites. .

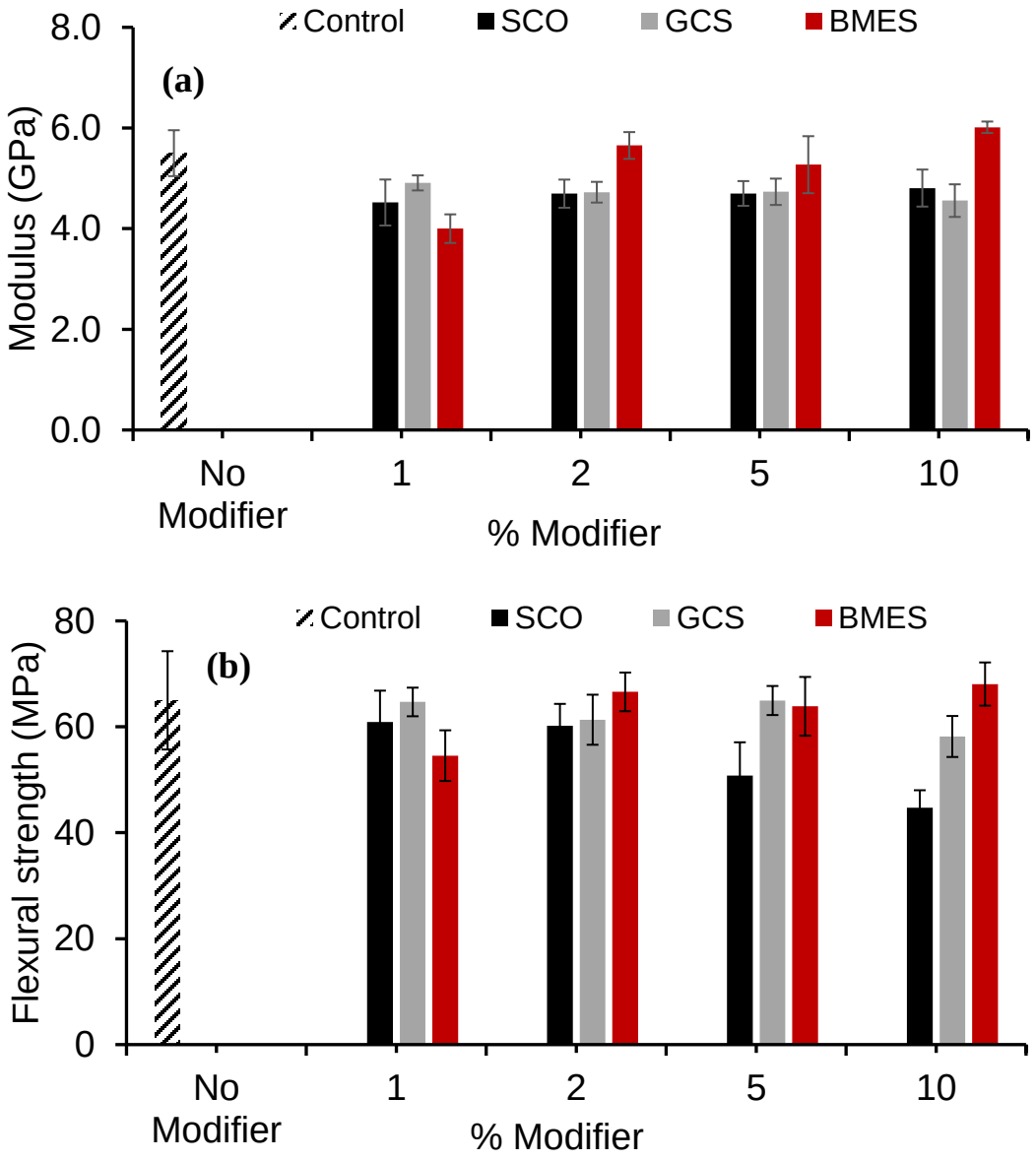

Figure 5.8: Flexural (a) modulus and (b) strength of extruded modified and unmodified PRF-wood composites

5.5. Conclusion

This study successfully modifed a PRF resin system with either BMES, GCS, SCO and reinforced it with 50 wt.% wood and denim fibers to form composite materials. Good shear thinning behaviors of the formulations were obtained via rheology for all PRF blends with and without reinforcemnt. Exothermic curing peak temperature from DSC for the modifed PRF blends was higher that the unmodified PRF sample. This also affected the

modified wood blends cause a shift to higher temperatures for all blends. The effect of the modifying agents was seen in the results of the mechanical properties of the cured samples. FS and FM increased for the compression molded modified PRF-wood blend in all cases. Thermal stability T_{onset} and residuals were optimal for modifed PRF wood composites and residuals reduced with the addition of wood. Extrusion of modified PRF-wood blends was successfully performed with all modifiers except for the denim fiber addition. Mechanical properties of the extruded modified PRF-wood composites were higher than the compression molded composites. This study is a proof of concept that modifiers improve the rheological (flowability), thermal and mechanical properties of PRF-wood composite systems and can be applied in AM applications.

5.6. Acknowledgment

The authors would like to acknowledge (i) the Idaho State Board of Education-Higher Education Research Council-IGEM award # IGEM 20-002 for their financial support, (ii) USDA-CSREES grant 2007-34158-17640 for support in the purchase of the DSC and, (iii) National Science Foundation award # 2119809 for their financial support.

Chapter 6: Conclusion, Limitations and Future Recommendations

6.1 Conclusion

From the stated objectives, and with the four detailed research projects in this dissertation, high filler loaded thermoset composites have been successfully fabricated and extruded for potential use in AM. Firstly, a geo-based binder SS was successfully used to fabricate composites with wood fiber reinforcements of different composites. Fabricated composites possessed good thermal, rheological and thermal stability properties which varied with wood content. Composites are extrudable and are currently being used in AM. Secondly, two commercially purchased thermosets; PRF and UF were used to produce composites using wood fiber as reinforcement. Curing kinetics of both resins in the presence of wood and without wood were successfully determined. PRF and its composites showed low curing peak temperatures with low kinetic parameters.in comparison to the UF and it composites. This validates the goal of the investigation for low energy thermosets. Thermal stability, flow properties and mechanical properties of the composites were also good. Thirdly, an alternative curing process for SS using CO_2 was successfully investigated. This was performed under different CO_2 pressure, time, particle size and curing temperatures. Data showed the significant effect of carbonation pressure, exposure time and particle size used on the mechanical properties of the cured blends. The use of low-cost modifiers of GCS, BMES and SCO were also successfully utilized in the flow optimization and mechanical properties of wood-PRF composites. Denim fibers were used as long fiber substitute for the wood in different percentages. Shear thinning properties were enhanced and suitable for extrusion. Feasible extrusion of these blends showed the workability of the modifiers with the wood and thermosets. Overall, there was a lot of research gap covered in this project with respect to the rheological, thermal, mechanical properties of thermosets and wood, denim fillers for use in future applications of AM.

6.2 Limitations and Future Recommendations

The use of thermosets for the fabrication of high filler loading composites in this study has covered some immense gap in research that has been shied away from, but a few

gaps will still need to be covered in future studies. Limitations to this area of study include, the absence of twin screw extruders specifically for compounding high filler loadings, and the availability of diverse binder options. Cold setting resins like PRF and geo-based resins of SS might have worked in this research, but the process cannot be applied to all types of resins or thermosets. In depth knowledge and research about other thermosets will have to be explored for a process like this. Controlled temperature environment for sensitive thermosets is essential for fast setting thermosets like PRF used in this study to avoid premature curing clogged extruder barrels.

Since PRF is a two-part resin system, a future recommendation would be to reduce the catalyst content to moderate the curing behavior and control the deposition rate of the extruded material. Biobased thermosets that have good properties can be mixed with PRF to obtain hybrid forms of the thermosets that will enhance the properties of the thermosets, and the composites fabricated. Other kinds of biobased or ecofriendly thermoset-like adhesives like SS should be considered for this type of study as well as other natural fibers and nano based reinforcements. Waste textiles are also a great option for reinforcement to help minimize waste. Integrating laboratory scale extruders to a 3D printer platform is the next step in understanding the AM process for these types of resin systems.

Comprehensive References

[1] N. Ayrilmis, M. Kariž, and M. Kitek Kuzman, “Effect of wood flour content on surface properties of 3D printed materials produced from wood flour/PLA filament,” *Int. J. Polym. Anal. Charact.*, vol. 24, no. 7, pp. 659–666, Oct. 2019, doi: 10.1080/1023666X.2019.1651547.

[2] J. Steenhuis and L. Pretorius, “ADDITIVE MANUFACTURING OR 3D PRINTING AND ITS ADOPTION,” *Conf. Proc.*, 2015.

[3] S. Adhikari and B. Ozarska, “Minimizing environmental impacts of timber products through the production process ‘From Sawmill to Final Products,’” *Environ. Syst. Res.*, vol. 7, no. 1, p. 6, Apr. 2018, doi: 10.1186/s40068-018-0109-x.

[4] “Wood and wood waste - U.S. Energy Information Administration (EIA).” https://www.eia.gov/energyexplained/biomass/wood-and-wood-waste.php (accessed Feb. 16, 2023).

[5] O. US EPA, “Wood: Material-Specific Data,” 2017. https://www.epa.gov/facts-and-figures-about-materials-waste-and-recycling/wood-material-specific-data (accessed Sep. 13, 2021).

[6] Q. Wang, J. Sun, Q. Yao, C. Ji, J. Liu, and Q. Zhu, “3D printing with cellulose materials,” *Cellulose*, vol. 25, no. 8, pp. 4275–4301, Aug. 2018, doi: 10.1007/s10570-018-1888-y.

[7] D. Krapež Tomec and M. Kariž, “Use of Wood in Additive Manufacturing: Review and Future Prospects,” *Polymers*, vol. 14, no. 6, p. 1174, Mar. 2022, doi: 10.3390/polym14061174.

[8] N. van de Werken, H. Tekinalp, P. Khanbolouki, S. Ozcan, A. Williams, and M. Tehrani, “Additively manufactured carbon fiber-reinforced composites: State of the art and perspective,” *Addit. Manuf.*, vol. 31, p. 100962, Jan. 2020, doi: 10.1016/j.addma.2019.100962.

[9] S. C. Daminabo, S. Goel, S. A. Grammatikos, H. Y. Nezhad, and V. K. Thakur, “Fused deposition modeling-based additive manufacturing (3D printing): techniques for polymer material systems,” *Mater. Today Chem.*, vol. 16, p. 100248, Jun. 2020, doi: 10.1016/j.mtchem.2020.100248.

[10] J. Trifol *et al.*, "3D-Printed Thermoset Biocomposites Based on Forest Residues by Delayed Extrusion of Cold Masterbatch (DECMA)," *ACS Sustain. Chem. Eng.*, vol. 9, no. 41, pp. 13979–13987, Oct. 2021, doi: 10.1021/acssuschemeng.1c05587.

[11] N. Nawafleh and E. Celik, "Additive manufacturing of short fiber reinforced thermoset composites with unprecedented mechanical performance," *Addit. Manuf.*, vol. 33, p. 101109, May 2020, doi: 10.1016/j.addma.2020.101109.

[12] A. Gholampour and T. Ozbakkaloglu, "A review of natural fiber composites: properties, modification and processing techniques, characterization, applications," *J. Mater. Sci.*, vol. 55, no. 3, pp. 829–892, Jan. 2020, doi: 10.1007/s10853-019-03990-y.

[13] O. Faruk, A. K. Bledzki, H.-P. Fink, and M. Sain, "Biocomposites reinforced with natural fibers: 2000–2010," *Prog. Polym. Sci.*, vol. 37, no. 11, pp. 1552–1596, Nov. 2012, doi: 10.1016/j.progpolymsci.2012.04.003.

[14] M. Mahmoudi, S. R. Burlison, S. Moreno, and M. Minary-Jolandan, "Additive-Free and Support-Free 3D Printing of Thermosetting Polymers with Isotropic Mechanical Properties," *ACS Appl. Mater. Interfaces*, vol. 13, no. 4, pp. 5529–5538, Feb. 2021, doi: 10.1021/acsami.0c19608.

[15] M. B. A. Tamez and I. Taha, "A review of additive manufacturing technologies and markets for thermosetting resins and their potential for carbon fiber integration," *Addit. Manuf.*, vol. 37, p. 101748, Jan. 2021, doi: 10.1016/j.addma.2020.101748.

[16] D. B. Miracle and S. L. Donaldson, "Introduction to Composites," Jan. 2001, doi: 10.31399/asm.hb.v21.a0003350.

[17] A. K. Sharma, R. Bhandari, A. Aherwar, and R. Rimašauskienė, "Matrix materials used in composites: A comprehensive study," *Mater. Today Proc.*, vol. 21, pp. 1559–1562, Jan. 2020, doi: 10.1016/j.matpr.2019.11.086.

[18] G. Mittal, K. Y. Rhee, V. Mišković-Stanković, and D. Hui, "Reinforcements in multi-scale polymer composites: Processing, properties, and applications," *Compos. Part B Eng.*, vol. 138, pp. 122–139, Apr. 2018, doi: 10.1016/j.compositesb.2017.11.028.

[19] A. Atmakuri, A. Palevicius, A. Vilkauskas, and G. Janusas, "Review of Hybrid Fiber Based Composites with Nano Particles—Material Properties and Applications," *Polymers*, vol. 12, no. 9, Art. no. 9, Sep. 2020, doi: 10.3390/polym12092088.

[20] E. Canedo, L. Carvalho, S. Farias Neto, and A. Lima, “Moisture Transport Process in Vegetable Fiber Composites: Theory and Analysis for Technological Applications,” 2013, pp. 37–62. doi: 10.1007/978-3-642-37469-2_2.

[21] V. Mazzanti, L. Malagutti, and F. Mollica, “FDM 3D Printing of Polymers Containing Natural Fillers: A Review of their Mechanical Properties,” *Polymers*, vol. 11, no. 7, Art. no. 7, Jul. 2019, doi: 10.3390/polym11071094.

[22] P. D. Pastuszak and A. Muc, “Application of Composite Materials in Modern Constructions,” *Key Eng. Mater.*, vol. 542, pp. 119–129, Feb. 2013, doi: 10.4028/www.scientific.net/KEM.542.119.

[23] N. Zobeiry, R. Vaziri, and A. Poursartip, “Computationally efficient pseudo-viscoelastic models for evaluation of residual stresses in thermoset polymer composites during cure,” *Compos. Part Appl. Sci. Manuf.*, vol. 41, no. 2, pp. 247–256, Feb. 2010, doi: 10.1016/j.compositesa.2009.10.009.

[24] Y. Min *et al.*, “Sonochemical Transformation of Epoxy–Amine Thermoset into Soluble and Reusable Polymers,” *Macromolecules*, vol. 48, no. 2, pp. 316–322, Jan. 2015, doi: 10.1021/ma501934p.

[25] S. Ma and D. C. Webster, “Degradable thermosets based on labile bonds or linkages: A review,” *Prog. Polym. Sci.*, vol. 76, pp. 65–110, Jan. 2018, doi: 10.1016/j.progpolymsci.2017.07.008.

[26] P. January 1 and 2010, “Thermosets: How to Avoid Incomplete Curing.” http://www.americanlaboratory.com/913-Technical-Articles/482-Thermosets-How-to-Avoid-Incomplete-Curing/ (accessed Feb. 19, 2023).

[27] E. Broitman, “Novel insights in polymer and composite materials,” *E-Polym.*, vol. 15, no. 5, pp. 285–286, Sep. 2015, doi: 10.1515/epoly-2015-0195.

[28] H. Standeven, “The Development of Decorative Gloss Paints in Britain and the United States C. 1910–1960,” *J. Am. Inst. Conserv.*, vol. 45, no. 1, pp. 51–65, Jan. 2006, doi: 10.1179/019713606806082210.

[29] E. Barr, “Degree of Cure in Thermosetting Resins,” *Ind. Eng. Chem.*, vol. 48, no. 1, pp. 72–74, Jan. 1956, doi: 10.1021/ie50553a024.

[30] N. R. Thomas, “Frederic Stanley Kipping—Pioneer in Silicon Chemistry: His Life & Legacy,” *Silicon*, vol. 2, no. 4, pp. 187–193, Oct. 2010, doi: 10.1007/s12633-010-9051-x.

[31] R. B. Seymour, “History of the Development and Growth of Thermosetting Polymers,” *J. Macromol. Sci. Part - Chem.*, vol. 15, no. 6, pp. 1165–1171, Apr. 1981, doi: 10.1080/00222338108066459.

[32] F.-L. Jin, X. Li, and S.-J. Park, “Synthesis and application of epoxy resins: A review,” *J. Ind. Eng. Chem.*, vol. 29, pp. 1–11, Sep. 2015, doi: 10.1016/j.jiec.2015.03.026.

[33] M. G. Wimmer and B. G. Compton, “Semi-solid epoxy feedstocks with high glass transition temperature for material extrusion additive manufacturing,” *Addit. Manuf.*, vol. 54, p. 102725, Jun. 2022, doi: 10.1016/j.addma.2022.102725.

[34] Y. Ming, S. Zhang, W. Han, B. Wang, Y. Duan, and H. Xiao, “Investigation on process parameters of 3D printed continuous carbon fiber-reinforced thermosetting epoxy composites,” *Addit. Manuf.*, vol. 33, p. 101184, May 2020, doi: 10.1016/j.addma.2020.101184.

[35] K. Liu *et al.*, “Additive manufacturing of traditional ceramic powder via selective laser sintering with cold isostatic pressing,” *Int. J. Adv. Manuf. Technol.*, vol. 90, no. 1, pp. 945–952, Apr. 2017, doi: 10.1007/s00170-016-9441-3.

[36] H. Dodiuk, *Handbook of Thermoset Plastics*. William Andrew, 2021.

[37] R. B. Durairaj, *Resorcinol: Chemistry, Technology and Applications*. Springer Science & Business Media, 2005.

[38] E. T. Zanoni, “Influence of resorcinol-formaldehyde molar ratio in the properties of Mesoporous Carbon Supports for PEMFC Catalysts,” Jan. 2020, Accessed: Feb. 20, 2023. [Online]. Available: https://www.academia.edu/44534954/Influence_of_resorcinol_formaldehyde_molar_ratio_in_the_properties_of_Mesoporous_Carbon_Supports_for_PEMFC_Catalysts

[39] T. Li, M. Cao, J. Liang, X. Xie, and G. Du, “Mechanism of Base-Catalyzed Resorcinol-Formaldehyde and Phenol-Resorcinol-Formaldehyde Condensation Reactions: A Theoretical Study,” *Polymers*, vol. 9, no. 9, p. E426, Sep. 2017, doi: 10.3390/polym9090426.

[40] E. Scopelitis and A. Pizzi, “The chemistry and development of branched PRF wood adhesives of low resorcinol content,” *J. Appl. Polym. Sci.*, vol. 47, no. 2, pp. 351–360, 1993, doi: 10.1002/app.1993.070470215.

[41] J. M. Ferra *et al.*, “Optimization of the Synthesis of Urea-Formaldehyde Resins using Response Surface Methodology,” *J. Adhes. Sci. Technol.*, vol. 24, no. 8–10, pp. 1454–1471, Jan. 2010, doi: 10.1163/016942410X501043.

[42] J. Li and Y. Zhang, “Morphology and Crystallinity of Urea-Formaldehyde Resin Adhesives with Different Molar Ratios,” *Polymers*, vol. 13, no. 5, Art. no. 5, Jan. 2021, doi: 10.3390/polym13050673.

[43] E. A. Publishers, *Proceedings of the Estonian Academy of Sciences, Chemistry*. Estonian Academy Publishers, 2006.

[44] M. Kariz, M. Sernek, and M. K. Kuzman, “Use of wood powder and adhesive as a mixture for 3D printing,” *Eur. J. Wood Wood Prod.*, vol. 74, no. 1, pp. 123–126, Jan. 2016, doi: 10.1007/s00107-015-0987-9.

[45] K. Pitt, O. Lopez-Botello, A. D. Lafferty, I. Todd, and K. Mumtaz, “Investigation into the material properties of wooden composite structures with in-situ fibre reinforcement using additive manufacturing,” *Compos. Sci. Technol.*, vol. 138, pp. 32–39, Jan. 2017, doi: 10.1016/j.compscitech.2016.11.008.

[46] A. Dotan, “15 - Biobased Thermosets,” in *Handbook of Thermoset Plastics (Third Edition)*, H. Dodiuk and S. H. Goodman, Eds., Boston: William Andrew Publishing, 2014, pp. 577–622. doi: 10.1016/B978-1-4557-3107-7.00015-4.

[47] S. Ma, T. Li, X. Liu, and J. Zhu, “Research progress on bio-based thermosetting resins: Research progress on bio-based thermosetting resins,” *Polym. Int.*, vol. 65, no. 2, pp. 164–173, Feb. 2016, doi: 10.1002/pi.5027.

[48] B. Çakmaklı, B. Hazer, İ. Ö. Tekin, and F. B. Cömert, “Synthesis and Characterization of Polymeric Soybean Oil-g-Methyl Methacrylate (and n-Butyl Methacrylate) Graft Copolymers: Biocompatibility and Bacterial Adhesion,” *Biomacromolecules*, vol. 6, no. 3, pp. 1750–1758, May 2005, doi: 10.1021/bm050063f.

[49] D. D. Andjelkovic, M. Valverde, P. Henna, F. Li, and R. C. Larock, “Novel thermosets prepared by cationic copolymerization of various vegetable oils—synthesis and their

structure–property relationships," *Polymer*, vol. 46, no. 23, pp. 9674–9685, Nov. 2005, doi: 10.1016/j.polymer.2005.08.022.

[50] Y. Xia, R. L. Quirino, and R. C. Larock, "Bio-based Thermosetting Polymers from Vegetable Oils," *J. Renew. Mater.*, vol. 1, no. 1, pp. 3–27, Jan. 2013, doi: 10.7569/JRM.2012.634103.

[51] C. Di Mauro, S. Malburet, A. Genua, A. Graillot, and A. Mija, "Sustainable Series of New Epoxidized Vegetable Oil-Based Thermosets with Chemical Recycling Properties," *Biomacromolecules*, vol. 21, no. 9, pp. 3923–3935, Sep. 2020, doi: 10.1021/acs.biomac.0c01059.

[52] J. Davidovits, *Geopolymer, Green Chemistry and Sustainable Development Solutions: Proceedings of the World Congress Geopolymer 2005*. Geopolymer Institute, 2005.

[53] J. Fiset, M. Cellier, and P. Y. Vuillaume, "Macroporous geopolymers designed for facile polymers post-infusion," *Cem. Concr. Compos.*, vol. 110, p. 103591, Jul. 2020, doi: 10.1016/j.cemconcomp.2020.103591.

[54] J. J. Chang, "A study on the setting characteristics of sodium silicate-activated slag pastes," *Cem. Concr. Res.*, vol. 33, no. 7, pp. 1005–1011, Jul. 2003, doi: 10.1016/S0008-8846(02)01096-7.

[55] A. A. Aliabdo, A. E. M. Abd Elmoaty, and H. A. Salem, "Effect of water addition, plasticizer and alkaline solution constitution on fly ash based geopolymer concrete performance," *Constr. Build. Mater.*, vol. 121, pp. 694–703, Sep. 2016, doi: 10.1016/j.conbuildmat.2016.06.062.

[56] M. H. Raza, R. Y. Zhong, and M. Khan, "Recent advances and productivity analysis of 3D printed geopolymers," *Addit. Manuf.*, vol. 52, p. 102685, Apr. 2022, doi: 10.1016/j.addma.2022.102685.

[57] M. Xia and J. Sanjayan, "Method of formulating geopolymer for 3D printing for construction applications," *Mater. Des.*, vol. 110, pp. 382–390, Nov. 2016, doi: 10.1016/j.matdes.2016.07.136.

[58] Z. Zhang and H. Wang, "22 - Alkali-activated cements for protective coating of OPC concrete," in *Handbook of Alkali-Activated Cements, Mortars and Concretes*, F. Pacheco-Torgal, J. A. Labrincha, C. Leonelli, A. Palomo, and P. Chindaprasirt, Eds.,

Oxford: Woodhead Publishing, 2015, pp. 605–626. doi: 10.1533/9781782422884.4.605.

[59] J. Davidovits and M. Davidovics, *"Geopolymer: Ultra-High Temperature Tooling Material for the Manufacture of Advanced Composites,"* vol. 36. 1991, p. 1949.

[60] A. Lazaro, G. Quercia, H. J. H. Brouwers, and J. W. Geus, "Synthesis of a Green Nano-Silica Material Using Beneficiated Waste Dunites and Its Application in Concrete," *World J. Nano Sci. Eng.*, vol. 3, no. 3, Art. no. 3, Sep. 2013, doi: 10.4236/wjnse.2013.33006.

[61] M. Xia and J. G. Sanjayan, "Methods of enhancing strength of geopolymer produced from powder-based 3D printing process," *Mater. Lett.*, vol. 227, pp. 281–283, Sep. 2018, doi: 10.1016/j.matlet.2018.05.100.

[62] K. Henke and S. Treml, "Wood based bulk material in 3D printing processes for applications in construction," *Eur. J. Wood Wood Prod.*, vol. 71, no. 1, pp. 139–141, Jan. 2013, doi: 10.1007/s00107-012-0658-z.

[63] Y. Wang *et al.*, "Rheology effect and enhanced thermal conductivity of diamond/metakaolin geopolymer fabricated by direct ink writing," *Rapid Prototyp. J.*, vol. 27, no. 5, pp. 837–850, Jan. 2021, doi: 10.1108/RPJ-06-2020-0124.

[64] M. Kaimonov, T. Safronova, T. Shatalova, Y. Filippov, I. Tikhomirova, and Y. Lukina, "Composite Ceramics Based on Pastes Including Tricalcium Phosphate and an Aqueous Solution of Sodium Silicate," *J. Compos. Sci.*, vol. 6, no. 9, Art. no. 9, Sep. 2022, doi: 10.3390/jcs6090267.

[65] C. Gao, J. Qiu, and S. Wang, "In-situ curing of 3D printed freestanding thermosets," *J. Adv. Manuf. Process.*, vol. 4, no. 3, p. e10114, 2022, doi: 10.1002/amp2.10114.

[66] D. Abliz, Y. Duan, L. Steuernagel, L. Xie, D. Li, and G. Ziegmann, "Curing Methods for Advanced Polymer Composites - A Review," *Polym. Polym. Compos.*, vol. 21, no. 6, pp. 341–348, Jul. 2013, doi: 10.1177/096739111302100602.

[67] D. Bomze, P. Knaack, T. Koch, H. Jin, and R. Liska, "Radical induced cationic frontal polymerization as a versatile tool for epoxy curing and composite production," *J. Polym. Sci. Part Polym. Chem.*, vol. 54, no. 23, pp. 3751–3759, 2016, doi: 10.1002/pola.28274.

[68] G. Coullerez, D. Léonard, S. Lundmark, and H. J. Mathieu, “XPS and ToF-SIMS study of freeze-dried and thermally cured melamine–formaldehyde resins of different molar ratios,” *Surf. Interface Anal.*, vol. 29, no. 7, pp. 431–443, 2000, doi: 10.1002/1096-9918(200007)29:7<431::AID-SIA886>3.0.CO;2-1.

[69] R. A. Haupt and T. Jr. Sellers, “Characterizations of Phenol-Formaldehyde Resol Resins,” *Ind. Eng. Chem. Res.*, vol. 33, no. 3, pp. 693–697, Mar. 1994, doi: 10.1021/ie00027a030.

[70] X. Xu *et al.*, “Stereolithography (SLA) 3D printing of an antihypertensive polyprintlet: Case study of an unexpected photopolymer-drug reaction,” *Addit. Manuf.*, vol. 33, p. 101071, May 2020, doi: 10.1016/j.addma.2020.101071.

[71] A. B. Kousaalya, “Sustainable Photo-curable Polymers in Additive Manufacturing Arena: A Review,” in *Sustainability & Green Polymer Chemistry Volume 1: Green Products and Processes*, in ACS Symposium Series, no. 1372, vol. 1372. American Chemical Society, 2020, pp. 89–98. doi: 10.1021/bk-2020-1372.ch005.

[72] J. N. Hay and P. O’Gara, “Recent developments in thermoset curing methods,” *Proc. Inst. Mech. Eng. Part G J. Aerosp. Eng.*, vol. 220, no. 3, pp. 187–195, Mar. 2006, doi: 10.1243/09544100JAERO35.

[73] A. Ribas-Massonis, M. Cicujano, J. Duran, E. Besalú, and A. Poater, “Free-Radical Photopolymerization for Curing Products for Refinish Coatings Market,” *Polymers*, vol. 14, no. 14, Art. no. 14, Jan. 2022, doi: 10.3390/polym14142856.

[74] G. Gershoni, Y. Gercci, H. Dodiuk, S. Kenig, and R. Tenne, “Chapter 19 - Radiation curing thermosets,” in *Handbook of Thermoset Plastics (Fourth Edition)*, H. Dodiuk, Ed., in Plastics Design Library. Boston: William Andrew Publishing, 2022, pp. 891–915. doi: 10.1016/B978-0-12-821632-3.00012-9.

[75] S. R. Chowdhury, *Radiation Technologies and Applications in Materials Science*. CRC Press, 2022.

[76] F. Y. C. Boey and S. K. Rath, “Microwave radiation curing of polymers: Using a temperature equivalent method for cure reaction analysis,” *Adv. Polym. Technol.*, vol. 19, no. 3, pp. 194–202, 2000, doi: 10.1002/1098-2329(200023)19:3<194::AID-ADV4>3.0.CO;2-1.

[77] M. Collinson, M. Bower, T. J. Swait, C. Atkins, S. Hayes, and B. Nuhiji, “Novel composite curing methods for sustainable manufacture: A review,” *Compos. Part C Open Access*, vol. 9, p. 100293, Oct. 2022, doi: 10.1016/j.jcomc.2022.100293.

[78] M. Smith, A. Payne, K. Edwards, S. Morris, B. Beckler, and R. L. Quirino, “Effect of Microwave Cure on the Thermo-Mechanical Properties of Tung Oil-Based/Carbon Nanotube Composites,” *Coatings*, vol. 5, no. 3, Art. no. 3, Sep. 2015, doi: 10.3390/coatings5030557.

[79] F. Y. C. Boey and B. H. Yap, “Microwave curing of an epoxy–amine system: effect of curing agent on the glass-transition temperature,” *Polym. Test.*, vol. 20, no. 8, pp. 837–845, Jan. 2001, doi: 10.1016/S0142-9418(00)00070-2.

[80] B. Herren, M. Charara, M. C. Saha, M. C. Altan, and Y. Liu, “Rapid Microwave Polymerization of Porous Nanocomposites with Piezoresistive Sensing Function,” *Nanomaterials*, vol. 10, no. 2, Art. no. 2, Feb. 2020, doi: 10.3390/nano10020233.

[81] W. R. Ashcroft, “Curing agents for epoxy resins,” in *Chemistry and Technology of Epoxy Resins*, B. Ellis, Ed., Dordrecht: Springer Netherlands, 1993, pp. 37–71. doi: 10.1007/978-94-011-2932-9_2.

[82] C. Acebo, X. Ramis, and A. Serra, “Improved epoxy thermosets by the use of poly(ethyleneimine) derivatives,” *Phys. Sci. Rev.*, vol. 2, no. 8, Aug. 2017, doi: 10.1515/psr-2016-0128.

[83] J.-C. Munoz, H. Ku, F. Cardona, and D. Rogers, “Effects of catalysts and post-curing conditions in the polymer network of epoxy and phenolic resins: Preliminary results,” *J. Mater. Process. Technol.*, vol. 202, no. 1, pp. 486–492, Jun. 2008, doi: 10.1016/j.jmatprotec.2007.10.025.

[84] H. Sukanto, W. W. Raharjo, D. Ariawan, J. Triyono, and M. Kaavesina, “Epoxy resins thermosetting for mechanical engineering,” *Open Eng.*, vol. 11, no. 1, pp. 797–814, Jan. 2021, doi: 10.1515/eng-2021-0078.

[85] K. Hęclik, J. Duliban, B. Dębska, and J. Lubczak, “Analysis of the Possibility and Conditions of Application of Methylene Blue to Determine the Activity of Radicals in Model System with Preaccelerated Cross-Linking of Polyester Resins,” *Int. J. Anal. Chem.*, vol. 2019, p. 2879869, Aug. 2019, doi: 10.1155/2019/2879869.

[86] Q. Mo *et al.*, “Study on Microwave Curing of Unsaturated Polyester Resin and Its Composites Containing Calcium Carbonate,” *Polymers*, vol. 14, no. 13, Art. no. 13, Jan. 2022, doi: 10.3390/polym14132598.

[87] W. Ashraf, “Carbonation of cement-based materials: Challenges and opportunities,” *Constr. Build. Mater.*, vol. 120, pp. 558–570, Sep. 2016, doi: 10.1016/j.conbuildmat.2016.05.080.

[88] N. Doğan-Sağlamtimur, “Waste Foundry Sand Usage for Building Material Production: A First Geopolymer Record in Material Reuse,” *Adv. Civ. Eng.*, vol. 2018, p. e1927135, May 2018, doi: 10.1155/2018/1927135.

[89] L. I. Solonenko, R. V. Usenko, K. I. Uzlov, A. V. Dziubina, and S. I. Repiakh, “Carbonization and Crushability of Structured Sand-Sodium-Silicate Mixtures,” *Natsionalnyi Hirnychyi Universytet Nauk. Visnyk*, no. 5, pp. 40–46, 2020, doi: 10.33271/nvngu/2020-5/040.

[90] Z. Liu and W. Meng, “Fundamental understanding of carbonation curing and durability of carbonation-cured cement-based composites: A review,” *J. CO2 Util.*, vol. 44, p. 101428, Feb. 2021, doi: 10.1016/j.jcou.2020.101428.

[91] D. Zhang, Z. Ghouleh, and Y. Shao, “Review on carbonation curing of cement-based materials,” *J. CO2 Util.*, vol. 21, pp. 119–131, Oct. 2017, doi: 10.1016/j.jcou.2017.07.003.

[92] P. Harirchi and M. Yang, “Exploration of Carbon Dioxide Curing of Low Reactive Alkali-Activated Fly Ash,” *Materials*, vol. 15, no. 9, Art. no. 9, Jan. 2022, doi: 10.3390/ma15093357.

[93] D. Zhang, X. Cai, and Y. Shao, “Carbonation Curing of Precast Fly Ash Concrete,” *J. Mater. Civ. Eng.*, vol. 28, no. 11, p. 04016127, Nov. 2016, doi: 10.1061/(ASCE)MT.1943-5533.0001649.

[94] S.-M. Park, J.-G. Jang, G.-M. Kim, and H.-K. Lee, “Strength Development of Alkali-Activated Fly Ash Exposed to a Carbon Dioxide-Rich Environment at an Early Age,” *J. Korean Ceram. Soc.*, vol. 53, no. 1, pp. 18–23, 2016, doi: 10.4191/kcers.2016.53.1.18.

[95] X. Pan, C. Shi, N. Farzadnia, X. Hu, and J. Zheng, “Properties and microstructure of CO2 surface treated cement mortars with subsequent lime-saturated water curing,”

Cem. Concr. Compos., vol. 99, pp. 89–99, May 2019, doi: 10.1016/j.cemconcomp.2019.03.006.

[96] V. W. Y. Tam, A. Butera, K. N. Le, and W. Li, "Utilising CO2 technologies for recycled aggregate concrete: A critical review," *Constr. Build. Mater.*, vol. 250, p. 118903, Jul. 2020, doi: 10.1016/j.conbuildmat.2020.118903.

[97] S. Monkman and M. MacDonald, "On carbon dioxide utilization as a means to improve the sustainability of ready-mixed concrete," *J. Clean. Prod.*, vol. 167, pp. 365–375, Nov. 2017, doi: 10.1016/j.jclepro.2017.08.194.

[98] S. Monkman, M. MacDonald, R. D. Hooton, and P. Sandberg, "Properties and durability of concrete produced using CO2 as an accelerating admixture," *Cem. Concr. Compos.*, vol. 74, pp. 218–224, Nov. 2016, doi: 10.1016/j.cemconcomp.2016.10.007.

[99] I. Mehdipour, G. Falzone, E. C. La Plante, D. Simonetti, N. Neithalath, and G. Sant, "How Microstructure and Pore Moisture Affect Strength Gain in Portlandite-Enriched Composites That Mineralize CO2," *ACS Sustain. Chem. Eng.*, vol. 7, no. 15, pp. 13053–13061, Aug. 2019, doi: 10.1021/acssuschemeng.9b02163.

[100] C. SHI, P. HE, Z. TU, and Z. CAO, "Effect of Preconditioning on Process and Microstructure of Carbon Dioxide Cured Concrete," *J. Chin. Ceram. Soc.*, vol. 42, no. 8, pp. 996–1004, Aug. 2014, doi: 10.7521/j.issn.04545648.2014.08.07.

[101] B. J. Zhan, D. X. Xuan, C. S. Poon, and C. J. Shi, "Effect of curing parameters on CO2 curing of concrete blocks containing recycled aggregates," *Cem. Concr. Compos.*, vol. 71, pp. 122–130, Aug. 2016, doi: 10.1016/j.cemconcomp.2016.05.002.

[102] X. Li and T.-C. Ling, "Instant CO2 curing for dry-mix pressed cement pastes: Consideration of CO2 concentrations coupled with further water curing," *J. CO2 Util.*, vol. 38, pp. 348–354, May 2020, doi: 10.1016/j.jcou.2020.02.012.

[103] L. Wang, L. Chen, J. L. Provis, D. C. W. Tsang, and C. S. Poon, "Accelerated carbonation of reactive MgO and Portland cement blends under flowing CO2 gas," *Cem. Concr. Compos.*, vol. 106, p. 103489, Feb. 2020, doi: 10.1016/j.cemconcomp.2019.103489.

[104] L. Liu, J. Ha, T. Hashida, and S. Teramura, "Development of a CO2 solidification method for recycling autoclaved lightweight concrete waste," *J. Mater. Sci. Lett.*, vol. 20, pp. 1791–1794, Jan. 2001, doi: 10.1023/A:1012591318077.

[105] B. Lu, S. Drissi, J. Liu, X. Hu, B. Song, and C. Shi, “Effect of temperature on CO2 curing, compressive strength and microstructure of cement paste,” *Cem. Concr. Res.*, vol. 157, p. 106827, Jul. 2022, doi: 10.1016/j.cemconres.2022.106827.

[106] X. Yang and X.-Y. Wang, “Strength and durability improvements of biochar-blended mortar or paste using accelerated carbonation curing,” *J. CO2 Util.*, vol. 54, p. 101766, Dec. 2021, doi: 10.1016/j.jcou.2021.101766.

[107] R. Hay and K. Celik, “Hydration, carbonation, strength development and corrosion resistance of reactive MgO cement-based composites,” *Cem. Concr. Res.*, vol. 128, p. 105941, Feb. 2020, doi: 10.1016/j.cemconres.2019.105941.

[108] D. Wang, J. Zhu, and F. He, “CO2 carbonation-induced improvement in strength and microstructure of reactive MgO-CaO-fly ash-solidified soils,” *Constr. Build. Mater.*, vol. 229, p. 116914, Dec. 2019, doi: 10.1016/j.conbuildmat.2019.116914.

[109] E. Grünhäuser Soares and J. Castro-Gomes, “Carbonation curing influencing factors of Carbonated Reactive Magnesia Cements (CRMC) – A review,” *J. Clean. Prod.*, vol. 305, p. 127210, Jul. 2021, doi: 10.1016/j.jclepro.2021.127210.

[110] B. G. Compton and J. A. Lewis, “3D-Printing of Lightweight Cellular Composites,” *Adv. Mater.*, vol. 26, no. 34, pp. 5930–5935, 2014, doi: 10.1002/adma.201401804.

[111] H. A. Pierson *et al.*, “Mechanical Properties of Printed Epoxy-Carbon Fiber Composites,” *Exp. Mech.*, vol. 59, no. 6, pp. 843–857, Jul. 2019, doi: 10.1007/s11340-019-00498-z.

[112] V. Marturano, P. Cerruti, and V. Ambrogi, “Polymer additives,” *Phys. Sci. Rev.*, vol. 2, no. 6, Jun. 2017, doi: 10.1515/psr-2016-0130.

[113] C. M. Hansen, “Polymer additives and solubility parameters,” *Prog. Org. Coat.*, vol. 51, no. 2, pp. 109–112, Nov. 2004, doi: 10.1016/j.porgcoat.2004.05.003.

[114] P. D. Bloom, K. G. Baikerikar, J. U. Otaigbe, and V. V. Sheares, “Development of novel polymer/quasicrystal composite materials,” *Mater. Sci. Eng. A*, vol. 294–296, pp. 156–159, Dec. 2000, doi: 10.1016/S0921-5093(00)01230-2.

[115] M. R. Saeb *et al.*, “Biowaste chicken eggshell powder as a potential cure modifier for epoxy/anhydride systems: competitiveness with terpolymer-modified calcium carbonate at low loading levels,” *RSC Adv.*, vol. 7, no. 4, pp. 2218–2230, Jan. 2017, doi: 10.1039/C6RA24772E.

[116] E. Nolasco *et al.*, “Application of Dried Egg White to Enhance the Textural Properties of Fresh and Frozen Pancakes,” *ES Food Agrofor.*, vol. Volume 2 (December 2020), no. 0, pp. 50–57, Dec. 2020.

[117] P. Jagadeesh, M. Puttegowda, Y. G. Thyavihalli Girijappa, S. M. Rangappa, and S. Siengchin, “Effect of natural filler materials on fiber reinforced hybrid polymer composites: An Overview,” *J. Nat. Fibers*, vol. 19, no. 11, pp. 4132–4147, Nov. 2022, doi: 10.1080/15440478.2020.1854145.

[118] D. A. Oliveira, P. Benelli, and E. R. Amante, “A literature review on adding value to solid residues: egg shells,” *J. Clean. Prod.*, vol. 46, pp. 42–47, May 2013, doi: 10.1016/j.jclepro.2012.09.045.

[119] S. Kowshik, S. Sharma, S. Rao, M. Shettar, and P. Hiremath, “Mechanical Properties of Post-Cured Eggshell-Filled Glass-Fibre-Reinforced Polymer Composites,” *J. Compos. Sci.*, vol. 7, no. 2, Art. no. 2, Feb. 2023, doi: 10.3390/jcs7020049.

[120] P. Johnson, P. B. Aurtherson, R. Suthan, and S. Madhu, “Experimental investigation of pineapple fiber and calcinated poultry egg shell powder epoxy composites,” *Biomass Convers. Biorefinery*, Dec. 2022, doi: 10.1007/s13399-022-03609-4.

[121] G. S. Sivagnanamani, S. R. Begum, R. Siva, and M. S. Kumar, “Experimental Investigation on Influence of Waste Egg Shell Particles on Polylactic Acid Matrix for Additive Manufacturing Application,” *J. Mater. Eng. Perform.*, vol. 31, no. 5, pp. 3471–3480, May 2022, doi: 10.1007/s11665-021-06464-y.

[122] B. Ashok Kumar *et al.*, “Study on the mechanical properties of a hybrid polymer composite using egg shell powder based bio-filler,” *Mater. Today Proc.*, vol. 69, pp. 679–683, Jan. 2022, doi: 10.1016/j.matpr.2022.07.114.

[123] S. I. Biscaia, T. F. Viana, H. A. Almeida, and P. J. Bártolo, “Production and Characterisation of PCL/ES Scaffolds for Bone Tissue Engineering,” *Mater. Today Proc.*, vol. 2, no. 1, pp. 208–216, Jan. 2015, doi: 10.1016/j.matpr.2015.04.024.

[124] F. A. Abdulla, M. S. Qasim, and A. A. F. Ogaili, “Influence Eggshells powder additive on thermal stress of fiberglass/polyester composite tubes,” *IOP Conf. Ser. Earth Environ. Sci.*, vol. 877, no. 1, p. 012039, Nov. 2021, doi: 10.1088/1755-1315/877/1/012039.

[125] H. Mutlu and M. A. R. Meier, “Castor oil as a renewable resource for the chemical industry,” *Eur. J. Lipid Sci. Technol.*, vol. 112, no. 1, pp. 10–30, 2010, doi: 10.1002/ejlt.200900138.

[126] R. Verhé and C. V. Stevens, *Renewable Bioresources: Scope and Modification for Non-Food Applications*. John Wiley & Sons, 2004.

[127] B. Liang, R. Li, C. Zhang, Z. Yang, and T. Yuan, “Synthesis and characterization of a novel tri-functional bio-based methacrylate prepolymer from castor oil and its application in UV-curable coatings,” *Ind. Crops Prod.*, vol. 135, pp. 170–178, Sep. 2019, doi: 10.1016/j.indcrop.2019.04.039.

[128] F. J. Kremers, “The sulfonation of castor oil with sulfur trioxide,” *J. Am. Oil Chem. Soc.*, vol. 48, no. 7, pp. 314–317, Jul. 1971, doi: 10.1007/BF02890753.

[129] F. C. Naughton, “Production, chemistry, and commercial applications of various chemicals from castor oil,” *J. Am. Oil Chem. Soc.*, vol. 51, no. 3, pp. 65–71, Mar. 1974, doi: 10.1007/BF00000015.

[130] D. Kania, R. Yunus, R. Omar, S. Abdul Rashid, and B. Mohamad Jan, “A review of biolubricants in drilling fluids: Recent research, performance, and applications,” *J. Pet. Sci. Eng.*, vol. 135, pp. 177–184, Nov. 2015, doi: 10.1016/j.petrol.2015.09.021.

[131] H. Wen, Y. Wang, H. Zhu, L. Jin, and F. Zhang, “A Fluorescent Tracer Based on Castor Oil for Monitoring the Mass Transfer of Fatliquoring Agent in Leather,” *Materials*, vol. 15, no. 3, Art. no. 3, Jan. 2022, doi: 10.3390/ma15031167.

[132] R. N. Darie-Niță *et al.*, “Evaluation of Natural and Modified Castor Oil Incorporation on the Melt Processing and Physico-Chemical Properties of Polylactic Acid,” *Polymers*, vol. 14, no. 17, Art. no. 17, Jan. 2022, doi: 10.3390/polym14173608.

[133] A. Farhadian *et al.*, “Sulfonated Castor Oil as an Efficient Biosurfactant for Improving Methane Storage in Clathrate Hydrates,” *ACS Sustain. Chem. Eng.*, vol. 10, no. 30, pp. 9921–9932, Aug. 2022, doi: 10.1021/acssuschemeng.2c02329.

[134] J. Domínguez-Robles *et al.*, “Antioxidant PLA Composites Containing Lignin for 3D Printing Applications: A Potential Material for Healthcare Applications,” *Pharmaceutics*, vol. 11, no. 4, Art. no. 4, Apr. 2019, doi: 10.3390/pharmaceutics11040165.

[135] J. Singh, O. J. McCarthy, H. Singh, P. J. Moughan, and L. Kaur, “Morphological, thermal and rheological characterization of starch isolated from New Zealand Kamo Kamo (Cucurbita pepo) fruit – A novel source,” *Carbohydr. Polym.*, vol. 67, no. 2, pp. 233–244, Jan. 2007, doi: 10.1016/j.carbpol.2006.05.021.

[136] N. V. Patil and A. N. Netravali, “Nonedible Starch Based ‘Green’ Thermoset Resin Obtained via Esterification Using a Green Catalyst,” *ACS Sustain. Chem. Eng.*, vol. 4, no. 3, pp. 1756–1764, Mar. 2016, doi: 10.1021/acssuschemeng.5b01740.

[137] P. Bajpai, “Chapter 3 - Properties of biobased packaging material,” in *Biobased Polymers*, P. Bajpai, Ed., Elsevier, 2019, pp. 25–111. doi: 10.1016/B978-0-12-818404-2.00003-5.

[138] *Chemical Properties of Starch*. BoD – Books on Demand, 2020.

[139] A. Guleria, A. S. Singha, and R. K. Rana, “Preparation of starch-based biocomposites reinforced with mercerized lignocellulosic fibers: Evaluation of their thermal, morphological, mechanical, and biodegradable properties,” *Int. J. Polym. Anal. Charact.*, vol. 22, no. 7, pp. 595–609, Oct. 2017, doi: 10.1080/1023666X.2017.1345558.

[140] Y. Wang, H. Li, X. Wang, H. Lei, and J. Huo, “Chemical modification of starch with epoxy resin to enhance the interfacial adhesion of epoxy-based glass fiber composites,” *RSC Adv.*, vol. 6, no. 87, pp. 84187–84193, 2016, doi: 10.1039/C6RA18347F.

[141] N. Supanchaiyamat, A. J. Hunt, P. S. Shuttleworth, C. Ding, J. H. Clark, and A. S. Matharu, “Bio-based thermoset composites from epoxidised linseed oil and expanded starch,” *RSC Adv.*, vol. 4, no. 44, pp. 23304–23313, 2014, doi: 10.1039/C4RA03935A.

[142] Y. Ai and J. Jane, “Gelatinization and rheological properties of starch,” *Starch - Stärke*, vol. 67, no. 3–4, pp. 213–224, 2015, doi: 10.1002/star.201400201.

[143] Z. Wang, H. Lv, and Y. Yang, “Mechanical properties of epoxy resin toughened with cornstarch,” *E-Polym.*, vol. 22, no. 1, pp. 851–857, Jan. 2022, doi: 10.1515/epoly-2022-0075.

[144] Y. Cheng *et al.*, “Effect of molecular structure changes during starch gelatinization on its rheological and 3D printing properties,” *Food Hydrocoll.*, vol. 137, p. 108364, Apr. 2023, doi: 10.1016/j.foodhyd.2022.108364.

[145] V. K. Balla, K. H. Kate, J. Satyavolu, P. Singh, and J. G. D. Tadimeti, “Additive manufacturing of natural fiber reinforced polymer composites: Processing and prospects,” *Compos. Part B Eng.*, vol. 174, p. 106956, Oct. 2019, doi: 10.1016/j.compositesb.2019.106956.

[146] M. Ziaee, J. W. Johnson, and M. Yourdkhani, “3D Printing of Short-Carbon-Fiber-Reinforced Thermoset Polymer Composites via Frontal Polymerization,” *ACS Appl. Mater. Interfaces*, vol. 14, no. 14, pp. 16694–16702, Apr. 2022, doi: 10.1021/acsami.2c02076.

[147] R. Temmink, B. Baghaei, and M. Skrifvars, “Development of biocomposites from denim waste and thermoset bio-resins for structural applications,” *Compos. Part Appl. Sci. Manuf.*, vol. 106, pp. 59–69, Mar. 2018, doi: 10.1016/j.compositesa.2017.12.011.

[148] C. H. Lee *et al.*, “The Challenges and Future Perspective of Woven Kenaf Reinforcement in Thermoset Polymer Composites in Malaysia: A Review,” *Polymers*, vol. 13, no. 9, Art. no. 9, Jan. 2021, doi: 10.3390/polym13091390.

[149] H. Singh, J. Inder Preet Singh, S. Singh, V. Dhawan, and S. Kumar Tiwari, “A Brief Review of Jute Fibre and Its Composites,” *Mater. Today Proc.*, vol. 5, no. 14, Part 2, pp. 28427–28437, Jan. 2018, doi: 10.1016/j.matpr.2018.10.129.

[150] X. He *et al.*, “3D printing of continuous fiber-reinforced thermoset composites,” *Addit. Manuf.*, vol. 40, p. 101921, Apr. 2021, doi: 10.1016/j.addma.2021.101921.

[151] W. Zhong, F. Li, Z. Zhang, L. Song, and Z. Li, “Short fiber reinforced composites for fused deposition modeling,” *Mater. Sci. Eng. A*, vol. 301, no. 2, pp. 125–130, Mar. 2001, doi: 10.1016/S0921-5093(00)01810-4.

[152] Z. Zhang *et al.*, “Direct writing of continuous carbon fibers/epoxy thermoset composites with high-strength and low energy-consumption,” *Addit. Manuf.*, vol. 47, p. 102348, Nov. 2021, doi: 10.1016/j.addma.2021.102348.

[153] A. Sarmah *et al.*, “Additive manufacturing of nanotube-loaded thermosets via direct ink writing and radio-frequency heating and curing,” *Carbon*, vol. 200, pp. 307–316, Nov. 2022, doi: 10.1016/j.carbon.2022.08.063.

[154] G. Bogoeva-Gaceva *et al.*, “Natural Fiber Eco-Composites,” *Polym. Compos.*, vol. 28, pp. 98–107, Feb. 2007, doi: 10.1002/pc.20270.

[155] H. T. N. Kuan, M. Y. Tan, Y. Shen, and Mohd. Y. Yahya, “Mechanical properties of particulate organic natural filler-reinforced polymer composite: A review,” *Compos. Adv. Mater.*, vol. 30, p. 26349833211007504, Jan. 2021, doi: 10.1177/26349833211007502.

[156] F. M. Monticeli, R. M. Neves, H. L. Ornaghi Jr, and J. H. S. Almeida Jr, “A systematic review on high-performance fiber-reinforced 3D printed thermoset composites,” *Polym. Compos.*, vol. 42, no. 8, pp. 3702–3715, 2021, doi: 10.1002/pc.26133.

[157] Z. Li *et al.*, “Glass Fiber-Reinforced Phenol Formaldehyde Resin-Based Electrical Insulating Composites Fabricated by Selective Laser Sintering,” *Polymers*, vol. 11, no. 1, Art. no. 1, Jan. 2019, doi: 10.3390/polym11010135.

[158] H. Dieringa and K. Kainer, “Dieringa, H., Kainer, K.U.: Magnesium Matrix Composites: State-of-the-art and whats the future; Adv. Mat. Research 410 (2012) 275-278,” *Adv. Mater. Res.*, vol. 410, pp. 275–278, Jan. 2012, doi: 10.4028/www.scientific.net/AMR.410.275.

[159] Y. Yuan *et al.*, “Influences of particle content, size and particle/matrix bonding strength on the gas transmission coefficient of carbon fiber reinforced epoxy,” *Compos. Sci. Technol.*, vol. 216, p. 109071, Nov. 2021, doi: 10.1016/j.compscitech.2021.109071.

[160] S.-Y. Fu, X.-Q. Feng, B. Lauke, and Y.-W. Mai, “Effects of particle size, particle/matrix interface adhesion and particle loading on mechanical properties of particulate–polymer composites,” *Compos. Part B Eng.*, vol. 39, no. 6, pp. 933–961, Sep. 2008, doi: 10.1016/j.compositesb.2008.01.002.

[161] M. Zamanian, M. Mortezaei, B. Salehnia, and J. E. Jam, “Fracture toughness of epoxy polymer modified with nanosilica particles: Particle size effect,” *Eng. Fract. Mech.*, vol. 97, pp. 193–206, Jan. 2013, doi: 10.1016/j.engfracmech.2012.10.027.

[162] B. Lauke, “On the effect of particle size on fracture toughness of polymer composites,” *Compos. Sci. Technol.*, vol. 68, no. 15, pp. 3365–3372, Dec. 2008, doi: 10.1016/j.compscitech.2008.09.011.

[163] B. S. Hayes and J. C. Seferis, “Modification of thermosetting resins and composites through preformed polymer particles: A review,” *Polym. Compos.*, vol. 22, no. 4, pp. 451–467, 2001, doi: 10.1002/pc.10551.

[164] A. Zhakeyev, P. Wang, L. Zhang, W. Shu, H. Wang, and J. Xuan, “Additive Manufacturing: Unlocking the Evolution of Energy Materials,” *Adv. Sci.*, vol. 4, no. 10, p. 1700187, 2017, doi: 10.1002/advs.201700187.

[165] I. Chiulan, A. N. Frone, C. Brandabur, and D. M. Panaitescu, “Recent Advances in 3D Printing of Aliphatic Polyesters,” *Bioengineering*, vol. 5, no. 1, Art. no. 1, Mar. 2018, doi: 10.3390/bioengineering5010002.

[166] B. Hong, K. Wang, and P. Gu, “Cold Spray-Based Additive Manufacturing of Thermosets,” *J. Therm. Spray Technol.*, vol. 31, no. 7, pp. 2003–2012, Oct. 2022, doi: 10.1007/s11666-022-01428-7.

[167] J. Dilag, T. Chen, S. Li, and S. A. Bateman, “Design and direct additive manufacturing of three-dimensional surface micro-structures using material jetting technologies,” *Addit. Manuf.*, vol. 27, pp. 167–174, May 2019, doi: 10.1016/j.addma.2019.01.009.

[168] D. Gilmer *et al.*, “An in-situ crosslinking binder for binder jet additive manufacturing,” *Addit. Manuf.*, vol. 35, p. 101341, Oct. 2020, doi: 10.1016/j.addma.2020.101341.

[169] E. D. Bain, “Polymer Powder Bed Fusion Additive Manufacturing: Recent Developments in Materials, Processes, and Applications,” in *Polymer-Based Additive Manufacturing: Recent Developments*, in ACS Symposium Series, no. 1315, vol. 1315. American Chemical Society, 2019, pp. 7–36. doi: 10.1021/bk-2019-1315.ch002.

[170] Y. Liu and T.-W. Chou, “Additive manufacturing of multidirectional preforms and composites: from three-dimensional to four-dimensional,” *Mater. Today Adv.*, vol. 5, p. 100045, Mar. 2020, doi: 10.1016/j.mtadv.2019.100045.

[171] J. Gonzalez-Gutierrez, S. Cano, S. Schuschnigg, C. Kukla, J. Sapkota, and C. Holzer, “Additive Manufacturing of Metallic and Ceramic Components by the Material Extrusion of Highly-Filled Polymers: A Review and Future Perspectives.,” *Mater. Basel Switz.*, vol. 11, no. 5, p. E840, May 2018, doi: 10.3390/ma11050840.

[172] M. Rosenthal, C. Henneberger, A. Gutkes, and C.-T. Bues, “Liquid Deposition Modeling: a promising approach for 3D printing of wood,” *Eur. J. Wood Wood Prod.*, vol. 76, no. 2, pp. 797–799, Mar. 2018, doi: 10.1007/s00107-017-1274-8.

[173] M. Invernizzi, G. Natale, M. Levi, S. Turri, and G. Griffini, “UV-Assisted 3D Printing of Glass and Carbon Fiber-Reinforced Dual-Cure Polymer Composites,” *Materials*, vol. 9, no. 7, Art. no. 7, Jul. 2016, doi: 10.3390/ma9070583.

[174] A. K. Sinha, H. K. Narang, and S. Bhattacharya, “Mechanical properties of hybrid polymer composites: a review,” *J. Braz. Soc. Mech. Sci. Eng.*, vol. 42, no. 8, p. 431, Jul. 2020, doi: 10.1007/s40430-020-02517-w.

[175] V. Arumuga prabu, M. Uthayakumar, V. Manikandan, N. Rajini, and P. Jeyaraj, “Influence of redmud on the mechanical, damping and chemical resistance properties of banana/polyester hybrid composites,” *Mater. Des.*, vol. 64, pp. 270–279, Dec. 2014, doi: 10.1016/j.matdes.2014.07.020.

[176] J. S. S. Neto, H. F. M. de Queiroz, R. A. A. Aguiar, and M. D. Banea, “A Review on the Thermal Characterisation of Natural and Hybrid Fiber Composites,” *Polymers*, vol. 13, no. 24, Art. no. 24, Jan. 2021, doi: 10.3390/polym13244425.

[177] A. Veerasimman *et al.*, “Thermal Properties of Natural Fiber Sisal Based Hybrid Composites – A Brief Review,” *J. Nat. Fibers*, vol. 19, no. 12, pp. 4696–4706, Dec. 2022, doi: 10.1080/15440478.2020.1870619.

[178] Z. Li, X. Zhang, S. Song, K. Xu, J. Lyu, and X. Li, “Curing characteristics of low molecular weight melamine-urea–formaldehyde (MUF) resin-impregnated poplar wood,” *Constr. Build. Mater.*, vol. 325, p. 126814, Mar. 2022, doi: 10.1016/j.conbuildmat.2022.126814.

[179] A. Yousefi, P. G. Lafleur, and R. Gauvin, “Kinetic studies of thermoset cure reactions: A review,” *Polym. Compos.*, vol. 18, no. 2, pp. 157–168, Apr. 1997, doi: 10.1002/pc.10270.

[180] M. Jouyandeh, S. M. R. Paran, A. Jannesari, D. Puglia, and M. R. Saeb, “Protocol for nonisothermal cure analysis of thermoset composites,” *Prog. Org. Coat.*, vol. 131, pp. 333–339, Jun. 2019, doi: 10.1016/j.porgcoat.2019.02.040.

[181] M. Carrier *et al.*, “Thermogravimetric analysis as a new method to determine the lignocellulosic composition of biomass,” *Biomass Bioenergy*, vol. 35, no. 1, pp. 298–307, Jan. 2011, doi: 10.1016/j.biombioe.2010.08.067.

[182] M. Asim *et al.*, “Thermal stability of natural fibers and their polymer composites,” *Iran. Polym. J.*, vol. 29, no. 7, pp. 625–648, Jul. 2020, doi: 10.1007/s13726-020-00824-6.

[183] J. C. Domínguez, “Rheology and curing process of thermosets,” in *Thermosets*, Elsevier, 2018, pp. 115–146. doi: 10.1016/B978-0-08-101021-1.00004-6.

[184] Z. Jiang, B. Diggle, M. L. Tan, J. Viktorova, C. W. Bennett, and L. A. Connal, “Extrusion 3D Printing of Polymeric Materials with Advanced Properties,” *Adv. Sci.*, vol. 7, no. 17, p. 2001379, 2020, doi: 10.1002/advs.202001379.

[185] D. Brzeski *et al.*, “Design of thermoset composites for high-speed additive manufacturing of lightweight sound absorbing micro-scaffolds,” *Addit. Manuf.*, vol. 47, p. 102245, Nov. 2021, doi: 10.1016/j.addma.2021.102245.

[186] J. Mewis and N. J. Wagner, *Colloidal Suspension Rheology*. Cambridge University Press, 2012.

[187] R. Alfani and G. L. Guerrini, “Rheological test methods for the characterization of extrudable cement-based materials—A review,” *Mater. Struct.*, vol. 38, pp. 239–247, Jan. 2005, doi: 10.1007/BF02479349.

[188] J. Gotro, “Rheology of Thermosets Part 2: Rheometers,” *Polymer Innovation Blog*, Aug. 25, 2014. https://polymerinnovationblog.com/rheology-thermosets-part-2-rheometers/ (accessed Feb. 25, 2023).

[189] C. Kukla, I. Duretek, J. G.-G. and C. Holzer, C. Kukla, I. Duretek, and J. G.-G. and C. Holzer, *Rheology of Highly Filled Polymers*. IntechOpen, 2018. doi: 10.5772/intechopen.75656.

[190] B. Falk and D. McKeever, “Generation and Recovery of Solid Wood Waste in the U.S.,” vol. 53, p. 3, 2012.

[191] N. G. Cherkasova, “How Adding Wood Dust Affects the Properties of Composite Construction Materials,” *IOP Conf. Ser. Earth Environ. Sci.*, vol. 459, p. 032054, Apr. 2020, doi: 10.1088/1755-1315/459/3/032054.

[192] A. N. Papadopoulos, “Advances in Wood Composites,” *Polymers*, vol. 12, no. 1, Art. no. 1, Jan. 2020, doi: 10.3390/polym12010048.

[193] P. Antov, V. Savov, and N. Neykov, “Sustainable bio-based adhesives for eco-friendly wood composites. a review,” *WOOD Res.*, vol. 65, p. 15, Feb. 2020, doi: 10.37763/wr.1336-4561/65.1.051062.

[194] “Additive Manufacturing Materials Market – Industry Reports,” 2019. https://www.industryresearch.co/additive-manufacturing-materials-market-13999766 (accessed Jan. 07, 2022).

[195] S. Whyman, K. M. Arif, and J. Potgieter, “Design and development of an extrusion system for 3D printing biopolymer pellets,” *Int. J. Adv. Manuf. Technol.*, vol. 96, no. 9–12, pp. 3417–3428, Jun. 2018, doi: 10.1007/s00170-018-1843-y.

[196] A. L. Woern, D. J. Byard, R. B. Oakley, M. J. Fiedler, S. L. Snabes, and J. M. Pearce, “Fused Particle Fabrication 3-D Printing: Recycled Materials’ Optimization and Mechanical Properties,” *Materials*, vol. 11, no. 8, Art. no. 8, Aug. 2018, doi: 10.3390/ma11081413.

[197] A. Bagheri and J. Jin, “Photopolymerization in 3D Printing,” *ACS Appl. Polym. Mater.*, vol. 1, no. 4, pp. 593–611, Apr. 2019, doi: 10.1021/acsapm.8b00165.

[198] Y. Ming, Y. Duan, B. Wang, H. Xiao, and X. Zhang, “A Novel Route to Fabricate High-Performance 3D Printed Continuous Fiber-Reinforced Thermosetting Polymer Composites,” *Materials*, vol. 12, no. 9, p. 1369, Jan. 2019, doi: 10.3390/ma12091369.

[199] A. V. Rahul, M. Santhanam, H. Meena, and Z. Ghani, “3D printable concrete: Mixture design and test methods,” *Cem. Concr. Compos.*, vol. 97, pp. 13–23, Mar. 2019, doi: 10.1016/j.cemconcomp.2018.12.014.

[200] D. Dimas, I. Giannopoulou, and D. Panias, “Polymerization in sodium silicate solutions: a fundamental process in geopolymerization technology,” *J. Mater. Sci.*, vol. 44, no. 14, pp. 3719–3730, Jul. 2009, doi: 10.1007/s10853-009-3497-5.

[201] Q. Chen, R. Zhang, D. Qin, Z. Feng, and Y. Wang, “Modification of the Physical-mechanical Properties of Bamboo-plastic Composites with Bamboo Charcoal after Hydrothermal Aging,” *BioResources*, vol. 13, no. 1, pp. 1661–1677, Jan. 2018, doi: 10.15376/biores.13.1.1661-1677.

[202] C. Mamun and M. Arifuzzaman, “Compressive Properties of Sawdust Composites Consisting of Sodium Silicate Solution and Corn Starch as Binder,” vol. 4, pp. 129–136, Jan. 2020, doi: 10.5281/zenodo.3605465.

[203] W. Chai, L. Zhang, W. Li, M. Zhang, J. Huang, and W. Zhang, “Preparation of Plastics- and Foaming Agent-Free and Porous Bamboo Charcoal based Composites Using Sodium Silicate as Adhesives,” *Materials*, vol. 14, no. 10, Art. no. 10, Jan. 2021, doi: 10.3390/ma14102468.

[204] Y. A. Owusu, “Physical-chemistry study of sodium silicate as a foundry sand binder,” *Adv. Colloid Interface Sci.*, vol. 18, no. 1–2, pp. 57–91, Sep. 1982, doi: 10.1016/0001-8686(82)85031-8.

[205] Y. Peng, Y. Han, and D. J. Gardner, “Sodium silicate coated wood,” *Proc. Int. Conv. Soc. Wood Sci. Technol. U. N. Econ. Comm. Eur. Comm. Pp 11–14 Geneva Switz.*, pp. 11–14, 2010.

[206] S. Pratheep Kumar, S. Takamori, H. Araki, and S. Kuroda, “Flame retardancy of clay–sodium silicate composite coatings on wood for construction purposes,” *RSC Adv.*, vol. 5, no. 43, pp. 34109–34116, 2015, doi: 10.1039/C5RA04682C.

[207] L. Ming-Li, L. Chun-Feng, and L. Yan-Long, “Physical and mechanical properties of modified poplar wood by heat treatment and impregnation of sodium silicate solution,” *WOOD Res.*, vol. 64, p. 10, 2019.

[208] C. W. Ng, M. W. Yip, and Y. C. Lai, “The Study on the Effects of Sodium Silicate on Particleboard Made from Sugarcane Bagasse,” *Mater. Sci. Forum*, vol. 911, pp. 66–70, Jan. 2018, doi: 10.4028/www.scientific.net/MSF.911.66.

[209] A. Bifulco *et al.*, “A New Strategy to Produce Hemp Fibers through a Waterglass-Based Ecofriendly Process,” *Materials*, vol. 13, no. 8, p. 1844, Apr. 2020, doi: 10.3390/ma13081844.

[210] K. Korniejenko, E. Frączek, E. Pytlak, and M. Adamski, “Mechanical Properties of Geopolymer Composites Reinforced with Natural Fibers,” *Procedia Eng.*, vol. 151, pp. 388–393, Jan. 2016, doi: 10.1016/j.proeng.2016.07.395.

[211] P. Yu. Mazhirin, “Influence of Various Factors on the Curing of Sodium-Silicate-Based Composites Cured by Carbon Dioxide,” *Int. Polym. Sci. Technol.*, vol. 29, no. 3, pp. 78–82, Mar. 2002, doi: 10.1177/0307174X0202900317.

[212] S. N. Sarmin, J. Welling, A. Krause, and A. Shalbafan, “Investigating the Possibility of Geopolymer to Produce Inorganic-Bonded Wood Composites for Multifunctional Construction Material – A Review,” *BioResources*, vol. 9, no. 4, Art. no. 4, Sep. 2014.

[213] J. R. Brown, “Sodium silicate bonded sand,” in *Foseco Ferrous Foundryman’s Handbook*, Elsevier, 2000, pp. 204–215. doi: 10.1016/B978-075064284-2/50015-6.

[214] L. T. Pham and D. G. Hatzignatiou, “Rheological evaluation of a sodium silicate gel system for water management in mature, naturally-fractured oilfields,” *J. Pet. Sci. Eng.*, vol. 138, pp. 218–233, Feb. 2016, doi: 10.1016/j.petrol.2015.11.039.

[215] E. Katoueizadeh, M. Rasouli, and S. M. Zebarjad, “A comprehensive study on the gelation process of silica gels from sodium silicate,” *J. Mater. Res. Technol.*, vol. 9, no. 5, pp. 10157–10165, Sep. 2020, doi: 10.1016/j.jmrt.2020.07.020.

[216] D. Yoo and B. Yoo, “Rheology of Rice Starch-Sucrose Composites,” *Starch - Stärke*, vol. 57, no. 6, pp. 254–261, 2005, doi: 10.1002/star.200400356.

[217] K. Lewandowski, K. Piszczek, S. Zajchowski, and J. Mirowski, “Rheological properties of wood polymer composites at high shear rates,” *Polym. Test.*, vol. 51, pp. 58–62, May 2016, doi: 10.1016/j.polymertesting.2016.02.004.

[218] M. A. Artner, P. H. G. de Cademartori, F. Avelino, D. Lomonaco, and W. L. E. Magalhães, “A novel design for nanocellulose reinforced urea–formaldehyde resin: a breakthrough in amino resin synthesis and biocomposite manufacturing,” *Cellulose*, vol. 28, no. 6, pp. 3435–3450, Apr. 2021, doi: 10.1007/s10570-021-03739-4.

[219] M. Sandomierski, T. Buchwald, B. Strzemiecka, and A. Voelkel, “Carbon black modified with 4-hydroxymethylbenzenediazonium salt as filler for phenol-formaldehyde resins and abrasive tools,” *J. Appl. Polym. Sci.*, vol. 137, no. 3, p. 48160, 2020, doi: 10.1002/app.48160.

[220] W. Zhu, B. G. Aitken, and S. Sen, “Communication: Non-Newtonian rheology of inorganic glass-forming liquids: Universal patterns and outstanding questions,” *J. Chem. Phys.*, vol. 146, no. 8, p. 081103, Feb. 2017, doi: 10.1063/1.4977085.

[221] X. Yang, W. Zhu, and Q. Yang, “The Viscosity Properties of Sodium Silicate Solutions,” *J. Solut. Chem.*, vol. 37, no. 1, pp. 73–83, Jan. 2008, doi: 10.1007/s10953-007-9214-6.

[222] M. Kaseem, K. Hamad, F. Deri, and Y. G. Ko, “Effect of Wood Fibers on the Rheological and Mechanical Properties of Polystyrene/Wood Composites,” *J. Wood Chem. Technol.*, vol. 37, no. 4, pp. 251–260, Jul. 2017, doi: 10.1080/02773813.2016.1272127.

[223] N. Laufer, H. Hansmann, and M. Koch, “Rheological Characterisation of the Flow Behaviour of Wood Plastic Composites in Consideration of Different Volume Fractions of Wood,” *J. Phys.: Conf. Ser.*, vol. 790, p. 012017, Jan. 2017, doi: 10.1088/1742-6596/790/1/012017.

[224] T. Q. Li and M. P. Wolcott, “Rheology of HDPE–wood composites. I. Steady state shear and extensional flow,” *Compos. Part Appl. Sci. Manuf.*, vol. 35, no. 3, pp. 303–311, Mar. 2004, doi: 10.1016/j.compositesa.2003.09.009.

[225] I. Duretek, S. Schuschnigg, A. Gooneie, G. R. Langecker, and C. Holzer, “Rheological properties of wood polymer composites and their role in extrusion,” *J. Phys.: Conf. Ser.*, vol. 602, p. 012014, Apr. 2015, doi: 10.1088/1742-6596/602/1/012014.

[226] V. Mazzanti and F. Mollica, “A Review of Wood Polymer Composites Rheology and Its Implications for Processing,” *Polymers*, vol. 12, no. 10, p. 2304, Oct. 2020, doi: 10.3390/polym12102304.

[227] R. Pongsawatmanit, T. Temsiripong, S. Ikeda, and K. Nishinari, “Influence of tamarind seed xyloglucan on rheological properties and thermal stability of tapioca starch,” *J. Food Eng.*, vol. 77, no. 1, pp. 41–50, Nov. 2006, doi: 10.1016/j.jfoodeng.2005.06.017.

[228] Y.-H. Feng, D.-W. Zhang, J.-P. Qu, H.-Z. He, and B.-P. Xu, “Rheological properties of sisal fiber/poly(butylene succinate) composites,” *Polym. Test.*, vol. 30, no. 1, pp. 124–130, Feb. 2011, doi: 10.1016/j.polymertesting.2010.11.004.

[229] K. B. Manning *et al.*, “Self Assembly–Assisted Additive Manufacturing: Direct Ink Write 3D Printing of Epoxy–Amine Thermosets,” *Macromol. Mater. Eng.*, vol. 304, no. 3, p. 1800511, Mar. 2019, doi: 10.1002/mame.201800511.

[230] P. Li, Y. Zhang, Y. Zuo, J. Lu, G. Yuan, and Y. Wu, “Preparation and characterization of sodium silicate impregnated Chinese fir wood with high strength, water resistance, flame retardant and smoke suppression,” *J. Mater. Res. Technol.*, vol. 9, no. 1, pp. 1043–1053, Jan. 2020, doi: 10.1016/j.jmrt.2019.10.035.

[231] S. S. Kelley, T. G. Rials, and W. G. Glasser, “Relaxation behaviour of the amorphous components of wood,” *J. Mater. Sci.*, vol. 22, no. 2, pp. 617–624, Feb. 1987, doi: 10.1007/BF01160778.

[232] M. J. Phiri, M. M. Phiri, K. Mpitso, and S. P. Hlangothi, “Curing, thermal and mechanical properties of waste tyre derived reclaimed rubber–wood flour composites,” *Mater. Today Commun.*, vol. 25, p. 101204, Dec. 2020, doi: 10.1016/j.mtcomm.2020.101204.

[233] X. Zhou, J. Yang, D. Su, and G. Qu, “The high-temperature resistant mechanism of α-starch composite binder for foundry,” *J. Mater. Process. Technol.*, vol. 209, no. 14, pp. 5394–5398, Jul. 2009, doi: 10.1016/j.jmatprotec.2009.04.010.

[234] Z. Candan, D. J. Gardner, and S. M. Shaler, “Dynamic mechanical thermal analysis (DMTA) of cellulose nanofibril/nanoclay/pMDI nanocomposites,” *Compos. Part B Eng.*, vol. 90, pp. 126–132, Apr. 2016, doi: 10.1016/j.compositesb.2015.12.016.

[235] R. Subasri and H. Näfe, “Phase evolution on heat treatment of sodium silicate water glass,” *J. Non-Cryst. Solids*, vol. 354, no. 10, pp. 896–900, Feb. 2008, doi: 10.1016/j.jnoncrysol.2007.08.037.

[236] J. C. Domínguez, “Chapter 4 - Rheology and curing process of thermosets,” in *Thermosets (Second Edition)*, Q. Guo, Ed., Elsevier, 2018, pp. 115–146. doi: 10.1016/B978-0-08-101021-1.00004-6.

[237] G. C. Vasconcelos, T. F. A. Santos, C. C. Angrizani, L. A. Sales, M. L. Costa, and E. C. Botelho, “Creep and Aging Evaluation of Phenol–Formaldehyde Carbon Fiber Composites in Overhead Transmission Lines,” *Appl. Compos. Mater.*, Jul. 2021, doi: 10.1007/s10443-021-09935-6.

[238] S. Joseph, S. P. Appukuttan, J. M. Kenny, D. Puglia, S. Thomas, and K. Joseph, “Dynamic mechanical properties of oil palm microfibril-reinforced natural rubber composites,” *J. Appl. Polym. Sci.*, vol. 117, no. 3, pp. 1298–1308, 2010, doi: 10.1002/app.30960.

[239] D. Lüthi *et al.*, “High-resolution carbon dioxide concentration record 650,000–800,000 years before present,” *Nature*, vol. 453, no. 7193, pp. 379–382, May 2008, doi: 10.1038/nature06949.

[240] C. Venet and B. Vergnes, “Stress distribution around capillary die exit: an interpretation of the onset of sharkskin defect,” *J. Non-Newton. Fluid Mech.*, vol. 93, no. 1, pp. 117–132, Sep. 2000, doi: 10.1016/S0377-0257(00)00105-1.

[241] J. Vlachopoulos and D. Strutt, “The Role of Rheology in Polymer Extrusion,” *Extrus. Minitec Conf. Basics Recent Dev.*, pp. 20–21, Jan. 2003.

[242] V. K. R. Kodur, P. P. Bhatt, P. Soroushian, and A. Arablouei, “Temperature and stress development in ultra-high performance concrete during curing,” *Constr. Build. Mater.*, vol. 122, pp. 63–71, Sep. 2016, doi: 10.1016/j.conbuildmat.2016.06.052.

[243] W. Gul, A. Khan, and A. Shakoor, “Impact of Hot Pressing Temperature on Medium Density Fiberboard (MDF) Performance,” *Adv. Mater. Sci. Eng.*, vol. 2017, p. e4056360, Jan. 2017, doi: 10.1155/2017/4056360.

[244] Bilgin Guller, “Effects of heat treatment on density, dimensional stability and color of Pinus nigra wood,” *Afr. J. Biotechnol.*, vol. 11, no. 9, Jan. 2012, doi: 10.5897/AJB11.3052.

[245] P. Izak, L. Ogłaza, W. Mozgawa, J. Mastalska-Popławska, and A. Stempkowska, “Influence of the type of aqueous sodium silicate on the stabilization and rheology of kaolin clay suspensions,” *Spectrochim. Acta. A. Mol. Biomol. Spectrosc.*, vol. 196, pp. 155–159, May 2018, doi: 10.1016/j.saa.2018.02.022.

[246] A. P. Rao, A. V. Rao, and G. M. Pajonk, “Hydrophobic and physical properties of the ambient pressure dried silica aerogels with sodium silicate precursor using various surface modification agents,” *Appl. Surf. Sci.*, vol. 253, no. 14, pp. 6032–6040, May 2007, doi: 10.1016/j.apsusc.2006.12.117.

[247] X. Cheng, “Superhydrophobic sodium silicate based silica aerogel prepared by ambient pressure drying,” *Mater. Chem. Phys.*, vol. 141, Aug. 2013, doi: 10.1016/j.matchemphys.2013.05.064.

[248] A. Bobrowski, B.Stypuła, B. Hutera, A. Kmita, D. Drożyński, and M. Starowicz, “FTIR spectroscopy of water glass - The binder moulding modified by ZnO nanoparticles,” *Metal. -Sisak Then Zagreb*, vol. 4, pp. 477–480, Apr. 2012.

[249] B. Koohestani, P. Mokhtari, E. Yilmaz, F. Mahdipour, and A. K. Darban, “Geopolymerization mechanism of binder-free mine tailings by sodium silicate,”

Constr. Build. Mater., vol. 268, p. 121217, Jan. 2021, doi: 10.1016/j.conbuildmat.2020.121217.

[250] R. Firdous, T. Hirsch, D. Klimm, B. Lothenbach, and D. Stephan, "Reaction of calcium carbonate minerals in sodium silicate solution and its role in alkali-activated systems," *Miner. Eng.*, vol. 165, p. 106849, May 2021, doi: 10.1016/j.mineng.2021.106849.

[251] H. Sayılkan, S. Erdemoğlu, Ş. Şener, F. Sayılkan, M. Akarsu, and M. Erdemoğlu, "Surface modification of pyrophyllite with amino silane coupling agent for the removal of 4-nitrophenol from aqueous solutions," *J. Colloid Interface Sci.*, vol. 275, no. 2, pp. 530–538, Jul. 2004, doi: 10.1016/j.jcis.2004.02.009.

[252] S. Cheng, A. Huang, S. Wang, and Q. Zhang, "Effect of Different Heat Treatment Temperatures on the Chemical Composition and Structure of Chinese Fir Wood," *Bioresources*, vol. 11, pp. 4006–4016, Mar. 2016, doi: 10.15376/biores.11.2.4006-4016.

[253] K. Pillai, A. Mcdonald, and F. Wagner, "Developing a model system in vitro to understand tracheary element development in Douglas-fir (Pseudostuga mensziesii)," *Maderas Cienc. Tecnol.*, vol. 13, pp. 3–18, Jan. 2011, doi: 10.4067/S0718-221X2011000100001.

[254] K. K. Pandey, "A study of chemical structure of soft and hardwood and wood polymers by FTIR spectroscopy," *J. Appl. Polym. Sci.*, vol. 71, no. 12, pp. 1969–1975, 1999, doi: 10.1002/(SICI)1097-4628(19990321)71:12<1969::AID-APP6>3.0.CO;2-D.

[255] C. M. Le and T.-H. Le, "The Study's Chemical Interaction of the Sodium Silicate Solution with Extender Pigments to Investigate High Heat Resistance Silicate Coating," *J. Anal. Methods Chem.*, vol. 2021, p. e5510193, Apr. 2021, doi: 10.1155/2021/5510193.

[256] E. Ukaji, T. Furusawa, M. Sato, and N. Suzuki, "The effect of surface modification with silane coupling agent on suppressing the photo-catalytic activity of fine TiO2 particles as inorganic UV filter," *Appl. Surf. Sci.*, vol. 254, no. 2, pp. 563–569, Nov. 2007, doi: 10.1016/j.apsusc.2007.06.061.

[257] H. Chen, Q. Lang, Z. Bi, X. Miao, Y. Li, and J. Pu, "Impregnation of poplar wood (Populus euramericana) with methylolurea and sodium silicate sol and induction of in-

situ gel polymerization by heating," *Holzforschung*, vol. 68, no. 1, pp. 45–52, Jan. 2014, doi: 10.1515/hf-2013-0028.

[258] A. Valadez-Gonzalez, J. M. Cervantes-Uc, R. Olayo, and P. J. Herrera-Franco, "Chemical modification of henequén fibers with an organosilane coupling agent," *Compos. Part B Eng.*, vol. 30, no. 3, pp. 321–331, Apr. 1999, doi: 10.1016/S1359-8368(98)00055-9.

[259] S.-N. Wang, F.-D. Zhang, A.-M. Huang, and Q. Zhou, "Distinction of four Dalbergia species by FTIR, 2nd derivative IR, and 2D-IR spectroscopy of their ethanol-benzene extractives," *Holzforschung*, vol. 70, no. 6, pp. 503–510, Jun. 2016, doi: 10.1515/hf-2015-0125.

[260] A. Berzins, A. Morozovs, U. Gross, and J. Iejavs, "Mechanical properties of wood-geopolymer composite," presented at the 16th International Scientific Conference "Engineering for Rural Development", Jelgava, Latvia, 24 - 26 May 2017., 2017, pp. 1167–1173. doi: 10.22616/ERDev2017.16.N251.

[261] V. B. Gupta, L. T. Drzal, C. Y.-C. Lee, and M. J. Rich, "The temperature-dependence of some mechanical properties of a cured epoxy resin system," *Polym. Eng. Sci.*, vol. 25, no. 13, pp. 812–823, 1985, doi: 10.1002/pen.760251305.

[262] Y. Tang, H. Su, S. Huang, C. Qu, and J. Yang, "Effect of Curing Temperature on the Durability of Concrete under Highly Geothermal Environment," *Adv. Mater. Sci. Eng.*, vol. 2017, p. e7587853, Jun. 2017, doi: 10.1155/2017/7587853.

[263] Z. Zuhua, Y. Xiao, Z. Huajun, and C. Yue, "Role of water in the synthesis of calcined kaolin-based geopolymer," *Appl. Clay Sci.*, vol. 43, no. 2, pp. 218–223, Feb. 2009, doi: 10.1016/j.clay.2008.09.003.

[264] T. T. Tran, H. Kang, and H.-M. Kwon, "Effect of Heat Curing Method on the Mechanical Strength of Alkali-Activated Slag Mortar after High-Temperature Exposure," *Materials*, vol. 12, no. 11, p. 1789, Jun. 2019, doi: 10.3390/ma12111789.

[265] W. Li, J. Peng, S. Guo, L. Zhang, G. Chen, and H. Xia, "Carbothermic reduction kinetics of ilmenite concentrates catalyzed by sodium silicate and microwave-absorbing characteristics of reductive products," *Chem. Ind. Chem. Eng. Q.*, vol. 19, no. 3, pp. 423–433, 2013, doi: 10.2298/CICEQ120421077L.

[266] M. Zaharescu, L. Predoana, and J. Pandele-Cusu, “Thermal Analysis on Gels, Glasses, and Powders,” in *Handbook of Sol-Gel Science and Technology: Processing, Characterization and Applications*, L. Klein, M. Aparicio, and A. Jitianu, Eds., Cham: Springer International Publishing, 2018, pp. 1833–1867. doi: 10.1007/978-3-319-32101-1_99.

[267] O. Nabinejad, S. Debnath, M. Rahman, and I. Davies, “Effect of filler load on the curing behavior and mechanical and thermal performance of wood flour filled thermoset composites,” *J. Clean. Prod.*, vol. 164, pp. 1145–1156, Oct. 2017, doi: 10.1016/j.jclepro.2017.07.036.

[268] S. N. Sarmin, “The Influence of Different Wood Aggregates on the Properties of Geopolymer Composites,” *Key Eng. Mater.*, vol. 723, pp. 74–79, Dec. 2016, doi: 10.4028/www.scientific.net/KEM.723.74.

[269] Y. Wang, V. Yadama, M.-P. Laborie, and D. Bhattacharyya, “Cure kinetics of PF/PVAc hybrid adhesive for manufacturing profiled wood-strand composites,” *Holzforschung*, vol. 64, pp. 603–608, Aug. 2010, doi: 10.1515/HF.2010.079.

[270] Y. Lei, Q. Wu, and K. Lian, “Cure kinetics of aqueous phenol–formaldehyde resins used for oriented strandboard manufacturing: Analytical technique,” *J. Appl. Polym. Sci.*, vol. 100, no. 2, pp. 1642–1650, 2006, doi: 10.1002/app.23756.

[271] B. Jeong and B.-D. Park, “Effect of molecular weight of urea–formaldehyde resins on their cure kinetics, interphase, penetration into wood, and adhesion in bonding wood,” *Wood Sci. Technol.*, vol. 53, no. 3, pp. 665–685, May 2019, doi: 10.1007/s00226-019-01092-1.

[272] Y. Top, “Waste generation and utilisation in micro-sized furniture-manufacturing enterprises in Turkey,” *Waste Manag.*, vol. 35, pp. 3–11, Jan. 2015, doi: 10.1016/j.wasman.2014.09.028.

[273] A. Laskowska and M. Mamiński, “Properties of particleboard produced from post-industrial UF- and PF-bonded plywood,” *Eur. J. Wood Wood Prod.*, vol. 76, no. 2, pp. 427–435, Mar. 2018, doi: 10.1007/s00107-017-1266-8.

[274] M. W. Feng, G. He, and A. W. Andersen, “Effects of Esters and Resorcinol on Phenolic Resins as Adhesives in Medium-Density Fiberboard Manufacturing,” *Wood Fiber Sci.*, pp. 192–201, Apr. 2010.

[275] G. E. Myers and J. A. Koutsky, “Formaldehyde Liberation and Cure Behavior of Urea-Formaldehyde Resins,” vol. 44, no. 2, pp. 117–126, Jan. 1990, doi: 10.1515/hfsg.1990.44.2.117.

[276] J. Lisperguer, C. Droguett, B. Ruf, and M. Nuñez, “Differential scanning calorimetry and dinamic mechanical analysis of phenol-resorcinol-formaldehyde resins,” *J. Chil. Chem. Soc.*, vol. 50, no. 2, pp. 451–453, Jun. 2005, doi: 10.4067/S0717-97072005000200002.

[277] B. Pang, M.-K. Li, S. Yang, T.-Q. Yuan, G.-B. Du, and R.-C. Sun, “Eco-Friendly Phenol–Urea–Formaldehyde Co-condensed Resin Adhesives Accelerated by Resorcinol for Plywood Manufacturing,” *ACS Omega*, vol. 3, no. 8, pp. 8521–8528, Aug. 2018, doi: 10.1021/acsomega.8b01286.

[278] S. Tohmura, A. Inoue, and S. H. Sahari, “Influence of the melamine content in melamine-urea-formaldehyde resins on formaldehyde emission and cured resin structure,” *J. Wood Sci.*, vol. 47, no. 6, Art. no. 6, Dec. 2001, doi: 10.1007/BF00767897.

[279] K. Siimer, T. Kaljuvee, and P. Christjanson, “Thermal behaviour of urea-formaldehyde resins during curing,” *J. Therm. Anal. Calorim.*, vol. 72, no. 2, pp. 607–617, May 2003, doi: 10.1023/A:1024590019244.

[280] K. Henke, D. Talke, F. Bunzel, B. Buschmann, and C. Asshoff, “Individual layer fabrication (ILF): a novel approach to additive manufacturing by the use of wood,” *Eur. J. Wood Wood Prod.*, vol. 79, no. 3, pp. 745–748, May 2021, doi: 10.1007/s00107-020-01646-2.

[281] M. E. Lamm *et al.*, “Material Extrusion Additive Manufacturing of Wood and Lignocellulosic Filled Composites,” *Polymers*, vol. 12, no. 9, Art. no. 9, Sep. 2020, doi: 10.3390/polym12092115.

[282] F. Murmura and L. Bravi, “Additive manufacturing in the wood-furniture sector: Sustainability of the technology, benefits and limitations of adoption,” *J. Manuf. Technol. Manag.*, vol. 29, no. 2, pp. 350–371, Feb. 2018, doi: 10.1108/JMTM-08-2017-0175.

[283] N. Ayrilmis, “Effect of layer thickness on surface properties of 3D printed materials produced from wood flour/PLA filament,” *Polym. Test.*, vol. 71, pp. 163–166, Oct. 2018, doi: 10.1016/j.polymertesting.2018.09.009.

[284] M. F. Demirbas, M. Balat, and H. Balat, “Potential contribution of biomass to the sustainable energy development,” *Energy Convers. Manag.*, vol. 50, no. 7, pp. 1746–1760, Jul. 2009, doi: 10.1016/j.enconman.2009.03.013.

[285] V. Sharma, H. Roozbahani, M. Alizadeh, and H. Handroos, “3D Printing of Plant-Derived Compounds and a Proposed Nozzle Design for the More Effective 3D FDM Printing,” *IEEE Access*, vol. 9, pp. 57107–57119, 2021, doi: 10.1109/ACCESS.2021.3071459.

[286] Y. Tao, L. Pan, D. Liu, and P. Li, “A case study: Mechanical modeling optimization of cellular structure fabricated using wood flour-filled polylactic acid composites with fused deposition modeling,” *Compos. Struct.*, vol. 216, pp. 360–365, May 2019, doi: 10.1016/j.compstruct.2019.03.010.

[287] B. O. Orji, C. Thie, K. Baker, M. R. Maughan, and A. G. McDonald, “Wood fiber - sodium silicate mixtures for additive manufacturing of composite materials,” *Eur. J. Wood Wood Prod.*, vol. 81, no. 2, Aug. 2022, doi: 10.1007/s00107-022-01861-z.

[288] G. Mashouf Roudsari, A. K. Mohanty, and M. Misra, “Study of the Curing Kinetics of Epoxy Resins with Biobased Hardener and Epoxidized Soybean Oil,” *ACS Sustain. Chem. Eng.*, vol. 2, no. 9, pp. 2111–2116, Sep. 2014, doi: 10.1021/sc500176z.

[289] L. M. H. Carvalho, M. R. N. Costa, and C. A. V. Costa, “A global model for the hot-pressing of MDF,” *Wood Sci. Technol.*, vol. 37, no. 3, pp. 241–258, Dec. 2003, doi: 10.1007/s00226-003-0170-z.

[290] S. K. Romberg *et al.*, “Linking thermoset ink rheology to the stability of 3D-printed structures,” *Addit. Manuf.*, vol. 37, p. 101621, Jan. 2021, doi: 10.1016/j.addma.2020.101621.

[291] I. Poljanšek, B. Likozar, N. Čuk, and M. Kunaver, “Curing kinetics study of melamine–urea–formaldehyde resin/liquefied wood,” *Wood Sci. Technol.*, vol. 47, no. 2, pp. 395–409, Mar. 2013, doi: 10.1007/s00226-012-0503-x.

[292] C. Fuerst, C. Unterweger, S. Senck, B. Plank, and M. Mihalic, *Bio-Based Silicon Carbide Ceramics from Extruded Thermoset-Based Wood Polymer Composites*. 2018.

[293] H. E. Kissinger, “Reaction Kinetics in Differential Thermal Analysis,” *Anal. Chem.*, vol. 29, no. 11, pp. 1702–1706, Nov. 1957, doi: 10.1021/ac60131a045.

[294] L. W. Crane, P. J. Dynes, and D. H. Kaelble, “Analysis of curing kinetics in polymer composites,” *J. Polym. Sci. Polym. Lett. Ed.*, vol. 11, no. 8, pp. 533–540, 1973, doi: 10.1002/pol.1973.130110808.

[295] A. Trubetskaya, G. Beckmann, J. Wadenbäck, J. K. Holm, S. P. Velaga, and R. Weber, “One way of representing the size and shape of biomass particles in combustion modeling,” *Fuel*, vol. 206, pp. 675–683, Oct. 2017, doi: 10.1016/j.fuel.2017.06.052.

[296] A. Atli, K. Candelier, and J. Alteyrac, “Mechanical, Thermal and Biodegradable Properties of Bioplast-Spruce Green Wood Polymer Composites,” *Int. J. Chem. Mater. Biomol. Sci.*, vol. 12, p. 226, May 2018, doi: 10.5281/zenodo.1317160.

[297] M. Cencer, Y. Liu, A. Winter, M. Murley, H. Meng, and B. P. Lee, “Effect of pH on the Rate of Curing and Bioadhesive Properties of Dopamine Functionalized Poly(ethylene glycol) Hydrogels,” *Biomacromolecules*, vol. 15, no. 8, pp. 2861–2869, Aug. 2014, doi: 10.1021/bm500701u.

[298] C.-Y. Hse, F. Fu, and H. Pan, “Melamine-modified urea formaldehyde resin for bonding particleboards,” *For. Prod. J.*, vol. 58, no. 4, p. 6, 2008.

[299] A. Pizzi, H. Pasch, C. Simon, and K. Rode, “Structure of resorcinol, phenol, and furan resins by MALDI-TOF mass spectrometry and 13C NMR,” *J. Appl. Polym. Sci.*, vol. 92, no. 4, pp. 2665–2674, 2004, doi: 10.1002/app.20297.

[300] H. Wang *et al.*, “Characterization of the Low Molar Ratio Urea–Formaldehyde Resin with 13C NMR and ESI–MS: Negative Effects of the Post-Added Urea on the Urea–Formaldehyde Polymers,” *Polymers*, vol. 10, no. 6, Art. no. 6, Jun. 2018, doi: 10.3390/polym10060602.

[301] X. Wang, Y. Deng, Y. Li, K. Kjoller, A. Roy, and S. Wang, “In situ identification of the molecular-scale interactions of phenol-formaldehyde resin and wood cell walls using infrared nanospectroscopy:,” *RSC Adv*, vol. 6, Jul. 2016, doi: 10.1039/C6RA13159J.

[302] C. Gonçalves *et al.*, “Study of the synthesis parameters of a urea-formaldehyde resin synthesized according to alkaline-acid process,” *Int. J. Adhes. Adhes.*, vol. 102, p. 102646, Oct. 2020, doi: 10.1016/j.ijadhadh.2020.102646.

[303] Y. M. Than, S. Suriyarak, and V. Titapiwatanakun, “Rheological Investigation of Hydroxypropyl Cellulose–Based Filaments for Material Extrusion 3D Printing,” *Polymers*, vol. 14, no. 6, Art. no. 6, Jan. 2022, doi: 10.3390/polym14061108.

[304] D. A. Anderson, Y. M. Le Hir, J.-P. Planche, D. Martin, and A. Shenoy, “Zero Shear Viscosity of Asphalt Binders,” *Transp. Res. Rec.*, vol. 1810, no. 1, pp. 54–62, Jan. 2002, doi: 10.3141/1810-07.

[305] P. J. Carreau, “Rheological Equations from Molecular Network Theories,” *Trans. Soc. Rheol.*, vol. 16, no. 1, pp. 99–127, Mar. 1972, doi: 10.1122/1.549276.

[306] S. A. Madbouly, Y. Xia, and M. R. Kessler, “Rheokinetics of Ring-Opening Metathesis Polymerization of Bio-Based Castor Oil Thermoset,” *Macromolecules*, vol. 45, no. 19, pp. 7729–7739, Oct. 2012, doi: 10.1021/ma301458n.

[307] J. Vlachopoulos and N. Polychronopoulos, “Basic Concepts in Polymer Melt Rheology and Their Importance in Processing,” in *Applied Polymer Rheology*, John Wiley & Sons, Ltd, 2011, pp. 1–27. doi: 10.1002/9781118140611.ch1.

[308] J. J. Fallon, S. H. McKnight, and M. J. Bortner, “Highly loaded fiber filled polymers for material extrusion: A review of current understanding,” *Addit. Manuf.*, vol. 30, p. 100810, Dec. 2019, doi: 10.1016/j.addma.2019.100810.

[309] Z. Ahmad, M. Ansell, D. Smedley, and P. M. Tahir, “Creep Behavior of Epoxy-Based Adhesive Reinforced with Nanoparticles for Bonded-In Timber Connection,” *J. Mater. Civ. Eng.*, vol. 24, pp. 825–831, Jul. 2012, doi: 10.1061/(ASCE)MT.1943-5533.0000453.

[310] S. Bechtel, R. Schweitzer, M. Frey, R. Busch, and H.-G. Herrmann, “Material Extrusion of Structural Polymer–Aluminum Joints—Examining Shear Strength, Wetting, Polymer Melt Rheology and Aging,” *Materials*, vol. 15, no. 9, p. 3120, Apr. 2022, doi: 10.3390/ma15093120.

[311] H. Lei and C. E. Frazier, “Curing behavior of melamine-urea-formaldehyde (MUF) resin adhesive,” *Int. J. Adhes. Adhes.*, vol. 62, pp. 40–44, Oct. 2015, doi: 10.1016/j.ijadhadh.2015.06.013.

[312] Y. Yan *et al.*, “Enhancement of Mechanical and Thermal Properties of Poplar through the Treatment of Glyoxal-Urea/Nano-SiO2,” *RSC Adv*, vol. 5, pp. 54148–54155, Jun. 2015, doi: 10.1039/C5RA07294H.

[313] A. Tcherbi-Narteh, M. Hosur, and S. Jeelani, “Effects of Different Montmorillonite Nanoclay Loading on Cure Behavior and Properties of Diglycidyl Ether of Bisphenol A Epoxy,” *J. Nanomater.*, vol. 2016, p. e3840348, Jul. 2016, doi: 10.1155/2016/3840348.

[314] H. A. Barnes, *A handbook of elementary rheology*. Aberystwyth: University of Wales Institute of Non-Newtonian Fluid Mechanics, 2000.

[315] A. Kumar, A. Gupta, and K. V. Sharma, “Thermal and mechanical properties of urea-formaldehyde (UF) resin combined with multiwalled carbon nanotubes (MWCNT) as nanofiller and fiberboards prepared by UF-MWCNT,” *Holzforschung*, vol. 69, no. 2, pp. 199–205, Feb. 2015, doi: 10.1515/hf-2014-0038.

[316] J. Zhang, X. Wang, S. Zhang, Q. Gao, and J. Li, “Effects of Melamine Addition Stage on the Performance and Curing Behavior of Melamine-Urea-Formaldehyde (MUF) Resin,” *BioResources*, vol. 8, no. 4, Art. no. 4, Sep. 2013, doi: doi:10.15376/biores.8.4.5500-5514.

[317] C. Xing, J. Deng, S. Y. Zhang, B. Riedl, and A. Cloutier, “Differential scanning calorimetry characterization of urea-formaldehyde resin curing behavior as affected by less desirable wood material and catalyst content,” *J. Appl. Polym. Sci.*, vol. 98, no. 5, pp. 2027–2032, Dec. 2005, doi: 10.1002/app.22118.

[318] L. Zhonghao, L. Xianjun, Z. Xiaomeng, L. Jianxiong, Z. Chuanling, and X. Kang, “Effects of moisture content on curing characteristics of low molecular mass melamine-urea-formaldehyde (MUF) resin by differential scanning calorimetry (DSC) method,” **北京林**业大学学报, vol. 43, no. 1, pp. 119–126, Feb. 2021, doi: 10.12171/j.1000-1522.20200317.

[319] M. Zolghadr, M. J. Zohuriaan-Mehr, A. Shakeri, and A. Salimi, “Epoxy resin modification by reactive bio-based furan derivatives: Curing kinetics and mechanical properties,” *Thermochim. Acta*, vol. 673, pp. 147–157, Mar. 2019, doi: 10.1016/j.tca.2019.01.025.

[320] C. Li, M.-H. Liu, Z.-Y. Liu, M.-L. Qing, and G. Wang, “DSC and curing kinetics of epoxy resin using cyclohexanediol diglycidyl ether as active diluents,” *J. Therm. Anal. Calorim.*, vol. 116, no. 1, pp. 411–416, Apr. 2014, doi: 10.1007/s10973-013-3471-y.

[321] J. C. Domínguez, M. V. Alonso, M. Oliet, and F. Rodríguez, “Chemorheological study of the curing kinetics of a phenolic resol resin gelled,” *Eur. Polym. J.*, vol. 46, no. 1, pp. 50–57, Jan. 2010, doi: 10.1016/j.eurpolymj.2009.09.004.

[322] B. Riedl and G. He, “Curing kinetics of phenol formaldehyde resin and wood-resin interactions in the presence of wood substrates,” *Wood Sci. Technol.*, vol. 38, no. 1, pp. 69–81, Apr. 2004, doi: 10.1007/s00226-003-0221-5.

[323] S. Kim, H.-J. Kim, H.-S. Kim, Y.-K. Lee, and H.-S. Yang, “Thermal analysis study of viscoelastic properties and activation energy of melamine-modified urea-formaldehyde resins,” *J. Adhes. Sci. Technol.*, vol. 20, no. 8, pp. 803–816, Jan. 2006, doi: 10.1163/156856106777638671.

[324] S. M. Blinder and C. E. Nordman, “Collision theory of chemical reactions,” *J. Chem. Educ.*, vol. 51, no. 12, p. 790, Dec. 1974, doi: 10.1021/ed051p790.

[325] K. Chen *et al.*, “Thermal Degradation Kinetics of Urea–Formaldehyde Resins Modified by Almond Shells,” *ACS Omega*, vol. 6, no. 39, pp. 25702–25709, Oct. 2021, doi: 10.1021/acsomega.1c03896.

[326] Z. Ren, S. Hao, Y. Xing, C. Yang, and S. Dai, “Asymmetric bismaleimide-based high-performance resins with improved processability and high T g over 400 °C,” *High Perform. Polym.*, vol. 31, p. 095400831982636, Feb. 2019, doi: 10.1177/0954008319826368.

[327] X. Cai, B. Riedl, H. Wan, S. Y. Zhang, and X.-M. Wang, “A study on the curing and viscoelastic characteristics of melamine–urea–formaldehyde resin in the presence of aluminium silicate nanoclays,” *Compos. Part Appl. Sci. Manuf.*, vol. 41, no. 5, pp. 604–611, May 2010, doi: 10.1016/j.compositesa.2010.01.007.

[328] M. Popović, J. Miljković, J. B. Simendić, J. Pavličević, and I. Ristić, “Curing characteristics of low emission urea-formaldehyde adhesive in the presence of wood,” *Wood Res.*, vol. 56, p. 12, 2011.

[329] J. Budinski-Simendić, “The Influence of Wood Extracts on the Curing Kinetics of Urea- Formaldehyde Adhesive Studied by Iso-Conversional Method,” *LIGNO*, vol. 9, pp. 153–163, Jan. 2013.

[330] E. S. Wibowo and B.-D. Park, “Cure kinetics of low-molar-ratio urea-formaldehyde resins reinforced with modified nanoclay using different kinetic analysis methods,” *Thermochim. Acta*, vol. 686, p. 178552, Apr. 2020, doi: 10.1016/j.tca.2020.178552.

[331] W. Gao and G. Du, “Curing kinetics of nano cupric oxide (CuO)-modified PF resin as wood adhesive: Effect of surfactant,” *J. Adhes. Sci. Technol.*, vol. 27, pp. 2421–2432, Nov. 2013, doi: 10.1080/01694243.2013.780137.

[332] R. R. de Melo and C. H. S. del Menezzi, “Influence of the density in physical-mechanical properties of particleboards.,” *Silva Lusit.*, vol. 18, no. 1, pp. 59–73, 2010.

[333] H. Younesi-Kordkheili, “Maleated lignin coreaction with phenol-formaldehyde resins for improved wood adhesives performance,” *Int. J. Adhes. Adhes.*, vol. 113, p. 103080, Mar. 2022, doi: 10.1016/j.ijadhadh.2021.103080.

[334] O. Zeleniuc, L.-M. Brenci, C. Cosereanu, and A. Fotin, “Influence of Adhesive Type and Content on the Properties of Particleboard Made from Sunflower Husks,” *BioResources*, vol. 14, no. 3, Art. no. 3, Jul. 2019.

[335] M. M. Maraghi, A. Tabei, and M. Madanipoor, “Effect of board density, resin percentage and pressing temprature on particleboard properties made from mixing of poplar wood slab, citrus branches and twigs of Beech,” *Wood Res.*, vol. 63, pp. 669–682, Jan. 2018.

[336] C. C. Tay, S. Hamdan, and M. S. B. Osman, “Properties of Sago Particleboards Resinated with UF and PF Resin,” *Adv. Mater. Sci. Eng.*, vol. 2016, p. e5323890, Jun. 2016, doi: 10.1155/2016/5323890.

[337] J. Luo, J. Zhang, Q. Gao, A. Mao, and J. Li, “Toughening and Enhancing Melamine–Urea–Formaldehyde Resin Properties via in situ Polymerization of Dialdehyde Starch and Microphase Separation,” *Polymers*, vol. 11, no. 7, p. 1167, Jul. 2019, doi: 10.3390/polym11071167.

[338] H. p. s. Abdul Khalil, A. H. Bhat, M. Jawaid, P. Amouzgar, R. Ridzuan, and M. r. Said, “Agro-wastes: Mechanical and physical properties of resin impregnated oil palm trunk core lumber,” *Polym. Compos.*, vol. 31, no. 4, pp. 638–644, 2010, doi: 10.1002/pc.20841.

[339] P. Mamza, E. Ezeh, E. Gimba, and D. Arthur, “Comparative Study Of Phenol Formaldehyde And Urea Formaldehyde Particleboards From Wood Waste For Sustainable Environment,” *Int. J. Sci. Technol. Res.*, vol. 3, pp. 53–61, May 2021.

[340] W. Xie, S. Huang, D. Tang, S. Liu, and J. Zhao, “Biomass-derived Schiff base compound enabled fire-safe epoxy thermoset with excellent mechanical properties and high glass transition temperature,” *Chem. Eng. J.*, vol. 394, p. 123667, Aug. 2020, doi: 10.1016/j.cej.2019.123667.

[341] X. Huang, S. Chen, S. Wan, B. Niu, X. He, and R. Zhang, “Effect of Phenolic Resin Oligomer Motion Ability on Energy Dissipation of Poly (Butyl Methacrylate)/Phenolic Resins Composites,” *Polymers*, vol. 12, no. 2, Art. no. 2, Feb. 2020, doi: 10.3390/polym12020490.

[342] Md. S. Islam, S. Hamdan, Z. A. Talib, A. S. Ahmed, and Md. R. Rahman, “Tropical wood polymer nanocomposite (WPNC): The impact of nanoclay on dynamic mechanical thermal properties,” *Compos. Sci. Technol.*, vol. 72, no. 16, pp. 1995–2001, Nov. 2012, doi: 10.1016/j.compscitech.2012.09.003.

[343] N. L. M. Hafiz *et al.*, “Curing and thermal properties of co-polymerized tannin phenol–formaldehyde resin for bonding wood veneers,” *J. Mater. Res. Technol.*, vol. 9, no. 4, pp. 6994–7001, Jul. 2020, doi: 10.1016/j.jmrt.2020.05.029.

[344] P. H. G. de Cademartori, M. A. Artner, R. Alves de Freitas, and W. L. E. Magalhães, “Alumina nanoparticles as formaldehyde scavenger for urea-formaldehyde resin: Rheological and in-situ cure performance,” *Compos. Part B Eng.*, vol. 176, p. 107281, Nov. 2019, doi: 10.1016/j.compositesb.2019.107281.

[345] Y. Zhang, M. Park, and S.-J. Park, “Implication of thermally conductive nanodiamond-interspersed graphite nanoplatelet hybrids in thermoset composites with superior thermal management capability,” *Sci. Rep.*, vol. 9, no. 1, Art. no. 1, Feb. 2019, doi: 10.1038/s41598-019-39127-z.

[346] A. Sangregorio, A. Muralidhara, N. Guigo, G. Marlair, E. de Jong, and N. Sbirrazzuoli, “Natural fibre composites with furanic thermoset resins. Comparison between polyfurfuryl alcohol and humins from sugar conversion,” *Compos. Part C Open Access*, vol. 4, p. 100109, Mar. 2021, doi: 10.1016/j.jcomc.2021.100109.

[347] U. Oliveira Costa *et al.*, “Dynamic Mechanical Behavior of Graphene Oxide Functionalized Curaua Fiber-Reinforced Epoxy Composites: A Brief Report,” *Polymers*, vol. 13, p. 1897, Jun. 2021, doi: 10.3390/polym13111897.

[348] B. Guo, D. Zha, B. Li, P. Yin, and P. Li, “Polyvinyl Alcohol Microspheres Reinforced Thermoplastic Starch Composites,” *Materials*, vol. 11, p. 640, Apr. 2018, doi: 10.3390/ma11040640.

[349] M. H. Mat Yazik *et al.*, “Effect of Nanofiller Content on Dynamic Mechanical and Thermal Properties of Multi-Walled Carbon Nanotube and Montmorillonite Nanoclay Filler Hybrid Shape Memory Epoxy Composites,” *Polymers*, vol. 13, no. 5, p. 700, Feb. 2021, doi: 10.3390/polym13050700.

[350] A. Hassan, N. M. M. Abd Rahman, and R. Yahya, “Moisture Absorption Effect on Thermal, Dynamic Mechanical and Mechanical Properties of Injection-Molded Short Glass-Fiber/Polyamide 6,6 Composites,” *Fibers Polym.*, vol. 13, pp. 899–906, Feb. 2012, doi: 10.1007/s12221-012-0899-9.

[351] K. P. Menard and N. R. Menard, “Dynamic Mechanical Analysis in the Analysis of Polymers and Rubbers,” in *Encyclopedia of Polymer Science and Technology*, John Wiley & Sons, Ltd, 2015, pp. 1–33. doi: 10.1002/0471440264.pst102.pub2.

[352] R. Dinu, N. Briand, and A. Mija, “Influence of Keratin on Epoxidized Linseed Oil Curing and Thermoset Performances,” *ACS Sustain. Chem. Eng.*, vol. 9, no. 46, pp. 15641–15652, Nov. 2021, doi: 10.1021/acssuschemeng.1c06112.

[353] Y. Peng, S. Q. Shi, and M. G. Kim, “Effect of temperature on the dynamic mechanical properties of resin film and wood,” *For. Prod. J.*, vol. 58, no. 12, pp. 68–75, Dec. 2008.

[354] Y. Shao, H. Chen, Y. Li, S. Xie, and B. Li, “Sintered metal fibers@carbon molecular sieve membrane (SMFs@CMSM) composites for the adsorptive removal of low concentration isopropanol,” *RSC Adv*, vol. 7, pp. 37604–37611, Jul. 2017, doi: 10.1039/C7RA04984F.

[355] S. Bockel *et al.*, “The role of wood extractives in structural hardwood bonding and their influence on different adhesive systems,” *Int. J. Adhes. Adhes.*, vol. 91, pp. 43–53, Jun. 2019, doi: 10.1016/j.ijadhadh.2019.03.001.

[356] R. Md Salim, J. Asik, and M. S. Sarjadi, “Chemical functional groups of extractives, cellulose and lignin extracted from native Leucaena leucocephala bark,” *Wood Sci. Technol.*, vol. 55, no. 2, pp. 295–313, Mar. 2021, doi: 10.1007/s00226-020-01258-2.

[357] S. Samaržija-Jovanović, V. Jovanović, S. Konstantinović, G. Marković, and M. Marinović-Cincović, “Thermal behavior of modified urea–formaldehyde resins,” *J. Therm. Anal. Calorim.*, vol. 104, no. 3, pp. 1159–1166, Jun. 2011, doi: 10.1007/s10973-010-1143-8.

[358] T. Zorba, E. Papadopoulou, A. Hatjiissaak, K. M. Paraskevopoulos, and K. Chrissafis, “Urea-formaldehyde resins characterized by thermal analysis and FTIR method,” *J. Therm. Anal. Calorim.*, vol. 92, no. 1, pp. 29–33, Apr. 2008, doi: 10.1007/s10973-007-8731-2.

[359] N. Bhandari, B. Dhungana, R. Lach, S. Henning, and R. Adhikari, “Synthesis and Characterization of Urea–Formaldehyde Eco-Friendly Composite Based On Natural Fibers,” *J. Inst. Sci. Technol.*, vol. 24, pp. 19–25, Jun. 2019, doi: 10.3126/jist.v24i1.24623.

[360] K. Salasinska, M. Barczewski, R. Górny, and A. Kloziński, “Evaluation of highly filled epoxy composites modified with walnut shell waste filler,” *Polym. Bull.*, vol. 75, no. 6, pp. 2511–2528, Jun. 2018, doi: 10.1007/s00289-017-2163-3.

[361] J. Liu, R.-Q. Chen, Y.-Z. Xu, C.-P. Wang, and F.-X. Chu, “Resorcinol in high solid phenol−formaldehyde resins for foams production,” *J. Appl. Polym. Sci.*, vol. 134, no. 22, 2017, doi: 10.1002/app.44881.

[362] Y. Wang, W. Liu, Y. Qiu, and Y. Wei, “A One-Component, Fast-Cure, and Economical Epoxy Resin System Suitable for Liquid Molding of Automotive Composite Parts,” *Materials*, vol. 11, p. 685, Apr. 2018, doi: 10.3390/ma11050685.

[363] A. Antunes *et al.*, “Introducing flexibility in urea–formaldehyde resins: Copolymerization with polyetheramines,” *J. Polym. Sci. Part Polym. Chem.*, vol. 56, no. 16, pp. 1834–1843, Aug. 2018, doi: 10.1002/pola.29064.

[364] F. Khammour, A. Ainane, M. Elmatar, A. Kenz, M. Elkouali, and M. Talbi, “Effect of Waste Mint in Urea Formaldehyde Adhesive on the Thermal Degradation of Plywood,” *Orient. J. Chem.*, vol. 34, no. 3, pp. 1375–1379, Jun. 2018, doi: 10.13005/ojc/340325.

[365] P. Bekhta *et al.*, “Properties of Eco-Friendly Particleboards Bonded with Lignosulfonate-Urea-Formaldehyde Adhesives and pMDI as a Crosslinker,” *Materials*, vol. 14, no. 17, Art. no. 17, Jan. 2021, doi: 10.3390/ma14174875.

[366] R. V. Gadhave, P. A. Mahanwar, and P. T. Gadekar, “Factor Affecting Gel Time/Process-Ability of Urea Formaldehyde Resin Based Wood Adhesives,” *Open J. Polym. Chem.*, vol. 7, no. 2, Art. no. 2, May 2017, doi: 10.4236/ojpchem.2017.72003.

[367] D. Kocaefe, X. Huang, and Y. Kocaefe, “Dimensional Stabilization of Wood,” *Curr. For. Rep.*, vol. 1, no. 3, pp. 151–161, Sep. 2015, doi: 10.1007/s40725-015-0017-5.

[368] M. Pervaiz and M. M. Sain, “Carbon storage potential in natural fiber composites,” *Resour. Conserv. Recycl.*, vol. 39, no. 4, pp. 325–340, Nov. 2003, doi: 10.1016/S0921-3449(02)00173-8.

[369] O. US EPA, “Inventory of U.S. Greenhouse Gas Emissions and Sinks,” Feb. 08, 2017. https://www.epa.gov/ghgemissions/inventory-us-greenhouse-gas-emissions-and-sinks (accessed Nov. 09, 2022).

[370] R. L. Ray, V. P. Singh, S. K. Singh, B. S. Acharya, and Y. He, “What is the impact of COVID-19 pandemic on global carbon emissions?,” *Sci. Total Environ.*, vol. 816, p. 151503, Apr. 2022, doi: 10.1016/j.scitotenv.2021.151503.

[371] “U.S. CO2 emissions 2021,” *Statista*. https://www.statista.com/statistics/183943/us-carbon-dioxide-emissions-from-1999/ (accessed Apr. 02, 2023).

[372] J. D. Figueroa, T. Fout, S. Plasynski, H. McIlvried, and R. D. Srivastava, “Advances in CO2 capture technology—The U.S. Department of Energy’s Carbon Sequestration Program,” *Int. J. Greenh. Gas Control*, vol. 2, no. 1, pp. 9–20, Jan. 2008, doi: 10.1016/S1750-5836(07)00094-1.

[373] E. R. McCaslin and C. E. White, “A parametric study of accelerated carbonation in alkali-activated slag,” *Cem. Concr. Res.*, vol. 145, p. 106454, Jul. 2021, doi: 10.1016/j.cemconres.2021.106454.

[374] M. R. Cabral, E. Y. Nakanishi, V. dos Santos, C. Gauss, S. F. dos Santos, and J. Fiorelli, “Evaluation of accelerated carbonation curing in cement-bonded balsa particleboard,” *Mater. Struct.*, vol. 51, no. 2, p. 52, Mar. 2018, doi: 10.1617/s11527-018-1179-y.

[375] S. F. Santos, R. Schmidt, A. E. F. S. Almeida, G. H. D. Tonoli, and H. Savastano, "Supercritical carbonation treatment on extruded fibre–cement reinforced with vegetable fibres," *Cem. Concr. Compos.*, vol. 56, pp. 84–94, Feb. 2015, doi: 10.1016/j.cemconcomp.2014.11.007.

[376] N. Anwar, K. Jalava, and J. Orkas, "Experimental Study of Inorganic Foundry Sand Binders for Mold and Cast Quality," *Int. J. Met.*, Oct. 2022, doi: 10.1007/s40962-022-00897-4.

[377] S. Pasca and I. D. Hartley, "Measuring carbonation depths for estimating CO2 uptake during the lifetime of Wood-Cement Products," *Int. Inorg. Bond. Fiber Compos. Conf.*, p. 10, 2019.

[378] L. Wang *et al.*, "Roles of Biochar and CO2 Curing in Sustainable Magnesia Cement-Based Composites," *ACS Sustain. Chem. Eng.*, vol. 9, no. 25, pp. 8603–8610, Jun. 2021, doi: 10.1021/acssuschemeng.1c02008.

[379] L. Hu, Z. Chen, and J. Hu, "Carbon Sequestration, Mechanical Properties and Carbonation Kinetics of PP-Fiber-Reinforced Cement-Based Composites with CO2-Curing Treatment," *Coatings*, vol. 12, no. 9, Art. no. 9, Sep. 2022, doi: 10.3390/coatings12091339.

[380] L. Wang and D. C. W. Tsang, "Carbon dioxide sequestration on composites based on waste wood," in *Carbon Dioxide Sequestration in Cementitious Construction Materials*, Elsevier, 2018, pp. 431–450. doi: 10.1016/B978-0-08-102444-7.00018-6.

[381] R. G. Liptai, "An experimental study of the effects of additives on the collapsibility of carbon dioxode-sodium silicate bonded foundry cores," p. 51, 1960.

[382] H. Shaik, D. Bhunia, and S. Singh, "An Experimental Investigation of Accelerated Carbonation on Properties of Concrete," *Eng. J.*, vol. 20, pp. 29–38, May 2016, doi: 10.4186/ej.2016.20.2.29.

[383] Y. Jun, S. H. Han, T. Y. Shin, and J. H. Kim, "Effects of CO2 Curing on Alkali-Activated Slag Paste Cured in Different Curing Conditions," *Materials*, vol. 12, no. 21, Art. no. 21, Jan. 2019, doi: 10.3390/ma12213513.

[384] H.-W. Song and S.-J. Kwon, "Permeability characteristics of carbonated concrete considering capillary pore structure," *Cem. Concr. Res.*, vol. 37, no. 6, pp. 909–915, Jun. 2007, doi: 10.1016/j.cemconres.2007.03.011.

[385] L. W. Gallagher and A. G. McDonald, “The effect of micron sized wood fibers in wood plastic composites,” *Maderas Cienc. Tecnol.*, vol. 15, no. 3, pp. 357–374, Oct. 2013, doi: 10.4067/S0718-221X2013005000028.

[386] S. Zhang, Z. Ghouleh, A. Mucci, O. Bahn, R. Provençal, and Y. Shao, “Production of cleaner high-strength cementing material using steel slag under elevated-temperature carbonation,” *J. Clean. Prod.*, vol. 342, p. 130948, Mar. 2022, doi: 10.1016/j.jclepro.2022.130948.

[387] T. R Core, “R: A language and environment for statistical computing. R Foundation for Statistical Computing, Vienna, Austria.” 2020. [Online]. Available: https://www.R-project.org/

[388] A. Zeileis and T. Hawthorne, “Diagnostic checking in regression relationships,” *Diagn. Checking Regres. Relatsh.*, vol. 2, no. 3, pp. 7–10, 2002.

[389] M. Nopens, U. Sazama, S. König, S. Kaschuro, A. Krause, and M. Fröba, “Determination of mesopores in the wood cell wall at dry and wet state,” *Sci. Rep.*, vol. 10, p. 9543, Jun. 2020, doi: 10.1038/s41598-020-65066-1.

[390] M. Miura, H. Kaga, A. Sakurai, T. Kakuchi, and K. Takahashi, “Rapid pyrolysis of wood block by microwave heating,” *J. Anal. Appl. Pyrolysis*, vol. 71, no. 1, pp. 187–199, Mar. 2004, doi: 10.1016/S0165-2370(03)00087-1.

[391] C. Russo, X. Fernández-Francos, and S. De la Flor, “Rheological and Mechanical Characterization of Dual-Curing Thiol-Acrylate-Epoxy Thermosets for Advanced Applications,” *Polymers*, vol. 11, no. 6, Art. no. 6, Jun. 2019, doi: 10.3390/polym11060997.

[392] A. Buis, “The Atmosphere: Getting a Handle on Carbon Dioxide,” *Climate Change: Vital Signs of the Planet*, Oct. 2019. https://climate.nasa.gov/news/2915/the-atmosphere-getting-a-handle-on-carbon-dioxide (accessed Apr. 06, 2023).

[393] W. Du, L. Tan, Y. Zhang, H. Yang, and H. Chen, “Dynamic Rheological Investigation during Curing of a Thermoset Polythiourethane System,” *Int. J. Polym. Sci.*, vol. 2019, p. e8452793, Mar. 2019, doi: 10.1155/2019/8452793.

[394] S. Chen *et al.*, “The effect of polytetrafluoroethylene particle size on the properties of biodegradable poly(butylene succinate)-based composites,” *Sci. Rep.*, vol. 11, Mar. 2021, doi: 10.1038/s41598-021-86307-x.

[395] J. Sun, X. Zhu, X. Wang, R. Lin, and Z. Gao, “Curing Kinetics of Phenol Formaldehyde Resin Modified with Sodium Silicate,” *Appl. Mech. Mater.*, vol. 184–185, pp. 1471–1479, Jun. 2012, doi: 10.4028/www.scientific.net/AMM.184-185.1471.

[396] E. Katoueizadeh, M. Rasouli, and S. M. Zebarjad, “A comprehensive study on the gelation process of silica gels from sodium silicate,” *J. Mater. Res. Technol.*, vol. 9, no. 5, pp. 10157–10165, Sep. 2020, doi: 10.1016/j.jmrt.2020.07.020.

[397] X. Liu, Y. Wu, X. Zhang, and Y. Zuo, “Study on the Effect of Organic Additives and Inorganic Fillers on Properties of Sodium Silicate Wood Adhesive Modified by Polyvinyl Alcohol,” *BioResources*, vol. 10, no. 1, Art. no. 1, Jan. 2015.

[398] B. Asante, J. Appelt, L. Yan, and A. Krause, “Influence of wood pretreatment, hardwood and softwood extractives on the compressive strength of fly ash-based geopolymer composite,” *J. Mater. Sci.*, Mar. 2023, doi: 10.1007/s10853-023-08371-0.

[399] M. Nikzamir, M. Mortezaei, and M. Jahani, “Effect of surface area of nanosilica particles on the cure kinetics parameters of an epoxy resin system,” *J. Appl. Polym. Sci.*, vol. 136, no. 37, p. 47958, 2019, doi: 10.1002/app.47958.

[400] T. X. Phuoc and R.-H. Chen, “Modeling the effect of particle size on the activation energy and ignition temperature of metallic nanoparticles,” *Combust. Flame*, vol. 159, no. 1, pp. 416–419, Jan. 2012, doi: 10.1016/j.combustflame.2011.07.003.

[401] L. K. Abidoye and D. B. Das, “Carbon Storage in Portland Cement Mortar: Influences of Hydration Stage, Carbonation Time and Aggregate Characteristics,” *Clean Technol.*, vol. 3, no. 3, Art. no. 3, Sep. 2021, doi: 10.3390/cleantechnol3030034.

[402] B. Zhan, C. S. Poon, Q. Liu, S. Kou, and C. Shi, “Experimental study on CO2 curing for enhancement of recycled aggregate properties,” *Constr. Build. Mater.*, vol. 67, pp. 3–7, Sep. 2014, doi: 10.1016/j.conbuildmat.2013.09.008.

[403] Z. Wang and J. Hou, “Measurement of CO_2 diffusion coefficients in both bulk liquids and carven filling porous media of fractured-vuggy carbonate reservoirs at 50 MPa and 393 K,” *RSC Adv.*, vol. 11, no. 32, pp. 19712–19722, 2021, doi: 10.1039/D1RA02549J.

[404] M. Mehdikhani, L. Gorbatikh, I. Verpoest, and S. V. Lomov, “Voids in fiber-reinforced polymer composites: A review on their formation, characteristics, and

effects on mechanical performance," *J. Compos. Mater.*, vol. 53, no. 12, pp. 1579–1669, May 2019, doi: 10.1177/0021998318772152.

[405] E. A. Chavez Panduro *et al.*, "Computed X-ray Tomography Study of Carbonate Precipitation in Large Portland Cement Pores," *Cryst. Growth Des.*, vol. 19, no. 10, pp. 5850–5857, Oct. 2019, doi: 10.1021/acs.cgd.9b00864.

[406] H. Bui, F. Delattre, and D. Levacher, "Experimental Methods to Evaluate the Carbonation Degree in Concrete—State of the Art Review," *Appl. Sci.*, vol. 13, no. 4, Art. no. 4, Jan. 2023, doi: 10.3390/app13042533.

[407] C. Liang, B. Pan, Z. Ma, Z. He, and Z. Duan, "Utilization of CO2 curing to enhance the properties of recycled aggregate and prepared concrete: A review," *Cem. Concr. Compos.*, vol. 105, p. 103446, Jan. 2020, doi: 10.1016/j.cemconcomp.2019.103446.

[408] B. L. de S. Costa, J. C. de O. Freitas, D. M. de A. Melo, R. G. da S. Araujo, Y. H. de Oliveira, and C. A. Simão, "Evaluation of density influence on resistance to carbonation process in oil well cement slurries," *Constr. Build. Mater.*, vol. 197, pp. 331–338, Feb. 2019, doi: 10.1016/j.conbuildmat.2018.11.232.

[409] M. Liu, S. Hong, Y. Wang, J. Zhang, D. Hou, and B. Dong, "Compositions and microstructures of hardened cement paste with carbonation curing and further water curing," *Constr. Build. Mater.*, vol. 267, p. 121724, Jan. 2021, doi: 10.1016/j.conbuildmat.2020.121724.

[410] N. Huang, X. Chen, R. Krishna, and D. Jiang, "Two-Dimensional Covalent Organic Frameworks for Carbon Dioxide Capture through Channel-Wall Functionalization," *Angew. Chem. Int. Ed.*, vol. 54, no. 10, pp. 2986–2990, 2015, doi: 10.1002/anie.201411262.

[411] K. Wu, S. Luo, J. Zheng, J. Yan, and J. Xiao, "Influence of carbonation treatment on the properties of multiple interface transition zones and recycled aggregate concrete," *Cem. Concr. Compos.*, vol. 127, p. 104402, Mar. 2022, doi: 10.1016/j.cemconcomp.2021.104402.

[412] B. Kottititum, Q. T. Phung, N. Maes, W. Prakaypan, and T. Srinophakun, "Early Age Carbonation of Fiber-Cement Composites under Real Processing Conditions: A Parametric Investigation," *Appl. Sci.*, vol. 8, no. 2, Art. no. 2, Feb. 2018, doi: 10.3390/app8020190.

[413] L. Wang, S. S. Chen, D. C. W. Tsang, C.-S. Poon, and J.-G. Dai, “CO2 curing and fibre reinforcement for green recycling of contaminated wood into high-performance cement-bonded particleboards,” *J. CO2 Util.*, vol. 18, pp. 107–116, Mar. 2017, doi: 10.1016/j.jcou.2017.01.018.

[414] Z. Shi, A. Leemann, D. Rentsch, and B. Lothenbach, “Synthesis of alkali-silica reaction product structurally identical to that formed in field concrete,” *Mater. Des.*, vol. 190, p. 108562, May 2020, doi: 10.1016/j.matdes.2020.108562.

[415] S. Park, J. G. Jang, and H. K. Lee, “Unlocking the role of MgO in carbonation of alkali-activated slag cements,” *Inorg. Chem. Front.*, vol. 5, Apr. 2018, doi: 10.1039/C7QI00754J.

[416] R. V. Lenth, “Response-Surface Methods in R, Using rsm,” *J. Stat. Softw.*, vol. 32, pp. 1–17, 2010, doi: 10.18637/jss.v032.i07.

[417] D. L. Nguyen, J. Luedtke, M. Nopens, and A. Krause, “Production of wood-based panel from recycled wood resource: a literature review,” *Eur. J. Wood Wood Prod.*, vol. 81, no. 3, pp. 557–570, Jun. 2023, doi: 10.1007/s00107-023-01937-4.

[418] U. Saal, H. Weimar, and U. Mantau, “Wood Processing Residues,” in *Biorefineries*, K. Wagemann and N. Tippkötter, Eds., in Advances in Biochemical Engineering/Biotechnology. Cham: Springer International Publishing, 2019, pp. 27–41. doi: 10.1007/10_2016_69.

[419] A. K. Das, D. A. Agar, M. Rudolfsson, and S. H. Larsson, “A review on wood powders in 3D printing: processes, properties and potential applications,” *J. Mater. Res. Technol.*, vol. 15, pp. 241–255, Nov. 2021, doi: 10.1016/j.jmrt.2021.07.110.

[420] B. Wang, Z. Zhang, Z. Pei, J. Qiu, and S. Wang, “Current progress on the 3D printing of thermosets,” *Adv. Compos. Hybrid Mater.*, vol. 3, no. 4, pp. 462–472, Dec. 2020, doi: 10.1007/s42114-020-00183-z.

[421] P. Zhuo, S. Li, I. A. Ashcroft, and A. I. Jones, “Material extrusion additive manufacturing of continuous fibre reinforced polymer matrix composites: A review and outlook,” *Compos. Part B Eng.*, vol. 224, p. 109143, Nov. 2021, doi: 10.1016/j.compositesb.2021.109143.

[422] J. Jiang and Y.-F. Fu, “A short survey of sustainable material extrusion additive manufacturing,” *Aust. J. Mech. Eng.*, pp. 1–10, Oct. 2020, doi: 10.1080/14484846.2020.1825045.

[423] M. Peerzada, S. Abbasi, K. T. Lau, and N. Hameed, “Additive Manufacturing of Epoxy Resins: Materials, Methods, and Latest Trends,” *Ind. Eng. Chem. Res.*, vol. 59, no. 14, pp. 6375–6390, Apr. 2020, doi: 10.1021/acs.iecr.9b06870.

[424] Q. Shi *et al.*, “Recyclable 3D printing of vitrimer epoxy,” *Mater. Horiz.*, vol. 4, no. 4, pp. 598–607, 2017, doi: 10.1039/C7MH00043J.

[425] B. O. Orji and A. G. McDonald, “Flow, curing and mechanical properties of thermoset resins – wood-fiber blends for potential additive-manufacturing applications,” *Wood Mater. Sci. Eng.*, vol. 0, no. 0, pp. 1–18, 2023, doi: 10.1080/17480272.2022.2155873.

[426] A. Pizzi, H. Pasch, C. Simon, and K. Rode, “Structure of resorcinol, phenol, and furan resins by MALDI-TOF mass spectrometry and 13C NMR,” *J. Appl. Polym. Sci.*, vol. 92, no. 4, pp. 2665–2674, 2004, doi: 10.1002/app.20297.

[427] M. Jouyandeh, S. M. R. Paran, A. Jannesari, and M. R. Saeb, “‘Cure Index’ for thermoset composites,” *Prog. Org. Coat.*, vol. 127, pp. 429–434, Feb. 2019, doi: 10.1016/j.porgcoat.2018.11.025.

[428] K. Olonisakin *et al.*, “Key Improvements in Interfacial Adhesion and Dispersion of Fibers/Fillers in Polymer Matrix Composites; Focus on PLA Matrix Composites,” *Compos. Interfaces*, pp. 1–50, Feb. 2021, doi: 10.1080/09276440.2021.1878441.

[429] N. Sienkiewicz, M. Dominic, and J. Parameswaranpillai, “Natural Fillers as Potential Modifying Agents for Epoxy Composition: A Review,” *Polymers*, vol. 14, no. 2, p. 265, Jan. 2022, doi: 10.3390/polym14020265.

[430] B. Wei *et al.*, “Fabrication and property of discarded denim fabric/polypropylene composites,” *J. Ind. Text.*, vol. 44, no. 5, pp. 798–812, Mar. 2015, doi: 10.1177/1528083714550055.

[431] M. Haque, “Processing and Characterization of Waste Denim Fiber Reinforced Polymer Composites,” *Int. J. Innov. Sci. Mod. Eng. IJISME*, vol. 2, pp. 24–28, May 2014.

[432] R. Temmink, B. Baghaei, and M. Skrifvars, “Development of biocomposites from denim waste and thermoset bio-resins for structural applications,” *Compos. Part Appl. Sci. Manuf.*, vol. 106, pp. 59–69, Mar. 2018, doi: 10.1016/j.compositesa.2017.12.011.

[433] R. Tan, C. K. Sia, Y. K. Tee, K. Koh, and S. Dritsas, “DEVELOPING COMPOSITE WOOD FOR 3D-PRINTING,” p. 10.

[434] M. V. Lobanov, A. I. Gulyaev, and A. N. Babin, “Improvement of the impact and crack resistance of epoxy thermosets and thermoset-based composites with the use of thermoplastics as modifiers,” *Polym. Sci. Ser. B*, vol. 58, no. 1, pp. 1–12, Jan. 2016, doi: 10.1134/S1560090416010048.

[435] A. Hejna, J. Korol, M. Przybysz-Romatowska, Ł. Zedler, B. Chmielnicki, and K. Formela, “Waste tire rubber as low-cost and environmentally-friendly modifier in thermoset polymers – A review,” *Waste Manag.*, vol. 108, pp. 106–118, May 2020, doi: 10.1016/j.wasman.2020.04.032.

[436] C. K. Riew and A. J. Kinloch, Eds., *Toughened Plastics I: Science and Engineering*, vol. 233. in Advances in Chemistry, vol. 233. Washington, DC: American Chemical Society, 1993. doi: 10.1021/ba-1993-0233.

[437] B. J. P. Jansen, K. Y. Tamminga, H. E. H. Meijer, and P. J. Lemstra, “Preparation of thermoset rubbery epoxy particles as novel toughening modifiers for glassy epoxy resins,” *Polymer*, vol. 40, no. 20, pp. 5601–5607, Sep. 1999, doi: 10.1016/S0032-3861(98)00774-5.

[438] C.-W. Su, “Effects of eggshell powder addition on the extrusion behaviour of rice,” *J. Food Eng.*, vol. 79, no. 2, pp. 607–612, Mar. 2007, doi: 10.1016/j.jfoodeng.2006.02.019.

[439] J. W. de L. Souza, N. G. Jaques, M. Popp, J. Kolbe, M. V. L. Fook, and R. M. R. Wellen, “Optimization of Epoxy Resin: An Investigation of Eggshell as a Synergic Filler,” *Materials*, vol. 12, no. 9, p. 1489, May 2019, doi: 10.3390/ma12091489.

[440] B. C. Ang, N. Ahmad, Z. C. Ong, S. C. Cheok, and H. F. Chan, “Study of the mechanical and the thermal insulation properties of polyurethane coating containing chicken eggshell and rice husk ash as fillers,” *Pigment Resin Technol.*, vol. 45, no. 5, pp. 313–319, Jan. 2016, doi: 10.1108/PRT-05-2015-0050.

[441] R. Aradhana, S. Mohanty, and S. K. Nayak, “High performance epoxy nanocomposite adhesive: Effect of nanofillers on adhesive strength, curing and degradation kinetics,” *Int. J. Adhes. Adhes.*, vol. 84, pp. 238–249, Aug. 2018, doi: 10.1016/j.ijadhadh.2018.03.013.

[442] R. L. Whistler and D. I. McGilvray, “Chemistry of the Carbohydrates,” *Annu. Rev. Biochem.*, vol. 23, no. 1, pp. 79–98, 1954, doi: 10.1146/annurev.bi.23.070154.000455.

[443] Y.-P. Wu, Q. Qi, G.-H. Liang, and L.-Q. Zhang, “A strategy to prepare high performance starch/rubber composites: In situ modification during latex compounding process,” *Carbohydr. Polym.*, vol. 65, no. 1, pp. 109–113, Jul. 2006, doi: 10.1016/j.carbpol.2005.12.031.

[444] S. W. Kariuki, J. Wachira, M. Kawira, and G. Murithi, “Formaldehyde Use and Alternative Biobased Binders for Particleboard Formulation: A Review,” *J. Chem.*, vol. 2019, p. e5256897, Oct. 2019, doi: 10.1155/2019/5256897.

[445] M. B. Mensah, J. A. M. Awudza, and P. O’Brien, “Castor oil: a suitable green source of capping agent for nanoparticle syntheses and facile surface functionalization,” *R. Soc. Open Sci.*, vol. 5, no. 8, p. 180824, Aug. 2018, doi: 10.1098/rsos.180824.

[446] I. Chakraborty and K. Chatterjee, “Polymers and Composites Derived from Castor Oil as Sustainable Materials and Degradable Biomaterials: Current Status and Emerging Trends,” *Biomacromolecules*, vol. 21, no. 12, pp. 4639–4662, Dec. 2020, doi: 10.1021/acs.biomac.0c01291.

[447] E. Abbasi, M. Vatankhah, Y. Hosseini, M. Amin Ariana, and M. Ayazi, “Synthesis, structure, and mechanical properties of castor oil-based polyamidoamines toughened epoxy coatings,” *J. Appl. Polym. Sci.*, vol. 128, no. 6, pp. 4023–4030, 2013, doi: 10.1002/app.38583.

[448] E. Aydoğmuş, M. Dağ, Z. G. Yalçın, and H. Arslanoğlu, “Synthesis and characterization of EPS reinforced modified castor oil-based epoxy biocomposite,” *J. Build. Eng.*, vol. 47, p. 103897, Apr. 2022, doi: 10.1016/j.jobe.2021.103897.

[449] I. S. Ristić *et al.*, “The properties of polyurethane hybrid materials based on castor oil,” *Mater. Chem. Phys.*, vol. 132, no. 1, pp. 74–81, Jan. 2012, doi: 10.1016/j.matchemphys.2011.10.053.

[450] N. P. Chauke, H. E. Mukaya, and D. B. Nkazi, “Chemical modifications of castor oil: A review,” *Sci. Prog.*, vol. 102, no. 3, pp. 199–217, Sep. 2019, doi: 10.1177/0036850419859118.

[451] J. H. Wertz, D. J. France, and A. Quye, “Spectroscopic analysis of Turkey red oil samples as a basis for understanding historical dyed textiles,” *Color. Technol.*, vol. 134, no. 5, pp. 319–326, 2018, doi: 10.1111/cote.12343.

[452] M. Tadesse, “SYNTHESIS OF WETTING AGENTS FROM CASTOR OIL FOR THE DYEING OF COTTON FABRIC,” *J. Appl. Res. Rev.*, vol. 1, pp. 1–8, Mar. 2015.

[453] Q. Chen *et al.*, “Turkey Red oil - An effective alkaline extraction booster for enhanced hemicelluloses separation from bamboo kraft pulp and improved fock reactivity of resultant dissolving pulp,” *Ind. Crops Prod.*, vol. 145, p. 112127, Mar. 2020, doi: 10.1016/j.indcrop.2020.112127.

[454] Y. Z. Jadhav, S. D. Deshpande, and M. A. A. Sindhikar, “Manufacturing of sulphated castor oil (Turkey red oil) by sulphonation process,” vol. 5, no. 7, p. 6, 2018.

[455] K. Lewandowski, K. Piszczek, S. Zajchowski, and J. Mirowski, “Rheological properties of wood polymer composites at high shear rates,” *Polym. Test.*, vol. 51, pp. 58–62, May 2016, doi: 10.1016/j.polymertesting.2016.02.004.

[456] T. A. Hassan, V. K. Rangari, R. K. Rana, and S. Jeelani, “Sonochemical effect on size reduction of CaCO3 nanoparticles derived from waste eggshells,” *Ultrason. Sonochem.*, vol. 20, no. 5, pp. 1308–1315, Sep. 2013, doi: 10.1016/j.ultsonch.2013.01.016.

[457] S. Dey *et al.*, “Effect of Flock Age, Egg Weight and Calcium Content of Egg Shell on Fertility and Hatchability of Vanaraja Breeder Chicken Egg,” Oct. 2020.

[458] N. Ononiwu and E. Akinlabi, “Effects of ball milling on particle size distribution and microstructure of eggshells for applications in metal matrix composites,” *Mater. Today Proc.*, vol. 26, pp. 1049–1053, Mar. 2020, doi: 10.1016/j.matpr.2020.02.209.

[459] Q. Zhang *et al.*, “Advances in Organic Rheology-Modifiers (Chemical Admixtures) and Their Effects on the Rheological Properties of Cement-Based Materials,” *Materials*, vol. 15, no. 24, Art. no. 24, Jan. 2022, doi: 10.3390/ma15248730.

[460] Lee Jie Shin, E. G. Barathi Dassan, M. S. Zainol Abidin, and A. Anjang, “Tensile and Compressive Properties of Glass Fiber-Reinforced Polymer Hybrid Composite with

Eggshell Powder," *Arab. J. Sci. Eng.*, vol. 45, no. 7, pp. 5783–5791, Jul. 2020, doi: 10.1007/s13369-020-04561-z.

[461] R. Bhoopathi and M. Ramesh, "Influence of Eggshell Nanoparticles and Effect of Alkalization on Characterization of Industrial Hemp Fibre Reinforced Epoxy Composites," *J. Polym. Environ.*, vol. 28, no. 8, pp. 2178–2190, Aug. 2020, doi: 10.1007/s10924-020-01756-1.

[462] M. Giovino, J. Pribyl, B. Benicewicz, S. Kumar, and L. Schadler, "Linear rheology of polymer nanocomposites with polymer-grafted nanoparticles," *Polymer*, vol. 131, pp. 104–110, Nov. 2017, doi: 10.1016/j.polymer.2017.10.016.

[463] I. O. Mohamed, "Effects of processing and additives on starch physicochemical and digestibility properties," *Carbohydr. Polym. Technol. Appl.*, vol. 2, p. 100039, Dec. 2021, doi: 10.1016/j.carpta.2021.100039.

[464] S. Pramanik, K. Sagar, B. K. Konwar, and N. Karak, "Synthesis, characterization and properties of a castor oil modified biodegradable poly(ester amide) resin," *Prog. Org. Coat.*, vol. 75, no. 4, pp. 569–578, Dec. 2012, doi: 10.1016/j.porgcoat.2012.05.009.

[465] J. J. Florio and D. J. Miller, *Handbook Of Coating Additives*. CRC Press, 2004.

[466] J. Cesarano TIl, T. A. Baer, and P. Calvert, "Recent Developments in Freeform Fabrication of Dense Ceramics From Slurry Deposition," 1997. doi: 10.15781/T2GF0NG4Z.

[467] J. L. R. Armenta and B. A. Salazar-Cruz, *Polymer Rheology*. BoD – Books on Demand, 2018.

[468] L. Lu *et al.*, "Calcium carbonate modified urea–formaldehyde resin adhesive for strength enhanced medium density fiberboard production," *RSC Adv.*, vol. 11, no. 40, pp. 25010–25017, doi: 10.1039/d1ra04316a.

[469] E. Vargun *et al.*, "Thermal degradation of oriental beech wood impregnated with different inorganic salts," *Maderas Cienc. Tecnol.*, vol. 21, no. 2, pp. 163–170, Mar. 2019, doi: 10.4067/S0718-221X2019005000204.

[470] S. P. Dwivedi *et al.*, "Effect of ball-milling process parameters on mechanical properties of Al/Al2O3/collagen powder composite using statistical approach," *J. Mater. Res. Technol.*, vol. 15, pp. 2918–2932, Nov. 2021, doi: 10.1016/j.jmrt.2021.09.082.

[471] S. Yahya, A. Azura, and B. Azahari, “The Influence of Starch Gelatinization on Mechanical Properties of Natural Rubber Latex Films,” *Adv. Mater. Res.*, vol. 1024, pp. 184–188, Aug. 2014, doi: 10.4028/www.scientific.net/AMR.1024.184.

[472] X. Meng *et al.*, “Recycling of denim fabric wastes into high-performance composites using the needle-punching nonwoven fabrication route,” *Text. Res. J.*, vol. 90, no. 5–6, pp. 695–709, Mar. 2020, doi: 10.1177/0040517519870317.

[473] X. Wang, X. Wang, X. Hu, and K. Wu, “Effects of hot extrusion on microstructure and mechanical properties of Mg matrix composite reinforced with deformable TC4 particles,” *J. Magnes. Alloys*, vol. 8, no. 2, pp. 421–430, Jun. 2020, doi: 10.1016/j.jma.2019.05.015.

[474] X. J. Wang *et al.*, “Influences of extrusion parameters on microstructure and mechanical properties of particulate reinforced magnesium matrix composites,” *Mater. Sci. Eng. A*, vol. 528, no. 21, pp. 6387–6392, Aug. 2011, doi: 10.1016/j.msea.2011.04.064.

[475] S. Li, Y. Xu, X. Jing, G. Yilmaz, D. Li, and L.-S. Turng, “Effect of carbonization temperature on mechanical properties and biocompatibility of biochar/ultra-high molecular weight polyethylene composites,” *Compos. Part B Eng.*, vol. 196, p. 108120, Sep. 2020, doi: 10.1016/j.compositesb.2020.108120.

[476] A. Asha and V. Sekhar, “Investigation on the Mechanical Properties of Egg Shell Powder Reinforced Polymeric Composites,” *Int. J. Eng. Res. Technol.*, Oct. 2014, Accessed: Apr. 22, 2023. [Online]. Available: https://www.semanticscholar.org/paper/Investigation-on-the-Mechanical-Properties-of-Egg-Asha-Sekhar/90d5610221e9e38550b4e4b4ae16590dab9f7be3

[477] G. Parande, V. Manakari, S. D. Sharma Kopparthy, and M. Gupta, “A study on the effect of low-cost eggshell reinforcement on the immersion, damping and mechanical properties of magnesium–zinc alloy,” *Compos. Part B Eng.*, vol. 182, p. 107650, Feb. 2020, doi: 10.1016/j.compositesb.2019.107650.

[478] C. E. Montilla-Buitrago, R. A. Gómez-López, J. F. Solanilla-Duque, L. Serna-Cock, and H. S. Villada-Castillo, “Effect of Plasticizers on Properties, Retrogradation, and Processing of Extrusion-Obtained Thermoplastic Starch: A Review,” *Starch - Stärke*, vol. 73, no. 9–10, p. 2100060, Sep. 2021, doi: 10.1002/star.202100060.

[479] M. C. Van Der Burgt, M. E. Van Der Woude, and L. P. B. M. Janssen, “The influence of plasticizer on extruded thermoplastic starch,” *J. Vinyl Addit. Technol.*, vol. 2, no. 2, pp. 170–174, 1996, doi: 10.1002/vnl.10116.

Appendix A

Figure A2.1: Herb Grinder

Figure A2.2: Hamilton Beach Food Processor

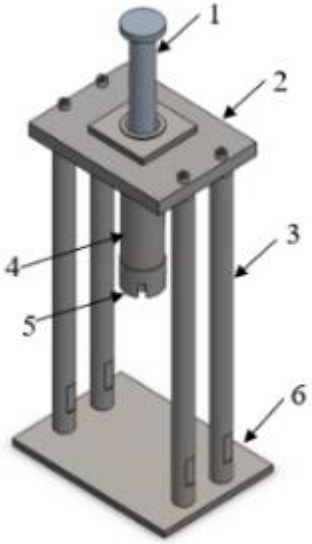

Figure A2.3: Custom-built large capillary rheometer schematic: (1) Plunger, (2) Top Plate, (3) Frame Leg, (4) Barrel, (5) Capillary Die, (6) Base Plate.

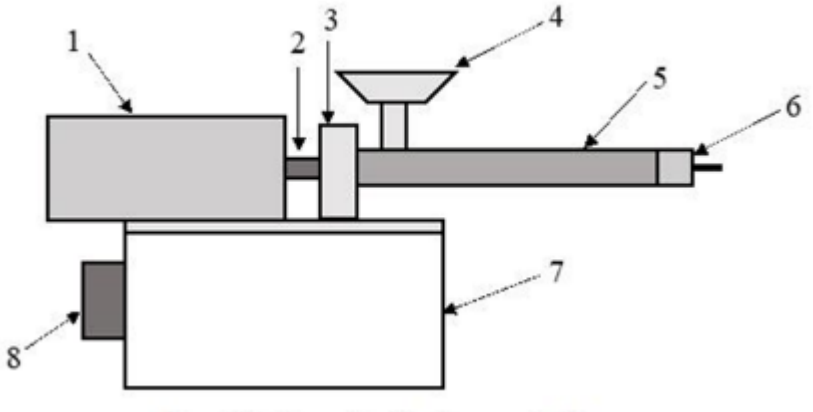

Figure A2.4: Schematic diagram of the developed screw extruder (1) NORD Motor, (2) Shaft Adapter, (3) Bearing Block, (4) Hopper, (5) Barrel, (6) Die, (7) Base, (8) VFD.

Figure A3.1: Wood-resin extruder setup

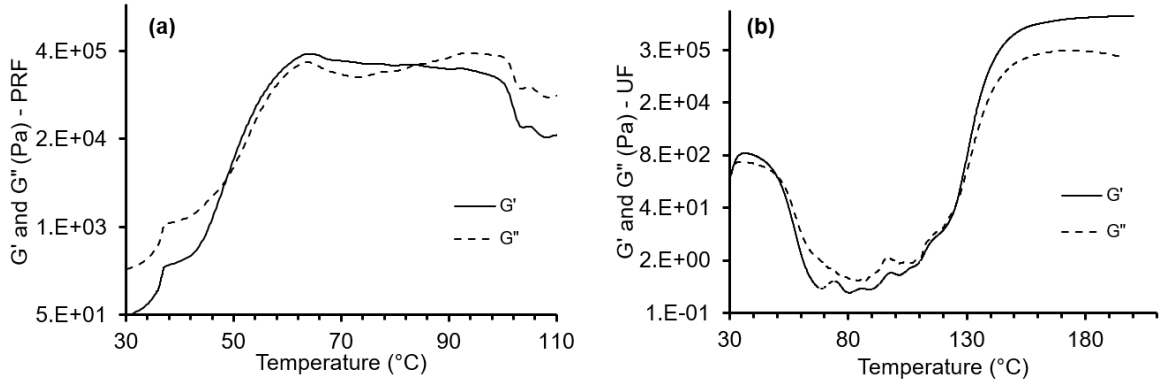

Figure A3.2: G′ and G″ plots versus temperature for (a) neat PRF resin and (b) neat UF resin

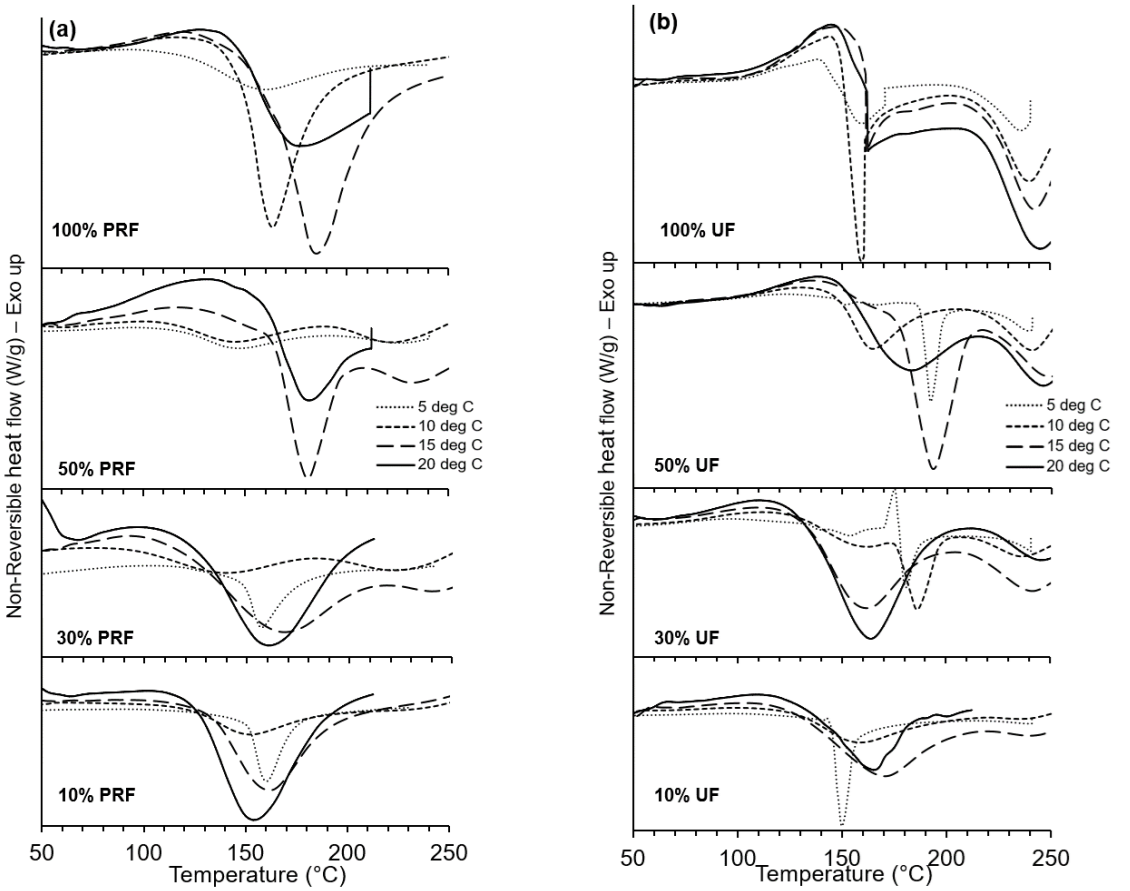

Figure A3.3: Full scale MDSC thermograms showing non-reversible heat flow curves for (a) neat PRF and wood-PRF blends and (b) neat UF and wood-UF blends at four different heating rates